



National Library
of Canada

Bibliothèque nationale
du Canada

Canadian Theses Service

Service des thèses canadiennes

Ottawa, Canada
K1A 0N4

NOTICE

The quality of this microform is heavily dependent upon the quality of the original thesis submitted for microfilming. Every effort has been made to ensure the highest quality of reproduction possible.

If pages are missing, contact the university which granted the degree.

Some pages may have indistinct print especially if the original pages were typed with a poor typewriter ribbon or if the university sent us an inferior photocopy.

Reproduction in full or in part of this microform is governed by the Canadian Copyright Act, R.S.C. 1970, c. C-30, and subsequent amendments.

AVIS

La qualité de cette microforme dépend grandement de la qualité de la thèse soumise au microfilmage. Nous avons tout fait pour assurer une qualité supérieure de reproduction.

S'il manque des pages, veuillez communiquer avec l'université qui a conféré le grade.

La qualité d'impression de certaines pages peut laisser à désirer, surtout si les pages originales ont été dactylographiées à l'aide d'un ruban usé ou si l'université nous a fait parvenir une photocopie de qualité inférieure.

La reproduction, même partielle, de cette microforme est soumise à la Loi canadienne sur le droit d'auteur, SRC 1970, c. C-30, et ses amendements subséquents.

**A time resolved x-ray study of spinodal decomposition in
aluminium-zinc**

by

Jacques Mainville, M.A.Sc.
Department of Physics, McGill University
Montreal, Canada

A Thesis submitted to the Faculty of Graduate Studies and Research
in partial fulfillment of the requirements for the degree of
Doctor of Philosophy

©Jacques Mainville, 1992



National Library
of Canada

Bibliothèque nationale
du Canada

Canadian Theses Service Service des thèses canadiennes

Ottawa, Canada
K1A 0N4

The author has granted an irrevocable non-exclusive licence allowing the National Library of Canada to reproduce, loan, distribute or sell copies of his/her thesis by any means and in any form or format, making this thesis available to interested persons.

The author retains ownership of the copyright in his/her thesis. Neither the thesis nor substantial extracts from it may be printed or otherwise reproduced without his/her permission.

L'auteur a accordé une licence irrévocable et non exclusive permettant à la Bibliothèque nationale du Canada de reproduire, prêter, distribuer ou vendre des copies de sa thèse de quelque manière et sous quelque forme que ce soit pour mettre des exemplaires de cette thèse à la disposition des personnes intéressées.

L'auteur conserve la propriété du droit d'auteur qui protège sa thèse. Ni la thèse ni des extraits substantiels de celle-ci ne doivent être imprimés ou autrement reproduits sans son autorisation.

ISBN 0-315-74828-1

Canada

Abstract

Time resolved small angle x-ray scattering (SAXS) using synchrotron radiation was applied to the study of the kinetics of spinodal decomposition (SD) in an AlZn binary alloy at critical composition quenched into the immiscible region. These millisecond time scale measurements, performed at the National Synchrotron Light Source (Brookhaven National Labs., N.Y.), constitute the first direct experimental verification in a binary alloy of the theory proposed by Langer, Bar-on and Miller in 1975 for SD. A scheme based on the composition distribution functional is proposed to account for the decomposition taking place during the quench. The interatomic mobility, a free energy gradient coefficient and two coefficients that suffice to determine a coarse-grained (intensive) free energy have been obtained in the framework of this theory. The mobilities obtained compare well with tracer diffusion measurements reported in literature. A dependence of the coarse-grained free energy coefficients on the coarse-graining length is found and a procedure is proposed to uniquely choose the values of these coefficients based on the predicted integrated intensity from the equilibrium concentrations and on the measured integrated intensities.

Late-stage coarsening regimes were also investigated. In these regimes, growth exponents higher than the value $1/3$ predicted by the Lifshitz-Slyozov-Wagner theory are obtained. These higher values, comprised between 0.40 and 0.45 are consistent with predictions that alloys in which elastic effects are important can present a transition regime from a $t^{1/3}$ growth law to a $t^{1/2}$ law. The structure factors do not quite scale. They also present a shoulder at high wavevectors, a feature not reported before in metallic alloys.

Résumé

Une étude temporelle de la décomposition spinodale de AlZn par diffusion centrale des rayons X

La diffusion centrale des rayons X *in situ* (SAXS) par rayonnement synchrotron a été appliquée à l'étude de la cinétique de la décomposition spinodale dans un alliage binaire AlZn à la composition critique, trempé dans la région immiscible. Ces mesures à l'échelle du millièème de seconde, effectuées au *National Synchrotron Light Source* du *Brookhaven National Labs.*, constituent la première vérification expérimentale directe dans un alliage binaire de la théorie développée par Langer, Bar-on et Miller en 1975 pour la décomposition spinodale. Une méthode basée sur la fonction de distribution de la composition est proposée pour tenir compte de la décomposition qui a lieu au cours de la trempe. La mobilité interatomique, un coefficient du gradient d'énergie libre et deux coefficients qui suffisent pour quantifier une énergie libre granulée (intensive) hors équilibre ont été obtenus dans le cadre de cette théorie. Les mobilités obtenues sont compatibles avec les mesures de diffusion de traceurs publiées. Les coefficients de l'énergie libre granulée dépendent de la longueur de granulation et une procédure est proposée pour choisir de manière unique les valeurs de ces coefficients. Cette procédure est basée sur les intensités intégrées calculées pour les concentrations à l'équilibre prédites et sur les intensités intégrées mesurées.

Les stades avancés de la décomposition ont également été étudiés. Dans ces régimes, des exposants de croissance supérieurs à $1/3$, la valeur prédite par la théorie de Lifshitz-Slyozov-Wagner, ont été obtenus. Ces valeurs élevées, comprises entre 0.40 et 0.45, sont consistantes avec la prédiction que les alliages pour lesquels les effets élastiques sont importants peuvent présenter un régime de transition passant d'une loi de croissance en $t^{1/3}$ à une loi en $t^{1/2}$. Les facteurs de structure n'obéissent pas tout à fait à une loi d'échelle. Ils présentent également une bosse aux vecteurs d'ondes élevés, ce qui n'a pas été rapporté auparavant pour un alliage métallique.

Acknowledgements

In the first place I would like to recognize the team effort that went into performing the experiments at the NSLS synchrotron. G.B. Stephenson, K. Ludwig Jr., Y.S. Yang, J.L. Jordan-Sweet and M. Sutton all directly contributed to the experiment reported in this thesis.

R. Richter, P. Rudlowski and Z. Altounian introduced me to the preparation of samples by melt spinning and F. Van Gils provided technical assistance. Without their help, sample preparation could not have been so easy.

I am grateful to M. Grant, K.R. Elder, R. Harris and M.J. Zuckermann who taught me a lot about statistical mechanics and critical phenomena. I have benefited enormously from conversations with them. M. Grant also greatly encouraged me during the difficult times. K.R. Elder wrote the computer code used to study the evolution of the structure factors following the theory of Langer, Bar-on and Miller. I am also grateful to J.O. Ström-Olsen and to Z. Altounian for their encouragements.

I would like to express gratitude to our computer system manager, L. Jorgenson, for being available at often uncivilised hours and also just for being so good at stitching loose ends together. I am also grateful to the more recent members of the computer management team, M. Lacasse and P. Mercure, for keeping the aging Frodo running.

D. Koziol and B. Pederson were a great help in dealing with all the administrative aspects of my degree at McGill.

I would like to thank my thesis supervisor Mark Sutton. It was Mark who first suggested I look at the spinodal decomposition in AlZn. Over the course of my work he was always a source of good sound advice. I thank him especially, for his careful reading of the thesis. I would also like to thank H. Fischer who read parts of the manuscript and provided many constructive comments on both style and content.

I express gratitude to all staff members and fellow graduate students at the

Physics Department. You have all contributed to make my stay at McGill a truly memorable experience.

I would like to express my gratitude to the Atmospheric Physics group for the use of their laser printer to print this thesis and to D.H. Ryan for frequent access to his graphics console.

Finally, I would like to thank my wife and my parents for their support and for helping me through the solitary task of "writing up".

Contents

Abstract	i
Résumé	ii
Acknowledgements	iii
Table of Contents	iv
List of Figures	vi
List of Tables	viii
1 Introduction	1
1.1 Motivation and outline	1
1.2 Critical and non-equilibrium phenomena	6
1.3 Solid solutions	10
1.4 Composition fluctuations and diffusion	19
2 Small angle x-ray scattering	31
2.1 X-ray scattering and correlations	31
2.2 Thermal diffuse scattering	35
2.3 Sum rules	37
3 Early descriptions of spinodal decomposition	39
3.1 A foreword	39
3.2 Linear theories	42
3.3 Experimental results	47
4 Experimental Method	63
4.1 Introduction	63
4.2 <i>In situ</i> time resolved x-ray spectra acquisition	65
4.2.1 Synchrotron radiation and the beamline	65
4.2.2 The sample	69
4.2.3 Sample chamber	71
4.2.4 Sample temperature control and measurement	73
4.2.5 Detector and measurement of scattering patterns	76

4.3	Conversion of scattering patterns to absolute structure factors	82
4.4	Temperature calibration	89
4.5	Instrumental resolution	92
4.5.1	Convolution	94
4.5.2	Deconvolution	97
5	Theoretical background	102
5.1	Coarse-grained free energy functional	103
5.2	Equation of motion for the non-equilibrium structure factor	107
5.3	Estimates of the importance of nonlinear terms	111
5.4	The Langer–Bar-on–Miller Theory	116
5.4.1	Equation of motion	116
5.4.2	Scaled LBM equation of motion	120
5.5	Late stages	124
5.5.1	Growth law	126
5.5.2	Scaling forms	134
6	Results and discussion	140
6.1	The data	140
6.2	Fit to early stage theories	150
6.2.1	An attempt at the CHC linear equation	150
6.2.2	The LBM scheme	155
6.2.3	Fit results	158
6.2.4	Coarse-graining length dependence of τ , u , κ and M	163
6.2.5	The coherent solubility curve	174
6.2.6	Interdiffusion	179
6.2.7	Breakdown of LBM	184
6.3	Late stages	188
6.3.1	Growth law and scaling	188
6.3.2	Interface width correction	197
7	Conclusions	203
	References	208

List of Figures

1.1	Phase separation process	2
1.2	Phase diagram for AlZn	11
1.3	Regular solution model for AlZn	14
1.4	Thermodynamic driving force	23
1.5	Estimates of the gradient energy coefficient κ	30
2.1	Standard definition of \mathbf{q}	32
3.1	Schematic morphologies of phase separation mechanisms	40
3.2	Amplification factor for Cahn's equation of motion	43
3.3	Equilibrium scattering due to thermal fluctuations	45
3.4	Structure factor evolution for the CHC equation of motion	46
4.1	IBM-MIT beamline X-20C	67
4.2	Setup in the hutch	70
4.3	Sample chamber	72
4.4	Nominal temperature during two runs	75
4.5	Dark current	79
4.6	Parasitic scattering	80
4.7	Scattering patterns measured at 541 K	81
4.8	Schematic of beamstop operation	83
4.9	Efficiency of the PSD	87
4.10	$S(q, t)$ at 541 K	88
4.11	Ornstein-Zernike structure factors for temperature calibration	91
4.12	Scattering geometry	95
4.13	Beam profile	98
4.14	PSD response function	99
4.15	Deconvolution examples	101
5.1	Coarse-grained free energy	105
5.2	Scaled LBM structure factor	123
5.3	Late stage coarsening configurations	130
5.4	Fratzl-Lebowitz scaling form	136
5.5	Ohta-Nozaki scaling form	138
6.1	Quenched-in scattering for three runs	142

6.2	Parametrization of quenched-in scattering for all runs	143
6.3	LBM fit below T_c	144
6.4	LBM fit above T_c	146
6.5	Integrated intensities	148
6.6	Integrated intensities parameterization results	151
6.7	Comparison of early stages $S(q, t)$ with CHC	153
6.8	Best fit LBM parameters κ , r , u and M	161
6.9	Best fit values of b_0 in LBM	162
6.10	Wavevector cutoff q_{max} for all early stage runs	165
6.11	Coupling term $A(t)$ and $b(t)$ for LBM for two values of α	166
6.12	One-point composition density functional $\rho\{\delta c\}$	167
6.13	Contributions to LBM equation	168
6.14	Coherent solubility line calculated from data	175
6.15	Mean field correlation length and coexistence line	176
6.16	Contact between the regular solution free energy and the Landau-Ginzburg free energy functional	178
6.17	Interdiffusivity	182
6.18	Breakdown of LBM after early stages	186
6.19	Late time coarsening with LBM	187
6.20	Scaling plot for run BB ($T = 537$ K)	189
6.21	Logarithmic scaling plot for run BB ($T = 537$ K)	190
6.22	Fratzl-Lebowitz scaling form for run BB ($T = 537$ K)	192
6.23	Porod plot for run CC ($T = 563$ K)	193
6.24	Late stages power law fits to $S_m(t)$ and $q_m^{-1}(t)$	194
6.25	Effective exponent for late stages runs	196
6.26	Interfacial width correction to Porod tails	199
6.27	Ohta-Nozaki scaling form with interfacial width correction (run BB)	201
6.28	Porod plot with interface width prefactor to $\Delta S(q, t)$ (run BB)	202

List of Tables

1.1	Critical exponents	9
1.2	Physical parameters for $\text{Al}_{0.62}\text{Zn}_{0.38}$	17
3.1	Work to date involving AlZn alloys	51
6.1	List of runs	141
6.2	Values of ϵ and τ	164
6.3	Zn tracer diffusion in $\text{Al}_{0.62}\text{Zn}_{0.38}$	180
6.4	Growth law parameters	195
6.5	Width correction parameters	200

Chapter 1

Introduction

1.1 Motivation and outline

Phase transitions and more generally, non-equilibrium phenomena, are presently at the center of intense scientific activity. This field has experienced a marked growth due both to advances in theoretical tools, such as renormalization group (RG) theory in the early seventies, and to improvements in the experimental techniques such as the use of intense x-ray radiation from synchrotron storage rings. This thesis is concerned primarily with a specific non-equilibrium phenomenon known as spinodal decomposition (SD) which occurs when a system of uniform density is forced into an unstable state resulting in the decomposition into regions of two different densities.

As well as testing current understanding of non-equilibrium phenomena, the study of SD presents technological importance since the use of kinetic measurements allows for the determination of atomic diffusivities in the solid-state. Indeed, SD theories are based directly on the concept of a thermodynamic driving force for diffusion in nonideal one-phase systems. Thus, comparison of theory and experiment on the kinetics of the early stage of SD also tests our fundamental understanding of interdiffusion in the one-phase region.

This thesis presents a study of SD in a binary alloy of Al and Zn. This binary alloy is isomorphous to many important physical systems such as ferromagnetic, superconducting and normal metal mixtures and vapour-liquid mixtures, binary fluids.

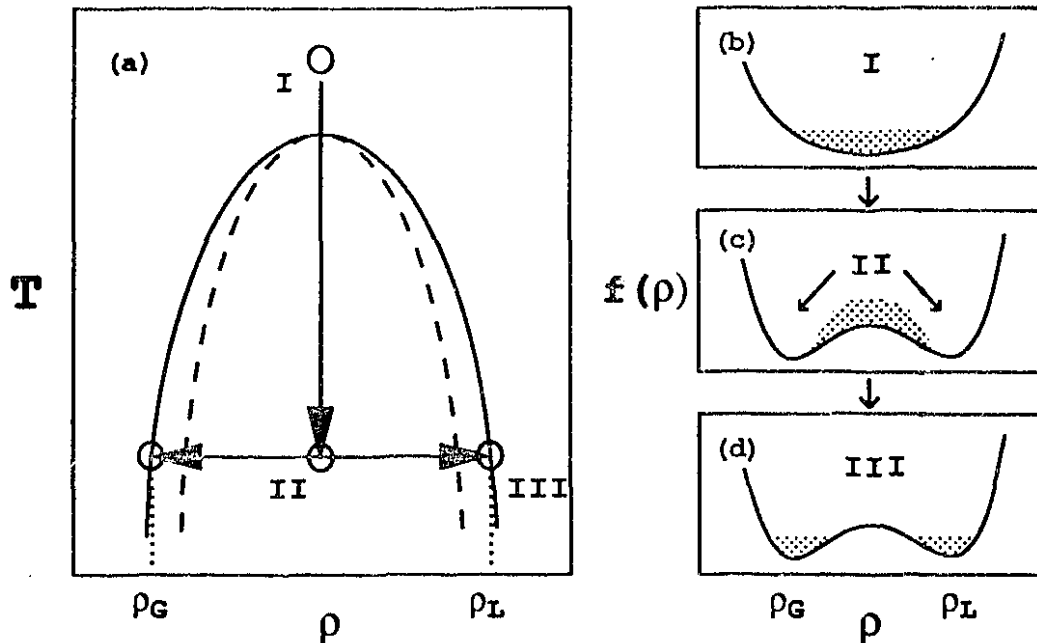


Figure 1.1: Representative description of a gas-liquid phase separation process. In (a) the phase diagram is represented with regions I, II and III the vapour, the coexistence and the liquid regions respectively. The arrows show a quench into the unstable region (II) followed by the phase separation into liquid (III) and vapour. The dotted line corresponds to the classical spinodal. In (b), (c) and (d) a “non-equilibrium” bulk free energy is plotted as a function of the density, ρ . The dots schematically represent the one point distribution function. In (b) the system is in single phase equilibrium. In (c) the system is in an unstable non-equilibrium state immediately following the quench from the single phase region. In (d) the system has reached final two phase equilibrium. (Courtesy of K.R. Elder.[1])

Before proceeding to describe the specifics of the $Al_{50}Ni_{50}$ alloy, some of the essential features of phase transitions can be understood by using an everyday example, the boiling of water (a vapour-liquid mixture). Schematically, the constant-volume phase diagram of water may be represented as in Figure (1.1). The important feature of this phase diagram is the presence of a coexistence region (region II). This is a region of forbidden density (ρ) which exists at temperatures below a critical temperature (T_c). If water is prepared at a density and temperature in this region it will spontaneously decompose into a high density liquid in equilibrium with a low density gas (*i.e.* it will boil). As the temperature is increased, the density difference between the gas and liquid phases decreases. At T_c the density difference becomes zero and above T_c , there is no longer a transition. The curve that bounds the co-

existence region and gives the densities $\rho_G(T)$ and $\rho_L(T)$ of the coexisting phases is called the coexistence line (the solid line in Part (a)).

The forbidden region of densities is only strictly forbidden in thermodynamic equilibrium. Superheated water and supercooled steam are proof that water can exist at temperatures and densities within the coexistence region, at least temporarily.

The coexistence region can be subdivided into two regions based upon thermodynamic stability. In one region water is said to be metastable and in the other unstable. The metastable region exists below T_c near the coexistence line. Water prepared with a density in the metastable region by a rapid decrease in pressure for example, must first overcome a nucleation barrier for it to decompose into liquid (water) and gas (steam). The kinetics of the transition in this region are determined by the nucleation of droplets and their subsequent growth. As the density of the initial state is forced further away from the coexistence line, the nucleation barrier decreases until it disappears altogether. Water forced into this barrier-free region is unstable and begins to phase separate on all length scales. Water forced to boil this way phase separates by spinodal decomposition. Similarly, the arrows on Fig. (1.1a) describe a temperature quench and the subsequent process of spinodal decomposition of gas into a mixture of liquid and steam. Parts (b), (c) and (d) of this figure show the bulk free energy $f(\rho)$ corresponding respectively to the high temperature state, the unstable state and the final coexistence state (two minima). Classical theories, exemplified by the Van der Waals equation of state, predict a sharp distinction between metastability and instability. Modern theories of phase transitions show that this sharp distinction is only an artifact of mean field theories. The dashed curve on Fig. (1.1a) which separates the metastable and the unstable region is called the spinodal line.

Alloys are essentially solid mixtures. Not unlike the phase diagram for a vapour-liquid mixture, some present a temperature-composition domain where the constituent atoms are not soluble in the ratios making up a given composition: the coexistence region, here called a region of immiscibility, or a miscibility gap.

The coexistence line now gives the compositions of the two coexisting phases. The maximum temperature of this region is also called the critical temperature and the corresponding composition is the critical composition. Phase segregation also occurs in other systems which possess a miscibility gap following a quench into that region from the one-phase region. Examples are binary fluids and polymer mixtures. The kinetics of the phase unmixing in these systems is an issue of both theoretical and practical interest as a typical example of non-equilibrium phenomena.[2,3]

The process of phase segregation when quenching an alloy, a liquid or a polymer from a uniform state into the miscibility gap can be conceptually divided into two stages. During the early stage, the initial phase transforms into domains of the final phase(s), driven by a bulk free-energy difference. During the late stage, the domains of the final phase(s) coarsen, driven by the interfacial free energy. The early stage of a first-order phase transition is expected to be either a nucleated process or, as is the case in the present work, a spinodal (continuous) process, depending upon whether the initial phase is metastable or unstable as in the case of the vapour-liquid mixture.[4]

The main subject of this thesis is the study of early-stage homogeneous phase decomposition (SD) in AlZn close to the critical composition by small angle x-ray scattering (SAXS). Though the phase separation in this alloy has been extensively investigated by conventional methods such as resistance and magnetic susceptibility measurements, transmission electron microscopy (TEM) and small angle x-ray and neutron scattering (SAXS and SANS), there are no early time measurements available for the separation near the composition of maximum separation rate (the critical composition). Previous studies of SD in AlZn have only been done at compositions or temperatures well removed from the critical point.

Time resolved small angle x-ray scattering (SAXS) offers a powerful experimental probe to study phase separation since the detailed kinetics of non-equilibrium states can be followed by the direct measure of fluctuations. The quantity measured is the time evolution of the equal-time two-point composition correlation

function (cf. § 2.1). The experiments were performed with synchrotron radiation at the National Synchrotron Light Source (NSLS), using beam line IBM-MIT X20C (Brookhaven National Laboratory). With the use of synchrotron x-ray sources for the study of dynamic phenomena, *in situ* time-resolved x-ray scattering is now possible on time scales orders of magnitudes shorter than with conventional x-ray sources.[5] To achieve subsecond time resolution, the synchrotron source is combined with a fast detector system, a beamline geometry to enhance high photon fluxes and a temperature controller capable of rapid quenches. Ref. [6] shows that it is possible with the experimental setup employed to acquire a complete diffraction pattern as fast as every 3 ms.

As mentioned above, this thesis raises two major aspects of interest in current research. From a fundamental point of view, this work yields new insight into the non-equilibrium process of SD. More specifically, the collected data provides a direct and quantitative experimental verification of a nonlinear theory proposed by Langer, Bar-On and Miller (LBM) in 1975.[7] The kinetic parameters obtained within the framework of this theory are the atomic mobility, a gradient free energy coefficient and two coefficients that suffice to determine a coarse-grained (intensive) free energy.

The second aspect follows from the coarse-grained free energy and the inter-diffusion coefficient obtained by using the LBM theory. These parameters have important predictive power for thermal and mechanical stability in all technological materials. Despite their importance, very little is known about them from phase decomposition experiments. In particular, no satisfactory diffusion model has been tested to interpret the kinetic parameters from x-ray data for early stage SD, when composition gradients are small. Sustained efforts have been given to the study of solid state diffusion. In particular, the use of synchrotrons to study diffusivity has gained recognition in the materials community[8]. To predict mixing or unmixing characteristics of materials, it is necessary first to know the diffusive properties.

The outline of this dissertation is the following. The remainder of the Introduction will examine fundamentals of critical phenomena, of solid solutions and of

solid-state diffusion. These concepts constitute the essential background to the work of this thesis. Chapter II presents an introduction to small angle scattering (SAS). This is followed by an historic perspective on SD which includes the presentation of a classical linear theory and a survey of measurements (Ch. III). Emphasis will be placed on measurements in AlZn alloys and on experimental methods. The description of the experimental procedure for the present work is given in Chapter IV, with particular attention given to the application of state-of-the-art time resolved SAXS and to the requirements to be met to produce data orders of magnitudes faster than achieved by previous workers. Necessary calibrations and data reduction are also described. The LBM theory is introduced in Chapter V. The presentation and discussion of the measurements in Chapter VI are divided in two parts: the “early stages” ($t < 1.6$ s) and the “late stages” (to $10 \lesssim t \lesssim 55$ s). It is in the framework of the LBM theory that the early stage data is analysed (§ 6.2). Late-stage considerations are also introduced (§ 5.5), and put to the test with the late stage measurements (§ 6.3). The results and discussion that form the body of Chapter VI especially shed light on the characteristic length inherent to the description of the LBM theory. The resulting predicted equilibrium phase diagram and interdiffusion constant are compared with that of the classical models and measurements.

1.2 Critical and non-equilibrium phenomena

In Figure (1.1), at low temperatures there is a rather large difference between the liquid and gas densities, ρ_L and ρ_G . However, as the critical temperature is approached this density difference tends to zero. The existence of a quantity which is non-zero below T_c and zero above T_c is a common feature associated with the critical points of a wide variety of physical systems. In the study of critical phenomena, the quantity $\rho_L - \rho_G$ is called the order parameter for the liquid-gas critical point.[9]

The region near T_c and ρ_c in the liquid-vapor phase diagram is of particular interest. Over a century ago, it was discovered during measurements on carbon

dioxide that when held in a state close to but above the critical point, this gas scattered incident light strongly. The phenomenon was called critical opalescence and opened up the field of critical phenomena.

There is a simple qualitative explanation for critical opalescence. Above T_c , the gas molecules move freely, with random collisions. As the temperature nears T_c , the time spent by the molecules near one (or more) molecules during collision events increases, and the interaction between molecules starts to play a role in their spatial distribution. Small "droplets" of correlated molecules start to appear. As the critical point is approached still closer, the droplets grow in their dimensions. In fact, when the fluid is brought close enough to its critical point for these droplets to acquire lateral dimensions on the order of the wavelength of light, the light is scattered strongly giving rise to the phenomenon of critical opalescence. These droplets, though not stable and constantly forming and dissolving, exist in sufficient number at any given time to produce the effect.

The boiling of water at the critical density has all the features of a continuous phase transition since the order parameter varies in a continuous way as T passes through T_c . Phase transitions are classified as first or second order if the order parameter is discontinuous or continuous at the transition temperature. Thus the phase transition of water at the critical density is a second order transition. First order phase transitions have discontinuous first derivatives of the free energy, such as the latent heat. Second order phase transitions have continuous first derivatives.

The qualitative picture offered for the behavior of a CO_2 as it approached T_c only required one condition: that the position of molecules be correlated over a certain range. The length scale of this correlation, the correlation length ξ , is the characteristic length scale of critical phenomena. It may be thought of as being roughly the diameter of a "droplet". At the critical point, the correlation length ξ diverges. In this region, characteristic functions such as the specific heat and the susceptibility also diverge due to the divergence of ξ . Indeed, the physically measurable extensive quantities follow simple power laws near the critical point. An

example of the singularities observed at T_c is that of the isothermal compressibility

$$K_T(T) = \frac{1}{\rho} \left(\frac{\partial \rho}{\partial P} \right)_T. \quad (1.1)$$

In a $\rho - P$ phase diagram, the isotherms acquire a flat portion in the immediate vicinity of the critical point. Thus the slope $(\partial P / \partial \rho)_T$ becomes zero as $T \rightarrow T_c^+$ and $K_T(T)$ diverges to infinity. Considering the huge density fluctuations associated with critical opalescence, it is not surprising that the response of the density to a very small pressure fluctuation is infinite. In fact, in § 2.3 the density fluctuations will be shown to be directly related to the isothermal compressibility (or equivalently, to the differential susceptibility when the system is probed by x-rays) and hence to the derivative $(\partial \rho / \partial P)_T$.

The singular functions observed at T_c are given in terms of power-laws and the exponents are called critical exponents. For instance, introducing a reduced temperature ε as

$$\varepsilon \equiv 1 - \frac{T}{T_c}, \quad (1.2)$$

K_T is described by

$$\begin{aligned} K_T &\sim (-\varepsilon)^{-\gamma'} & (\varepsilon < 0) \\ &\sim (\varepsilon)^{-\gamma} & (\varepsilon \geq 0). \end{aligned} \quad (1.3)$$

An important element of critical phenomena is the universality of the singular functions in the critical regions of the phase diagrams, of very differing systems. Guggenheim was the first to recognize this fact when he found that the temperature dependence of the liquid-gas density difference $\rho_L - \rho_G$ (the order parameter) for various fluids, properly normalized, fall on one and the same curve.[10] Effectively, this corresponds to the following critical relation

$$\rho_L - \rho_G \sim \varepsilon^\beta. \quad (1.4)$$

There are universal classes generic to critical regions in which many physical systems with differing order parameters fall into, leading to the same critical exponents. Thus the description of critical phenomena in the liquid-vapour system can

Exponent	Definition	Value		Quantity
		Mean field	Ising 3d	
α	$C_V \sim A\epsilon^{-\alpha}$	0	0.12	specific heat
β	$(\delta c)_{\text{coex}} \sim \pm B\epsilon^\beta$	$\frac{1}{2}$	0.339	coexistence curve
γ	$\chi_s \sim C\epsilon^{-\gamma}$	1	1.25	differential susceptibility
ν	$\xi \sim \xi_0\epsilon^{-\nu}$	$\frac{1}{2}$	0.62	correlation length
η	$G(r) \sim \frac{W}{r^{3-2+\eta}}$ ($\epsilon = 0$)	0	$\frac{1}{18}$	pair correlation function ¹

Table 1.1: Power law relations for critical phenomena in binary alloys with critical exponent values for the mean field approximation and the Ising 3d Monte Carlo model. The critical amplitudes are given by A , B , C , ξ_0 and W in this Table. ϵ is the reduced temperature as defined by Eq. (1.2) and r is the radial distance in $G(r)$. The Ising 3d exponents are quoted from Refs. [11,12].

¹The pair correlation function will be formally introduced in § 2.1.

apply to binary alloys with a miscibility gap. The order parameter in a binary alloy is the composition difference between the bulk and any of the two coexisting phases, $(\delta c)_{\text{coex}}$. This quantity near the critical point maps onto the density difference $\rho_L - \rho_C$ of the liquid-vapour system.[9] Eq. (1.4) now takes the form ($\epsilon < 1$)

$$(\delta c)_{\text{coex}} \propto \epsilon^\beta. \quad (1.5)$$

Table (1.1) lists the power laws with the corresponding critical exponents for thermodynamics response functions relevant in this work. The differential susceptibility, χ_s , is given instead of the isothermal compressibility for convenience since x-ray scattering is performed. These two quantities are essentially equivalent and possess the same critical exponent, γ . Expressions for the differential susceptibility will be derived in § 2.1. The notation for the critical amplitudes (A , B , etc.) is also introduced in Table (1.1). Numerical values are given for the case of mean field interactions and for numerical simulation results from Monte Carlo studies with an Ising 3d model.

Table (1.1) describes the thermodynamics, *i.e.* the statics, of a system such as a binary alloy near T_c . The universal character of the singular functions makes it such

that the study of a particular system can yield insight into very differing systems. Non-equilibrium systems also present some unifying characteristics. These systems are described by a (somewhat larger) number of standard models. Two such models are the "model A" with a nonconserved order parameter only (the crystallization of amorphous alloys, Glauber Monte Carlo dynamics, etc.), and "model B" with a conserved order parameter only (the phase separation in a binary alloy as studied here, Kawasaki Monte Carlo dynamics, etc.)[13] The study of non-equilibrium systems attempts to describe as accurately as possible the dynamic evolution of the structure of the system by equations of motion based on these models. Thus the equations of motion should apply to physical systems which can be very different provided they can be described by the same dynamic model. Not unlike the study of the thermodynamics of critical phenomena, the study of the dynamics of a particular system can also be mapped onto very differing systems. Hence, the study of the dynamics of SD in the binary alloy AlZn (model B) in the critical region has relevance in many physical systems displaying critical behavior as it constitutes a probe of a model equation of motion for the structure.

Although the dynamics of phase separation are studied, the best fit values of the parameters that enter the model equation to describe the time-evolution of the system will be compared against the predictions from critical phenomena. This provides a self-consistency check on the model equation as well as on the calibration of the experimental measurements.

1.3 Solid solutions

This section introduces the miscibility gap of the AlZn phase diagram and estimates of the classical lines that limit the metastable (the solvus) and unstable regions (the spinodal). To achieve this, the classical conditions for phase stability are first summarized and applied to a classical model of solid solutions. The description of alloys used here corresponds essentially to a mean field theory.

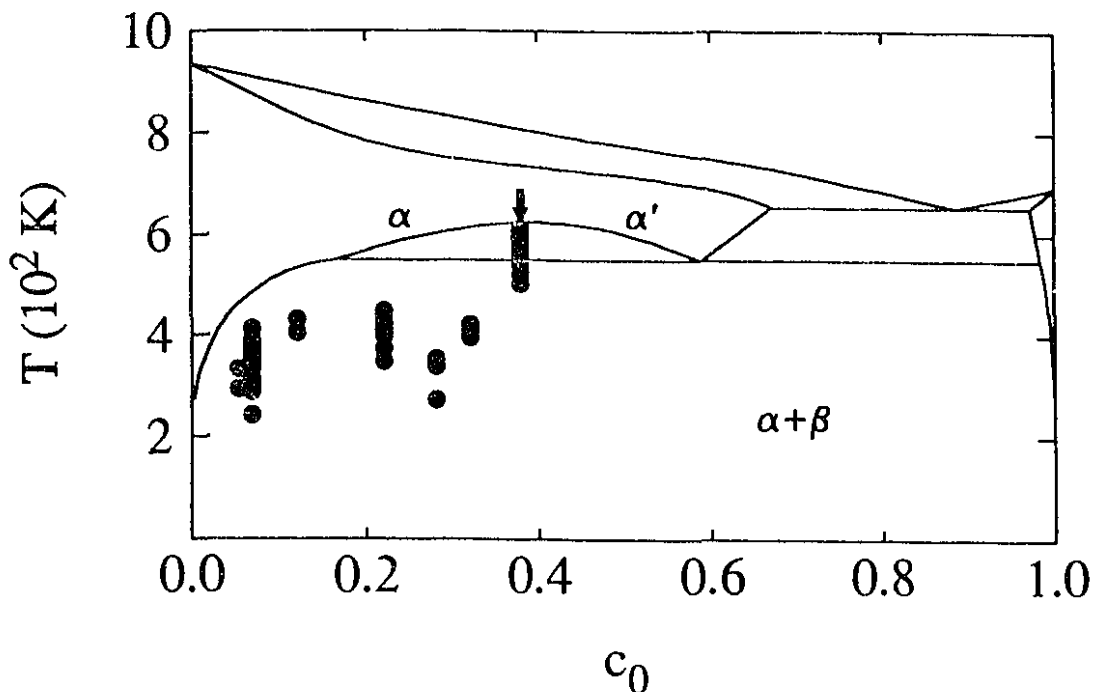


Figure 1.2: Phase diagram for AlZn. The compositions and aging temperatures of published studies of spinodal decomposition are shown (this will be the topic of § 3.3 and Table 3.1) along with those of the present study (below the arrow). (c_0 is the atomic fraction of Zn.)

Before proceeding, it is important to become familiar with the phase diagram for AlZn (Fig. 1.2).[14,15] The Al-Zn system is a eutectic system and involves a monotectoid reaction and a miscibility gap in the solid state. The top of the miscibility gap, the critical point, lies at 624.5 K and at $c_0 = 0.395$.¹ Either side of the miscibility gap has a face centered cubic (fcc) solid solution which only differs in lattice parameter as the ratio of Al to Zn atoms differ. The Al-rich phase is usually denoted as α Al and the Zn-rich phase as α' Al. The eutectoid reaction (α' Al \rightleftharpoons α Al + Zn) is located at 550 K with compositions for α' Al, α Al and β Zn of 0.59, 0.165 and 0.984 respectively. The (Al) liquidus and solidus descend to a eutectic equilibrium with close packed hexagonal (Zn) at 654 K.

From the first law of thermodynamics, a system at equilibrium everywhere will not perform any work, *i.e.* there must not be any gradient in the thermodynamic

¹Unless stated otherwise, the concentrations c_0 will be given in atomic fractions of Zn, thus 0.395 is equivalent to 39.5 at. % Zn.

potential at any location. This can only be accomplished when the thermodynamic potential of the system is at a minimum value. In a solid, the independent variables are pressure and temperature, and the intensive value of the thermodynamic potential should be the chemical potential of each atomic species at equilibrium. Therefore, it is appropriate to consider the Gibbs free energy (also called the excess enthalpy)

$$G = H - TS \quad (1.6)$$

where H is the enthalpy and S the entropy. The area inside a two phase region, the miscibility gap, cannot in principle be described by thermodynamics since a system cannot be kept in such a state forever. However, just as in the case of superheated water or supercooled steam mentioned in § 1.1, a system can be pushed into a state away from equilibrium in this region. An extension of the thermodynamic potential from the one-phase region can be performed and used to describe whether the state reached is expected to be metastable or unstable. This is described below.

Figure (1.1a) showed two curves (solid and dashed) separating three regions on the liquid-vapour phase diagram. These regions correspond to composition ranges of the non-equilibrium free energy $f(\rho)$ after a quench, shown in Part (b) and (c), namely two convex regions separated by a concave region.² The spinodal line which bounds the concave region corresponding to unstable states is given by the locus of all points where $\frac{\partial^2 G}{\partial c^2} = 0$.³ The coexistence line is given by the points of contact of the common tangent to the two convex regions of $G(c, T)$ since this is the free energy a mixture of phases would have. In solids for which the phase diagram presents a miscibility gap such that two phases coexist at equilibrium, the spinodal line is obtained as in the case of the liquid-vapour system. The compositions of the two phases coexisting at equilibrium also satisfy the common tangent construct *i.e.* the

²A function $f(x)$ is a convex function of x providing the cord joining the points $f(x_1)$ and $f(x_2)$ lies above or on the curve $f(x)$ for all x in the interval $x_1 < x < x_2$. A function $f(x)$ is a concave function of x if the function $-f(x)$ is convex.[9]

³The origin of the term "spinodal" decomposition comes from the appearance of the turning points of an isotherm in a G-P diagram, looking like cusps or spinodes.[16]

two phases must have equal chemical potentials. The relative fraction of the two phases satisfy the lever rule.

Models of solid solution are based on simplifying assumptions. Without these, the treatment of solid solutions, in particular near a discontinuity in the solubility, quickly becomes a formidable task. Modeling of the equilibrium phase diagram often starts from ideal solution theory which considers a mixture of noninteracting atoms, *i.e.* a system with no heat of mixing ($H = 0$ in Eq. 1.6) and only configurational contribution to the entropy. The free energy of mixing per atom is then

$$g_m(c_0, T) = RT [c_0 \ln c_0 + (1 - c_0) \ln(1 - c_0)] \quad (1.7)$$

where R is Rydberg's constant (8.314 J/(mol·K)). The value $g_m(c_0, T)$ differs from the chemical potential $\mu = \mu_{Al} = \mu_{Zn}$ only by a linear offset. Indeed if μ_i^0 ($i = Al, Zn$) is the chemical potential in the pure constituent then $g_m = c_0 \Delta\mu_{Al} + (1 - c_0) \Delta\mu_{Zn}$ where $\Delta\mu_i \equiv \mu_i - \mu_i^0$.

The departure from an ideal mixture is accomplished by modeling the interaction between the atoms. To first order, the interaction will depend on the composition and the temperature. The enthalpy of mixing can thus be phenomenologically obtained by fitting a chosen polynomial in c_0 and T to reproduce the experimentally obtained boundary of the miscibility gap. Model equations generally differ in the form of the polynomials used to express the temperature and composition dependence of the mixing energy. They correspond to the presence of mean field interactions between atoms and are analogous to the zeroth order approximation in numerical simulations. These models are referred to in literature as "regular solution models", owing this appellation to the regular behavior of the physical quantities with composition (a solution having ideal configurational entropy and an enthalpy of mixing which varies parabolically with composition[17]).

Unlike liquids, in crystalline solids atoms are arranged into a lattice. To maintain the lattice coherency when local composition fluctuations occur, coherency stresses exist and the associated (elastic) strain energies contribute to the Gibbs free energy. This coherency constraint changes both the solubility limits and the

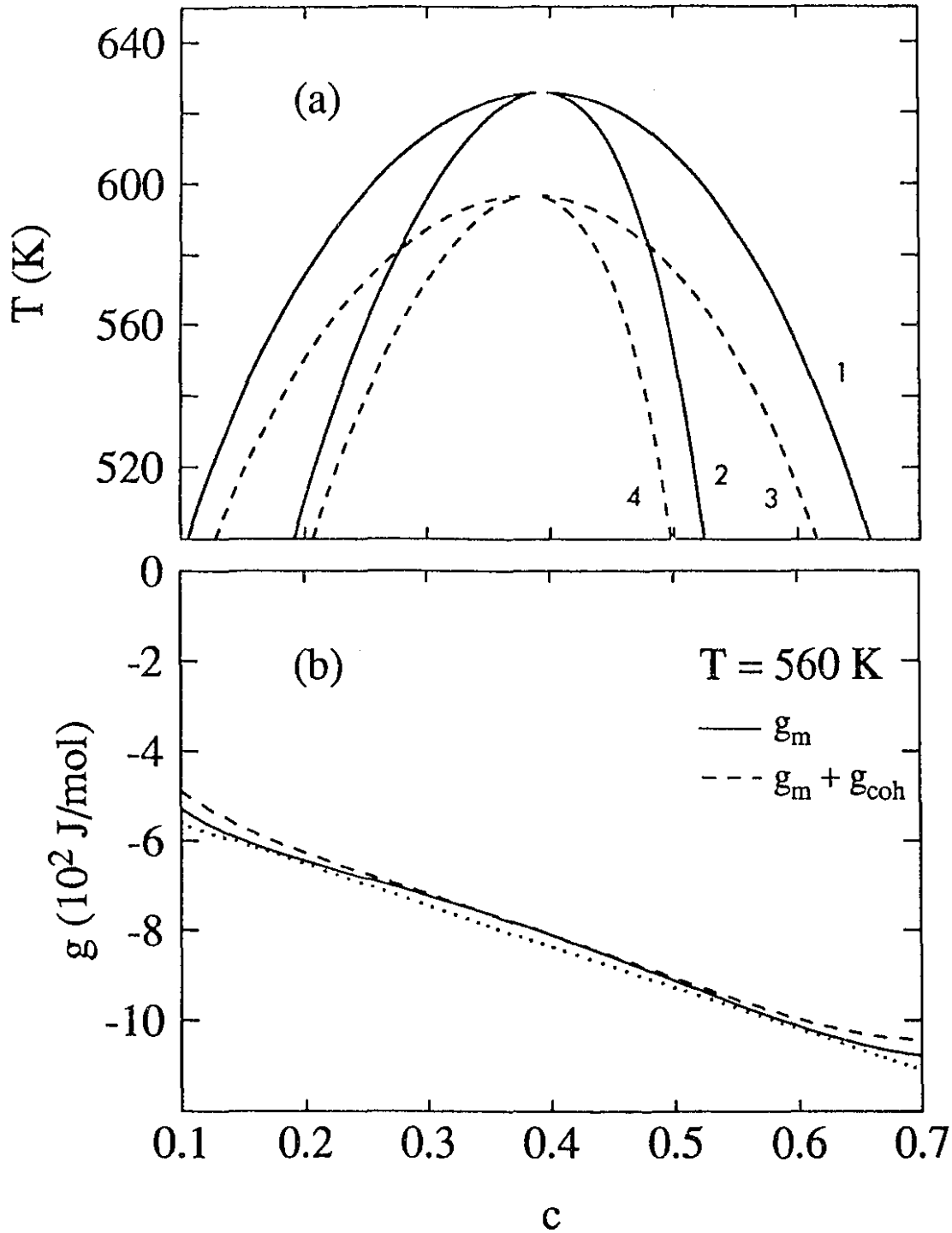


Figure 1.3: (a) Incoherent (chemical) coexistence and spinodal lines (1 and 2 respectively), coherent coexistence and spinodal lines (3 and 4 respectively) from calculations by a regular solution model for AlZn with $c_0 = 0.395$ (see text). (b) Excess enthalpy (Gibbs free energy) at 560 K with g_m the mixing contribution and g_{coh} the elastic strain energy contribution. The coexisting phases have compositions $c_\alpha = 0.176$ and $c_{\alpha'} = 0.593$. The inflection points ($\partial^2 g / \partial c^2 = 0$) of $g_m + g_{coh}$ (the dashed line) are located at $c = 0.279$ and 0.462 and define the coherent spinodal. The dotted line shows the common tangent to the chemical free energy.

limits of metastability. Thus for solids coherent and incoherent (also called chemical) boundaries can be calculated depending upon whether the strain energy has been included in the free energy or not. Figure (1.3a) shows four curves. The solid lines (1 and 2) are the coexistence line, also called the solvus, and the spinodal line for the incoherent free energy and are similar to those introduced in Fig. (1.1) for the liquid water - vapour system.⁴ The dashed lines (3 and 4) represent the corresponding coherent solvus and the coherent spinodal line. The top of the dashed lines is the critical composition to coherent fluctuations. The incoherent solvus (1) bounds the solubility (or miscibility) gap and is thus the boundary appearing on Fig. (1.2). The incoherent spinodal (2) has the same maximum and is inside the incoherent solvus. The region of metastability lies between the incoherent solvus (1), and the the coherent spinodal (4) which represents the true limit of metastability. Thus, the coherency constraint is responsible for the lowering of the spinodal line from the chemical spinodal (2) *i.e.* it effectively causes a shift of the unstable region (where $\frac{\partial^2 G}{\partial c^2} < 0$) to a lower temperature. Consequently, the (coherent) critical point does not touch the stable region (above the solvus) and the region of metastability above the unstable region is extended to lower temperatures. The strain energy can be looked at as stabilizing the system against infinitesimal composition fluctuations for some undercooling below the chemical spinodal.[4]

The construction of the curves on Fig. (1.3a) is now described. To this effect, two parametrizations of the chemical miscibility gap currently existing in the literature are examined. They differ by the possibility of existence of an upper miscibility gap in the AlZn alloy. The simplest diagram, with no upper miscibility gap, was presented in Fig. (1.2).⁵ It is not the purpose of this work to determine which parametrization is more accurate. In both cases, the parameters needed were found by fitting the free energy *versus* concentration curves to reproduce the miscibility

⁴It should be emphasized that the dashed lines in Fig. (1.3) do not all represent spinodals as was the case in Fig. (1.1).

⁵The diagram with an upper miscibility gap is shown in Ref. [18]. For a comparison of the two, see Ref. [19].

gap. The parametrization without an upper miscibility gap was chosen to produce Fig. (1.3a) as it is most frequently quoted in the more recent literature (most often reproduced from Ref. [20]). In this parametrization initiated by Lašek[21] the miscibility gap as measured by Münster *et al.*[22] is reproduced by modeling the correction to the ideal free energy of mixing (Eq. 1.7) by

$$g_m(c_0, T) = RT [c_0 \ln c_0 + (1 - c_0) \ln(1 - c_0)] + c_0(1 - c_0)\Omega(c_0, T) R \quad (1.8)$$

where

$$\Omega(c_0, T) = D + E c_0 + F T + H T c_0 \quad (1.9)$$

with $D = 1244$, $E = -1512$, $F = 0.219 \text{ K}^{-1}$ and $H = 1.795 \text{ K}^{-1}$. The coexistence line (curve 1) is obtained by performing Maxwell's construction⁶ on isotherms of the chemical potential. Since the parameters entering the empirical relation for g_m were chosen from fits to the coexistence line, reproducing it in this way provides a check on the model. It is important for the work in this thesis to note that the solvus is asymmetric in composition. The chemical spinodal (curve 2) is obtained by finding the roots of $\partial^2 g_m / \partial c^2$. The top of the calculated chemical spinodal coincides with the top of the solvus at $c_0 = 0.395$ and 625.6 K . These values agree well with the generally accepted location of the top of the chemical solvus (*cf.* p. 11).

The derivation of the coherent curves (3 and 4) is difficult when elastic anisotropy is included. Thus, to simplify, the alloy is assumed isotropic. The elastic energy introduced by lattice distortions depends on Poisson's ratio ν , on Young's modulus E , and on the fractional change in lattice parameter a with composition $\eta = (1/a)(da/dc)$, evaluated at the average composition c_0 [4]:

$$g_{coh} = (c - c_0)^2 \eta^2 Y, \quad (1.10)$$

⁶Maxwell's construction consists essentially in finding the values of c_α and $c_{\alpha'}$ such that

$$\int_{c_\alpha}^{c_{\alpha'}} \frac{\partial g_m(c, T)}{\partial c} dc = 0.$$

Symbol	$\text{Al}_{0.62}\text{Zn}_{0.38}$	
a_0	$4.054 \times 10^{-10} \text{ m}$	FCC unit cell side ¹ [24]
N_{NV}	$6.00 \times 10^{28} \text{ atoms/m}^3$	atomic density ²
η	-2.5×10^{-2}	relative change of lattice parameter ^{1,3} [24]
ν	0.34	Poisson's ratio[4]
E	$[-0.0010T + 1.1] \times 10^{-11} \text{ J/m}^3$	Young's modulus[23]
ρ/μ	$12.53 \text{ m}^2/\text{kg}$	mass absorption coefficient ⁴

Table 1.2: Physical parameters for $\text{Al}_{0.62}\text{Zn}_{0.38}$. T is the absolute temperature.

¹Extrapolated from measured values above the miscibility gap.

²Calculated from the value of a_0 .

³The value $\eta = -0.023$ is used in g_{coh} for the calculations based on the Lašek parametrization of the free energy (Eqs. 1.8 and 1.9).

⁴Calculated in § 4.3.

where the usual definition for Y has been used, $Y \equiv E/(1 - \nu)$. Values of η and ν for $\text{Al}_{0.62}\text{Zn}_{0.38}$ are given in Table (1.2). The empirical relationship used for the temperature and concentration dependence of E was obtained by Kardasev *et al.*[23] based on a comprehensive measurement in the composition range 0 — 0.629 (given in Table 1.2 for $c_0 = 0.38$). At the average alloy concentration c_0 , the strain energy does not raise the free energy.

The common tangent was found for $g_m + g_{coh}$ by using Maxwell's construction in order to obtain the coherent coexistence line (curve 3), and the coherent spinodal (curve 4) was found by determining the roots of $(\partial^2 g_m / \partial c^2) + (\partial^2 g_{coh} / \partial c^2) = 0$. The calculated coherent spinodal lies entirely inside the chemical spinodal. The depression of the temperature of the coherent curves below the chemical curves, depends on the magnitude of η . The profile of the coherent curves will also depend on the bulk alloy composition, c_0 .

The obtained coherent spinodal is asymmetric in composition as shown on Fig. (1.3a) and the coherent critical point (the top of the coherent spinodal) is at

a lower composition (0.383 at 597 K) than the incoherent critical point (top of the solvus and, identically, of the incoherent spinodal at $c_0 = 0.395$).⁷

In Fig. (1.3b), isotherms ($T = 560$ K) are shown for the free energy with and without the coherency energy (dashed and solid lines respectively). The common tangent to g_m is also shown as a dotted line and the tangency points correspond to the coexistence compositions c_α and $c_{\alpha'}$ (points on curve (1) at 560 K in Part (a)). The two (unmarked) points of inflection comprised between c_α and $c_{\alpha'}$ locate the position of the chemical spinodal at that temperature (points on curve (2) at 560 K in Part (a)). Similarly, the points of inflection on the dashed curve locate the coherent spinodal concentrations (points on curve (4) at 560 K in Part (a)). The latter are, of course, nearer to the center of the miscibility gap. Indeed, as noted in Part (a), the rise in free energy due to the coherency energy is accompanied by a narrowing of the concave range. At 560 K, as for the entire temperature range 530 – 630 K, the departure of the free energy from the common tangent inside the miscibility gap is a small fraction of the overall change in free energy between each of the pure constituents. This figure will be revisited in § 1.4 in the context of the driving force for unmixing (*cf.* Fig. 1.4).

A last comment about the spinodal line is in order before closing this section. The “classical” spinodal (either with or without the inclusion of elastic energy) calculated to produce Figure (1.3) was computed from the extension of equilibrium

⁷These values were obtained with $\eta = -0.023$. This value of η was chosen such that the calculated T_c matched that suggested in Ref. [25]. (With the value of η given in Table 1.2 T_c is calculated at 591 K.) If, instead of using parametrisation (1.9), the phase diagram is produced following the work of Löffler *et al.*[26] which makes provisions for the existence of an upper miscibility gap, *i.e.* with

$$g_m(c, T) = RT [c \ln c + (1 - c) \ln(1 - c)] + c(1 - c) [a_0 + b_0 T + c(a_1 + b_1 T)] RT$$

with the values of the empirical coefficients $a_0 = 4.20$, $b_0 = -3.13 \times 10^{-3} \text{K}^{-1}$, $a_1 = -2.60$ and $b_1 = 2.89 \times 10^{-3} \text{K}^{-1}$, then the top of the chemical spinodal and of the solvus line is obtained at 0.372 (629 K) and that of the coherent spinodal at 0.367 (597 K) with the value $\eta = -0.025$ listed in Table (1.2).

properties by empirical models into a region where equilibrium thermodynamics is unphysical. In practice, it cannot be thought of as a sharp transition between a metastable and an unstable region, *i.e.* one where segregation takes place by a nucleation process and one where fluctuations are unstable on all length scales, respectively. Only in the case of a mean field theory, is there a sharp boundary between these two mechanisms. The concept of a spinodal line and, in particular its existence or position, depends on the thermal history and on the way the measurement is performed since it is only in the dynamic evolution of a system prepared off-equilibrium (such as supercooled vapour) that it is effectively observable. In practice, the location of the spinodal line cannot be measured directly.[27]

1.4 Composition fluctuations and diffusion

Atomic diffusion is often the underlying mechanism for the kinetic evolution of alloys. This section introduces the terminology relevant to experimental diffusion studies by first examining the atomic mobility, then the thermodynamic driving force and, finally, the interatomic diffusion. Diffusion constants are obtained in this work and although the temperature domain for the measurements is lower than that covered by conventional methods, the values obtained can be checked against more classical measurements.

I. ATOMIC MOBILITY — It is helpful to first consider Brownian motion of particles in a colloidal suspension. The collision events between the underlying solution and the particles impart movement to the particles. Due to the nature of the thermally generated impulses, the motion is characteristically random. These impulses give a viscous drag of the solution on the particles. Since the drag is proportional to the velocity, a “mobility” can be defined for the particles as the inverse of the proportionality constant. Now, any system in thermodynamic equilibrium is constantly subjected to thermally activated composition fluctuations and responds to these microscopic perturbations by changing composition locally. Just as in the case of

Brownian motion in a colloid solution, the return to a configuration of minimal energy is not instantaneous but is “slowed down” by a frictional force, essentially the resistance to motion of an atom, a particle, etc. by its surroundings.

In solids in which the motion of atoms is governed by thermal noise alone, self diffusion occurs.[28] Self diffusion coefficients D_i^* ($i = A, B$),⁸ also called tracer diffusion coefficients, are measured by the atomic flux of a tracer isotope introduced at low concentration in an alloy in thermodynamic equilibrium *i.e.* from the time evolution of prepared radioisotopes concentration profiles.⁹

The self-diffusion coefficients often obey an Arrhenius relation, described by two parameters, an activation energy E_0 and a prefactor, the “frequency factor”, D_0^* ,

$$D_i^*(T) = D_{0i}^* e^{\frac{-E_0i}{k_B T}} . \quad (1.11)$$

What is now required is an atomic “mobility”, *i.e.* the inverse of the drag to the atomic motion resulting from a unit potential gradient. Since the “thermal” driving force $\frac{N_V k_B T}{c_0(1-c_0)}$ [30] gives rise to measured diffusion constants $D_i^*(T)$ or, a total diffusion of tracer atoms in the alloy approximated by the weighted sum $c_0 D_A^* + (1 - c_0) D_B^*$ then, in analogy to Brownian motion, the mobility, M , can be obtained by taking the ratio of the observed diffusion to the driving force:

$$M = \frac{c_0(1 - c_0)}{N_V k_B T} [c_0 D_A^* + (1 - c_0) D_B^*] \quad (1.12)$$

where N_V the number of atoms per unit volume. This relation, introduced heuristically, conveniently relates the mobilities M (always positive) to the tracer diffusivities.[31-33] It is not expected to apply in all solid systems but should be

⁸It will now be useful to talk in terms of a mixture of A and B atoms. The notation employed here follows that of the previous section and will be used in the remainder of the thesis, namely c_0 is the atomic fraction of B atoms in the AB binary alloy, hence $1 - c_0$ is the atomic fraction of A atoms.

⁹Strictly, if the tracer is of the same species as the major component then the (tracer) self-diffusion coefficient is measured, otherwise the tracer impurity coefficient (or solute diffusion coefficient) is measured.[29] However, in concentrated alloys, the nomenclature is relaxed and either D_{A1}^* or D_{Zn}^* will be referred to as self-diffusion coefficients in $Al_{0.62}Zn_{0.38}$.

valid for metallic solid solutions in which atom sizes are not too different. The atomic mobility will be further introduced in § 5.2.

II. THERMODYNAMIC DRIVING FORCE — When an alloy is not in thermodynamic equilibrium, the diffusion which is responsible for its return to equilibrium is driven by a thermodynamic force. In contrast to other phenomena described by linear thermodynamics of irreversible processes, the conservation of solute imposes a constraint on the return to equilibrium, *i.e.*

$$\int (c - c_0) d\mathbf{r} = 0. \quad (1.13)$$

To satisfy this condition, the equilibrium state will consist of a spatial inhomogeneity in the concentration *i.e.* with B-rich and A-rich macroscopic regions. The process is assumed to be controlled by an intensive free energy density. Though it had been convenient to use Gibbs' free energy in § 1.3 to generate the phase diagram for AlZn, the Helmholtz free energy $f(\mathbf{r})$ will now be used since integrations will be performed over the volume of the alloy to compute the minima while satisfying condition (1.13). However, locally $g(c) = f(\mathbf{r})/N_V$ and the two can be interchanged. Implicit in this choice is a "coarse-graining" or local averaging of the composition about points over the volume of the alloy. The actual role of this mesoscopic scale will become apparent in Chapter V. As a general rule, reference to the chemical potential will still require the use of $g(c)$.

For small composition variations at the point \mathbf{r} , $f(\mathbf{r})$ can be expanded in terms of the concentration $c(\mathbf{r})$

$$f(c, \nabla c, \nabla^2 c, \dots) = f_0(c) + f_1 \nabla^2 c + f_2 |\nabla c|^2 + \dots \quad (1.14)$$

where, since f is a scalar and must be invariant with respect to the direction of the gradient (assuming isotropy or a cubic lattice), only the terms in even powers of ∇ are nonvanishing[17]. Ignoring higher order terms, integrating using the divergence theorem for $\int (f_1 \nabla^2 c) dV$ and defining

$$\kappa \equiv -\frac{df_1}{dc} + f_2 \quad (1.15)$$

to be the gradient energy coefficient, theories use:

$$f(\mathbf{r}) = f_0(c(\mathbf{r})) + \kappa |\nabla c(\mathbf{r})|^2. \quad (1.16)$$

The gradient energy term thus expresses the energy change of a volume element of given composition if it is surrounded by material of different composition and will appear macroscopically as the surface free energy if the composition gradient is sharp.

The driving force for phase separation will be the gradient of the generalized thermodynamic potential corresponding to departures from the concentration profile $c(\mathbf{r})$ that will minimize $\int f(\mathbf{r})d\mathbf{r}$. This minimization problem requires an undetermined Lagrange multiplier[32,34], say $\lambda(c - c_0)$, such that Eq. (1.13) is satisfied. This multiplier turns out to be

$$\lambda = -2\kappa\nabla^2 c + \frac{\partial f_0}{\partial c}. \quad (1.17)$$

This λ is precisely the generalized chemical potential. Indeed, if κ is set to zero, $\frac{\partial f_0}{\partial c} = \lambda$ which is just the usual condition of uniformity of chemical potential. The presence of the gradient energy coefficient κ opposes the growth of short wavelength concentration fluctuations since κ is positive for clustering systems (κ is negative for ordering systems[35]). The driving force for phase separation will be given by gradients of the potential λ . As a rule, it increases with the undercooling below T_c , *i.e.* with the depth of the quench.

Figure (1.4) illustrates some key aspects of phase separation in binary alloys ($T < T_c$) based on the thermodynamic driving force. As previously, c_0 is the average alloy composition. Firstly, two free energy curves (the solid and dashed curves with a concave region) are examined independently to discuss the difference between the unstable and the metastable regions. The common tangent to the convex regions for each curve (dotted lines, see footnote p. 12) determine the coexistence values ($c_{\alpha_1}, c_{\alpha_1'}$ for the solid curve and $c_{\alpha_2}, c_{\alpha_2'}$ for the dashed curve).

- With $g(c)$ given by the solid curve, c_0 is located between the inflection points of $g(c)$ (*i.e.* inside the concave region) and the tangent to $g(c_0)$ is above the

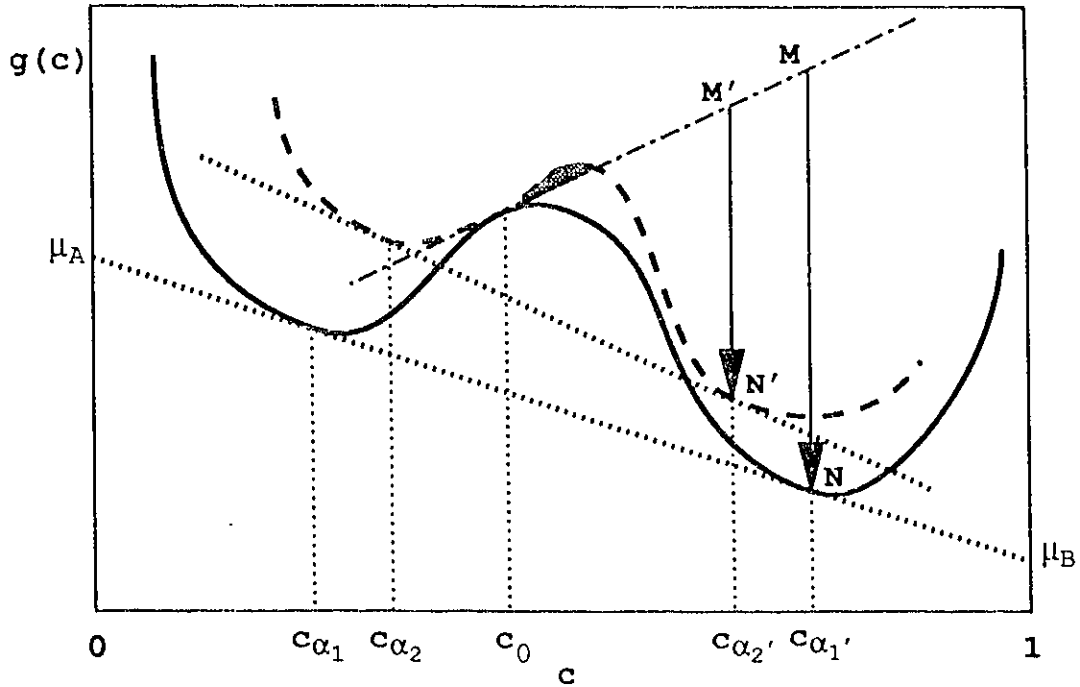


Figure 1.4: Schematic representation of the thermodynamic driving force for phase separation from average composition c_0 . The dashed and solid curves with concave regions show respectively the free energy $g(c)$ with and without inclusion of the contribution from coherency stresses. The incoherent coexistence concentrations are c_{α_1} and $c_{\alpha_1'}$ and the coherent values are c_{α_2} and $c_{\alpha_2'}$. The values μ_A and μ_B are the chemical potentials of A and B atoms at equilibrium (to within a linear offset). The driving force is greater for incoherent (MN) than for coherent (M'N') unmixing. (Schematization of Fig. 1.3.)

free energy curve in the entire composition range $[c_{\alpha_1}, c_{\alpha_1'}]$. The driving force (such as MN) for decomposition is positive for all local composition fluctuations between c_{α_1} and $c_{\alpha_1'}$. Thus, the alloy is unstable against fluctuations of amplitude comprised over the entire miscibility gap and decomposition begins immediately. This case corresponds to spinodal decomposition (SD).

- If, instead, $g(c)$ is given by the dashed curve, there is a range where the tangent to $g(c_0)$ is below the free energy curve (the shaded region immediately to the right of c_0). In this composition range, the driving force for local fluctuations is negative. Hence an energy barrier exists (a surface energy) and there has to be a sufficient local departure from c_0 for decomposition to occur, *i.e.* a

nuclei of the second phase has to form. Precipitates will not nucleate instantly and the state is metastable. This case corresponds to nucleation and growth (NG).

Next, the effect of coherency stresses on the driving force, hence on the phase diagram are examined by considering that the solid curve represents $g_m(c)$, *i.e.* without contributions from coherency stresses while the dashed curve represents the corresponding $g_m(c) + g_{coh}(c)$ at the same temperature. Locally, the driving force is proportional to $c_0(1 - c_0)\frac{\partial^2 g}{\partial c^2}$. Figure (1.4) thus allows to examine the effect of elastic strains on the driving force after a quench from the one-phase region. At a given temperature, coherency stresses result in:

- A lowering of the thermodynamic driving force. Indeed, (MN) is the driving force for incoherent phase separation from c_0 to $c_{\alpha'_1}$ and (M'N') is the driving force for coherent phase separation from c_0 to $c_{\alpha'_2}$. The lower thermodynamic driving force results in slower diffusion. (The actual calculation of (MN) would require the knowledge of the chemical activities.)
- A narrowing of the composition range of the unstable region. This is exemplified at the concentration c_0 . With no coherency stresses (solid curve for $g(c)$), after a quench from the one-phase region of the phase diagram, the alloy starts off in the unstable region (region comprised inside curve 2 of Fig. 1.3a) and the phase decomposition occurs by SD. However, for the same quench, it is in the metastable region of the coherent phase diagram (region comprised between curves 1 and 3 of Fig. 1.3a) and the decomposition is expected to occur by NG instead of SD. Thus, the coherency stresses which raise the free energy also always lower the thermodynamic driving force, narrowing the composition range of the unstable region. This is precisely the effect mentioned in § 1.3.

III. INTERDIFFUSION — The mobility introduced in Eq. (1.12) to relate the observed atomic diffusion with the thermal driving force also relates the atomic diffusion under

the influence of a thermodynamic driving force. If the departure from equilibrium is not too important then linear thermodynamics of irreversible processes says that the solute flux \mathbf{J} is proportional to the gradient of the thermodynamic potential λ . [4,32] The gradient of λ is taken across an interface at rest with respect to a moving frame of reference such that the flux of B atoms is equal and opposite to the flux of A atoms (the Matano interface). With \mathbf{y} the direction normal to the interface,

$$\begin{aligned}\mathbf{J} &= -M \frac{d\lambda}{d\mathbf{y}} \\ &= -M \left[\frac{\partial^2 f_0}{\partial c^2} \nabla c - 2\kappa \nabla^3 c \right].\end{aligned}\quad (1.18)$$

If M is assumed concentration independent, the conservation of solute leads to:

$$\begin{aligned}\frac{\partial c}{\partial t} &= -\nabla \cdot \mathbf{J} \\ &= M \left[\nabla \cdot \frac{\partial^2 f_0}{\partial c^2} \nabla c - 2\kappa \nabla^4 c \right].\end{aligned}\quad (1.19)$$

Assuming that the concentration does not depart too much from the average concentration c_0 , a series expansion of the free energy density curvature ($\partial^2 f_0 / \partial c^2$) about this value

$$\frac{\partial^2 f_0}{\partial c^2} = \left. \frac{\partial^2 f_0}{\partial c^2} \right|_{c_0} + (c - c_0) \left. \frac{\partial^3 f_0}{\partial c^3} \right|_{c_0} + \frac{(c - c_0)^2}{2} \left. \frac{\partial^4 f_0}{\partial c^4} \right|_{c_0} + \dots \quad (1.20)$$

allows one to write the linearized form of the diffusion equation as:

$$\frac{\partial c}{\partial t} = \left(\frac{M}{N_V} \right) \left[\left. \frac{\partial^2 f_0}{\partial c^2} \right|_{c_0} \nabla^2 - 2\kappa \nabla^4 \right] c. \quad (1.21)$$

In this equation and in the following expressions, f will be taken to denote the free energy including the contribution from the coherency strains according to Eq. (1.10) i.e. the second derivative with respect to composition of the expression for the coherency energy.

However, in concentrated solutions (neither A, nor B, is present in a small concentration), and where composition gradients exist, it is practical to introduce new coefficients. The flux of B atoms in an AB alloy containing concentration

gradients is described by the intrinsic diffusion coefficient, D_B , and given by

$$\frac{\partial c}{\partial t} = D_B \nabla^2 c \quad (1.22)$$

Similarly for A atoms, D_A is introduced. The intrinsic diffusion coefficients (when composition gradients exist) and the tracer diffusion coefficients (with no composition gradient) are related through¹⁰

$$\frac{D_A}{D_A^*} = c_0(1 - c_0) \frac{1}{N_V k_B T} \frac{\partial^2 g}{\partial c^2} = \frac{D_B}{D_B^*}. \quad (1.23)$$

The rate of mixing (or unmixing) of the two species, is described by the chemical or interdiffusion coefficient \tilde{D} :

$$\tilde{D} = c_0 D_A + (1 - c_0) D_B. \quad (1.24)$$

\tilde{D} has units of m^2/s . Both the intrinsic and the interdiffusion coefficients relate the time rate of change of local concentration with the concentration gradients. The free energy dependence is included in the coefficient \tilde{D} . From Eqs. (1.12) and (1.23), keeping in mind the rationale for the use of f , the Helmholtz free energy per unit volume, instead of g (cf. p. 21):

$$\tilde{D} = M f'' \quad (1.25)$$

where primes denote derivatives with respect to the atomic fraction evaluated at c_0 as in Eq. (1.21). The diffusion equation (Eq. 1.21) expressed with the coefficient \tilde{D} is then:

$$\frac{\partial c}{\partial t} = \tilde{D} \nabla^2 \left(c + \frac{\kappa}{f''} |\nabla c|^2 \right). \quad (1.26)$$

(To simplify the notation, the subscript "0" has been dropped.) Both Eq. (1.21) and Eq. (1.26) are generalizations of Fick's second law. Indeed, if the contribution

¹⁰In the metallurgical literature, an equivalent form of this relation is the Darken[36] relation between the intrinsic diffusion coefficients and the tracer diffusion coefficients in an AB alloy :

$$\frac{D_A}{D_A^*} = \frac{\partial(g_A/k_B T)}{\partial \ln(1 - c_0)} = \frac{D_B}{D_B^*}.$$

where g_A is the $c = 0$ intercept of the tangent of the curve $g = g(c)$ at c_0 .

from the gradient energy to the thermodynamic potential (Eq. 1.17) is neglected, then Eq. (1.26) simply becomes $\partial c/\partial t = \widetilde{D}\nabla^2 c$. In the region below the spinodal line, *i.e.* where $\partial^2 g/\partial c^2 < 0$, the intrinsic diffusion coefficients D_A and D_B , and the interdiffusion coefficient \widetilde{D} will be negative. In this case, the solution of A - B atoms will "unmix".

Equation (1.21) (and Eq. 1.26) is known as Cahn's formulation of the diffusion equation.[4] This equation lacks the Langevin "thermal" driving force responsible for tracer self-diffusion mentioned in the discussion leading to the introduction of the atomic mobility, M (*cf.* p. 20). In the case of diffusion in an alloy with a concentration gradient, this term also plays a physical role. It will be discussed in the context of SD, resulting in the Cahn-Hilliard-Cook equation, in Chapter III. The quantities f'' , κ and M in Eq. (1.21) are precisely the same as those appearing in the LBM equation of motion employed to model the kinetic evolution of the measured structure factors in this work. So, it will be crucial to examine the possible comparisons between the values measured in phase separating experiments performed and the more conventional measurements of diffusion in solids of other workers.

The determination of the interdiffusion constant \widetilde{D} can be performed on unmixing systems, *i.e.* in phase separation studies as in this work, or on mixing systems. In mixing systems, a class of experiments use the decay of the intensity of x-ray reflection with time during the annealing of artificially made composition modulated materials (multilayers).[35]

Though knowledge about x-ray scattering is required to discuss these experiments and will be the topic of Chapter II, a brief survey of the scattering predicted by Eq. (1.21) for mixing multilayers is proposed at this point. It was stressed as part of the motivation for the work presented in this dissertation that measurements in phase separating systems offered an alternative for the determination of solid state diffusivities and free energy gradients other than by the application of an equation of motion such as Eq. (1.21) to artificially modulated multilayers.

In a scattering experiment, it is the Fourier transform of the composition

modulation spectrum which is measured. For a wave vector of modulus q , the amplitude of the corresponding modulation $I(q)$, will be the Fourier transform of Eq. (1.21):

$$\frac{\partial I(q)}{\partial t} = -q^2 M \left[\left. \frac{\partial^2 f_0}{\partial c^2} \right|_{c_0} + 2\kappa q^2 \right] I(q). \quad (1.27)$$

A small amplitude concentration modulation then decays exponentially with an inverse relaxation time τ :

$$\frac{1}{\tau_q} = q^2 M \left[\left. \frac{\partial^2 f_0}{\partial c^2} \right|_{c_0} + 2\kappa q^2 \right] \quad (1.28)$$

or, according to Eq. (1.25):

$$\frac{1}{\tau_q} = q^2 \widetilde{D} \left[1 + 2\kappa q^2 / f'' \right]. \quad (1.29)$$

One then measures the evolution of the scattering intensity for several values of q , or composition modulations, to allow for the verification of the $aq^2 + bq^4$ dependence of τ_q and to determine the physical parameters.

The first tests of Eq. (1.28) or conversely of Eq. (1.21), came from preparing multilayers of two components by vapour deposition of individual layers of 1 — 3 nm and following the homogenization process upon annealing (CuAu[37], AuAg[38] and CuPd[39]). In particular, for AuAg and CuPd, confirmation of both gradient energy and coherency energy effects was obtained and values of the gradient energy coefficient κ were measured. These experiments served to demonstrate unambiguously the general validity of Cahn's diffusion equation in describing the kinetics of multilayers homogenizing in time.

To close this section, an estimate of the gradient energy term κ is introduced by assuming an interatomic (pair) interaction energy for the computation of $f(\mathbf{r})$ and reevaluating Eqs. (1.14) and (1.16). The interaction energy depends on the number of participating pairs at each pairing distance or shell, and on the contribution of the n^{th} shell to the ordering energy. The pairing energy is written as

$$\omega_n = \epsilon_{AB_n} - \frac{1}{2} (\epsilon_{AA_n} + \epsilon_{BB_n}) \quad (1.30)$$

with ϵ_{ij_n} the interaction strength between atom i located at a site \mathbf{R} and atom j located on the n^{th} shell at position \mathbf{r} . As empirical model equations for $g(c)$ were used to reproduce the miscibility gap, Eq. (1.30) is just a different starting point to derive the regular solution model through the temperature-dependent values of the interaction parameters ϵ_{AB_n} . In Eq. (1.30), as A and B atoms increasingly tend to cluster with atoms of their own species, ω_n becomes increasingly negative and, conversely, for complete solubility between A and B atoms, ω_n will be positive.

The probability of having a pair BA with B at \mathbf{R} and A at $\mathbf{R} + \mathbf{r}$ is $c(\mathbf{R})[1 - c(\mathbf{R} + \mathbf{r})]$. Expanding $c(\mathbf{R} + \mathbf{r})$ about \mathbf{R} and assuming cubic symmetry, the number of pairs with B at \mathbf{R} and A on the n^{th} shell about site \mathbf{R} with radius r_n is therefore

$$Z_n \left\{ c(\mathbf{R}) [1 - c(\mathbf{R})] - c(\mathbf{R}) \nabla^2 c(\mathbf{R}) r_n^2 \right\} \quad (1.31)$$

where Z_n is the number of sites contributing to the n^{th} shell. The contribution of site \mathbf{R} to the internal energy is then

$$U(\mathbf{R}) = \sum_n Z_n \omega_n c(\mathbf{R}) [1 - c(\mathbf{R})] - \sum_n Z_n r_n^2 \omega_n c(\mathbf{R}) \nabla^2 c(\mathbf{R}). \quad (1.32)$$

With

$$\omega \equiv \sum_n Z_n \omega_n \quad (1.33)$$

and the mean square range of the pair interaction ψ^2 , written as

$$\psi^2 = \frac{\sum_n Z_n r_n^2 \omega_n}{\sum_n Z_n \omega_n}, \quad (1.34)$$

Eq. (1.32) becomes

$$U(\mathbf{R}) = \omega c(\mathbf{R}) [1 - c(\mathbf{R})] - c(\mathbf{R}) \nabla^2 c(\mathbf{R}) \frac{\omega \psi^2}{2}. \quad (1.35)$$

Since $F = U - TS$, and the configurational entropy (S) only contributes to $f_0(c)$, after integration over the volume of the sample (compare with Eq. 1.16), it follows that

$$\kappa = \frac{\omega \psi^2}{2}. \quad (1.36)$$

The gradient energy term κ therefore corresponds to the product of an interaction energy per unit volume times a mean square range of interaction. For a regular

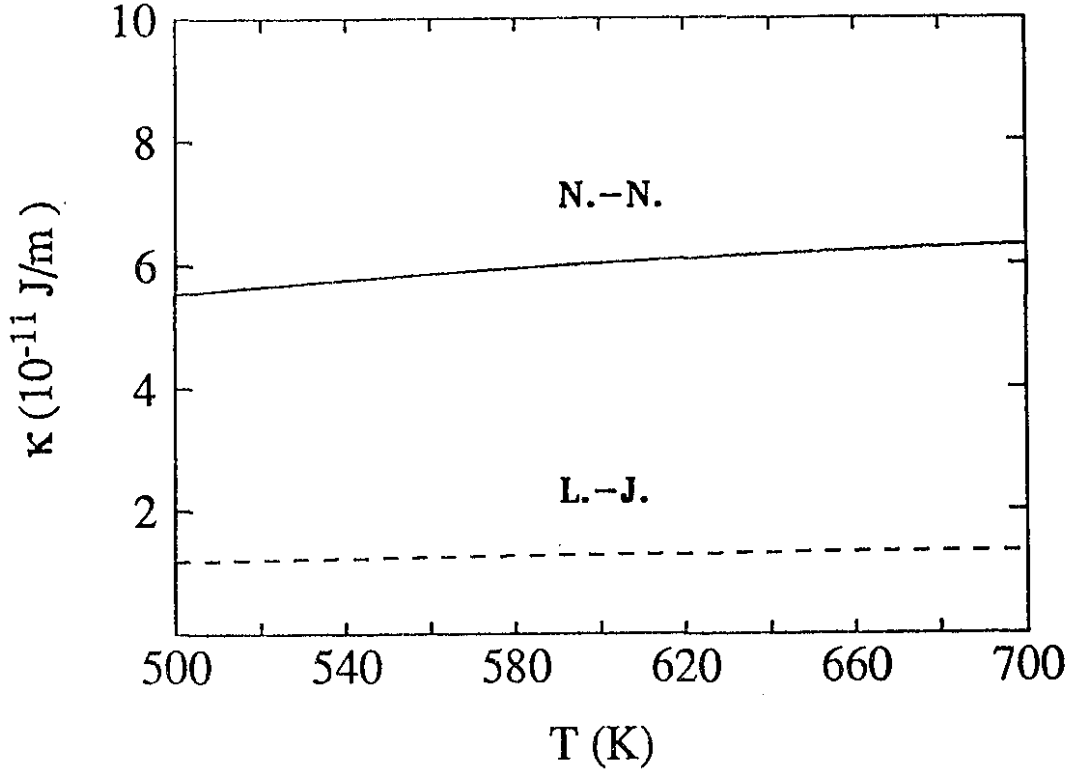


Figure 1.5: Estimates of κ from Eq. (1.37) with the regular solution model given by Eq. (1.9) for the temperature range measured. The solid line corresponds to nearest-neighbor interactions only and the dashed line to a Lennard-Jones potential.

solution with the interaction given as in Eq. (1.30), if h is the enthalpy per unit volume $c_0(1 - c_0)\Omega$, then $\omega = 4h$ at $c = 0.5$ [17] and

$$\kappa = 2h\psi^2. \quad (1.37)$$

For an estimate of κ , the empirical equation with four constants D , E , F and H introduced earlier (Eq. 1.9) is used to calculate h . With r_0 as the nearest neighbor distance, Eq. (1.34) gives $\psi = \sqrt{\frac{1}{3}}r_0$ for nearest-neighbor interactions only and $\psi = \sqrt{\frac{11}{7}}r_0$ for a Lennard-Jones potential. The calculated estimates are shown on Fig. (1.5). The values obtained remain only empirical estimates of the order of magnitude of κ and of its relative temperature dependence. To refine the values obtained, the coefficient in Eq. (1.37) should have been corrected for the actual alloy composition and the mean interaction potential distance ψ should have been more appropriate for a fcc lattice.

Chapter 2

Small angle x-ray scattering

This Chapter introduces small angle x-ray scattering (SAXS) and its relationship with density correlations in real space. Sum rules for the scattering intensity are also presented.

2.1 X-ray scattering and correlations

Electrons in solids or molecules scatter incident x-rays. Each part of the electron distribution acts as a scattering center. Thus if a group of atoms arranged in some arbitrary manner is placed in a parallel monochromatic beam of x-rays, each atom can also be considered as a scattering center emitting a scattered wave which is coherent with the incident radiation. The total scattered photon wave will be the combination of the waves scattered by all scattering centers. The scattered waves interfere with each other and the resulting intensity will thus depend on the direction of observation and is related to the 'real' space atomic structure of the object by a Fourier transform. Thus x-ray scattering allows one to determine the distribution of atoms in solids, on surfaces, in liquid metals, etc.

The scattering vector is defined in terms of the incident and scattered wavevectors k_0 and k as in Fig. (2.1) by:

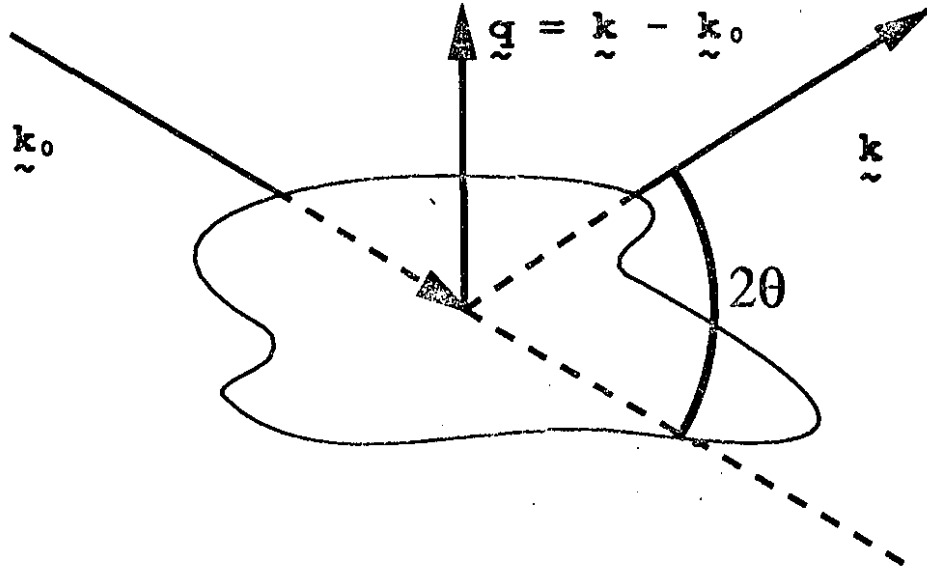


Figure 2.1: Standard definition of \mathbf{q} .

$$\mathbf{q} = \mathbf{k} - \mathbf{k}_0 \quad (2.1)$$

with $k = 2\pi/\lambda$ where λ is the photon wavelength. Since $k = k_0$, the angle of scattering θ is related to the scattering vector q by

$$q = 2k_0 \sin \theta \quad (2.2)$$

i.e. $q = 4\pi \sin \theta / \lambda$.

The coherent scattering intensity $I(\theta, \phi)$ (in a solid angle $d\Omega$) from the scattering centers normalized to the incident photon flux I_0 (per m^2) is equivalent to the differential scattering cross-section (in $\text{m}^2/\text{steradians}$):

$$\frac{d\sigma}{d\Omega} = \frac{I(\theta, \phi)}{I_0}. \quad (2.3)$$

The arrangement of atoms $A(\mathbf{r})$ at discrete sites \mathbf{r}_n , with \mathbf{r} the position vector, can be expressed as the sum over all sites of the corresponding form factor:

$$A(\mathbf{r}) = \sum_n f_n \delta(\mathbf{r} - \mathbf{r}_n) \quad (2.4)$$

where f_n is the atomic form factor for the atom at site n . The Fourier transform of $A(\mathbf{r})$ is

$$A(\mathbf{q}) = \sum_n f_n e^{-i\mathbf{q} \cdot \mathbf{r}_n} \quad (2.5)$$

and the scattering intensity will be given by the square of $A(\mathbf{q})$. Thus, the differential scattering cross-section is given by

$$\frac{d\sigma}{d\Omega} = \sum_m \sum_n f_m f_n e^{-i\mathbf{q} \cdot (\mathbf{r}_m - \mathbf{r}_n)}. \quad (2.6)$$

With expression (2.6), the maxima in scattering intensity will occur when

$$\mathbf{q} \cdot (\mathbf{r}_m - \mathbf{r}_n) = 2\pi n \quad (2.7)$$

where n is any integer. This is known as Bragg's condition and Bragg scattering will occur at the wavevectors \mathbf{q} in crystals where $\mathbf{r}_m - \mathbf{r}_n = 2\pi n$ when the number of scattering atoms is large.

To examine the more general case of the scattering of electromagnetic radiation by an arbitrary electron density, the atoms at discrete sites are replaced by radial electron density functions $\rho_e(\mathbf{r})$ in Eq. (2.6):

$$\frac{d\sigma_V}{d\Omega} = \frac{\sigma_T}{V} \int \int \rho_e(\mathbf{r}_m) \rho_e(\mathbf{r}_n) e^{-i\mathbf{q} \cdot (\mathbf{r}_m - \mathbf{r}_n)} d\mathbf{r}_n d\mathbf{r}_m \quad (2.8)$$

where σ_T is the Thomson electron cross-section (the square of the classical electron radius) $\sigma_T = \frac{e^4}{m^2 c^4} = 7.94 \times 10^{-30} \text{ m}^2/\text{el.}^2$ and $d\sigma_V/d\Omega$ (in m^{-1}) is the differential cross-section per unit volume of the sample. Equation (2.8) is precisely the Fourier transform of the equal-time two-point electron density correlation function

$$\frac{d\sigma_V}{d\Omega} = \sigma_T \int e^{i\mathbf{q} \cdot \mathbf{r}} \langle \rho_e(\mathbf{r}) \rho_e(\mathbf{0}) \rangle d\mathbf{r} \quad (2.9)$$

where translational invariance has been assumed and

$$\langle \rho_e(\mathbf{r}) \rho_e(\mathbf{0}) \rangle \equiv \int \rho_e(\mathbf{r}) \rho_e(\mathbf{0}) d\mathbf{r} / \int d\mathbf{r} \quad (2.10)$$

where $\langle \rangle$ denotes the thermal average.

The alloy composition c (in atomic fraction of one constituent in a binary alloy, at. fract.) is used in this work instead of the electronic densities, ρ_e . A structure factor in real space $S(\mathbf{r})$ is defined with this units convention:

$$\begin{aligned} S(\mathbf{r}) &\equiv \langle c(\mathbf{r}_0)c(\mathbf{r}_0 + \mathbf{r}) \rangle \\ &= \left(\frac{d\rho_e}{dc} \right)^{-2} \langle \rho_e(\mathbf{r}_0)\rho_e(\mathbf{r}_0 + \mathbf{r}) \rangle. \end{aligned} \quad (2.11)$$

Thus $S(\mathbf{r})$ is in (at. fract.)² (or mol²/m⁶). The units of $\hat{S}(\mathbf{q})$, the Fourier transform of $S(\mathbf{r})$,

$$\hat{S}(\mathbf{q}) = \int e^{i\mathbf{q}\cdot\mathbf{r}} S(\mathbf{r}) d\mathbf{r} \quad (2.12)$$

are (at. fract.)²m³ (or mol²/m³). From Eqs. (2.9) and (2.11), the structure factor is proportional to the differential scattering cross-section

$$\hat{S} = \sigma_T^{-1} \left(\frac{d\rho_e}{dc} \right)^{-2} \frac{d\sigma_V}{d\Omega}. \quad (2.13)$$

Thus the differential scattering cross-section is the Fourier transform of the two-point pair correlation function $\langle c(\mathbf{r}_0)c(\mathbf{r}_0 + \mathbf{r}) \rangle$ and $\hat{S}(\mathbf{q})$ is simply the product of $\frac{d\sigma_V}{d\Omega}$ with a prefactor. Certain conditions have to be satisfied for this derivation to be valid. i. The Born approximation has to apply, *i.e.* multiple scattering events in the sample can be neglected. ii. The scattering must occur exclusively elastically, through Thomson scattering, *i.e.* as if the electrons were free electrons. This would not be the case if the energy of the x-ray photon was close to a core-level binding energy since the corresponding optical absorption edge would influence the scattering resulting in inelastic scattering (anomalous scattering). In this work the energy used (~ 6 keV) is far from absorption edges in Al and Zn (1.56 and 9.69 keV for the K edge of Al and Zn respectively). It is not necessary to include inelastic effects from Compton scattering either since at very small scattering angles it vanishes. iii. In the definition of the scattering cross-section, conditions for Fraunhofer diffraction were assumed, *i.e.* it was tacitly assumed that the source and the detector were both effectively at infinity.

Our choice of units to express $S(\mathbf{r})$ and $\hat{S}(\mathbf{q})$ will allow a direct comparison between the measured scattering and the equations of motion for kinetic theories of SD.¹

The term ‘small angle’ scattering (SAS) can be misleading. Indeed, SAS does not imply small diffraction angles but rather small values of the magnitude q of the scattering vector. The angle range of SAS is usually of order $0 < q < \pi/d_a$, where d_a is the interatomic distance.[42] For $\text{Al}_{0.62}\text{Zn}_{0.38}$, using the fcc lattice spacing from Table 1.2, d_a equals 2.87 \AA ($a_0/\sqrt{2}$). Thus this gives an upper limit of about $q = 1 \text{ \AA}^{-1}$ to the SAS range. For Cu K_α radiation ($\lambda = 1.54 \text{ \AA}$) this corresponds to a diffraction angle of 14° but for neutrons with a wavelength of 8 \AA this angle increases to 80° . At the beam energy in this work ($E = 5.989 \text{ keV}$, *i.e.* $\lambda = 2.07 \text{ \AA}$) this would correspond to a diffraction angle of 19° . The lowest order Bragg reflection (111) would occur at a diffraction angle of 52.4° ($q = 2.68 \text{ \AA}^{-1}$). In this work, reciprocal vectors cover the range 0.01 to 0.085 \AA^{-1} and thus features with length scales between 60 and 600 \AA are probed.

2.2 Thermal diffuse scattering

At equilibrium, the structure factor of a binary alloy, *i.e.* the scattering due to thermal composition fluctuations can be estimated from the equipartition of the free energy. Ignoring terms of higher order than quadratic, taking the integral of $f(\mathbf{r})$ (Eq. 1.16),

$$G = \int d^3\mathbf{r} \left[\kappa |\nabla \delta c(\mathbf{r})|^2 + f'' \delta c^2(\mathbf{r}) \right] \quad (2.14)$$

¹This choice of units is a departure from the usual scattering power in terms of “electron units per atom” (Laue Units) where the intensity per atom is compared to a number of diffracting electrons giving the same intensity.[40] The corresponding quantity in neutron diffraction is the coherent differential cross-section per atom, $d\sigma/d\Omega$, expressed in units of “ cm^2 per sterad per atom”[41]. In this sense, the units used in this work are closer to those of neutron scattering than those conventionally used in x-ray scattering.

with f'' in J/m^3 and κ in J/m and where the notation

$$\delta c(\mathbf{r}) = c(\mathbf{r}) - c_0 \quad (2.15)$$

has been introduced to neglect the constant offset to G provided by c_0 . The Fourier transform $\mathcal{F}\{\delta c(\mathbf{r})\}$ is introduced as

$$\delta c(\mathbf{r}) = \frac{1}{2\pi^3} \int d\mathbf{q} \widetilde{\delta c}(\mathbf{q}) e^{i\mathbf{q}\cdot\mathbf{r}}. \quad (2.16)$$

Then, by substituting the inverse Fourier transform, $\mathcal{F}^{-1}\{\widetilde{\delta c}(\mathbf{q})\}$ to $\delta c(\mathbf{r})$ in Eq. (2.14) the following expression is obtained[43]

$$G = \frac{1}{(2\pi)^3} \int d\mathbf{q} (\kappa q^2 + f'') |\widetilde{\delta c}(\mathbf{q})|^2 \quad (2.17)$$

Hence the free energy in the q^{th} Fourier mode is

$$G(\mathbf{q}) = (\kappa q^2 + f'') |\widetilde{\delta c}(\mathbf{q})|^2 \quad (2.18)$$

whose average value should be $k_B T$, by equipartition of energy. Hence

$$\begin{aligned} \langle |\widetilde{\delta c}(\mathbf{q})|^2 \rangle &= \frac{k_B T}{\kappa q^2 + f''} \\ &\equiv S_{OZ}(q)|_T \end{aligned} \quad (2.19)$$

which is precisely the Fourier transform of the expression in Eq. (2.11). Hence, the equilibrium structure factor is given by a Lorentzian centered at $q = 0$. Using the correlation length ξ ,

$$\xi^2 = \frac{\kappa}{f''} \quad (2.20)$$

Eq. (2.19) can be rewritten as

$$S_{OZ}(q)|_T = \frac{k_B T}{\kappa(q^2 + \xi^{-2})} \quad (2.21)$$

and $S_{OZ}(q)|_T$, as in Eq. (2.13), is in m^3 . Equation (2.19) is known as the Ornstein-Zernike structure factor.

When the alloy is not in equilibrium, Eq. (2.19) should be the asymptotic state (or infinite time limit) of the dynamic equation of motion employed to predict the kinetics of the return to equilibrium.

2.3 Sum rules

Since the measured scattering intensity relates so simply to the equal-time two-point correlation function (*cf.* Eq. 2.9), it is straightforward to make some predictions about the observed scattering intensity, independent of models of the correlation function. These are often called "sum rules". Once established, these rules provide easy checks for both the experimentalist and the theorist.

The differential electric susceptibility is given by

$$\chi_s = \lim_{q \rightarrow 0} \frac{1}{a_0^3} S(q). \quad (2.22)$$

where a_0 is the lattice parameter. The first sum rule is obtained from Eq. (2.19) by setting $q = 0$. This rule is thus a susceptibility sum rule :

$$S(q=0) = \frac{k_B T}{f''}. \quad (2.23)$$

where f'' is evaluated along $c = c_\alpha$.

Two more sum rules are introduced. The first applies at all times whereas the second is valid when interfaces exist, that is at the late stages of the decomposition.

The fluctuations are related to correlations by noticing that $S(\mathbf{r})$ as defined in Eq. (2.11) has the property $S(0) = \overline{c^2}$. Taking the inverse Fourier transform of Eq. (2.13),

$$S(\mathbf{r}) = \frac{1}{(2\pi)^3} \int_0^\infty S(\mathbf{q}) e^{i\mathbf{q} \cdot \mathbf{r}} d\mathbf{q} \quad (2.24)$$

and, for $\mathbf{r} = 0$, an expression for the integrated intensity Q_0 is obtained[44]

$$Q_0 = \frac{1}{(2\pi)^3} \int_0^\infty S(\mathbf{q}) d\mathbf{q} = \overline{(c - c_0)^2} \quad (2.25)$$

where c_0 is the average composition. The averaging in Eq. (2.25) involves the integral over the scattering volume,

$$Q_0 = \int (c - c_0)^2 dV. \quad (2.26)$$

When, as in the case of bulk alloy compositions and temperatures inside a miscibility gap as in Fig. (1.3), two phases coexist in the alloy near or at equilibrium, the volume

fraction of each phase is obtained by the lever rule:

$$V_v^\alpha = \frac{c_{\alpha'} - c_0}{c_{\alpha'} - c_\alpha}, \quad (2.27)$$

$$\begin{aligned} V_v^{\alpha'} &= 1 - V_v^\alpha \\ &= \frac{c_0 - c_\alpha}{c_{\alpha'} - c_\alpha}. \end{aligned} \quad (2.28)$$

Then, Eq. (2.26) can be approximated by

$$\begin{aligned} Q_0 &= (c_\alpha - c_0)^2 V_v^\alpha + (c_{\alpha'} - c_0)^2 V_v^{\alpha'} \\ &= (c_0 - c_\alpha)(c_{\alpha'} - c_0) \end{aligned} \quad (2.29)$$

where Eqs. (2.27) and (2.28) have been used. This expression can alternately be written as

$$Q_0 = V_v^\alpha V_v^{\alpha'} (c_{\alpha'} - c_\alpha) \quad (2.30)$$

which is equivalent to the formulation of the sum rule by Tomita[45] where $c_{\alpha'} - c_\alpha = 1$. Eq. (2.25) was originally[46] written in terms of the local fluctuations of the electron density $\overline{(\rho - \rho_0)^2}$.

The next rule applies for systems which possess regions of uniform composition, either c_α or $c_{\alpha'}$, separated by interfaces. The scattering contrast in the small angle range then comes solely from the interfaces. If the area element of an interface is written da and V is the volume of the whole system, the interface area density can be defined by

$$\mathcal{A} = \int da/V. \quad (2.31)$$

The first term of a large q expansion for the Fourier transform of the correlation function of a system with interfaces is the Porod law[47]

$$\lim_{q \rightarrow \infty} q^4 S(q) = 2\pi\mathcal{A}. \quad (2.32)$$

According to this equation if there is a sharp interface between two phases the value of $q^4 S(q)$ should be constant for large q .

Chapter 3

Early descriptions of spinodal decomposition

This Chapter makes a review of the early descriptions of spinodal decomposition (SD), in particular of linear theories, and of the measurements to date, mainly for binary alloys. Before doing so, the text below summarizes some key differences between SD and the other decomposition process introduced in Chapter I, nucleation and growth (NG). The relevance of such distinctions is also questioned.

3.1 A foreword

The main features of NG and SD described in § 1.1 for phase transitions in a gas-liquid system also apply for a binary alloy. As shown in Fig. (3.1a) the decay of a metastable phase to a stable phase by NG occurs in roughly two stages. The first stage involves the formation of nuclei of the precipitate phase (nucleation) through fluctuations in the one-phase medium and often requires an incubation period. Afterwards, the nuclei grow in time. However, SD displays long-wavelength fluctuations that lower the excess enthalpy immediately after the quench into an unstable state as schematized in Part (b). These fluctuations grow in time on all length scales.

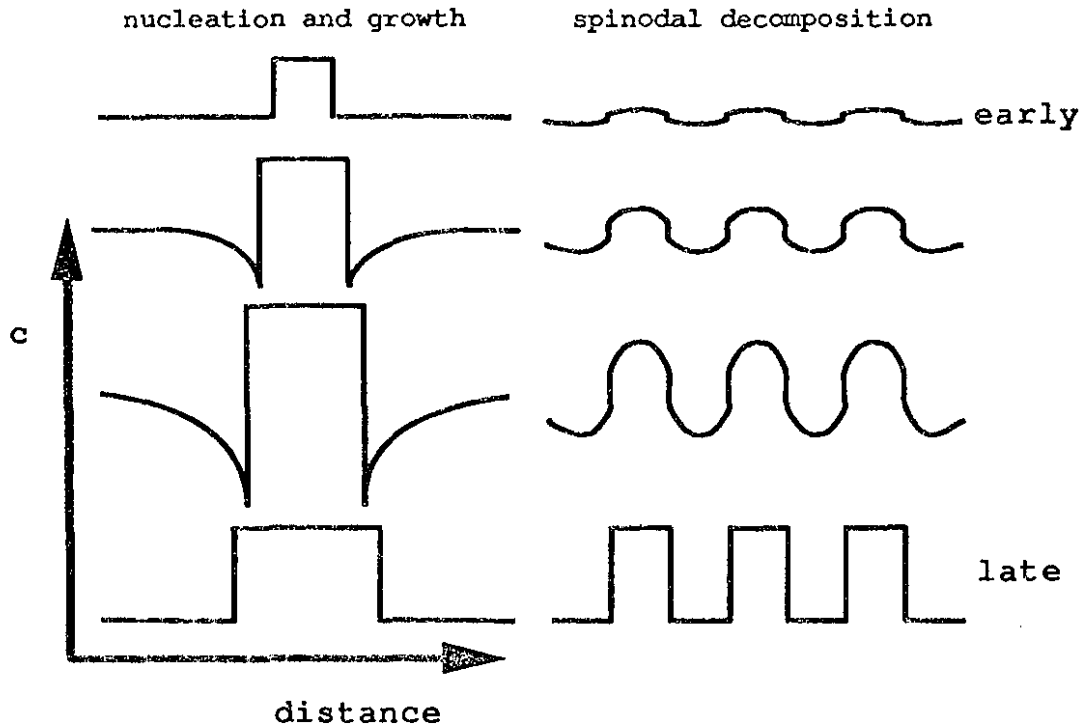


Figure 3.1: Schematic morphologies of phase separation mechanisms. (From Ref. [48], p. 87.)

Before considering exclusively the SD process, it is appropriate to consider the nature of the spinodal curve. This will lead to some comments on the important choice of interpretation that measurements of the kinetics of unmixing processes have to present the characteristics of only one or the other of these processes.

I. COHERENCY STRAINS: THE SPINODAL CURVE, A KINETIC BOUNDARY —

A priori schematization (3.1b) of the SD process could suggest that near T_c where the decomposition is only thermally activated, it would present continuous characteristics reminiscent of water near its critical point (*cf.* § 1.2). In the case of water, the order parameter varies in a continuous way as T_c is crossed, suggesting a second order transition. However, in crystalline solids such as the AlZn alloy there is a metastable region above T_c (*i.e.* above the spinodal region) where the alloy will decompose by NG after an incubation time § 1.3. Thus, as SD proceeds after a quasistatic crossing of T_c ($T \rightarrow T_c^-$) the order parameter evolves asymptotically to the difference between the chemical solvus compositions at that tempera-

ture, $c_{\alpha'} - c_{\alpha} \neq 0$. Clearly, in this case the order parameter is discontinuous at T_c . The decomposition is thus a fluctuation-induced first order transition.[49] Hence, even at T_c , the spinodal curve represents a kinetic boundary rather than a static boundary.¹[50]

II. FINITE RANGE INTERACTIONS: THE SPINODAL CURVE, A TRANSITION REGION

Chapter I gave a description of phase transitions based on mean field interactions between molecules, atoms, etc. which corresponds to the classical (Landau) theory of phase transitions. In practice, this description remains valid in the limit of weak long range interactions. In systems where interactions have a finite range, it is often argued that the spinodal curve, if it exists, is a smooth transition region between metastable states and unstable states. Descriptions not based on mean field interactions have been developed, such as cluster dynamics.[50-52] These do not have a sharp transition between SD and NG: all states inside the miscibility gap are metastable and the nucleation rate increases continuously with the undercooling (*i.e.* the over-saturation). Thus, for instance, results from Monte-Carlo simulations of the kinetics 3d Ising model in the “unstable region” have been interpreted using either analyses appropriate for nucleation or heterophase fluctuations[50-54] or coarse-graining cooperative models, as in this work (*cf.* Chap. V).[7]

This dissertation assumes a sharp spinodal and thus that SD can be distinguished from NG by the differences introduced above. Since, the alloy composition is close to the critical composition, and thus as far as possible from the classical spinodal for any given quench temperature, the smearing of the spinodal line is not a direct issue. A direct casting of the measurements to the study of the kinetics of SD can thus be justified without having to evaluate alternate decomposition mech-

¹The point at the top of the miscibility gap is also a first order transition point. Strictly, an alloy quenched into the region below this point is metastable and the decomposition occurs by NG. This process is inherently discontinuous and requires a surface energy, and has consequently a discontinuity in the first derivatives of the free energy. A discontinuity in the order parameter is also implied since at the onset of decomposition, it goes exactly to $c_{\alpha'} - c_{\alpha} \neq 0$.

anisms. However, measurements reported in the literature at compositions closer to the classical spinodal are not free from this concern (*cf.* § 3.3).

3.2 Linear theories

The groundwork for the current ideas of spinodal decomposition was laid by Hillert[55] in a paper in 1961, and more generally the first equation to predict the time-evolution of the scattered intensity is due to Cahn[4,56] in the years 1961 and 1962. Excellent reviews have been written on this topic.[32,57] The Cahn-Hilliard (CH) equation of motion and the Cahn-Hilliard-Cook (CHC) equation of motion are described in this section as the two main linear equations of motion proposed to describe the early stage evolution of an alloy during SD.

The generalized diffusion equation developed by Cahn was introduced in Chapter I (Eq. 1.21). This equation was formulated for an elastically continuous decomposing system. Eq. (1.27) provided the corresponding equation of motion (the CH equation) for the scattered x-ray intensity $I(q, t)$ associated with the Fourier component of wavenumber q for an isotropic body at a constant aging temperature. The solution to Equation (1.27) predicts the scattering at time t to be:

$$I(q, t) = I(q, 0) \exp[2R(q) \cdot t]. \quad (3.1)$$

In this expression, $I(q, 0)$ is the initial scattering intensity before any evolution at the aging temperature, and $R(q)$ is an amplification factor given by²:

$$R(q) = -(\widetilde{D}/f'') (f'' + 2\eta^2 Y + 2\kappa q^2) q^2 \quad (3.2)$$

where as in Chapter I, \widetilde{D} is the interdiffusion coefficient, f'' the second composition derivative of the free energy per unit volume and $2\eta^2 Y$ the second derivative of the elastic energy (*cf.* p. 17).

Figure (3.2) shows the calculated amplification factor with parameter values taken from Rundmand and Hilliard's work on an AlZn alloy[58] (*cf.* § 3.3). Equation

²Exceptionally, in this section the elastic energy contribution to f'' is written explicitly.

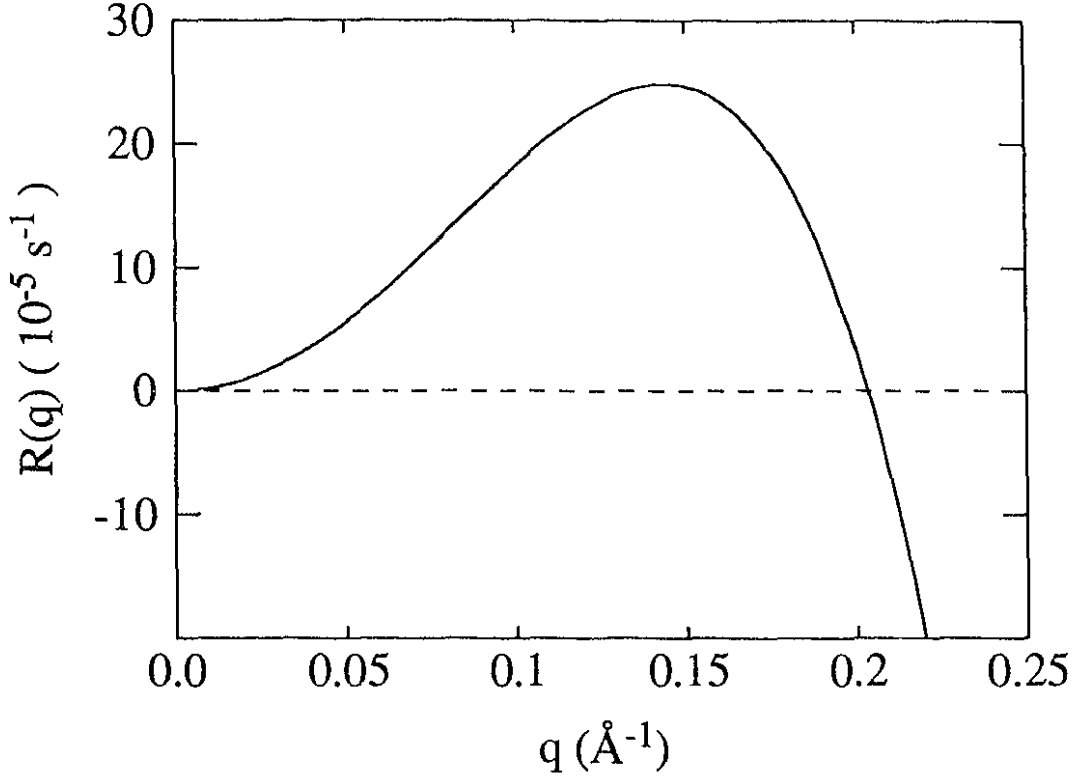


Figure 3.2: Schematic diagram showing the variation of the amplification factor $R(q)$, with the wavevector q (cf. Eq. 3.2) inside the spinodal. Numerical values used are $\bar{D}[1 + (2\eta^2 Y/f'')] = -2.4 \times 10^{-22} \text{ m}^2/\text{s}$ and $\kappa\bar{D}/f'' = 2.9 \times 10^{-41} \text{ m}^4/\text{s}$ (cf. Table 2 of Ref. [58]). This curve has a maximum at $q_m = 1.44 \times 10^9 \text{ m}^{-1}$ ($\lambda_m = 43.7\text{\AA}$) and intersects the abscissa (dashed line) at $q_c = 2.03 \times 10^9 \text{ m}^{-1}$ ($\lambda_c \equiv 2\pi/q_c = 30.9\text{\AA}$).

(3.1) predicts that the intensity corresponding to a given Fourier component will either grow or decay, depending on the sign of $R(q)$. For one nontrivial value q_c such that $R(q_c) = 0$,

$$q_c = \sqrt{-(f'' + 2\eta^2 Y)/2\kappa} \quad (3.3)$$

$$= \xi^{-1} \quad (3.4)$$

the associated Fourier component does not change with time. The wavenumber q_c thus corresponds to a time-independent crossover in $J(q, t)$. The amplification factor also has a maximum at $R(q_m)$ for which the growth rate of the associated Fourier component will also be maximum and, from Eq. (3.2),

$$q_m = q_c/\sqrt{2}. \quad (3.5)$$

Cahn's theory was expanded by Cook[30] to include the effects of thermal

fluctuations by adding a Langevin source term. The resulting Cahn-Hilliard-Cook (CHC) linearized equation of motion applies to the *absolute* scattering intensity $S(q, t)$,

$$\frac{\partial S(q, t)}{\partial t} = 2R(q)S(q, t) + 2Mk_B T q^2 \quad (3.6)$$

where the time-independent amplification factor $R(q)$ is as in the Cahn-Hilliard equation and M is the atomic mobility.

According to Cook's theory, the intensity is no longer given by Eq. (3.1) but by the solution of Eq. (3.6) with appropriate boundary conditions:

$$S(q, t) = [S(q, 0) - S_{Oz}(q)|_{T_q}] \exp[2R(q)t] + S_{Oz}(q)|_{T_q}. \quad (3.7)$$

In this equation $S_{Oz}(q)|_{T_q}$ is the scattering associated with thermal fluctuations at the aging temperature as given by Eq. (2.19) (replacing f'' by $f'' + 2\eta^2 Y$). Figure (3.3) shows typical equilibrium Ornstein-Zernike structure factors $S_{Oz}(q)$ for a phase separated alloy *i.e.* at a temperature below T_c (solid line) and for the same alloy in the one-phase region (dashed line). For bulk alloy compositions in the unstable region of the phase diagram the solid line shows that $S_{Oz}(q) < 0$ for $q < q_c$, since $(f'' + 2\eta^2 Y < 0)$. Thus, coherent equilibrium fluctuations do not occur over length scales larger than ξ since these would contribute to the structure factor at wavenumbers below q_c (*cf.* Eq 3.4).

Fig. (3.4) shows the solution of the CHC equation for a hypothetical quench from an annealing temperature T_a in the one-phase region to an aging temperature T_q inside the miscibility gap at selected times. The equilibrium structure factors corresponding to the anneal and the aging temperatures are as given in Fig. (3.3). The amplification factor is as given in Fig. (3.2). As in the case of the CH equation of motion, Fig. (3.4) shows that there is a fixed crossover of the $S(q, t)$, which is now labeled q'_c . However, q'_c is larger than q_c . Fourier modes with $q < q'_c$ grow and those with $q > q'_c$ decay asymptotically to the equilibrium value at the aging temperature (solid line in Fig. 3.3). This is also verified by taking the large time limit when $\frac{\partial S(q)}{\partial t} = 0$ in Eq. (3.6) for the case $R(q) < 0$ which gives $S(q) = \frac{k_B T}{\kappa q^2 + f'' + 2\eta^2 Y}$ which is

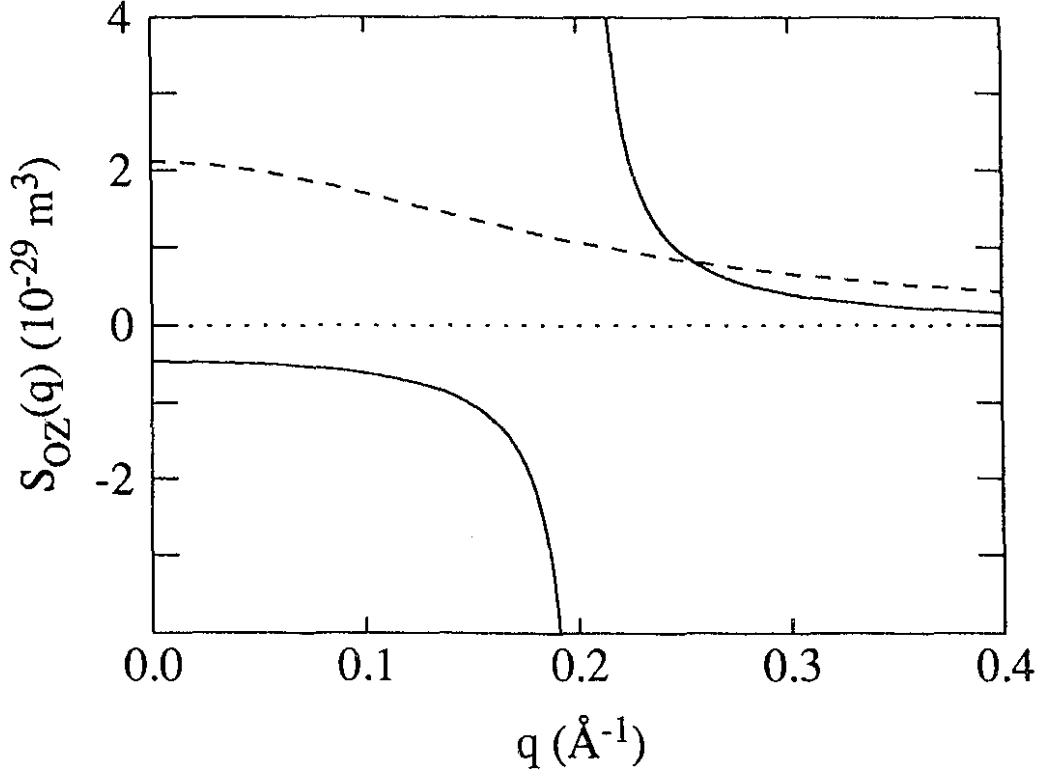


Figure 3.3: Equilibrium scattering due to thermal fluctuations above (dashed line) and below the critical temperature (solid line), Eq. (2.19), computed for $q_c = 2.03 \times 10^9 \text{ m}^{-1}$ (cf. Fig. 3.2 and Eq. 3.3) and $f'' + \eta^2 Y = -9.9 \times 10^{10} \text{ J/m}^3$ (cf. Table 2 of Ref. ([58]) for $T = 338 \text{ K}$ in $\text{Al}_{0.78}\text{Zn}_{0.22}$ (solid line). The dashed line shows the equilibrium scattering above T_c corresponding to the same correlation length, $\xi = q_c^{-1}$, taking arbitrarily $f'' + \eta^2 Y = 2.475 \times 10^{-10} \text{ J/m}^3$ and $T = 378 \text{ K}$.

the expected equilibrium scattering at the wavenumber q (Eq. 2.19). This limit and the expected stationary solution will only be approached for the wavevectors larger than q_c .

The nontrivial wavenumber q'_c which corresponds to the cross-over in the CHC equation of motion is also the wavenumber for which $S_{OZ}(q)|_{T_*} = S_{OZ}(q)|_{T_*}$ in Fig. (3.3) i.e. 0.255 \AA^{-1} . Indeed, from Eq. (3.6), solving $\partial S(q, t)/\partial t = 0$, gives $S(q'_c, t) = S_{OZ}(q'_c)|_{T_*}$. As expected, setting $S(q'_c, 0) = S_{OZ}(q'_c)|_{T_*}$ in Eq. (3.7) gives the same result.

The CHC equation of motion predicts a linear growth of the amplitude of the wavevector q_c , as shown by the inset in Fig. (3.4). This can be checked by expanding

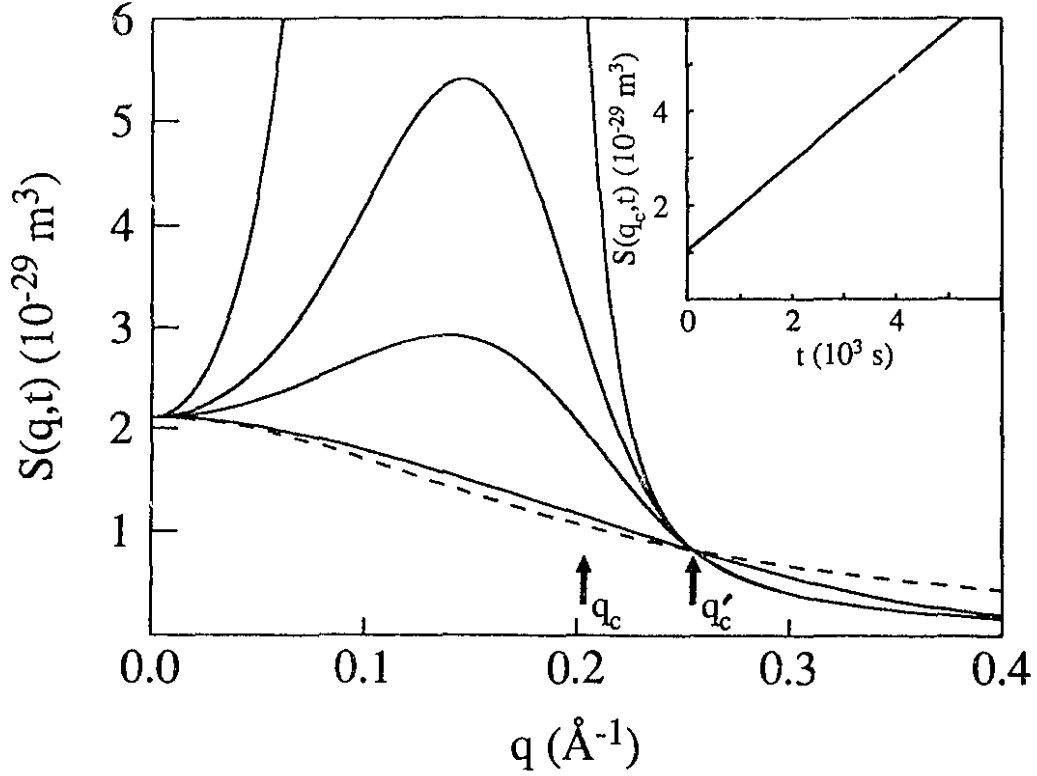


Figure 3.4: Structure factor for the CHC equation of motion. The dashed line shows $S(q, t = 0) = S_{OZ}(q)|_{T=300 \text{ K}}$ and corresponds to the dashed line in Fig. (3.3). The solid lines correspond to Eq. (3.7) solved with the same $R(q)$ shown in Fig. (3.2) for $t = 100, 1000, 2000, 6000 \text{ s}$. The inset shows the linear growth for $S(q_c, t)$.

$e^{2R(q)t} \approx 1 + 2R(q)t$ in Eq. (3.7)³ and, after substitution of the expressions for R (Eq. 3.2) and $S_{OZ}(q)|_{T_e}$ (Eq. 2.19), by taking the limit $q^2 \rightarrow -(f'' + 2\eta^2 Y)/2\kappa$ (cf. Eq. 3.3) which gives

$$S(q_c, t) = S(q_c, 0) + 2Mk_B T q_c^2 t. \quad (3.8)$$

Modes with wavenumbers $q < q_c$ will grow exponentially without bound as in the CH equation and those comprised in $q_c < q < q'_c$ will grow asymptotically to the equilibrium scattering value $S_{OZ}(q)|_{T_e}$.

The CHC equation reduces to Eq. (3.1) when random fluctuations can be

³It is necessary to expand $R(q)$ since

$$\lim_{q \rightarrow q_c} S_{OZ}(q)|_{T_e} \rightarrow \infty.$$

considered negligible. However, in the very early stages of decomposition when the amplitudes of the composition waves are small the random fluctuations will constitute a significant fraction of the composition fluctuation amplitudes and the CHC equation is more appropriate. At high wavenumbers, the CHC equation predicts the correct asymptotic behavior of the structure factor.

3.3 Experimental results

This section presents a brief survey of experimental studies of spinodal decomposition. The works are critically reviewed with respect to whether they unambiguously prove the occurrence of a SD process. Although much theoretical work has stressed SD, it has proven remarkably difficult to obtain experimental results. The first experimental studies of SD were carried out on alloys and, in particular, on AlZn alloys, and a number of review papers appeared a decade ago (for example, see Ref. [42]). Subsequently, the investigation has spread to other systems such as binary fluids, glasses and polymers. The account of experimental results first concentrates on SD measurements in AlZn alloys. This is followed by a review of some recent SD studies in other systems. Finally, an overview of the reported studies on the late stages of SD is presented.

Many efforts have been made to verify the CH and the CHC theories of spinodal decomposition. However, to date, there is no unconditionally accepted experimental verification of these theories in a phase transition context for a metallic system (in § 1.4, some diffusion studies in multilayers were mentioned in the context of the CH equation). In a lot of measurements, the practical difficulties in unambiguously measuring features unique to SD seriously restrict the interpretation of the data.

There is abundant experimental literature on AlZn binary alloys. The criteria for inclusion in this review is whether or not the workers examined their data in the framework of SD. The interpretation of experimental results is somewhat dependent on the idea that a sharp spinodal line can be drawn as in Figure (1.3) to separate

SD processes from NG processes. Though a sharp spinodal line does not exist in fact it is convenient to use it to justify the use of SD theories inside the region it bounds. However, in some cases, alloys aged at the same point on the phase diagram have been alternately analysed in terms of a NG theory (such as Langer and Schwartz's cluster dynamics[59]) or a SD theory by different authors. For example, in a very comprehensive study by Guyot *et al.* using small angle neutron scattering (SANS)[60], transmission electron microscopy (TEM)[61,62] and resistivity measurements[63] clustering has been studied in $\text{Al}_{0.932}\text{Zn}_{0.068}$ aged at 293 K, whereas Murakami *et al.*[64] present measurements on the same alloy at 313 K interpreted in terms of the CH equation. These analyses represent two different phenomenological pictures of the decomposition process. As models, they are idealizations. It is beyond the scope of this dissertation to examine in detail decomposition models other than SD. As a point of interest, the principal conclusions of Guyot's studies were the lack of an observed sharp spinodal transition and an increase in the nucleation rate of the Guinier-Preston (GP) zones with the undercooling (*i.e.* with Zn supersaturation). The lack of signature of the SD process is also found in some cases to work the other way. Indeed, for some measurements of AlZn alloys outside the spinodal, scattering reminiscent of SD was observed.

Though SD can be divided up into at least two stages, early and late, rigorously, it is only at the onset of the phase separation process, in the very early stage, that SD can be discriminated against NG. Indeed, it is in this stage that the most typical characteristics of spinodal decomposition — homogeneous buildup of fluctuations — should appear. The most critical work on SD should then aim at the study of the very early stages of the phase-separation process. Critical comparison of the theory and observations is, however, not easy for the early stages, partly because of the experimental difficulty in distinguishing these stages from the late stages *i.e.* the scaling stage.

A full and significant determination of the early time kinetics is not an easy task. The quench must be perfect: it must preserve the high temperature disorder,

a condition which is difficult to meet with highly over-saturated systems. Defects which lead to heterogeneous nucleation must be avoided. Small composition fluctuations are difficult to characterize. In all kinetic studies, it is imperative that any change occurs on time scales comparable to the time scales on which the measurement is performed. The choice of a system for the study of SD will depend, amongst other things, on the expected rate of decomposition. In the set of binary alloys that possess a miscibility gap, decomposition rates will vary widely and will be, of course, temperature dependent at any given composition. In general, the driving force increases with undercooling but the atomic mobilities decrease as the temperature is lower. So, near the spinodal line, decomposition will be slower due to the small driving force and at low temperatures the decomposition will be slow due to the low mobility. Few experiments have been performed with sufficient time resolution to study the range of early-stage behaviour between these limiting cases. Higher time resolution is needed for the faster reaction processes so that the measurements will be faster than the total transformation time of the fastest reaction of interest.

Alternately, instead of speeding up the experiment, one can try to slow down the decomposition. Small quantities of certain alloying elements (Sn[65], Cu[66] and Mg) are known to retard the decomposition rate in the early stages of the coarsening of modulations in AlZn alloys. Some of the studies have hence been performed on AlZnX alloys. For instance, Hoyt *et al.*[67] added 0.01 at.% Mg to retard discontinuous grain boundary precipitation. These studies have shown that as the alloying composition gets closer to the critical composition, the decomposition kinetics for coherent decomposition (SD) becomes faster and in cases where there might be competition with incoherent precipitation processes (NG), the time scales over which the latter would occur become much longer than those for SD and the incoherent precipitation essentially vanishes. Thus, if sufficient time resolution can be achieved to measure SD near the critical composition where the kinetics are faster, the measurement will be more reliable.

Table 3.1 lists the experimental investigations of SD in AlZn to date. This

list does not include studies of NG and experimental determinations of the location of the solvus curve such as the early investigations performed by resistivity measurements.

These studies (except that of Hoyt *et al.*[67]) were performed at compositions or temperatures well removed from the critical point. The points on the phase diagram of Fig. (1.2) showed the aging compositions and temperatures of all studies listed in Table (3.1). The points on the phase diagram corresponding to the measurements reported in this thesis were also shown, pointed at by the arrow. These are practically at the critical composition and cover temperatures both near T_c and at the temperature of maximum decomposition rate (about 560 K). The tail end of the arrow is at the anneal temperature in this work.

Workers have interpreted their measurements, looking for a number of signatures of spinodal decomposition in the alloy AlZn. The main landmarks are enumerated below. This should serve the purpose of putting in perspective the measurements reported in this dissertation.

I.(A) SCATTERING FUNCTION: THE NAIVE PICTURE — Most of the measurements reported in Table (3.1) are of the scattering function, either by SANS or SAXS. The measurements of scattering functions constitute the most direct route to verification of SD theories. Indeed the structure factor at the very early times is one of the two most specific characteristics of SD; the other being the absence of an incubation time for the decomposition to commence. However, to date, experimental conditions for such measurements have not been controlled sufficiently to allow conclusive comparison with existing theories. The first evidence of spinodal decomposition was inferred from measurements of the kinetic evolution of the scattering function in *relative units* and fitting to the CH equation. However, with the introduction of the thermal fluctuations in the CH equation (Eq. 3.1), knowing the scattering function only in *relative units* became insufficient and it became necessary to obtain *absolute* structure factors to check measurements against the CHC equation (Eq. 3.6). In both cases, with the diffusion equations, it is possible to derive κ and \tilde{D} . To

Author ¹	Year	Composition (at. % Zn)	Method	Early time	Late time	Analysis
Bonfiglioli[68]	1966	9.7, 20.5 and 28.5	SAXS	No	No	$Q(t)$ and scattering profiles
Rundman[58]	1967	22	SAXS	Yes	No	CH
Murakami[64]	1969	6.8	SAXS	Yes	No	CH
Agarwal[69,70]	1973	22 and 28	SAXS,TEM	Yes	No	CH
Junqua[71]	1974	6.8	MS ²	No	No	discriminate between SD and nucleation
Naudon[72]	1974	6.8	SAXS	Yes	No	SAS profiles Evolution of GP zones
Acuña[73]	1974	15	SAXS	Yes	No	CH,CHC
Delafond[74]	1975	6.8	ER ³	No	No	discriminate between SD and NG
Bartel[75]	1975	22 ⁴	SAXS	No	Yes	$t^{1/3}$ coarsening, $Q(t)$ and \bar{D}
Laslaz[61,76]	1977	6.8	TEM	No	No	Evolution of GP zones
Ciach[66]	1979	22 ⁵	SAXS, TEM	No	No	Obtain T_c from qualitative observation of scattering
Ungár[77]	1981	6 - 21	SAXS	No	No	Determination of T_c by $Q(t)$
Furusaka[78]	1985	6.8	SANS	Yes	Yes	$S(q) \sim q^{-2}$ at high q for early times
Hoyt[67,79]	1989	12, 22 and 32 ⁶	SAXS	Yes	Yes	CHC ⁷

Table 3.1: Published studies of spinodal decomposition in AlZn. By late time, it is meant a "scaling-like" analysis. This list does not include studies in which the data is analysed exclusively from the perspective of NG though there exists some overlap on the phase diagram with measurements presented above. The most notable case is that of Hennion et al.[60] who performed SANS on alloys $Al_{0.927}Zn_{0.053}$ (293 and 333 K) and $Al_{0.932}Zn_{0.062}$ (363 and 383 K) (see text).

¹Only the first author is given for succinctness.

²Magnetic susceptibility measurements.

³Electrical resistivity measurements.

⁴0.1 at.% Mg alloy.

⁵0, 1 and 3 at.% Cu alloys.

⁶0.01 at.% Mg for the three alloys.

⁷These authors also present what could be termed a qualitative discussion of LBM with their data.

this day most authors have worked in relative scattering intensity increase and have not reported absolute scattering cross-sections. They introduce an arbitrary normalization constant for the scattering due to thermal fluctuations (for example, see Ref. [67] and the text below).

The first experiment to quantitatively verify the theory of SD by checking the CH theory was undertaken by Rundman and Hilliard in 1967[58] (RH), who applied SAXS on an $\text{Al}_{0.78}\text{Zn}_{0.22}$ alloy aged at 338 K. The evidence seemed to agree favorably with the expectations from the CH theory. Namely, the measured scattering intensity (in relative units) presented a time-independent crossover point at q_c (*cf.* p. 43), the obtained amplification factor $R(q)$ possessed a maximum at $q_c/\sqrt{2}$ and had the right functional dependence and, in the framework of the theory, the data, when interpreted according to the theory, yielded an interdiffusion coefficient that agreed in magnitude and sign with that obtained by an extrapolation of high-temperature measurements. For instance, for wavenumbers below a critical wavenumber, q_c , the intensity is increasing, whereas for $q > q_c$ the intensity decreases continuously. However, despite these expected features, the very nature of what was being measured was debated.[80,81] Namely, the alloy seemed to show marked SAXS right at the beginning of the aging and it could be speculated that the later stages of decomposition, when coarsening is occurring were being observed.

Other workers repeated the RH experiment for other compositions (see Table 3.1).[64,70,73] In general, these early investigators looked for a time-invariant crossover point in the scattering intensity q_c and a time-invariant nonzero wavevector of the maximum in scattering intensity, q_m .

In all these studies, the measurements have generally been interpreted in terms of an analysis of the amplification factor $R(q)$. [58] What is required is the values of the parameters \widetilde{D} and κ .

With the CH equation of motion (3.1), the slope of $\log I(q)$ vs. t yields $R(q)$. The obtained $R(q)$ plotted against q are generally found to agree in shape with the theoretically calculated one[82]. It is observed that as the aging temperature is

increased, q_m and q_c shift to smaller wavenumber and $R(q)$ decreases. This agrees with the expected temperature dependence of q_m^2 and q_c^2 . Indeed, for q_c^2 , [57]

$$-\frac{T - T_s}{T_c} = \psi^2 [c(1 - c)] \frac{q_c^2}{2} \quad (3.9)$$

where T_c is the critical unmixing temperature at composition c and ψ is an interaction distance. A similar relation holds for q_m since $q_m = q_c/\sqrt{2}$. In theory, if the experimentally determined values of q_m^2 and q_c^2 were equal to zero, the corresponding aging temperature T should be equal to the spinodal temperature T_s . So, in theory the amplification factor $R(q)$ and the wavenumber q at a few values of temperature should provide a means to determine the spinodal temperature for that alloy composition. But in experiments [64], the exponential growth of the intensity slows down after some time and the slope $\Delta I(q)/\Delta t$ that is required to obtain $R(q)$ should only be taken for the aging times shorter than this time.

If instead, measurements are analysed in terms of the CHC equation, the simplest route to extract κ , the gradient energy coefficient, and \tilde{D} , the interdiffusion coefficient, is to rewrite Equation (3.7) in the form

$$\ln \left(\frac{S(q, t) - S_{OZ}(q)|_{T_s}}{S(q, 0) - S_{OZ}(q)|_{T_s}} \right) = 2R(q)t. \quad (3.10)$$

The amplification factor $R(q)$ is as given by Eq. (3.2), making use of the relation between M and \tilde{D} (Eq. 1.25)

$$\frac{R(q)}{q^2} = -\tilde{D} \left(1 + \frac{2\eta^2 Y}{f''} \right) - \frac{2\kappa \tilde{D}}{f''} q^2. \quad (3.11)$$

In this analysis, a plot of the left side of equation (3.10) versus aging time will yield $R(q)$ and a plot of $R(q)/q^2$ versus q^2 should be a straight line with slope and intercept related to the parameters κ and \tilde{D} . In their recent synchrotron work on $\text{Al}_{0.32}\text{Zn}_{0.68}$ Hoyt *et al.* [67] obtained a straight line for $R(q)/q^2$ versus q^2 from which $\kappa \approx 3.5 \times 10^{-10}$ J/m and $\tilde{D} \approx -2.54 \times 10^{-22}$ m²/s were obtained. These are close to the RH values. Hoyt *et al.* [67,79] measure intensities in counts per second whereas the function $S_{OZ}(q)$ is expressed in absolute units and to overcome this difficulty they have multiplied $S_{OZ}(q)$ by a factor such that the best straight line fit is obtained

according to equation (3.11). This procedure was suggested in the original work by Cook[30].

From the first measurements aimed at verifying the CHC equation[73] it was obvious that it does not constitute an adequate description of experimentally determined, time-dependent, structure functions; the notable exception being the very recent Cu-Mn study of Gaulin *et al.*[83]. In a typical experiment, the position of the peak in the structure function shifts to smaller values of q with increased aging time, whereas the CHC theory predicts an exponential increase in the scattered intensity with virtually no shift in the peak position. This discrepancy between theory and experiment is due to the neglect of nonlinear terms in the diffusion equation. As pointed out in an early paper by Cahn[84], nonlinear effects play an important role soon after the quench and thus any successful theory of spinodal decomposition should include the contributions to the higher derivatives of the free energy with respect to concentration (Eq. 1.20).

Central to the interpretation of most investigations is that there be a unique crossover and maximum growth wavevector and that the intensity for wavenumbers below q_c grow exponentially *ad infinitum*. These features were found to be lacking in studies on AlZn, first by Bartel *et al.*[75] and in more recent studies[67]. This opens the question that if early stage is what is truly measured, then nonlinear terms have to be included.

The time-resolution is an open issue in all investigations so far reported as it cannot be asserted that any reported measurement was performed at an early enough stage, *i.e.* before the formation of interfaces when SD and NG can be distinguished. The coupling of dynamic measurement of $S(q, t)$ with integrated intensity values can provide some further information on the reliability of the measurement. The presence or lack of an incubation period in integrated intensity measurements becomes the new criterion to distinguish between NG and SD respectively.

I.(B) SCATTERING FUNCTION: PATCHING UP FOR FINITE TIME QUENCHES —
Complications in the practical measurements of SD arise from two major sources

during the quench. (i) A finite time is required to lower the temperature from the annealing to the aging temperature, the quench time. (ii) In most cases when the kinetics are faster than the available experimental time resolution, the quench is performed to a temperature much lower than the aging temperature to “freeze” the “initial” structure for measurement. This quench is then followed by one or more up-quenches to measure the time dependence of the scattering function. Each of these two experimental “compromises” has an effect on the measured scattering function though the effect of the second has sometimes not been recognized.

A consequence of reaching the aging temperature *via* an up-quench which has been alluded to by some researchers, but more often neglected, is that some phase separation has occurred during the initial quench to a low temperature. Thus the alloy can potentially evolve towards points on the phase diagram that are further from c_0 than the coherent coexistence values at the aging temperature. When nonlinear terms are included in the equation of motion for the structure factor (*cf.* Chap. V), the critical wavevector q'_c is expected to decrease with time. However, if during the quench, the alloy has evolved towards compositions beyond the equilibrium compositions at the aging temperature, a lower q'_c than would otherwise exist during initial stages of SD at the aging temperature will be observed. This rationale is supported by the experimental observations[67] that the wavenumbers relaxing the fastest to equilibrium amplitudes lie on the high- q side of the quenched-in peak.⁴ Thus, during the initial stages of isothermal aging the decrease in q'_c predicted by nonlinear terms combined with the increase in q'_c resulting from the up-quench can result in the observation of a stationary value of q'_c at early times. A stationary q'_c is precisely what linear theory predicts and the analysis of the data in the framework of this theory would be erroneous.

This points out more the necessity to perform SD experiments with a single quench to the aging temperature directly from the one phase region above the miscibility gap. These considerations have been brought up in light of the early time

⁴This is also obvious in the LBM theory; *cf.* Chapter V.

behavior of the structure function data for $\text{Al}_{0.68}\text{Zn}_{0.32}$ reported by Hoyt *et al.*[67]

To circumvent the shortcoming of finite time quenches, in some case model equations have been proposed to theoretically predict the effects of continuous cooling on spinodal decomposition. The first to do so were Huston *et al.*[31] in terms of the CH theory. Carmesin *et al.*[85] also offer a detailed account of continuous cooling. These researchers rederive expressions for the time dependent reduced structure function in the framework of both a nonlinear theory (LBM) and the CHC theory allowing the temperature dependent mobility and free energy to be functions of time. Hoyt *et al.*[67] put a lot of emphasis in their analysis on the importance of modeling the time evolution of the structure function *during the quench* as well as during the isothermal aging.

In this dissertation, the issue of modeling the phase decomposition during the quench is treated differently. The quench times used are faster by two orders of magnitude than any previously reported study and quenches directly to the aging temperature are performed. Furthermore, whereas Hoyt *et al.* favor more effort to be put on the analysis of the evolution during the quench, a quantitative analysis from the quenched-in structure is presented here. It is believed that by achieving faster quenches to the aging temperature and dealing explicitly with the quenched-in structure factor spinodal decomposition theories can be critically evaluated.

II. INTEGRATED INTENSITY — According to the sum rule given by Eq. (2.25), the integrated intensity, Q_0 , about the origin of reciprocal space can be used for the determination of the percent completion of the decomposition. Indeed, when the alloys are aged below the coherent critical temperature, T_c , the value of $\overline{(c - c_0)^2}$ and hence Q_0 should increase with aging time until the decomposition is completed. Furthermore, a signature of SD is that this increase in Q_0 should proceed with no incubation period. After the decomposition is completed Q_0 should remain constant. The determination of the presence or the absence of an incubation period before Q_0 starts to increase can, in theory, be used to discriminate between NG and SD. However, in practice, since the experimental procedure between the onset of

the quench and the first measure of the integrated intensity cannot be monitored absolutely, it is difficult to affirm that the absence of incubation really indicates a SD process. However, the measure of an incubation period certainly indicates that the system is phase separating by a NG mechanism.

In addition to the interpretation problems posed by the sample conditioning procedure for the isothermal studies on $Q(t)$, there exists the possibility of competing transformations occurring while SD is taking place. Such transformations, such as supposed NG at the grain boundaries in the RH measurements can complicate the interpretation of $Q(t)$ data.

Nevertheless, on the basis of their own measurement of the evolution of the integrated intensity at room temperature, Gerold and Merz[80,81] proposed that that the RH results were in fact obtained in decomposition stages where only coarsening was occurring. In this decomposition regime Eq. (3.1) should not even have been used.

Murakami *et al.*[64] calculated $Q_0(t)$ for $Al_{0.932}Zn_{0.068}$ specimens aged at four different temperatures (313, 333, 353 and 373 K). In all cases, the calculated $Q_0(t)$ increase during the initial few minutes and show little change afterwards. This suggests that, at the time when $Q(t)$ has stabilized, the decomposition has progressed to the stage where the sample consists of domains of compositions lying on the solvus line (metastable miscibility gap boundary).

Attempts were made to capture an earlier stage in the decomposition process than the RH measurement, at the same alloy composition. Agarwal and Herman[70] performed a SAXS experiment using liquid-quenched specimens and calculated $Q(t)$ as well as reporting the measured scattering intensities. Their results, while offering somewhat different estimates of \tilde{D} , the interdiffusion coefficient, and κ , the gradient energy coefficient, were substantially in agreement with those of RH.

The attempts to separate SD from NG on the basis of the absence of an incubation period for decomposition are not limited to calculations of $Q(t)$ from scattering experiments. Junqua *et al.*[71] distinguish between the nucleation process and SD

by magnetic susceptibility measurements on $\text{Al}_{0.932}\text{Zn}_{0.068}$ samples (*cf.* Table 3.1). The time change of the magnetic susceptibility and the presence or the absence of a delay before this change is then taken as a signature of the decomposition process.

III. HIGH q BEHAVIOR — Another of the sum rules introduced in § 2.3, Porod's law (Eq. 2.32), can contribute to distinguish between SD and NG processes. This sum rule indeed provides a means to verify the existence of sharp interfaces since $q^4 S(q, t)$ should then be constant for large q . If the decomposition proceeds by the spinodal mechanism, the mixture consists of composition fluctuations of growing amplitude. The concentration of solutes inside the "clusters-to-be" should increase with increasing aging time, while the concentration in the matrix should decrease. There should be no clearly definable interface between the clusters and the matrix until later times, when coarsening sets in. On the other hand for NG, as was depicted in schematic (3.1), the concentration of solutes inside the particles should be constant throughout the course of the entire decomposition process and the concentration gradient at the interface should be infinitely large. Thus, for NG Porod's law should apply from the onset of the isothermal measurement whereas in the case of SD a time delay is expected. It was argued above that the sole argument of the absence of incubation period for the increase in integrated intensity wasn't sufficient to confirm that decomposition occurs by SD. Similarly, the onset of a q^4 tail for the first isothermal scattering profile, though in theory a signature of NG, is not sufficient in practice to affirm that the decomposition mechanism should be NG rather than SD. Indeed, there could have been a time regime shorter than the quench time scale in which continuous composition fluctuations existed.

Murakami *et al.*[64], whose measurement of an incubation time before the increase in $Q(t)$ was mentioned above, have also examined the high- q behavior of the measured scattering functions for the same alloy ($\text{Al}_{0.932}\text{Zn}_{0.068}$). They report a monotonous increase of $q^4 S(q)$ with q over the complete q -range measured in the first scattering profiles during the isothermal annealing. However, after a certain

time, $q^4 S(q)$ becomes constant for large q and Porod's law is then satisfied.⁵ This time becomes longer for the lower temperatures (ranging from 2 mins at 373 K to 6 mins at 313 K after a quench from 573 K). These results mean that sharp interfaces exist only after that time is reached. The time values at which Porod's law starts to apply almost coincide with their measured time of saturation of $Q(t)$. This result indicates that until the time when Porod's law applies for high- q is reached the concentrations of solutes inside and outside the clusters and the concentration gradient at the interface do not have any fixed value, but they increase with the aging time. The two facts together support the occurrence of SD and argue against a NG mechanism.

The same authors observe that at 413 K $q^4 S(q)$ is a constant even after the earliest aging time they could observe, which was 30 s. From this they conclude that the mechanism of decomposition at this higher temperature is not spinodal as for lower temperatures, but nucleation and growth. Though this is likely the case, on the basis of their observations alone, it is not possible to be positive for the reasons argued above. Hence, at the temperatures above T_c , the particles will be formed by the nucleation and growth mechanism and the constancy of $q^4 S(q)$ with respect to q will be found from the beginning of the aging. This constancy will not be found if the aging temperature is below T_c where the decomposition occurs by the spinodal mechanism.

From the experimental point of view the whole unmixing kinetics must be determined and closely compared with the theoretical predictions. Partial observations, such as the search for an incubation period whose lower limit varies considerably with experimental technique, or observation of a periodic two-phase morphology are clearly insufficient.

Binary alloys with slower decomposition kinetics than AlZn near the critical composition have recently been investigated. Perhaps the most interesting measure-

⁵These workers use a slit-collimation and the corresponding expression for Porod's law: $q^3 J(q)$ is constant for large q where $J(q)$ is their measured scattered intensities.[47]

ments were performed on FeCr alloys, an alloy which has small elastic strains. This alloy has been studied by SANS.[78,86,87] Nonlinearities in the SD of FeCr alloys have been reported. For instance, Furusaka *et al.*[78,88] even present approximations to compute the LBM equation of motion on $\text{Fe}_{0.60}\text{Cr}_{0.40}$ and $\text{Fe}_{0.70}\text{Cr}_{0.30}$. The shortest time incremental step they use is 5 mins for $\text{Fe}_{0.60}\text{Cr}_{0.40}$ aged at 100 K.[78] During the early stages, these authors report a q^{-2} dependence of the structure factor at high q . Nonlinear effects were also observed in the more recent SANS work of Furusaka *et al.*[87] (four alloy compositions including $\text{Fe}_{0.60}\text{Cr}_{0.40}$, $\text{Fe}_{0.70}\text{Cr}_{0.30}$) and of LaSalle *et al.*[86] ($\text{Fe}_{0.68}\text{Cr}_{0.32}$).

Studies of spinodal decomposition have also been performed in non-metallic systems. Light scattering measurements in binary fluids and in polymers offer valuable information on the decomposition process in these systems. The CHC equation of motion was shown to describe well the unmixing of pseudobinary polymer systems in the early-time regime.[89,90] Studies[91] near the consolute point in binary liquids, demonstrate the importance of nonlinear effects at early times even though an earlier study[92] had conclusively analysed scattering results in terms of the CH equation. Studies of systems of glasses[93,94] also present a conclusive verification of the CHC theory. The systems with a time regime during which the CHC theory is found to be valid share one common characteristic: they all have long range interaction forces.

Table (3.1) includes a column labeled "late time". Investigations into the later time regime of SD are included as they complement the early stage dynamic studies. A discussion of the dynamics of the late stages of spinodal decomposition will be given in § 5.5. The late stages measurements performed in the course of the work presented in this dissertation will be introduced and discussed in § 6.3.

The late stages dynamics regime is characterized by a time independent structure function which scales the structure factors by a length scale varying as a power law $\sim t^{-n}$. Such a scaling has been found to hold in phase-separation processes in liquid mixtures,[95] a glass system,[96] and a number of binary alloys.[60,97,98]

Studies of the late-stage or scaling regime have primarily focused on the value of the growth exponent n , as well as the scale invariant function for the structure factor. The value of n is of importance, because it is the signature of the thermodynamic forces which are responsible for the phase transition. However, at present, there exists no successful analytical theory for the late stages of SD (*cf.* § 5.5).

During the late stages, domains of each phase coexist and are thus separated by interfaces. From measurements in this regime alone, it is not possible to separate SD and NG processes.

The late stages have been studied for most of the systems mentioned above in the discussion of the early stages.

Furusaka[78] shows a scaled function obtained for $\text{Al}_{0.932}\text{Zn}_{0.068}$ alloys aged at 389 K for up to 60 mins. Indeed, he observes that after a certain aging time, dynamical scaling holds for the scattering function. The time regime during which the scaling holds coincides with the time for which a q^{-4} dependence of the structure factor is obtained for high q values (*cf.* Eq. 2.32). Hoyt *et al.*[79] have also shown that the late stages scattering in AlZn alloys ($\text{Al}_{0.91}\text{Zn}_{0.09}$, $\text{Al}_{0.78}\text{Zn}_{0.22}$ and $\text{Al}_{0.56}\text{Zn}_{0.44}$) quenched inside the spinodal region present a universal scaled structure function. However, neither of these two studies present a value for the growth exponent, n . A study of coarsening in $\text{Al}_{0.779}\text{Zn}_{0.220}\text{Mg}_{0.001}$ aged at 398 K by Forouhi and De Fontaine[99] revealed a three part late stages with a growth exponent of 1/3 in the latest part and lower values in the earlier parts. However, it is not clear how these earlier (attributed to cluster coagulation) parts would relate to the mechanism of SD near critical composition.

In their work on $\text{Mn}_{0.67}\text{Cu}_{0.33}$, Gaulin *et al.*[83] have obtained strong evidence for the late stages dynamic scaling regime. They found that a universal scaling function is sufficient to describe the time-dependent structure factor and a growth exponent of -0.37 ± 0.03 .

A scaling function was also obtained in the late stages in three FeCr alloys ($\text{Fe}_{0.60}\text{Cr}_{0.40}$, $\text{Fe}_{0.68}\text{Cr}_{0.32}$ and $\text{Fe}_{0.76}\text{Cr}_{0.24}$)[100]. For these measurements, it was also

found that the time independent growth exponent fell in the range $0.12 < n < 0.22$ depending on composition and aging temperature. However, Katano *et al.*[101] have obtained a striking result during the aging of $\text{Fe}_{0.68}\text{Cr}_{0.34}$ at 773 K. The growth exponent changes from $0.17(\pm 0.02)$ to $0.33(\pm 0.03)$ around 30 h. During this “crossover” phenomenon there is also a change in the dynamical scaling function.

Finally scaling functions and growth exponents have also been measured in non-metallic systems. Phase separating binary fluids[95,102,103] present a scaling function and a growth exponent close to $1/3$. A crossover between $1/3$ and 1 was found at some late time (and was explained by Siggia[104]). Fluctuations relaxing in the single phase region above the critical point after a pressure jump also reveal a scaling function and an exponent of $n = 1/3$ [105]. The late stages studies in polymer mixtures by light scattering of Bates *et al.*[90] exhibit a scaling function as well but, whereas in the previous systems, the growth exponent was independent of temperature, in this case it was found to be temperature dependent. However, in agreement with the earlier results of Nojima *et al.*[106], the exponent is of order $n = 0.29 \pm 0.05$ for relatively small supersaturation. Finally, Craievich *et al.*[96] found a scaling function and a growth exponent of $n = 0.23$ in a quasibinary glass phase-separating by SD.

This Chapter has limited the discussion to linear theories and left out the nonlinear theories for early times. The overview of the investigations of SD presented in this section suggests that the CH and the CHC theories may not apply in the case of binary alloys. This is also supported by theoretical estimates of the nonlinear terms (*cf.* § 5.3). A good indicator of the importance of nonlinear effects was exemplified by the work mentioned on FeCr alloys. A recent exception is the SANS work of Gaulin *et al.*[83] in $\text{Mn}_{0.67}\text{Cu}_{0.33}$. This work makes no provisions for the points raised in I.(B) above.

As the experimental investigations improve and capture *earlier* stages of the decomposition process studies that were first taken as evidence of the application of linear theories of SD may have to be reevaluated.

Chapter 4

Experimental Method

4.1 Introduction

The experiment is described with an emphasis on two principal aspects. The first describes how to take full advantage of the high intensity synchrotron radiation to perform *in situ* time resolved x-ray scattering at time resolutions orders of magnitude faster than has ever previously been reported for a study of phase separation in binary alloys. The necessity of achieving high time resolution has been emphasized in chapters I and III. In addition to high x-ray fluxes, high time resolution experiments require: (i) abrupt quenches, (ii) rapid data acquisition, and (iii) a sensitive temperature control. The second describes how to obtain reliable absolute structure factors for use in the study of phase separation.

The first two sections of this chapter will treat these two aspects. The next section will cover temperature calibration. To conclude, the instrumental response of the position sensitive detector (PSD), or convolution of the measured scattering patterns is examined and a deconvolution proposed.

Of course, the minimal requirement is that the time required for acquiring a scattering pattern be less than the time scale of the return to equilibrium after a departure from equilibrium. This requirement is met to an unprecedented level at a

composition very close to the critical composition and at temperatures both above and below the critical temperature, including the temperature of fastest kinetics. Further, the elaborate discussion dividing the previous researchers on the evolution of the phase separation during the quench and the reheating to the aging temperature is substantially obviated in two very important ways: by quenching directly to the aging temperature and performing truly *in situ* measurements and by the sheer rapidity of the experiment (it's all over in two seconds!)

During a typical spinodal decomposition run, a ribbon of AlZn, is first resistively self-heated *in situ* in a helium atmosphere (slightly above 1 atm) to an anneal temperature T_a well above T_c . It is then quenched directly to a constant aging temperature T_q by decreasing the current. For some time preceding and during the quench, and while aging, x-ray diffraction profiles and the sample temperature are recorded as functions of time. To study the isothermal phase decomposition kinetics, the same sample was repeatedly cycled through annealing and aging cycles. As a test of reproducibility, identical temperature cycles were often repeated and they showed the same temperature evolution. An infrared pyrometer monitored the sample temperature. By control of the power to the sample, the sample temperature could be dropped 150 K to a constant aging temperature in less than 100 ms (to within an estimated standard deviation of 0.5 K). These high cooling rates allow quenches directly to the aging temperature quickly enough to take advantage of the time resolution of the x-ray measurement.

The bright synchrotron source, detector and data collection software allowed for entire spectra to be obtained as rapidly as every 0.005 s. X-ray diffraction profiles are recorded in real-time every 5 or 10 ms by a linear position-sensitive detector (PSD) based on a photodiode array.[107]

The high incident intensity is provided by synchrotron radiation from the National Synchrotron Light Source at the Brookhaven National Laboratory using the IBM-MIT bending-magnet beamline X-20C optimized for time-resolved scattering studies. This dissertation does not focus on the operation of the beamline. Re-

garding the design and operation of the detector or beamline X-20C, the reader is referred to Refs. [107–110] for a description with more details than provided in the sections to follow.

4.2 *In situ* time resolved x-ray spectra acquisition

With the ability to heat and cool the sample fast, parameters have to be monitored simultaneously and rapidly. Examples of such parameters are the sample temperature and resistance, incident beam intensity and running time. However, the most important quantity is the scattered x-ray intensity since it provides the measurement of the structure of the sample.

Scattering data were acquired in “runs” in which the sample would be first annealed at a temperature T_a in the single phase region, well above the miscibility gap, and then quenched to a lower temperature T_q , either above or below the solvus line, and held isothermally. The evolution of the scattering was measured by recording a series of consecutive scattering patterns as the sample phase separated, or, above T_c , as the thermal fluctuations re-equilibrated. In order to characterize and as a verification of initial conditions, each run was initiated so that several patterns were recorded before the quench. The runs were always started from the same anneal temperature, T_a .

4.2.1 Synchrotron radiation and the beamline

Is it of course paramount to the measurement performed for this work that the x-ray source be very intense. To a very large extent, it is the availability of synchrotron sources that prompted this investigation of spinodal decomposition in AlZn, a system where no decisive measurement could be performed, due to the experimental limitations stressed in chapters I and III.

Synchrotron are circular particle accelerators. They are used for various charged particles and in particular as electron storage rings. Synchrotron radiation is the electromagnetic radiation that is emitted tangentially to the trajectory of the charged particles which are moving at relativistic speeds in the circular orbits of the synchrotron.

Today, synchrotron radiation is widely used in physics, biology, medical science, chemistry and technology. Synchrotron radiation has two characteristics which cannot be obtained from conventional radiation sources. One is the wide range of wavelengths or energies (from 10^{-1} to 10^3 Å). With these photon energies, studies on atoms, molecules, solids and biological systems can be accomplished. The other is the high incident photon flux. This allows experiments on systems where the ratio of the scattered to the incident beam intensity would be too small using a conventional x-rays source.

The electron storage ring at NSLS used to generate x-rays has a circumference of 170.1 m and operates at an electron energy of 2.5 GeV.

The electrons in the storage ring circulate in bunches and the number of circulating bunches is adjusted so that the current is of order 100 mA. The beamline is connected to the ring by a water cooled fast valve and the radiation is delivered to the beamline at every passage of an electron bunch in the ring at the point of tangency. The electrons travel at a relativistic speed and a typical bunch length is 10 cm. The photons are thus radiated with a pulse duration of nanoseconds. The repetition rate between bunches determined by the number of bunches and the size of the storage ring is typically around 500 ns for a single bunch at NSLS. Hence, the storage ring radiation can be considered continuous when measurements are performed on times scales of a millisecond or longer, as is the case in this work.

The source produces a transverse electromagnetic wave polarized in the horizontal plane of the orbit.[111] The radiation pattern exiting the ring at the porthole is confined to a forward-directed narrow cone, when viewed by an observer in the laboratory frame. The aperture angles are proportional to $\gamma = mc^2/E$, where m is

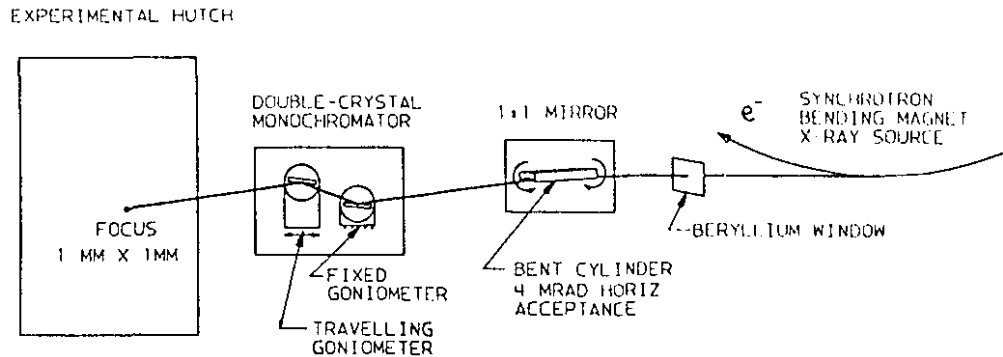


Figure 4.1: Schematic optical configuration of IBM/MIT beamline X-20C at the National Synchrotron Light Source (reproduced from Ref. [107]).

the rest mass of the electron, c is the velocity of light and E is the electron energy. The vertical angular divergence of the beam is $\frac{1}{\gamma}$, which for a ring energy of 2.5 GeV gives $\gamma^{-1} = 0.2$ mrad (or 0.012° FWHM).

Figure (4.1) shows a diagram of the beamline. The main optical components are a 1:1 focusing mirrors and a double crystal monochromator. With the monochromator used, these provide a typical intensity of 10^{13} photons per second at energies between 5 and 8 keV with the synchrotron ring current of 100 mA. The entire optical path to the hutch, 22 m long, is under vacuum (10^{-7} torr).

The mirror focusses 4 mrad into a 1×1 mm² spot at the sample. Indeed, despite the small angular divergence, the length of the beamline makes it necessary to focus the beam. The mirror is silicon coated with platinum and is toroidal with 4 cm and 1.5 km radii. The refraction index of materials for x-rays is less than one and so for small angles total external reflection occurs. Four rods allow to adjust

both the meridional radius and the incident glancing angle. The beam can thus be focussed in both vertical and horizontal directions. Since the size of x-ray source is 0.38 mm horizontal \times 0.12 mm vertical, with an aperture angle 5 mrad \times 0.23 mrad without a mirror, the beam size at 22 m would be $110 \times 5 \text{ mm}^2$, with the ensuing decrease in flux. By using the mirror, the increase in the intensity achieved by focusing is nearly 10^3 times.[109]

The wide-bandpass monochromator at NSLS beamline X-20C has been the subject of a paper.[107] The monochromator, 14 m away from the source, selects the desired photon energy by eliminating photons of all energies except those with values within a bandpass. The monochromator incorporates artificial W-Si multilayers with a period of 23 Å rather than crystals. The bandpass of the monochromator is relatively wide, at the energy used, $\Delta E/E = 1 \times 10^{-2}$ (FWHM) (or, equivalently, $\Delta\lambda/\lambda = 1\%$), which is almost two orders of magnitude larger than a typical crystal monochromator. Compared to a conventional Ge(111) monochromator, the multilayers used here have low resolution. For relatively low resolution measurements (such as diffuse or small-angle scattering), this translates into almost two orders of magnitude increase in signal. It has been designed to trade-off resolution for intensity. The monochromator uses two antiparallel multilayers, one fixed and the other movable. The energy is selected by adjusting the angle of incidence.[112]

The incident beam intensity, focusing and positioning at the center of the spectrometer are optimized at the time of beam alignment. The alignment of the beam is mostly controlled by the mirror and the monochromator.

The energy of the beam was tuned to just below the Cr K edge, i.e. at $\lambda = 2.070 \text{ Å}$ or $E = 5.989 \text{ keV}$.

The operation of the beamline is computer controlled, with the spec^{TM1} software. The computer controls the slits which adjust the beam size, the mirror to focus the beam on the center of the sample chamber, the monochromator to select the proper wavelength, and the spectrometer which orients the sample and

¹From Certified Scientific Software, P.O. Box 329, Cambridge, MA.

detector. Also, it controls the horizontal and vertical position of the table on which the spectrometer is mounted. This equipment is controlled by 32 stepping motors.

At the experimental area end of the beamline, the experiment is assisted by a second computer acquiring the diffracted intensity via a detector, the incident beam intensity via an ion chamber, the transmitted intensity via a beamstop current, the sample temperature via a pyrometer, sample voltage and resistance via voltmeters. The computer also controls the experimental timing and the heating schedule of the sample.

The ion chamber is used to measure the incident beam intensities. The apparatus which is enclosed within the experimental hutch is shown schematically in Fig. (4.2). Two sets of front slits are used to collimate the beam and intensity data are collected via a Si photodiode linear position sensitive detector (PSD). The flight paths connect directly to the sample chamber in order to avoid parasitic small angle scattering that could be produced by windows. Thus the slits are effectively in the sample chamber. Be windows are placed at the ends of the flight paths, away from the sample chamber. A pyrometer monitors the temperature.

4.2.2 The sample

The optimization of the sample is one factor that contributes to the performance of *in situ* time resolved studies. High x-ray fluxes allow the use of thin samples whereas by comparison, neutron scattering would require much larger samples. As a direct consequence of using thin targets, the thermal mass is appreciably lower and the surface area to volume ratio is large, enabling fast quenches. The very technique of heating and cooling the sample can then depart from the conventional furnaces (*cf.* § 4.2.4).

All the results reported in this dissertation were collected from a single sample, near critical composition, repeatedly cycled through anneal and quench-to-aging schedules.²

²More than one sample was prepared at different compositions and results of measurements at

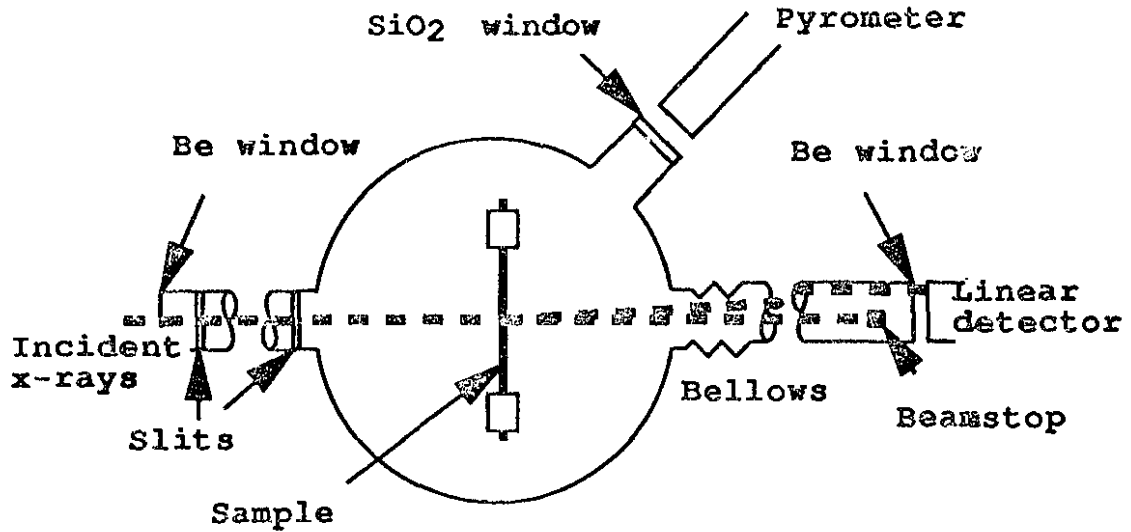


Figure 4.2: Setup in the hutch (reproduced from Ref. [112]).

The sample was prepared by melt spinning small alloy ingots (1 g). The melting points of pure Al and Zn are relatively close to each other (660.452°C and 419.58°C), making the alloying by melting relatively easy. Calculated masses of high purity Al and Zn^3 are first melted and mixed in an arc furnace under a titanium gettered argon gas atmosphere to prepare the alloy ingots. This was repeated three times to ensure homogeneity, turning over the pellet between each melting. Any surface oxide layer was removed by a chemical etch. A section was cut by diamond saw, etched again, and put in a quartz crucible for melt spinning. The melt spinning was performed in 35 kPa He to prevent oxidation and high purity argon gas was used to eject the molten material onto the copper wheel. The tangential wheel speed, at 60 m/s, and ejection pressure (about 50 kPa Ar) were optimized so that

two off-critical compositions will be the topic of a separate publication.

³Al 99.999% from Alfa Products (MA.), cut from ingot; Zn 99.95% from Merk and Co. (Montreal), cut from rod.

the resulting ribbon size was 1.5 mm wide and about 15 μm thick (*cf.* p. 86).

The target composition for the sample used in the present work was $\text{Al}_{0.605}\text{Zn}_{0.395}$, the composition of the top of the miscibility gap (*cf.* p. 11). However, weighing the ingot after the alloying in the arc furnace revealed a weight loss of a few percent. Spectrographic composition analysis was performed at IBM and a composition of 59.4 ± 0.2 wt. % Zn and 40.2 ± 0.2 wt. % Al was obtained. The samples are therefore $\text{Al}_{0.62}\text{Zn}_{0.38}$ indicating evaporation of Zn, which has the lower melting point and higher partial pressure. The obtained composition is very close to the coherent critical composition calculated in § 1.3.

Each sample was then cut from the ribbon to be about 35 mm long. The samples were polycrystalline and a grain size of $\sim 1 \mu\text{m}$ was measured by TEM.

4.2.3 Sample chamber

The sample chamber is mounted on a Huber spectrometer. Its design allows a flexibility in experiment geometries. There are five windows, positioned so that each covers 20° and a pair exists for each 20° range from 0 to 180° . For the SAXS experiments, three windows are used: an incident beam window and the straight through window (180°), and a window for the pyrometer reading. The first window is open to the beam path, *i.e.* the He filled flight tube, and the second is a thin beryllium foil, which has small x-ray absorption (absorption depth $\simeq 1.4$ mm for $\lambda = 2.1 \text{ \AA}$ [113]). The window for pyrometer reading is covered with quartz which is relatively transparent to infrared light. The sample chamber is evacuated and back-filled with helium (slightly above 1 atm).

A schematic view of the interior of the sample chamber is shown on Fig. (4.3). The sample holder is mounted on a sample manipulator which is positioned along the center of the cylindrical chamber. The sample holder can be freely rotated about its axis. Hence, diffraction patterns can be measured in reflection as well as in transmission. One end of the sample is attached to a rotating spindle. When

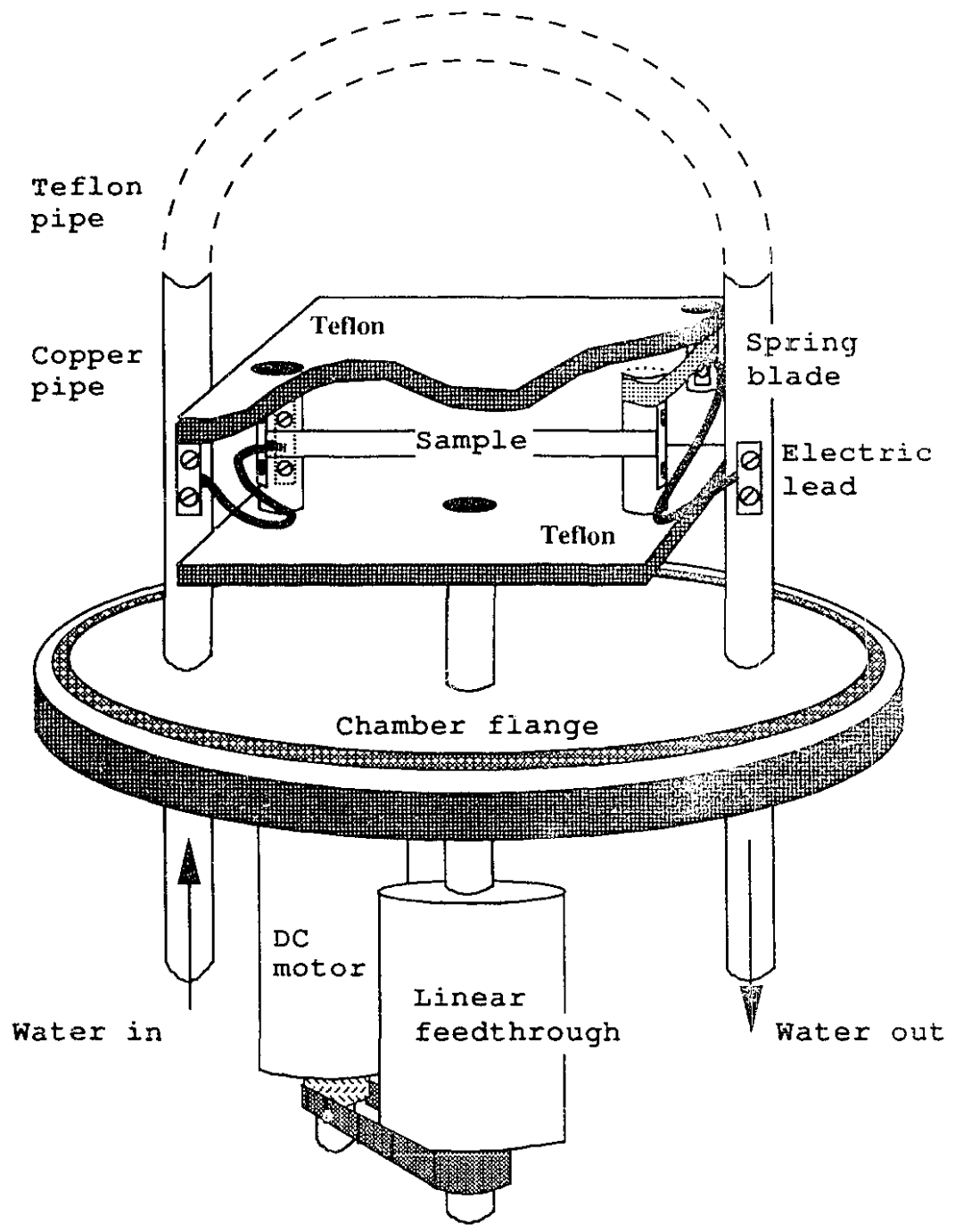


Figure 4.3: Schematic of the sample chamber.

thermal expansion of the sample occurs, the spindle rotates under spring tension and keeps the surface of the ribbon in a fixed plane. Electric leads on both ends of the sample are connected to a copper cooling pipe for water or gas, tightly mounted to the chamber flange. Temperature drifts were minimized by keeping a constant temperature at the extremities of the sample by flowing water in the cooling pipe. The current is delivered to the sample by the same pipe. An electrically insulating teflon pipe is used to connect the top of the cooling pipes to ensure that electrical conduction from one post to the other occurs only through the sample (any ionic conduction in the water is negligible). At the other end of the sample manipulator, a linear vacuum feedthrough is located and it is connected to a dc motor. The motor allows the translation of the sample holder in and out of the beam and to center the sample in the beam.

4.2.4 Sample temperature control and measurement

One of the most important experimental challenges of *in situ* studies of phase separation kinetics is the necessity to heat the samples in a manner that allows the rapid change in sample temperature as well as control of stability and uniformity.

The first motive for achieving high cooling rates is to satisfy isothermal conditions for the range of kinetics to be measured for the system. Specifically, as the quench is performed, a high cooling rate is required, so that any phase separation occurring before the aging temperature is reached can be minimized.

In general, to reduce the quench time and the time constant for stabilizing at the quench temperature, the thermal mass of the sample must be reduced. Thus with conventional furnaces which typically have a large thermal mass, the cooling rate during an *in situ* quench is limited by the furnace itself. The thin metal ribbons of uniform cross section used in the presented measurements can be self-heated just by passing a current through them and this has the effect of producing a large central region of uniform temperature.

A few parameters of the set-up also contribute to optimizing the quench rate. The most important is the pressure of the surrounding He. This high thermal conductivity atmosphere means more input power is required to get to the same temperature. However, upon dropping the current through the sample, the quench rates achieved are much faster than in vacuum. He also absorbs much less x-rays than air. As was mentioned in the previous section, the sample holder was water cooled, to prevent slow temperature drifts.

The obtained experimental conditions can be summed up as follows. The samples, ribbons produced by melt spinning typically 1.5 mm wide by 15 μm thick, fulfill well the condition of low thermal mass. The ribbons are resistively heated to the anneal temperature (689.9 K, cf. p. 92) by circulating a current through a 35 mm length in one atmosphere of helium gas. By lowering the current abruptly, the quench was performed to the *in situ* aging temperature. The quench time was about 15 ms for shallow quenches and 100 ms for deep quenches (see Fig. 4.4). The cooling rates obtained are then in excess of 10^3 K/s.

For the experiments reported it has been possible to cycle a single sample through repeated anneals and quenches to the aging temperature.

The temperature was monitored by an infrared pyrometer. Two reasons prevail for choosing a pyrometer over a thermocouple. Firstly, if the sample were put in contact with a thermocouple, heat diffusion from the sample surface through the thermocouple junction would result and locally the temperature would be lowered. This effect would be particularly dramatic in regard to the low thermal mass of the sample. Secondly, ideally the temperature reading position on the sample should be coincident with the location of the incident x-rays. X-ray scattering from the thermocouple would be unavoidable in that case.

A pyrometer which uses infrared radiation is the best alternative to overcome the above mentioned difficulties. The pyrometer used was manufactured by IRCON (series 60) and accepts infrared radiation (wavelength $\simeq 2.3\mu\text{m}$). It has a focal spot of 1 mm radius. As mentioned in the previous subsection, the port on the

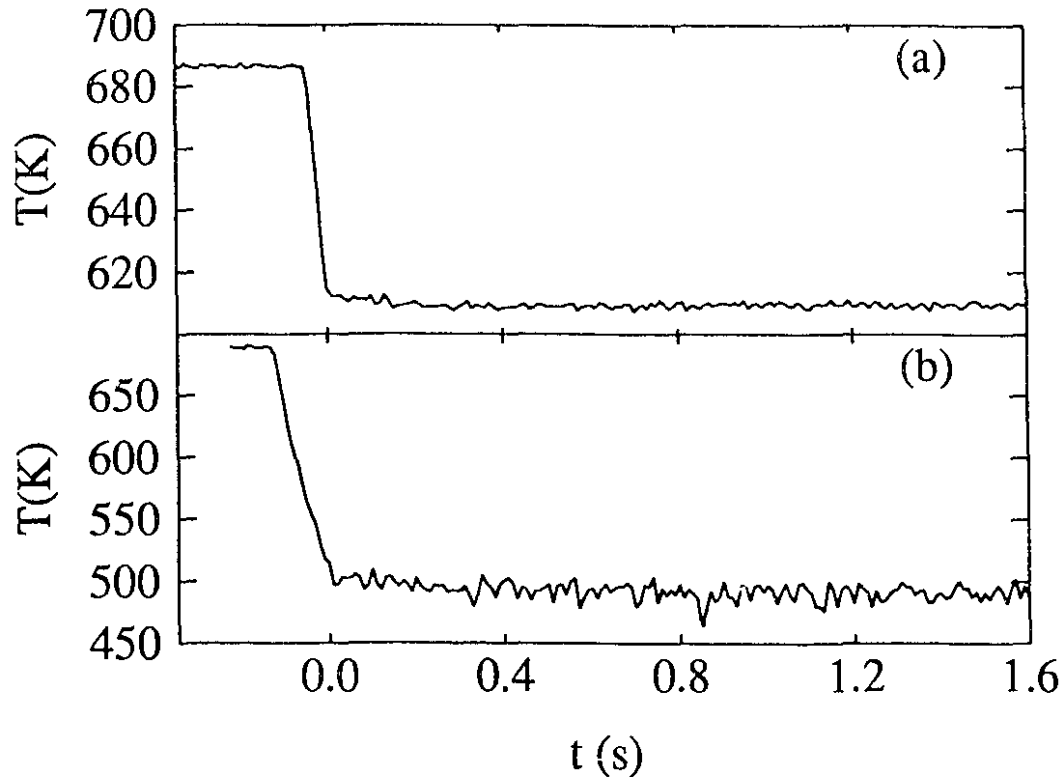


Figure 4.4: Temperature during a run for a shallow quench $T_q = 611.8$ K (a) and a deep quench $T_q = 502.2$ K (b) from the anneal temperature $T_a = 689.9$ K. The convention used is that $t = 0$ s at the first scan after the quench, when isothermal aging begins.

sample chamber through which the pyrometer monitors the sample temperature is covered by a quartz (SiO_2) window, which is transparent to infrared radiation. The calibration of the pyrometer reading will be the topic of § 4.4.

Finally, controlling the sample temperature is challenging. A conventional temperature controller has a long response time (for example, 100 ms for Eurotherm). With this long time constant, the quench times cannot be as short as required by the experiment. The choice of a pyrometer with a faster response time, namely 10 ms, to read and to control the sample temperature should contribute to satisfy better these two conditions.

At steady state, heat generated throughout the volume of the sample is radiated at the surface or conducted away along the length. Conduction by convection dominates the heat removal in the He gas. The temperature profile along the sample will vary. It will be cooler at the clamping positions but flat near the center.

However, since the point on which the pyrometer is focused is made coincident with the location illuminated by the x-ray beam, the temperature recorded should correspond fairly closely to that of the region where the scattering is measured. To get the right transformation temperature during the experiment, the focal spot of the pyrometer is manually made coincident to the point illuminated by the x-ray beam.⁴ The voltage across the ribbon was controlled. This led to a constant temperature as the sample resistance did not vary with time. Through this method, a constant temperature to within 0.5 K is obtained.

A ballast resistor is used in the electric circuit in series with the sample to minimize the power fluctuation caused by any change of sample resistance which might happen during the transformation. The resistance is chosen to satisfy the condition $\frac{\partial P(t)}{\partial R(t)} = 0$, where P is the power at the sample and R is the resistance of the sample. This means that the ballast resistor should be of the same resistance value as the sample. By working near this point, the changes in resistance which occur during phase separation have minimal effect on the power applied to the sample and minimize the effect on the sample temperature.

4.2.5 Detector and measurement of scattering patterns

The detector is the last topic of section 4.2 because of its importance both for fast diffraction acquisition and for obtaining *absolute* structure factors which will be the topic of Section 4.3.

An important aspect to increasing the time resolution is decreasing the time required to acquire each scattering pattern, *i.e.* the time to perform a scan. With conventional detectors, of which the most generally used is the scintillation detector, the maximum count rate is typically 10^5 counts per seconds and photons are counted at a given angle for a given time. To acquire a scattering pattern, it is necessary to physically move the detector to a new location, count again, and so on. The detector

⁴This is performed by first exposing x-ray sensitive paper to the beam and then aiming the pyrometer at the exposed spot.

used in this study is a position sensitive detector (PSD) made from a linear array of photodiodes. It can simultaneously record scattering at many angles. Using such a detector eliminates the need to move the detector and appreciably reduces the time to record a complete scattering pattern. In contrast to the photoemission in a scintillation detector, an x-ray photon produces electron-hole pairs in a photodiode and the signal is produced as they discharge the biased photodiode[114].

The PSD used in this study has been described in a paper.[107] It has been built by modifying a commercial system based on a 1024-element photodiode array designed for visible light detection. Each diode is 25 μm in width and 2.5 mm in height and the total array length is 25.6 mm.

The PSD is attached on the 2θ arm of the spectrometer allowing the central angle to be easily varied and was positioned with the direct beam near one end of the array.

The control system of the PSD is the optical multichannel analyzer (OMA) console from EG&G Princeton Applied Research. A model 1462 detector interface (OMA III) controls the information retrieved from the detector array. Operationally, four quantities have to be defined SS, I, J and ET.

The first, SS, is an integer that sets the electronic bunching of diodes into pixels. As more diodes are grouped together, higher time resolutions can be achieved at the expense of spatial resolution. For example, if 16 pixels are binned together, there will be 64 pixels to scan and the time to visit the entire array will be lower than if all 1024 diodes have to be scanned individually. It takes 16.4 ms to scan 1024 pixels and 2.5 ms when the pixels are grouped by 16 into 64 detectors. For our experiments the pixels were mostly bunched by 4 or 16.

Since every pixel is read once during the scanning time, the output signal of a pixel is a time integrated intensity of all photons counted since the last access. Other than for the very brief interval required to perform the read/reset operation, each detector element continuously integrates the photon flux falling on it throughout its exposure time, ET.

The detector interface cumulates the values in an internal memory for I times before a readout is provided for each pixel. The total number of readouts for each pixel (or number of scans of the array) during a run is set by a parameter J . Hence, each scan is performed over $(ET)(I)$ seconds and the total run time is $(ET)(I)(J)$ seconds and results in J diffraction patterns. The digitization of the signal by the detector interface is limited to 2^{14} counts. If the accumulated counts are in excess of this value, the readout will be "saturated". Since a noise is associated with each readout, the optimum ET is so that the largest count rate is close to but under 2^{14} counts per ET .

The general rules for the selection of SS , I , J and ET can be summed up as follows. To achieve higher time resolution where necessary the pixel bunching, SS , is increased at the expense of resolution and the exposure time, ET , is decreased. This contributes to the better time resolution in two ways: the total array scan visit time is reduced and the intensity per pixel for a given ET is increased by a factor SS , allowing the decrease in ET for a same signal level. Fortunately, in the case of the system studied, the faster kinetics happen at temperatures for which the scattering intensity is the highest and the signal to noise ratio never becomes a problem.

For a given set of conditions, all pixel exposure times are equal. However, because the pixels are serially scanned, the exposure time for any given pixel is skewed by one pixel time with respect to that of the preceding or following pixel. This skewness in pixel visit time would be of no consequence for a static structure factor measurement. In a dynamic measurement, this non-simultaneity of pixel visit has to remain negligible with respect to the exposure time. In the case of the work reported here, this skewness from one end of the array to the other is not negligible *vis-à-vis* the exposure time. The scattering patterns obtained for the early stage data (bunching by 4) have a difference of 7 ms between pixels near the beamstop and pixels farthest from the beamstop. However, since the time scale for the evolution of the system studied is much larger than 7 ms, this effect will not be important. The late stage data has longer exposure times (1 s) and the pixel visit time becomes

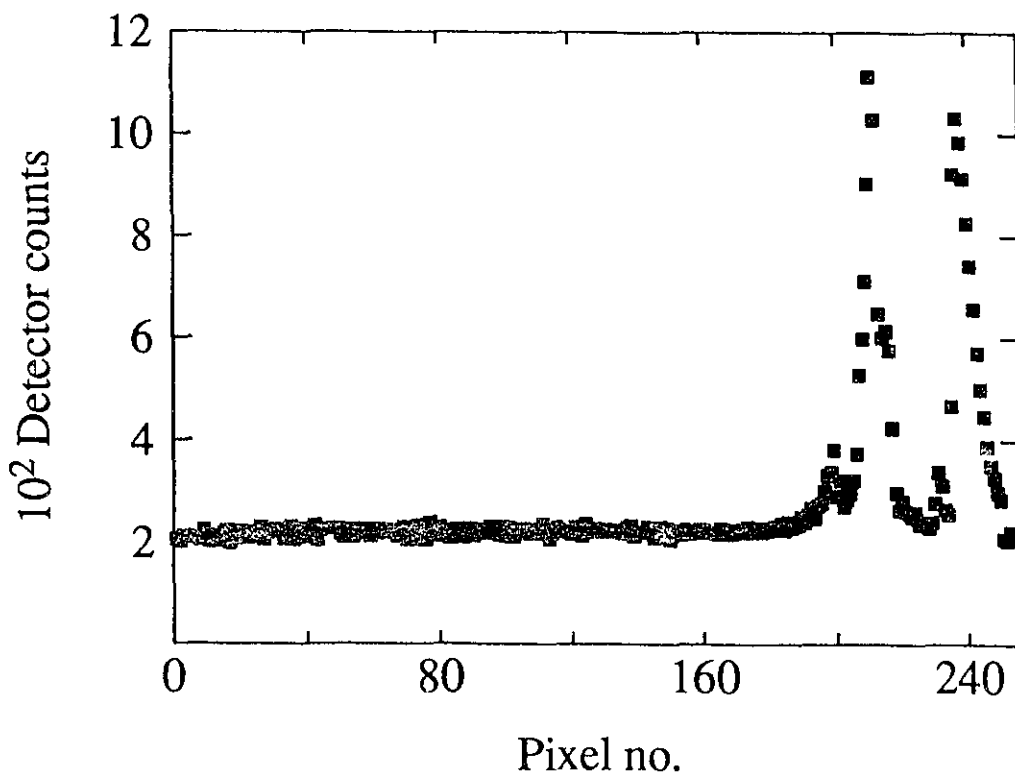


Figure 4.5: Dark current.

time becomes negligible.

Each pixel of the PSD has a temperature dependent dark current, a fluctuating leakage current in the detector elements due to thermally generated charge carriers in the semiconductor junction when voltage is applied. To keep this dark current constant, the temperature of the PSD has to be kept constant and to keep this current low, the PSD array is cooled to -40°C . (The dark current is halved with approximately each 7° cooled[114].) The dark current is integrated during the exposure. If the scattered intensity to be measured is low, the dark current would limit the maximum practical exposure time; if an integration continues long enough, the dark current will saturate the detector.

Patterns of the dark current were necessary to correct for the offset in the output from each PSD pixel at zero x-ray signal. Dark patterns were periodically taken during runs with the shutters closed with counting times taken to be the same as the (ET)(I) of the scans. A typical dark pattern can be seen from Fig. (4.5). The

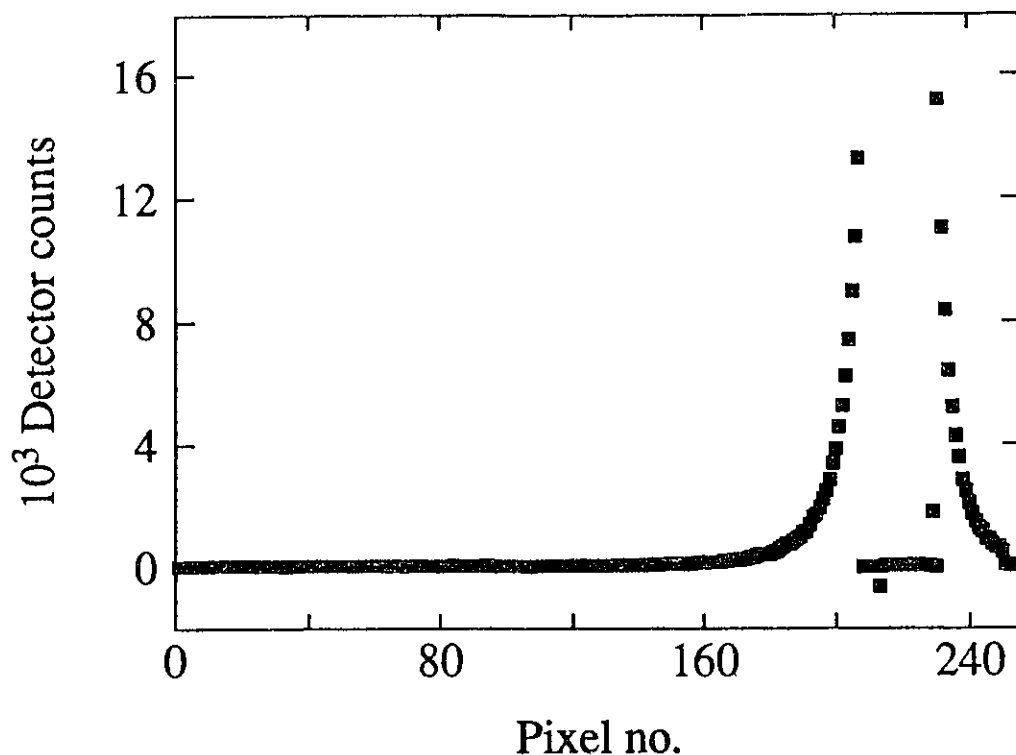


Figure 4.6: Typical parasitic pattern. The dark pattern has been subtracted.

“detector counts” units, or analog-to-digital units (ADU) on the ordinate axis are directly obtained from the controller. This figure also shows that some pixels on the PSD that have a “burnt in” pattern. It results from radiation damage to the photodiode by exposure to intense x-rays.

A parasitic scattering pattern, *i.e.* the scattering originating from slits or the helium in the beam path was taken without the sample in place and is shown in Fig. (4.6) after subtraction of the dark pattern. The shadow of the beamstop used to prevent the main beam from hitting the detector is shown.

In principle, the correction to a given diffraction pattern should consist mainly of a subtraction of a “parasitic” pattern which includes the “dark” pattern. However, the actual procedure followed depended on the analysis performed and will be introduced with the description of the results. In all cases, the dark pattern was removed from all scans simply by subtracting it from all recorded patterns of a run.

Figure (4.7) presents the scattering patterns obtained at representative times

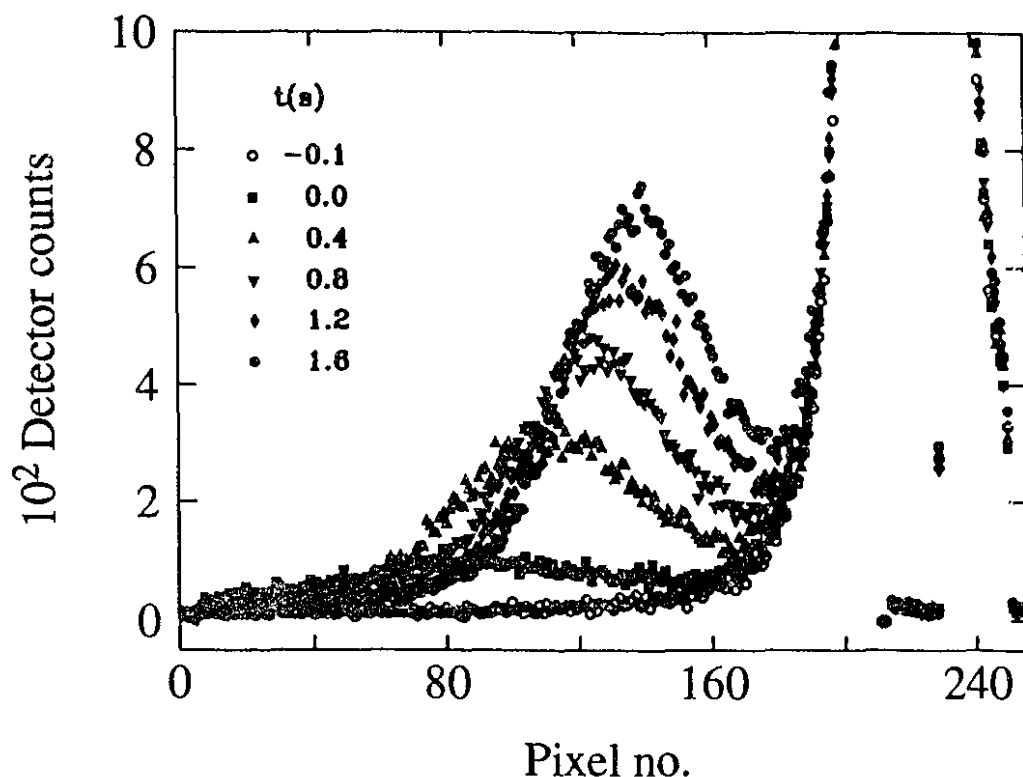


Figure 4.7: Scattering measured during a run at 541 K with the PSD diodes bunched by four. The negative time (\circ) corresponds to the last scan before the quench began. The time $t = 0.0$ (\blacksquare) corresponds to the first scan after the aging temperature was reached. In this run, since $ET = 0.01$ and $I = 1$, one scan was measured every 0.01 s and the scans shown in this figure are 40 scans apart. The dark pattern has been subtracted.

during a run at 541 K after subtraction of a dark pattern taken just before the run. The time of recording of the first scan after equilibration at the aging temperature is taken to be $t = 0$ s. The bottom pattern (\blacksquare) corresponds to the last scan before the quench was initiated. Thus, the difference in scattering between the first two profiles corresponds to the increase during the quench.

The output of the control system, containing the scattering patterns is fed into the control computer but can also be monitored by oscilloscope. This way, the evolution of SAXS intensities can be observed in real time, thus allowing immediate adjustment of experimental conditions.

4.3 Conversion of scattering patterns to absolute structure factors

The preceding section described how to obtain scattering patterns such as displayed in Fig. (4.7). To convert the measured scattering into absolute structure factors $S(q)$ the differential cross-section per unit volume of the sample $d\sigma_V(q)/d\Omega$ must first be evaluated and Equation (2.13) is used to complete the calculation. This quantity is the measured intensity in the pixel p centered at a wavevector $q = 2\pi\theta/\lambda$ normalized to the incident beam intensity I_0 for unit sample thickness, t , and unit solid angle, Ω ,

$$\frac{d\sigma_V(q)}{d\Omega} = \frac{I(p)}{I_0} \times \frac{1}{\Omega} \times \frac{1}{t}. \quad (4.1)$$

But first, a calibration of the detector is necessary in order to convert detector counts (ADU) into counts per seconds (cps). A conversion factor can be obtained, based on counting statistics. Since the dominant noise on each pixel is given by Poisson statistics, the variance σ^2 should be simply equal to the number of events N . The calibration of counts per ADU for each individual pixel was determined by recording the number of counts in each pixel resulting from exposing the detector to a uniform distribution of radiation for an exposure time of 1 s, 25 times. In each pixel, the variance over the 25 exposures of the measured number of counts should then be equal to the average of all the counts (after subtraction of the dark current in each pixel).

The efficiency (ADU to counts) was measured by scattering from Kapton in air at 6 keV with $2\theta \sim 60^\circ$ with the detector located 140 mm away from the Kapton foil. Fig. (4.9) displays the measured signal across the detector array averaged over 25 scans of one second each. There is little variability and that which is present can be ascribed to systematic errors as checked by comparison to the reading from a scintillation counter. The calculation of the noise of the PSD gives less than one

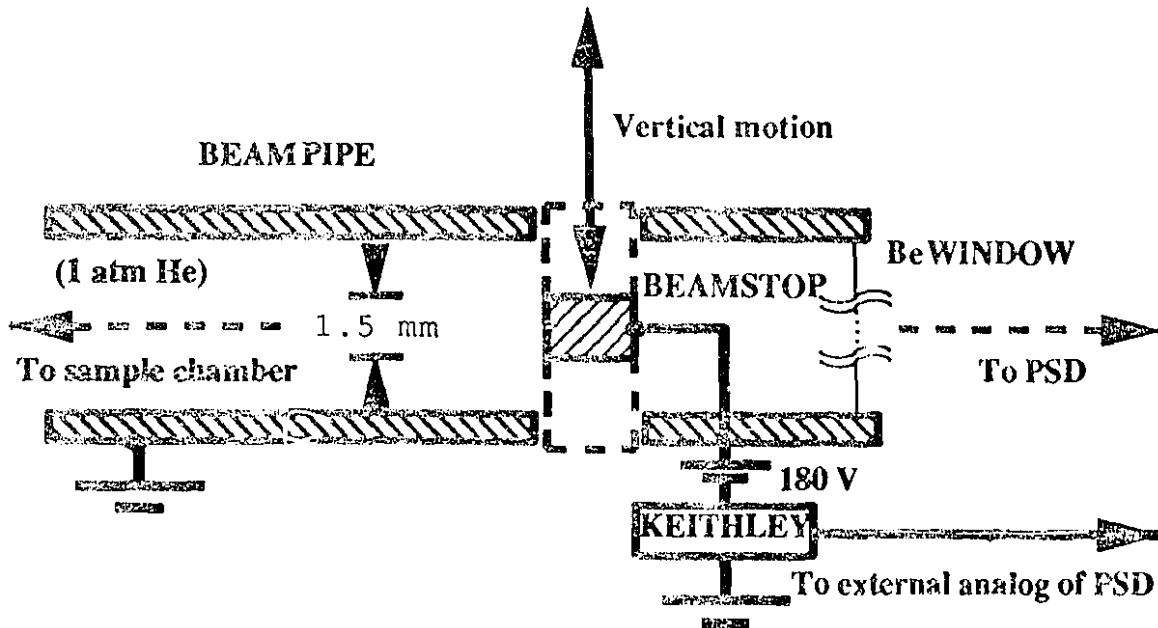


Figure 4.8: Schematic of beamstop operation.

ying that this adopted calibration works. The efficiency, is then⁵

$$\mathcal{E}_{PSD} = \frac{\sigma^2}{N}. \quad (4.2)$$

The conversion factor \mathcal{E}_{PSD} was set to the average value of 0.685 for all diodes.

The incident beam intensity is monitored by the beamstop which has been instrumented to measure the x-rays incident upon it. Fig. (4.8) presents a diagram of the operation of the beamstop. The beamstop is about 1.5 mm wide (cf. Fig. 4.6) in the scattering direction (\hat{z}), and spans the full width of the detector in the perpendicular direction. The front of the beamstop is about 3 cm upstream from the detector surface. The beamstop casts a shadow about the size of its width on the PSD. The beamstop is made of copper and is mounted on a linear motion feedthrough so that it is electrically insulated from the feedthrough and from the

⁵It should be remarked upon that though this number is less than unity here, it could be greater than one if the gain to the ADU converter is increased. This emphasizes that this number is really a calibration of counts/ADU.

grounded beam pipe. The motion is along the detector to allow placement of the beamstop in the incident beam. Two 90 V batteries in series located between the beamstop and the input to the current amplifier (Keithley) provide a voltage bias. A floating voltage source is required since one side of the beamstop ion chamber, the beam pipe, is grounded and the other, the current amplifier (Keithley) is also grounded. With the configuration used, the beamstop is biased positive with respect to the beam pipe. The positive output voltage from the Keithley is fed to the External Analog input of the PSD. The PSD digitizes the signal from the Keithley with each scattering pattern. This allows for easy recovery of the beamstop intensity for analysis of the scattering profiles. Essentially the x-rays hit the beamstop, generating a current which is measured.

The main part of the signal comes from ionization of the helium gas by electrons ejected from the surface of the copper. The beamstop is run similar to an ion chamber, with the bias set "on the plateau" *i.e.* in the range where all the ions are collected. However, the acceleration is not great enough to produce secondary ionization, so that the current measured by the Keithley current amplifier is independent of the biasing voltage. The signal is also relatively independent of the polarity of the bias. It would be difficult to calculate from first principles the efficiency of conversion of x-rays to ejected electrons. Such a calculation would have to account for many factors such as an effective escape depth, smaller than the absorption length of the x-rays, from which electrons can escape. However, if the signal is assumed proportional to the incident intensity I_0 , it turns out that the photocurrent efficiency of the beamstop is similar to that of a 12 cm helium gas ion chamber. The helium is much less efficient at absorbing x-rays than copper, and seems to compensate for the inefficiency of the copper at ejecting electrons.

Because of the analogy between the beamstop and an ion chamber, it is instructive to start by looking at I_{meas} , the expected current measured from an ion chamber bombarded by I_0 photons per second. The current depends on the photon energy E , the photoionization potential V_0 , the linear absorption coefficient μ

(in cm^{-1}) as well as on the length of the chamber, ℓ . The measured current (in Amperes) in an ion chamber is then

$$I_{meas} = I_0 \times \frac{E}{V_0} \times \ell \times \mu \times 1.6 \times 10^{-19}. \quad (4.3)$$

In the range $E \sim 5 - 8$ keV, the following empirical relationship between the linear absorption coefficient and energy holds for the total cross-section data[115] :

$$\frac{\mu_1}{\mu_2} = \left(\frac{E_1}{E_2} \right)^{\log(\mu_1/\mu_2)/\log(E_1/E_2)} \quad (4.4)$$

with

$$\log(\mu_1/\mu_2)/\log(E_1/E_2) = -3.538. \quad (4.5)$$

The efficiency calibration of an ion chamber at detecting photons of energy E_1 can be defined as

$$\mathcal{E}_I(E_1) \equiv I_{meas}/I_0, \quad (4.6)$$

and in Eq. (4.3) the efficiency groups the terms $\frac{E}{V_0} \times \ell \times \mu \times 1.6 \times 10^{-19} \text{C}$. Combining (4.5) and (4.3) with reference to an energy, say E_1 , of known efficiency $\mathcal{E}(E_1)$, in He,

$$I_{meas}(E) = \mathcal{E}_I(E_1) \times \left(\frac{E}{E_1} \right)^{-2.538}. \quad (4.7)$$

The ratio $I_0/I_{meas} = 2.6 \times 10^{19}$ cps/A was obtained from an efficiency calibration at 6.91 keV for the beamstop using a bolometer. Thus,

$$\mathcal{E}_B(6.91 \text{keV}) = 3.8 \times 10^{-20} \text{A/cps}. \quad (4.8)$$

The calculation of the beamstop efficiency, denoted as \mathcal{E}_B is only an estimate. Since, to first order, the energy dependence of absorption is about the same for any material and the photoelectrons are produced from absorption on the top few thousand Angstroms of the copper in the beamstop, the correction for the energy difference between 6.91 and 5.99 keV is performed using (4.7). This agrees with a comparison to an incident beam on an ion chamber. The correction for energy thus gives

$$(6.910/5.989)^{2.538} = 1.438, \quad (4.9)$$

or 1.81×10^{19} cps/A at 5.989 keV ($\mathcal{E}_B(5.989\text{keV}) = 5.53 \times 10^{-20}$ A/cps).

There is also absorption in the windows between the photodiode array and the beamstop. If photons arriving at the photodiode array are used as the reference, and considering absorption in 250 μm Be, 75 μm Kapton, and 10 mm air (24%), one obtains 1.38×10^{19} cps/A at 5.989 keV ($\mathcal{E}_B(5.989\text{keV}) = 7.27 \times 10^{-20}$ A/cps).

The thickness of the sample is calculated using the ratio of the current at the beamstop with and without the sample in the beam and the (total) linear absorption coefficient, μ (its inverse, $\frac{1}{\mu}$ is the absorption length). If an intensity I_0 of photons is incident to the surface of a material of density ρ , then the intensity at a depth x inside the material will be obtained from

$$\begin{aligned} I &= I_0 e^{-\mu x} \\ &= I_0 e^{-\left(\frac{\mu}{\rho}\right)\rho x}. \end{aligned} \quad (4.10)$$

The quantity $\left(\frac{\mu}{\rho}\right)$ is known as the mass absorption coefficient (in m^2/kg) and can be found in tables. For Al and Zn [115], $\left(\frac{\mu}{\rho}\right)_{\text{Al}} = 11.77 \text{ m}^2/\text{kg}$ and $\left(\frac{\mu}{\rho}\right)_{\text{Zn}} = 13.03 \text{ m}^2/\text{kg}$. For $\text{Al}_{0.62}\text{Zn}_{0.38}$ a weighted average is performed,

$$\left(\frac{\mu}{\rho}\right)_{\text{Al}_{0.62}\text{Zn}_{0.38}} = w_{\text{Al}} \left(\frac{\mu}{\rho}\right)_{\text{Al}} + w_{\text{Zn}} \left(\frac{\mu}{\rho}\right)_{\text{Zn}} \quad (4.11)$$

where w_{Al} and w_{Zn} are the weight fractions of Al and Zn (0.40 and 0.60 respectively) giving $\left(\frac{\mu}{\rho}\right)_{\text{Al}_{0.62}\text{Zn}_{0.38}} = 12.53 \text{ m}^2/\text{kg}$. With $\rho = 4.130 \times 10^3 \text{ kg/m}^3$, the value $\mu = 5.175 \times 10^4 \text{ m}^{-1}$ is obtained, *i.e.* $\mu^{-1} = 19.3 \mu\text{m}$.

Substituting into Eq. (4.10) with the measured values for I and I_0 of 0.31×10^{-7} and 0.78×10^{-7} A respectively gives $x = -\frac{1}{\mu} \ln \frac{I}{I_0} = 0.922 \mu^{-1}$ or $x = 17.7 \times 10^{-6} \text{ m}$, *i.e.* the sample is evaluated to be 17.7 μm or 0.922 absorption lengths thick. This agrees with estimates from a micrometer.

The detector was centered so that the unscattered beam is near one of the detector's extremities (the beamstop blocks the direct beam). The diodes were physically grouped either by 4 or 16 to form an array of 256 or 64 pixels respectively. The sample to detector distance, R , was set at 733.5 mm such that

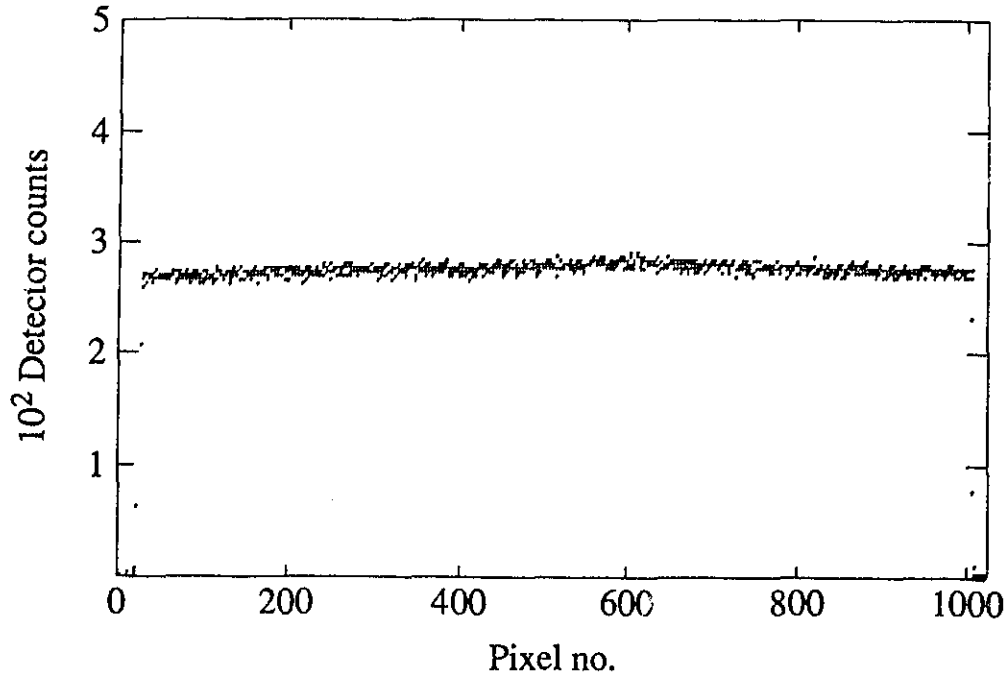


Figure 4.9: Scattering averaged over 25 scans after subtraction of the dark current from kapton in air with $2\theta \sim 60^\circ$, 140 mm from detector surface.

the 26.5 mm long photodiode array covered reciprocal vectors in the range 0.01 to 0.085 \AA^{-1} at an x-ray wavelength λ of 2.07 \AA . A single diode spanned a range of $\Delta q = 1.03 \times 10^{-4} \text{ \AA}^{-1}$. The difference between the solid angle $\Delta\Omega$ subtended by a pixel near the direct beam and a more distant pixel is of order 0.09 %. An average value of 9.283×10^{-8} steradians is used for the surface of a diode in the conversion to absolute structure factors. Depending on the bunching, this surface is multiplied by 4, 16, etc.

The incident beam intensity is obtained from the recorded monitor counts in the last pixel of the PSD. Taking account of the ADU conversion (in volts) by the current amplifier and the efficiency of the beamstop (\mathcal{E}_B), I_0 is given by :

$$I_0 = \frac{[\text{monitor counts}]}{1638.4 \times \mathcal{E}_B \times I} \quad (4.12)$$

where I , in the denominator, is the multiple of ET setting the the scan time ($I \times ET$).

The numerical value of the variation of electron density with composi-

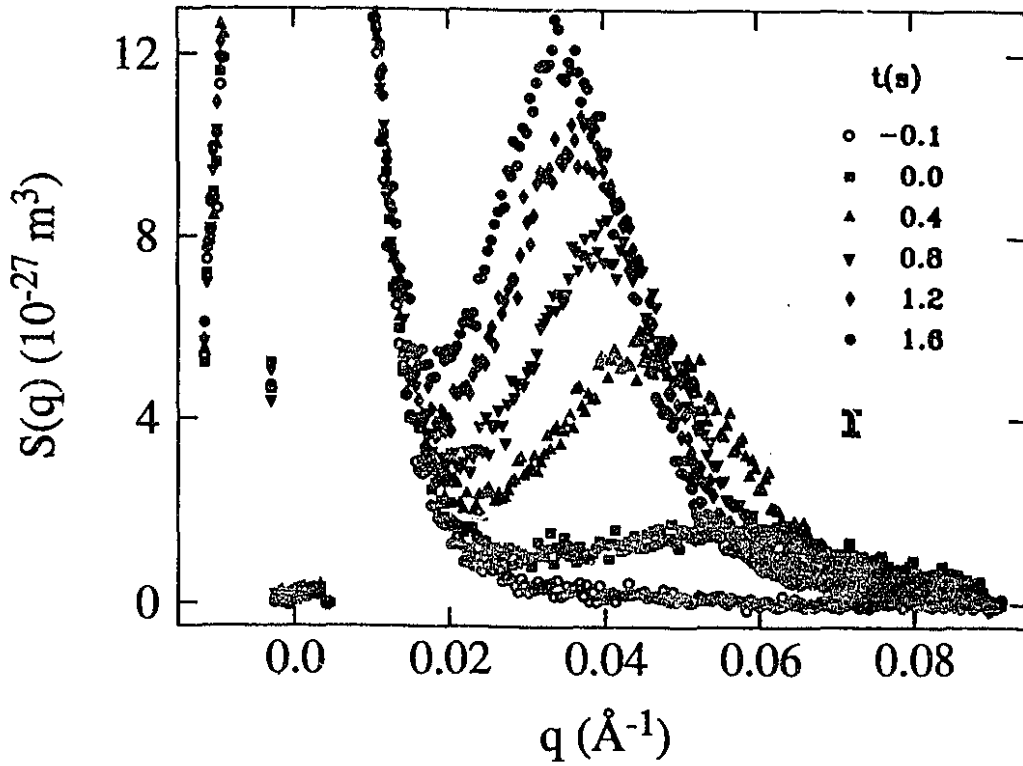


Figure 4.10: Absolute structure factors after conversion from measured scattering for a run at 541 K (cf. Fig. 4.7). The negative time (\circ) corresponds to the last scan before the quench began. The time $t = 0.0$ (\blacksquare) corresponds to the first scan after the aging temperature was reached. A representative error bar corresponding to $S(q, t) = 4.0 \times 10^{-27} \text{ m}^3$ is displayed on the right.

tion, $d\rho_e/dc$, in Eq. (2.13) is estimated for a fcc lattice with lattice constant $a_0 = 4.054 \times 10^{-10} \text{ m}$ (cf. Table 1.2), *i.e.*

$$\begin{aligned} \frac{d\rho_e}{dc} &= (Z_{Zn} - Z_{Al}) \frac{4}{a_0^3} \\ &= 1.017 \times 10^{30} \text{ m}^{-3}. \end{aligned} \quad (4.13)$$

Finally, with $\sigma_T = 7.94 \times 10^{-30} \text{ m}^2/\text{el.}^2$ (cf. p. 33) Eq. (2.13) gives

$$S(q) = 7.408 \times 10^{-8} (\text{at. fract.})^2 \text{ m}^3 \times \frac{I}{I_0} \quad (4.14)$$

for the conversion between measured scattering intensities I and structure factors $S(q)$ in the case of unbunched pixels. The units agree with those derived in § 2.1 and the numerical factor is multiplied by the bunching number (4 or 16) as needed.

Figure (4.10) shows the result of the conversion applied to the scattering patterns that were given on Fig. (4.7). An error bar given by Poisson statistics is given

at the right of the structure factors and is representative for $S(q, t) = 4.0 \times 10^{-27} \text{ m}^3$. The high intensity below $q = 0.02 \text{ \AA}^{-1}$ is mostly due to grain-boundary scattering.

To obtain Eq. (4.14), it was implicitly assumed that the scattering from correlated domains is sufficiently isotropic so that $\rho(\mathbf{r}) = \rho(r)$. In particular, it is assumed that any texture present in the sample will not affect appreciably the density correlations over the length scales measured.

The absolute calibration is susceptible to many systematic errors. A discussion of the uncertainty introduced by each step of the calculation was not performed. It is through comparisons of the results obtained with expected quantities derived from other measurements that the level of confidence in the calibration will be evaluated in Chapter VI.

4.4 Temperature calibration

The temperature was measured by a commercial infrared pyrometer. For the measurement, a nominal body emissivity was set on the pyrometer. This section describes the conversion of the pyrometer temperatures to real temperatures.

The expression used by the pyrometer to determine the temperature can be derived starting from Planck's law for the radiated power at a wavelength λ from a body at temperature T , [116]

$$R_B(\lambda) = \epsilon \left(\frac{c}{4} \right) \left(\frac{8\pi}{\lambda^4} \right) \left[\frac{hc}{\lambda} \frac{1}{\exp\left(\frac{hc}{\lambda k_B T}\right) - 1} \right] \quad (4.15)$$

where c is the speed of light, h is Planck's constant and ϵ an emissivity prefactor. Expression (4.15) reduces to Wien's law at the wavelength used ($2.3 \times 10^{-6} \text{ m}$) since $hc/\lambda k_B = 6259 \text{ K}$ and $\exp(6259/T) \gg 1$:

$$R = \frac{\epsilon A}{\exp\left(\frac{6259}{T}\right)}. \quad (4.16)$$

All constants have been combined in the numerator.

If T_{pyro} is the temperature read by the pyrometer and $\mathcal{A}_{\text{pyro}}$ includes the emissivity setting on the pyrometer, the emissivity correction to the pyrometer reading will satisfy

$$\frac{\mathcal{A}}{\exp\left(\frac{6259}{T}\right)} = \frac{\mathcal{A}_{\text{pyro}}}{\exp\left(\frac{6259}{T_{\text{pyro}}}\right)} \quad (4.17)$$

where T is the true temperature and \mathcal{A} includes the real emissivity. This relation simplifies to

$$\frac{1}{T} = \frac{1}{T_{\text{pyro}}} + C. \quad (4.18)$$

Thus, only one constant, C , needs to be determined to obtain corrected temperatures (T) from nominal ones (T_{pyro}). The constant C can be calculated given one known temperature. This is performed below using T_c .

Five runs performed at aging temperatures above T_c are used to determine T_c . For these runs, the equilibrium structure factors should have the Ornstein-Zernicke form (Eq. 2.19). It is assumed that over a range of high q wavevectors the asymptotic regime was reached within the time of the run (2 s). The difference in structure factor between the last and the first five scans of each run was taken. The latter group being before the onset of the quench, this removes the grain-boundary scattering but the equilibrium scattering at T_a is also removed. For the fit, $S_{O.Z.}(q)|_{T_a}$ was included.

Fig. (4.11) shows the measured ‘‘equilibrium’’ structure factors (symbols) with data over the full range of wavenumbers resulting from the manipulation described above. It also shows the Ornstein-Zernike forms (curves) drawn from results of the fitting procedure. The bottom curve shows the structure factor calculated for the anneal temperature, $S_{O.Z.}(q)|_{T_a}$. It is small comparative to any other structure factor displayed in the Figure.

In the temperature range of these runs, the parameters κ and f'' can be taken, to first order, to be linear functions of temperature, *i.e.*

$$\kappa(T) = \kappa_a + \kappa_m(T - T_c) \quad (4.19)$$

$$f''(T) = F(T - T_c), \quad (4.20)$$

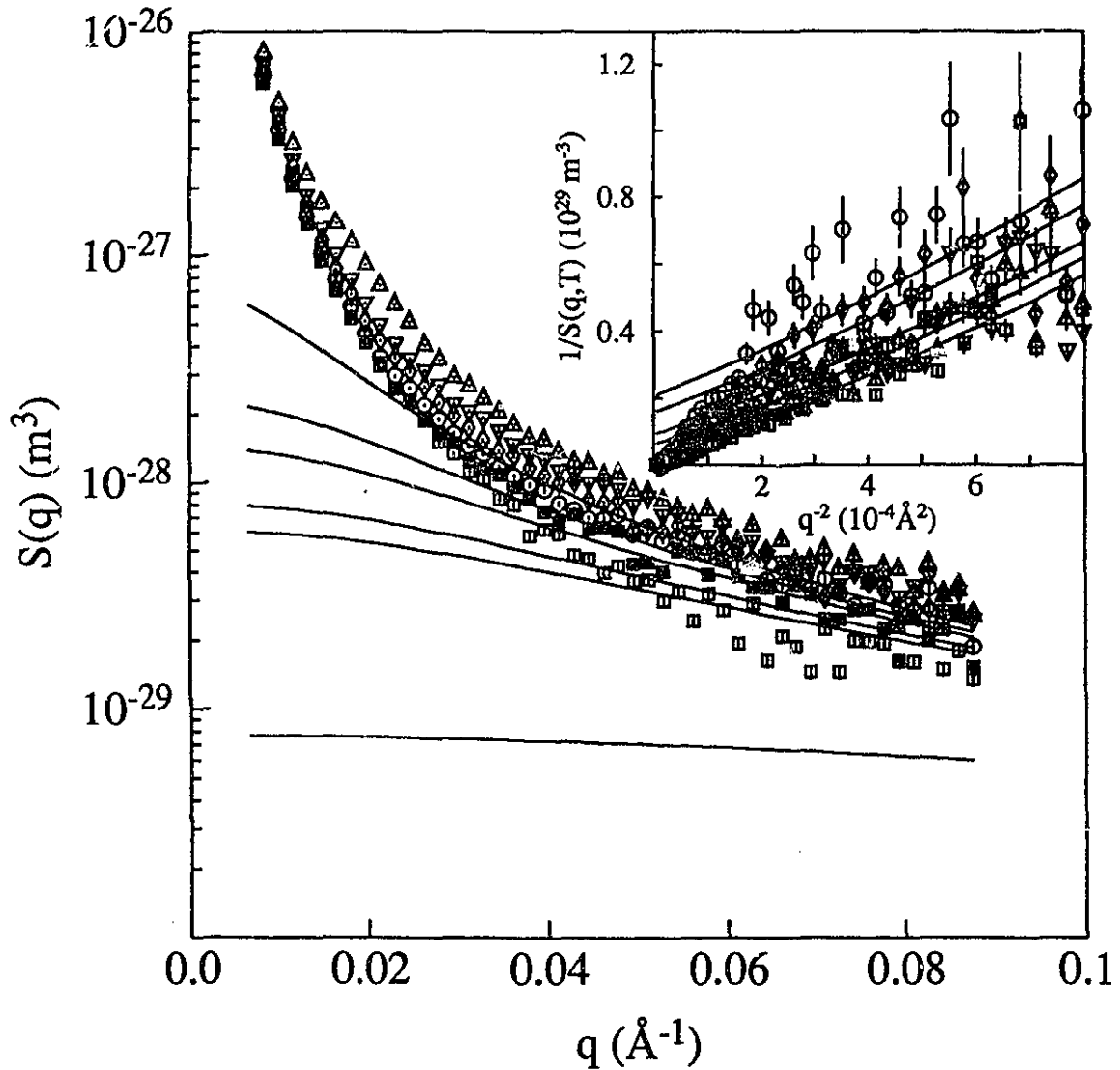


Figure 4.11: Best fit Ornstein-Zernike structure factors $S_{OZ}(q)$ for 598.0 (\square), 599.8 (Δ), 601.4 (∇), 604.8 (\diamond) and 607.2 K (\circ) (from top to bottom). The fit was performed on a restricted range from 0.046 to 0.089 \AA^{-1} . The bottom curve shows $S_{OZ}(q)$ at $T_* = 688.4$ K (obtained from the calculated values of T_* , $f''(T_*)$ and $\kappa(T_*)$). This curve is added onto all other curves. The insert shows the a linearized form of the equilibrium structure factors ($1/S(q)|_T$ versus q^2) with solid lines representing the calculated equilibrium structure factors.

In Eq. (4.20), f'' vanishes at T_c .

When using expressions (4.19) and (4.20), a three parameter fit was found to be sufficient and κ_m was fixed to zero. The fit to

$$S(q, T_i) - S(q, T_a) = \frac{k_B T_i}{2\kappa_a q^2 + F(T_i - T_c)} - \frac{k_B T_a}{2\kappa_a q^2 + F(T_a - T_c)} \quad (4.21)$$

was done *simultaneously* for five runs at temperatures above that nominally taken to be T_c . In this expression, T_a was nominally taken as the annealing temperature measured by the pyrometer. In this step, the value obtained for T_c is the critical temperature measured by the pyrometer.

With the help of Eq. (4.18), the value found above for $T_{c\text{pyro}}$ and the literature value $T_c = 597.15$ K were sufficient to determine the correction constant C to be $-4.3976 \times 10^{-5} \text{ K}^{-1}$. As a check, all five temperatures in the fit are changed to their real values through Eq. (4.18) and the fit is performed a second time resulting in the same best fit values $F = (14.978 \pm 1.091) \times 10^6 \text{ J/m}^3\text{K}$, $\kappa_a = (2.3143 \pm 0.090) \times 10^{-10} \text{ J/m}$ and $T_c = 597.15 \pm 0.47 \text{ K}$.

The calibrated annealing temperature is calculated to be $T_a = 689.9 \text{ K}$, and $f''(T_a) = 1.269 \times 10^9 \text{ J/m}^3$. These values, along with $\kappa(T_a) = \kappa_a$ are sufficient to characterize $S_{O.Z.}(q)|_{T_a}$.

In Chapter VI, it will be shown that the results of the fits to the dynamic evolution of the structure factor agree independently with this choice of T_c to within 0.5 K.

4.5 Instrumental resolution

An account of collimation distortions is one of the most complicated tasks in small-angle experimental data evaluation.[117] Ideally, the quantity that has to be measured is the structure factor $S(\mathbf{q})$. Instead, what is measured is the scattering which results from the convolution (or "smearing") of the intrinsic $S(\mathbf{q})$ by the response function of the instrument. Further, the scattering is measured only at several

discrete points. The two principal sources of smearing of $S(\mathbf{q})$ will be taken into account: the detector area, which effectively acts like a slit with a width and a height, and the finite size of the beam.

The first question that should be asked when considering the quantification of the instrumental resolution is: how to account for it?

There are two possible ways to include instrumental resolution. If a specific model has to be compared to the experimentally determined scattering function, then the structure factor generated by the model should be convoluted by the instrumental response function and the result compared to the experimental data. If, on the other hand, no model exists, then the experimental scattering function should be deconvoluted with the instrumental response function to provide a structure factor. The first procedure is better because it is preferable to convolve the structure factor predicted by a model to take account of the instrumental resolution than to modify the data by a deconvolution procedure. Indeed, only in the first case is the form obtained unique.

In the context of this work, it was found that for the early stage study runs, where an equation of motion for the structure factor is checked against the data, the convolution of the model structure factors produces a small effect. Indeed, at this stage, most of the critical features are located away from the beamstop where the "smearing" is most important. For the late stages runs, in which the maximum of the peak moves towards and into the beamstop, there is no satisfactory analytic theory for the profile and evolution of the structure factor and the experimental data was deconvoluted. The quantitative analysis of the structure factor measured at late times therefore takes into account the instrumental resolution. Should a theory become available to predict $S(\mathbf{q}, t)$ at late times, then this structure factor could be convoluted and compared to the data.

4.5.1 Convolution

The convolution, or "smearing" of the structure factor $S(\mathbf{q})$ depends on the beam profile, the width and the height of the pixel and the q -range detected will depend on the sample-to-detector distance, L . Figure (4.12) shows the scattering geometry. The origin of \mathbf{u} is chosen for convenience at the center of the intensity distribution of the beam. The incident beam profile is quantified by an intensity density function, $j(\mathbf{u})$, with \mathbf{u} a vector in the plane normal to the incident beam at the sample. Similarly, a function $W_p(\mathbf{v})$ defines the shape of the pixel p , with \mathbf{v} a vector in the detector plane. It is unity when \mathbf{v} is inside the pixel area and zero elsewhere.

The measured scattering efficiency per unit thickness $E^S(p)$ into pixel p resulting from scattering at a wavenumber q is the integration over the beam profile that fall on the surface of pixel p after scattering with a wavevector q . For an isotropic sample, *i.e.* $S(\mathbf{q}) = S(q)$, this is

$$E^S(p) = \int \int \frac{1}{L^2} S(q) j(\mathbf{u}) W(\mathbf{v}) d^2 \mathbf{u} d^2 \mathbf{v}. \quad (4.22)$$

These integrals can be considered as the definition of a linear operator R_p

$$R_p[S(q)] \equiv E^S(p). \quad (4.23)$$

The structure factor $S(q)$ can only be measured at a finite number of q values. Suppose a discrete set of $S(q_i)$ sufficient to numerically approximate $S(q)$ for all q -wavevectors by an interpolation scheme. Then $S(q)$ is given by the sum

$$S(q) = \sum_i S(q_i) \phi_i(q). \quad (4.24)$$

where $\phi_i(q)$ determines the interpolation scheme, for a linear interpolation it would be a hat function centered about q_i . The measured scattering in a pixel p becomes

$$\begin{aligned} E^S(p) &= R_p \left[\sum_i S(q_i) \phi_i(q) \right] \\ &= \sum_i S(q_i) R_p [\phi_i(q)]. \end{aligned} \quad (4.25)$$

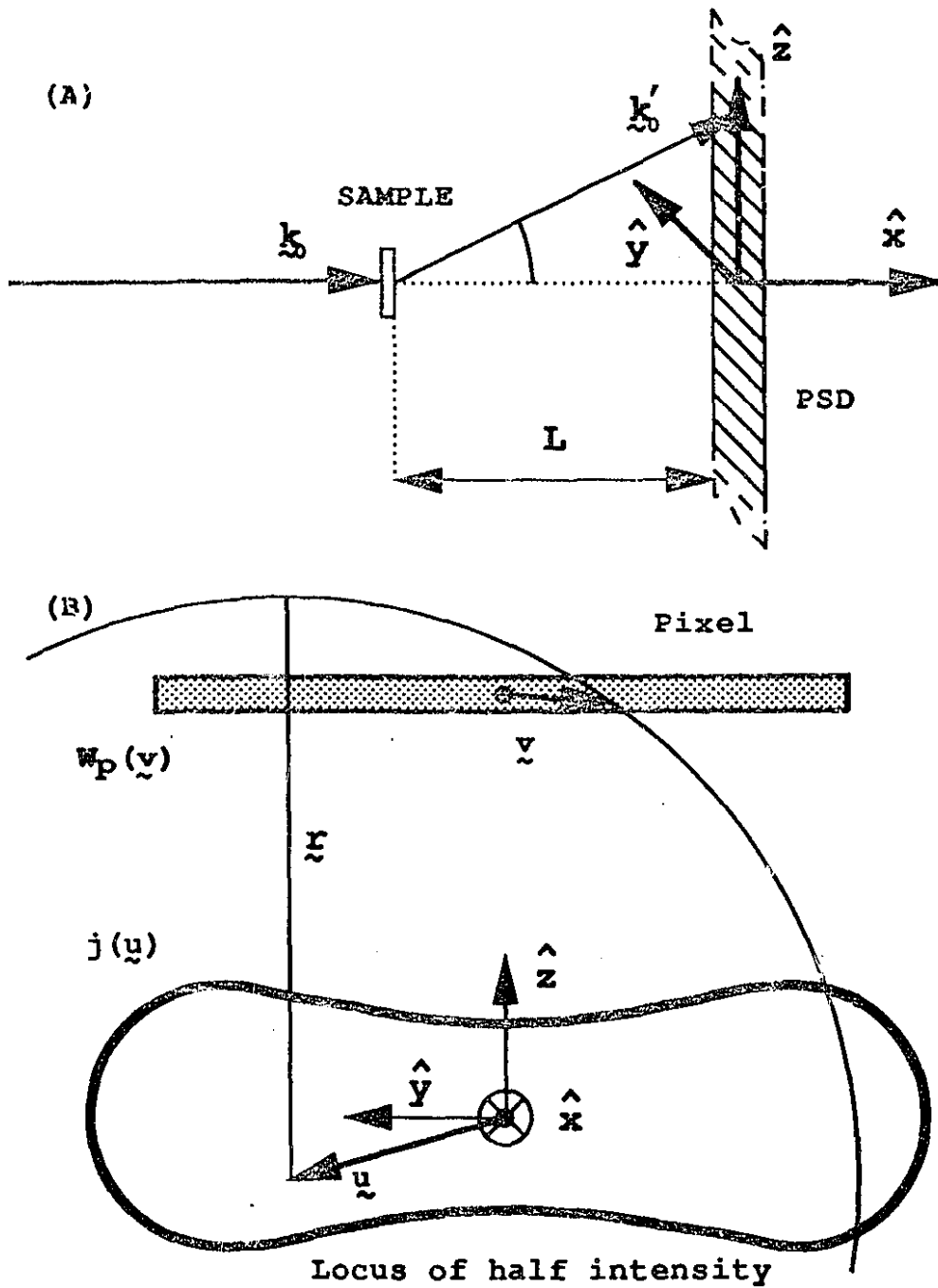


Figure 4.12: Scattering geometry. (a) Side view. The beam is along the horizontal \hat{x} -axis. The scattering is measured along the vertical \hat{z} axis. (b) Projection in the detector plane of the beam incident on the sample.

Expression (4.25) presents the important advantage that once $\phi_i(q)$ is selected $R_p\phi_i(q)$ can be computed for all q_i and the transpose of the resulting matrix,

$$M_{pi}^T \equiv R_p[\phi_i(q)] \quad (4.26)$$

is independent of sample scattering. The matrix M relates "pixel"-space (rows) to q -space (columns). Column q gives the spread of $\phi_i(q)$ into each pixel resulting from all illuminated points in the sample. Conversely row p stores the fractions of pixel p covered by the "scattering" function $\phi_i(q)$ from all illuminated points in the sample, for all i . As constructed, each row is normalized to unity.

Since the detector geometry is fixed for all the scans in a run and for all the runs reported in this work, Eq. (4.25) can now conveniently be rewritten as the matrix product⁶

$$E^S(p_j) = M_{ji} S(q_i). \quad (4.27)$$

The approach presented above allows the inclusion of other factors in the instrumental resolution. For instance, a wavelength distribution could be considered. Though the evaluation of M would be more complex, it needs to be performed only once for a given geometry of the experiment and wavelength distribution. For the measurements reported in this thesis, the wavelength spectrum is not important.

In this work $R_p[\phi_i(q)]$ is calculated using the defined integration weighting functions $j(\mathbf{u})$ and $W_p(\mathbf{v})$. Four independent variables are sufficient to compute Eq. (4.26). The numerical procedure of convolution depends on the choice of these variables. In polar coordinates,

$$q = \frac{2\pi}{\lambda L} r \quad (4.28)$$

which is conveniently independent of θ for isotropic scattering⁷, the integration weight over a pixel can be expressed as

$$W_p(\mathbf{v}) = W_p(\mathbf{u}, q, \theta). \quad (4.29)$$

⁶An added convenience is that M is a block-diagonal matrix and thus requires relatively little computer storage.

⁷For a discussion of the solution in cartesian coordinates with u_y, u_x, y and z as independent variables, see ref. [48].

$W_p(\mathbf{v})$ is unity inside pixel p and zero outside. The computation of (4.26) becomes

$$M_{pi}^r = \frac{1}{L^2} \int_{-\infty}^{\infty} \phi_i(q) \int_{\theta=0}^{2\pi} W_p(\mathbf{u}, q, \theta) d\theta j(\mathbf{u}) d^2\mathbf{u}. \quad (4.30)$$

In the \hat{z} -direction, the beam profile was measured with the PSD. In the \hat{y} -direction, the dumbbell-like shape was captured on polaroid film and modelled as the sum of two gaussians of equal FWHM separated by a distance measured by ruler.

Figure (4.13) shows a contour plot of the beam profile where it has been assumed that $j(\mathbf{r})$ can be expressed as:

$$j(\mathbf{r}) = j_1(z) j_2(y) \quad (4.31)$$

and where the intensity distribution is normalized such that

$$\int j(\mathbf{u}) d\mathbf{u} = 1. \quad (4.32)$$

Fig. (4.14) shows how six regularly spaced delta-function scattering rings would be measured or smeared by the detector array. For comparison, a span of five pixels (bunched by four, *i.e.* 20 diodes) is shown.

At the smaller q values (*i.e.* closer to the beamstop) the asymmetry (lopsided towards low q) of the measured scattering is more important and reflects the high degree of curvature of the annuli shown in Fig. (4.12) whereas as q increases, the annuli segments appear closer to parallel lines through the pixel and the smearing results principally from the finite size of the beam (Fig. 4.13).

4.5.2 Deconvolution

The deconvolution is the inverse of the convolution. It is numerically unstable. One solution is by iteration, a numerical technique to invert the matrix.

The aim is to find a set of $\hat{S}(q_i)$ such that

$$E^S(p) = M_{pi} \hat{S}(q_i). \quad (4.33)$$

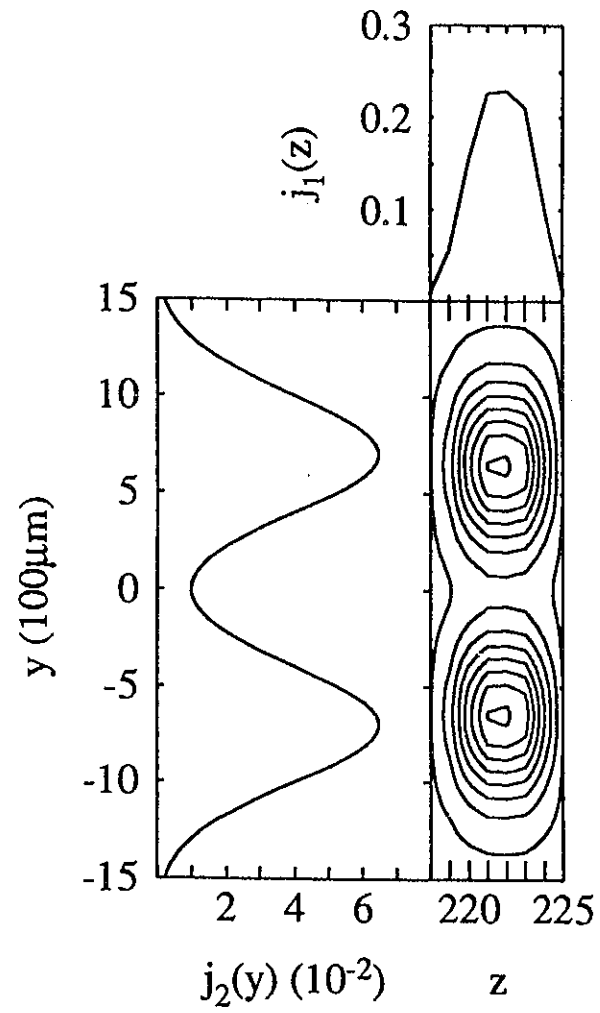


Figure 4.13: Beam profile. The z axis is in bunched pixels coordinates, with one unit equal to $100 \mu\text{m}$.

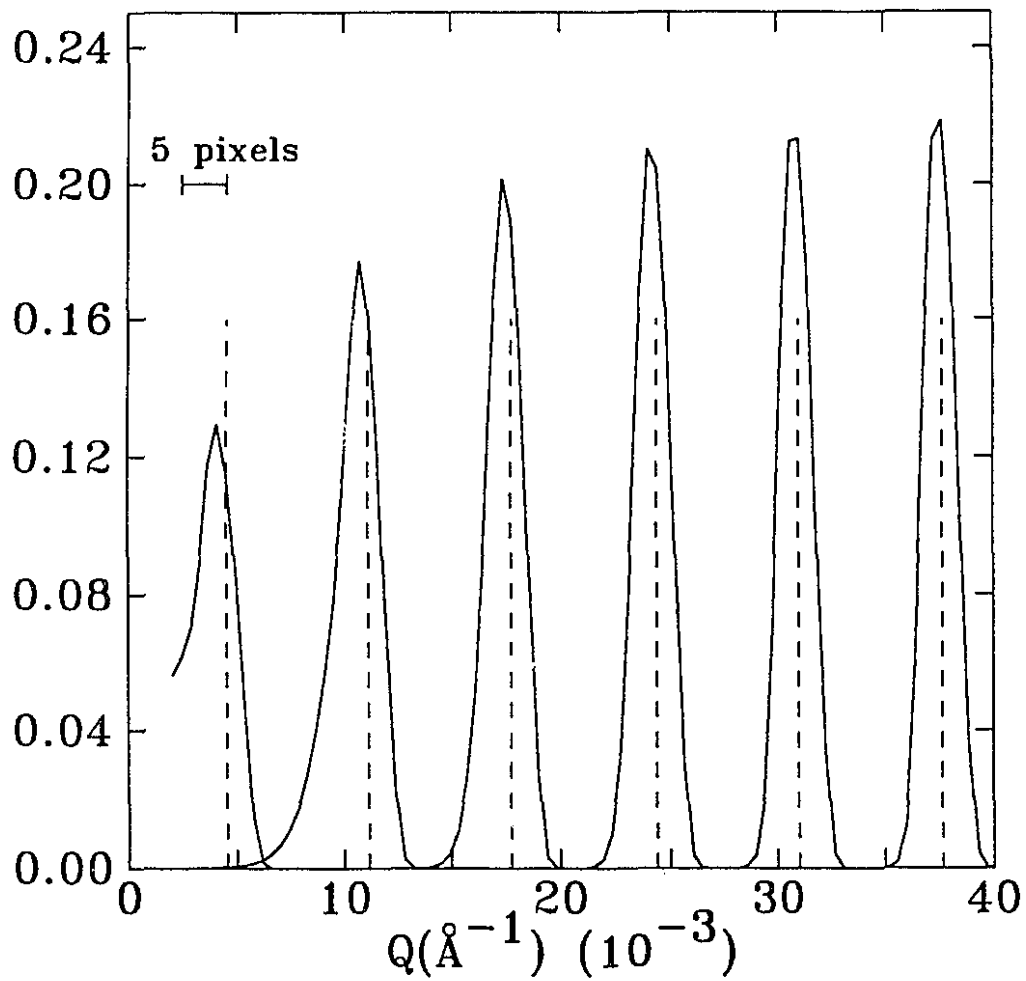


Figure 4.14: Position sensitive detector (PSD) response function. The dashed vertical lines are stylized idealized δ -functions, annuli in reciprocal space, and the solid curves represent the measured profile by the PSD. The resolution (FWHM) ranges from 0.0024 to 0.0017 \AA^{-1} . The resolution varies very little between 0.04 \AA^{-1} and the end of the detector range, 0.085 \AA^{-1} .

Such a set may be found by the iteration of

$$\hat{S}(q)_n = \hat{S}(q)_{n-1} + (E^S(p) - M_{pq}\hat{S}(q)_{n-1}) \quad (4.34)$$

and n is the deconvolution iteration number. It is convenient to use $E^S(p)$ as the first trial function, *i.e.* $\hat{S}(q)_0 \equiv E^S(p)$.

The deconvolution, or unsmearing, will pull features from lower q to higher q and will be important only for the lower q range measured. In effect, it can be said that the deconvolution pulls some signal out of, and away from the beamstop.

The “smearing” also smears sharp features of the structure factor and, conversely, the deconvolution will amplify any noise in $S(q)$. To circumvent this problem, the measured $E(p)$ is first smoothed with a spline function before deconvolution and the noise removed by the smoothing is added back-in to $S(q)$ after the deconvolution has converged.

To conclude, the result of the deconvolution for representative structure factors during two runs is presented on Figure (4.15). The convolution correction is only important when the peak maximum moves below $.01\text{\AA}^{-1}$. Typically this will occur at earlier times at higher quench temperatures due both to higher decomposition rates and a lower initial wavevector for the maximum of $S(q,t)$ (a) than for deep quenches (b). However, in all cases, the deconvolution has little effect at the early times of the fast runs (2 s). As expected for scans with peak maxima near the beamstop edge, the deconvolution has the effect of moving the maxima to higher q and sharpening the peak itself. In this figure, the last structure factor before the quench was subtracted off all shown $S(q,t)$ to remove the low q high intensity scattering. This procedure, used in the analysis of the data, will be introduced in § 6.1.

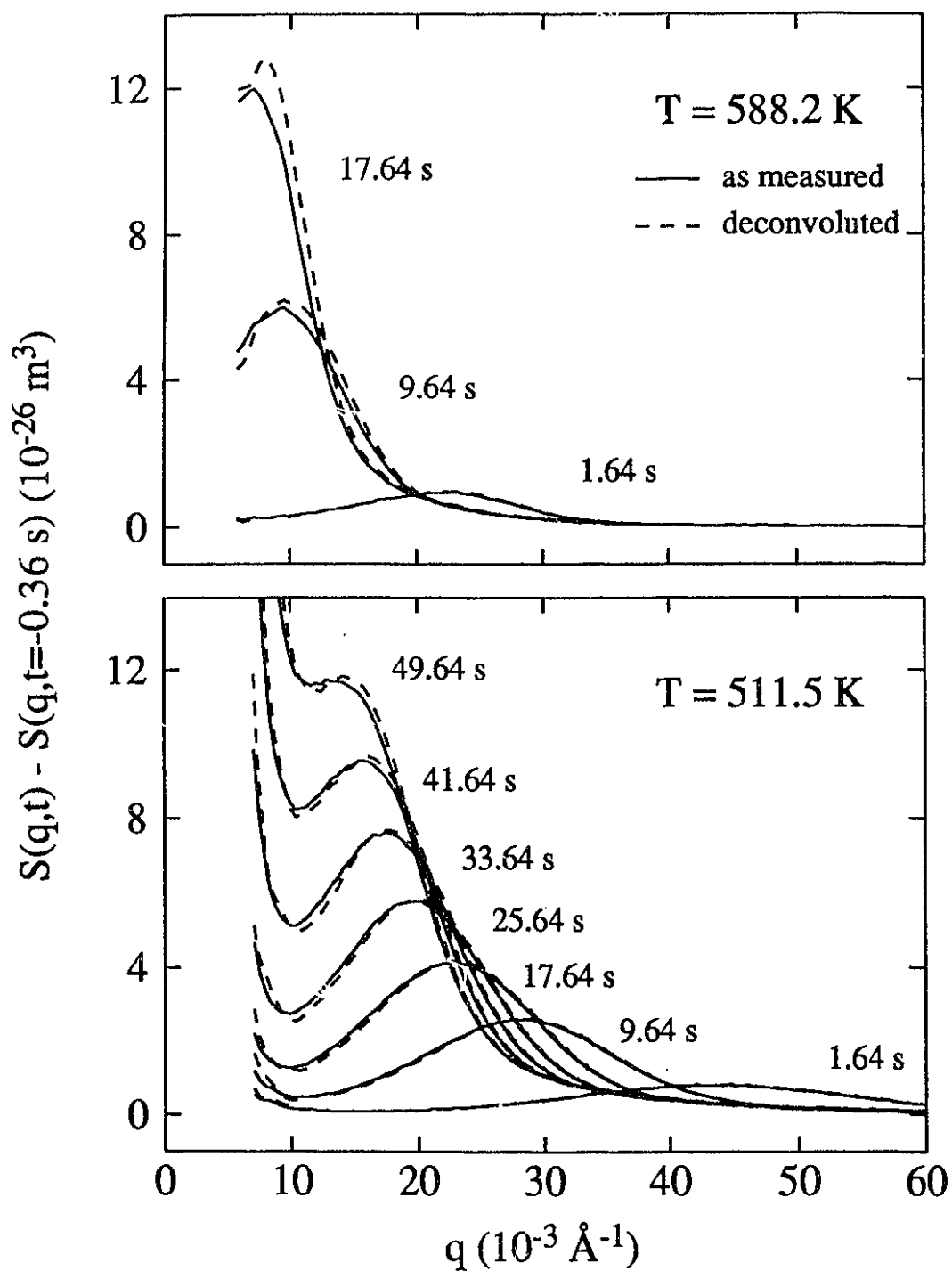


Figure 4.15: Effect of the deconvolution on the structure factors for a shallow quench (a) and a deeper quench (b). The zero of time corresponds to the time at which the temperature crossed T_c . The ordinate axis has the last structure factor before the quench subtracted off all shown $S(q, t)$.

Chapter 5

Theoretical background

Chapter III has presented a review of the early descriptions of spinodal decomposition. The equations of motion for the structure factor that were introduced were linear. However, both experiments and theory indicate that nonlinear terms have to be included when dealing with binary alloys. Discrepancies between linear theories and SAS measurements of SD were reported in Chapter III. This Chapter will present theoretical estimates of the nonlinearity in the SD of binary alloys.

This review of theory comprises two parts. The first deals with early stages of SD while the second is concerned by the late stages of SD. After an introduction to coarse-graining for the statistical description of a binary alloy, the equation of motion for the structure factor is derived. Following this, estimates of the importance of nonlinear terms are presented. The nonlinear theory developed by Langer, Bar-on and Miller[7] (LBM) is then introduced (§ 5.4). The late stages cannot be described by the LBM equation of motion. The second half of this Chapter will review late stages scaling predictions and phenomenological scaling forms for the structure factor.

5.1 Coarse-grained free energy functional

On a microscopic scale, binary alloys can be modelled by some Hamiltonian with interatomic interactions. Since these interactions are short range they are often modeled by an Ising model.[118] This Ising Hamiltonian should be adequate for computing equilibrium properties of the system. The resulting equilibrium free energy using this Hamiltonian is a convex function of composition and contains no information about metastable or unstable states. A mechanism is needed which includes irreversible effects to express the non-equilibrium dynamics. This section introduces a coarse grained free energy to describe the metastable and unstable states for systems.

The coarse graining can be justified heuristically by proposing that equilibrium thermodynamics apply locally in each region but that the thermodynamic variables differ from region to region. The approach to equilibrium of the system is then governed by the evolution of this generalized non-equilibrium free energy to the true equilibrium free energy in much the same way that two blocks of different temperatures will approach a common temperature when put in thermal contact.

The system is coarse grained by breaking it down in subvolumes of edge length a , each containing a large number of atoms.[118,119] A discrete cell composition, $c(\mathbf{r}_\alpha)$, is introduced as the average local composition in the mesoscopic region centered at \mathbf{r}_α . Each cell must be sufficiently large such that the composition and the free energy can be regarded as smoothly varying from one cell to the next and yet, it cannot be made arbitrarily large in order to ensure that SD does not occur in any cell. Ideally, the block size should be of order the characteristic length of critical phenomena, *i.e.* the correlation length ξ (*cf.* p. 7). In principle, a coarse graining length is selected *i.e.* a length scale for the averaging, then the calculation of averages is performed and the result is checked for consistency with the phenomenological dynamics measured.

The calculation of the grand canonical partition function of the coarse-grained

system from a microscopic model would involve two steps. First, the average over the microscopic configurations $\{c_i\}$ compatible with a given constraint $\{c_\alpha\}$, corresponding to a specific configuration of cell variables has to be performed. Next, the average over all the possible configurations $\{c_\alpha\}$ has to be computed:

$$e^{-\frac{F\{c_\alpha\}}{k_B T}} \equiv \sum_{\{c_i\}} e^{-\frac{H\{c_i\}}{k_B T}} . \quad (5.1)$$

In Eq. (5.1), $F\{c_\alpha\}$ is the generalized free energy for the set of coarse-grained cells $\{c_\alpha\}$ and $H\{c_i\}$ is the Hamiltonian for each of the statistical ensembles $\{c_i\}$. As the coarse-graining length is increased, *i.e.* the number of cells is decreased, the number of microscopic configurations $\{c_i\}$ compatible with the constraint $\{c_\alpha\}$ increases.

Instead of working with discrete cell composition variables $\{c_\alpha\}$, defined at discretized points \mathbf{r}_α , a field $c(\mathbf{r})$ defined for all \mathbf{r} which extrapolates smoothly the $c_\alpha(\mathbf{r}_\alpha)$ is introduced and thus $F\{c(\mathbf{r})\} \equiv F\{c_\alpha\}$. Further, the quantity $\delta c(\mathbf{r}, t)$ is introduced similarly to Eq. (2.15), except that it is now time-dependent :

$$\delta c(\mathbf{r}, t) = c(\mathbf{r}, t) - c_0 . \quad (5.2)$$

Figure (5.1) presents a schematic of the true equilibrium free energy $\bar{F}(\delta c)$, and of a coarse grained free energy density $f(\delta c)$ (the part of $F\{c(\mathbf{r})\}$ which is independent of gradients of $c(\mathbf{r})$). The true free energy differs from the coarse grained free energy density in one important respect, $\bar{F}(\delta c)$ is a convex function of c whereas $f(\delta c)$ has two distinct minima for temperatures and compositions within the miscibility gap and exhibits a region of negative curvature. The best argument to justify the composition dependence of $f(\delta c)$ is the *a posteriori* test of the predicted dynamics obtained for the convex region. It is not easy to perform explicitly the coarse graining procedures described above starting from a fully microscopic model. Instead, one assumes a phenomenological Ginzburg-Landau form for the coarse grained free energy $F\{c(\mathbf{r})\}$.

The process of averaging inside subvolumes, *i.e.* coarse-graining is implicit in the regular solution model (mean field) description of the miscibility gap of § 1.3

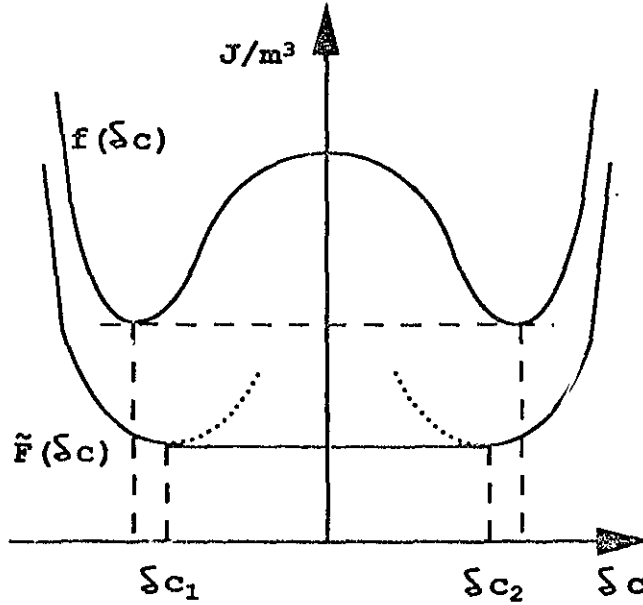


Figure 5.1: Schematic graph of the coarse-grained free energy density $f(\delta c)$ and the corresponding equilibrium free energy $\tilde{F}(\delta c)$. The dashed sections denote the analytic continuation of $\tilde{F}(\delta c)$ into the metastable region.[120]

where Gibbs' free energy possessed a convex region and the introduction of the intensive free energy of § 1.4. The integral over Eq. (1.16), provides the Landau-Ginzburg form for the coarse-grained free energy,

$$F\{c(\mathbf{r})\} = \int d\mathbf{r} \left[\frac{1}{2} \kappa |\nabla c(\mathbf{r})|^2 + f(c(\mathbf{r})) \right] \quad (5.3)$$

where the subscript to $f_0(c(\mathbf{r}))$ has been dropped to simplify the notation. As previously, κ is the coefficient to the free energy gradient term. $F\{c(\mathbf{r})\}$ will depend on the limits of integration. The lower integration limit will correspond to the size of the coarse-graining cell and the upper limit of integration will be the system size. The cutoffs are often referred to as the short wavelength or ultra-violet cutoff and the long wavelength or infrared cutoff. Thus, the Landau-Ginzburg free energy functional $F\{c(\mathbf{r})\}$ contains only spatial variation $c(\mathbf{r})$ with wavelengths larger than

the coarse-graining length.¹

$F\{c(\mathbf{r})\}$ has to be such as to reflect the physical properties of the microscopic model. In particular it has to account for the phase transition which occurs at $T_c(c)$. A simple expression for $f(\delta c)$ that satisfies this condition can be written down for the case of the critical composition, assuming symmetry of the miscibility gap. This is the usual “ c^4 ” approximation

$$f(\delta c) = \frac{r}{2}(\delta c)^2 + \frac{u}{4}(\delta c)^4 \quad (5.4)$$

where r , the prefactor to $(\delta c)^2$, is temperature dependent. It is negative when $T < T_c$ and positive for $T > T_c$. Thus, below the critical point, $f(\delta c)$ has a double well structure not unlike the regular solution model of Chapter I.[17,34] Both r and u have dimensions of J/m^3 . With the free energy functional defined in this way, the coexistence points δc_{coex} at a given temperature are given by the roots of $\frac{\partial f}{\partial(\delta c)} = 0$ i.e.

$$\delta c_{coex} = \pm \sqrt{-r/u}. \quad (5.5)$$

Similarly, in the mean field limit the compositions on the spinodal line are given by $\frac{\partial^2 f}{\partial(\delta c)^2} = 0$ i.e.

$$\delta c_{sp} = \pm \sqrt{-r/3u}. \quad (5.6)$$

The mean field correlation length is temperature-dependent. In particular, near T_c , it diverges to infinity and infinite wavelength fluctuations are predicted (and observed as critical opalescence in binary fluids). Consequently, the coarse

¹A heuristic argument for the existence of the convex region in $f(\delta c)$ based on the coarse graining procedure can be suggested based on surface energy σ associated with the breaking down of the bulk into subvolumes. The intensive coarse grained free energy would then tend towards the true free energy as the coarse graining length is made arbitrarily large $\lim_{a \rightarrow \infty} \frac{\sigma A}{V} = 0$ with the disappearance of the concave region. In the microscopic model of nearest-neighbor interacting atoms, as the system is partitioned into boxes, atoms at the surface contribute more energy to the total energy of a cell than atoms in the bulk (in effect, these atoms contribute an additional surface energy). So the obtained coarse-grained free energy is always larger than the true thermodynamic free energy. This was the case in Figure (5.1).

graining length should also be temperature dependent, increasing as T gets closer to T_c , both from above and below. In the limiting case where it is comparable to the size of the system, then the coarse grained free energy tends towards the exact equilibrium convex free energy.[121]

The location of the spinodal curve is found to depend on the coarse-graining size. This dependence of the location of the spinodal curve on the coarse-graining size is consistent with predictions by Langer [121] and Binder *et al.*[52] on the smoothness of the dynamical transition between nucleation and spinodal decomposition.

The determination of the free energy functional is important for a dynamical description of a given system. The first attempts were quite phenomenological. They involved determining relevant parameters in (5.3) from extrapolations of measured thermodynamic quantities in the stable region of the phase diagram.[58]

5.2 Equation of motion for the non-equilibrium structure factor

The equation of motion for the non-equilibrium $S(q, t)$ can be calculated *via* the appropriate Fokker-Planck equation. A derivation of the Fokker-Planck equation is outlined below, based on a paper by Langer.[119]

The state of the phase separation is quantized by the time dependent statistical distribution of all coarse grained composition variations, denoted as $\rho(\{(\delta c)_\alpha\}, t)$. [119,122] Instead of the complex microscopic description of the interactions required to account for the dynamic evolution of the alloy, a simple procedure is to simulate their combined effects by coupling the coarse grained system to a heat bath.[123] One source of energy for the heat bath could presumably be the phonon modes which reequilibrate rapidly in comparison with the composition changes. A master equation can be written for $\rho(\{(\delta c)_\alpha\}, t)$:

$$\frac{\partial \rho(\{(\delta c)\}, t)}{\partial t} = \sum_{\{c_\alpha\}} [W(\{\delta c\}, \{\delta c'\})\rho(\{\delta c'\}, t) - W(\{\delta c'\}, \{\delta c\})\rho(\{\delta c\}, t)] \quad (5.7)$$

where the summation is over all the possible composition configurations $\{c_\alpha\}$ and $W(\{c\}, \{c'\})$ is the rate at which the thermal bath induces transitions from $\{c'\}$ to $\{c\}$. The central aspect to the phenomenological description of the separation process has become the transition rates $W(\{\delta c'\}, \{\delta c\})$.

A detailed description of the derivation of the transition rates performed by Langer is not done here. However, some remarks on the phenomenological assumptions are given. The coarse grained free energy (Eq. 5.3) is the appropriate energy for the system for a configuration $\{(\delta c)\}$ and thus $\rho(\{(\delta c)_\alpha\}, t)$ will be proportional to $\exp(-F\{(\delta c)\})$. Making use of the condition of detailed balance the transition probability can be expressed as

$$W(\{\delta c\}, \{\delta c'\}) = \exp \left[\frac{1}{2k_B T} (F(\{\delta c\}) - F(\{\delta c'\})) \right] \Omega(\{\delta c'\}, \{\delta c\}) \quad (5.8)$$

where $\Omega(\{\delta c'\}, \{\delta c\})$ is an atomic jump frequency. The function Ω is assumed to depend only on the change in δc , and thus is composition independent. This point is important in the derivation of the rates. Since the coarse graining cells contain a large number of sites, the change in δc corresponding to a single transition is small. Thus Ω must be sharply peaked around δc . The sites are assumed saturated with atoms, so the local composition has to be conserved and the changes in cell concentrations are always symmetric *i.e.* if a particular cell composition c_α changes by $+\vartheta$, the composition of the neighboring cell will change from c'_α to $c'_\alpha - \vartheta$. Consequently Ω will be symmetric in ϑ . An atomic jump rate, Γ is introduced. For this, the only changes in the solute atoms distribution between the cells allowed is the swap of unlike atoms between two specific neighboring cells. If there are N_v sites per cell, then $N_v^{2/3}$ sites in cell α (or α') are nearest neighbors to sites in cell α' (or α) and Γ to within a constant factor is given by :

$$\Gamma = N_v^{-2/3} \Omega(\{\dots, (\delta c + 1/N_v)_\alpha, (\delta c - 1/N_v)_{\alpha'}, \dots\}, \{\dots, (\delta c)_\alpha, (\delta c)_{\alpha'}, \dots\}). \quad (5.9)$$

Taking the second moment over all ϑ first noticing that for $\vartheta = 1/N_v$, $\vartheta^2 \Omega = N_v^{-4/3} \Gamma$

$$\int_{-\infty}^{+\infty} \vartheta^2 \Omega(\vartheta) d\vartheta = N_v^{-5/3} \Gamma \quad (5.10)$$

where the condition that Γ is a sharp function centered at $\vartheta = 0$ has been used. Equation (5.7) then becomes:

$$\begin{aligned} \frac{\partial}{\partial t} \rho(\{\delta c\}, t) = & \frac{\Gamma}{2N_v^{5/3}} \sum_{\alpha} \frac{\partial}{\partial c_{\alpha}} \left[\frac{1}{k_B T} \left(6 \frac{\partial}{\partial c_{\alpha}} F - \sum_{\langle \alpha' \alpha \rangle} \frac{\partial}{\partial c_{\alpha'}} F \right) \rho(\{\delta c\}, t) \right. \\ & \left. + \left(6 \frac{\partial}{\partial c_{\alpha}} \rho(\{\delta c\}, t) - \sum_{\langle \alpha' \alpha \rangle} \frac{\partial}{\partial c_{\alpha'}} \rho(\{\delta c\}, t) \right) \right], \end{aligned} \quad (5.11)$$

where $\sum_{\langle \alpha' \alpha \rangle}$ means summation over α' nearest neighbors to α and $F = F(\{\delta c\})$.

As in the introduction of the coarse grained free energy in the previous section, it is convenient to introduce a continuous field $\delta c(\mathbf{r})$ which extrapolates smoothly the variables $\{\delta c_{\alpha}\}$. After some algebra, using the functional derivative $\partial/\partial c_{\alpha} = (N_v a_0^3) \delta/\delta c(\mathbf{r})$ and replacing the summation on cells by $(N_v a_0^3)^{-1} \int d\mathbf{r}$, Equation (5.11) takes the form of a Fokker-Planck equation for the $\rho\{\delta c(\mathbf{r}), t\}$:

$$\frac{\partial \rho\{c(\mathbf{r}), t\}}{\partial t} = - \int d\mathbf{r} \frac{\delta J(c(\mathbf{r}), t)}{\delta c(\mathbf{r})}. \quad (5.12)$$

The integral extends over all space and $J(\mathbf{r})$ is a probability current given by

$$J(c(\mathbf{r}), t) = - \frac{a_0^5}{2k_B T} \Gamma \nabla^2 \left(\frac{\delta F}{\delta c(\mathbf{r})} \rho(c(\mathbf{r}), t) + k_B T \frac{\delta \rho(c(\mathbf{r}), t)}{\delta c(\mathbf{r})} \right). \quad (5.13)$$

In Chapter II, it was shown that SAXS probed the two-point equal time density (or composition) correlation function of the system. The derivation of sum rules also required knowledge of moments of the composition distribution. Moments of the composition fluctuations in a coarse-grained system are taken over the distribution functional $\rho\{c(\mathbf{r})\}$

$$\langle (\delta c)^n \rangle \equiv \int \rho\{(\delta c)\} (\delta c)^n d(\delta c). \quad (5.14)$$

While in Chapter II angular brackets $\langle \rangle$ implied a thermal average, here they take the meaning of a sum over all configurations of a non-equilibrium ensemble. As a consequence, the first moment (average) of a composition dependent quantity will generally not be equal to the value this quantity would take at a composition value equal to the bulk composition, *i.e.* if a simple thermal average was performed for which normalization is done to the volume of integration. However, in the limit when

$\rho(\{\delta c\})$ is a sharply peaked function of c in the neighborhood of $\{c\} = \{\bar{c}\}$ [119] then the average of any function of $\{c\}$ can be approximated by the value taken by the same function at $\{\bar{c}\}$. In that limit, the Fokker-Planck equation reduces to the generalized diffusion equation (Eq. 1.26) with the identification

$$\Gamma = \frac{2Mk_B T}{a_0^5} \quad (5.15)$$

where M is the atomic mobility as introduced in § 1.4.²

The n^{th} order non-equilibrium two-point equal-time correlation can be written as:

$$S_n(\mathbf{r} - \mathbf{r}_0) \equiv \langle \delta c^{n-1}(\mathbf{r}, t) \delta c(\mathbf{r}_0, t) \rangle \quad (5.16)$$

where omission of the subscript n will mean $S_2(\mathbf{r} - \mathbf{r}_0)$. Again, in Eq. (2.11) the angular brackets $\langle \rangle$ implied a thermal average and they now take the meaning of an average over a non-equilibrium ensemble

$$S(|\mathbf{r} - \mathbf{r}_0|) = \int \mathcal{D}[\delta c] \rho_2[\delta c(\mathbf{r}), \delta c(\mathbf{r}_0)] \delta c(\mathbf{r}) \delta c(\mathbf{r}_0). \quad (5.17)$$

The functional integral on the right-hand side denotes the integral over the fields $\{\delta c\}$.

Expression (5.12) allows one to derive the equation of motion for the structure factor $S(\mathbf{q}, t)$, which is the Fourier transform of the two-point equal time real space correlation function $S(\mathbf{r} - \mathbf{r}_0, t)$ (cf. § 2.1)

$$S(\mathbf{q}, t) = \mathcal{F}[\langle \delta c(\mathbf{r}, t) \delta c(\mathbf{r}_0, t) \rangle]. \quad (5.18)$$

The real space correlation function is obtained by multiplying both sides of Eq. (5.12) by $\delta c(\mathbf{r}, t) \delta c(\mathbf{r}_0, t)$ and a sum is performed over all possible configurations $\{\delta c(\mathbf{r})\}$ to obtain $S(\mathbf{r} - \mathbf{r}_0, t)$. Taking the Fourier transform of the result gives³

$$\frac{\partial \hat{S}(\mathbf{q}, t)}{\partial t} = -2Mq^2 \left[\left(\kappa q^2 + \frac{\partial^2 f}{\partial c^2} \Big|_{c_0} \right) \hat{S}(\mathbf{q}, t) + \sum_{n=3}^{\infty} \frac{1}{(n-1)!} \frac{\partial^n f}{\partial c^n} \Big|_{c_0} \hat{S}_n(\mathbf{q}, t) \right] + 2Mk_B T q^2 \quad (5.19)$$

²An alternate derivation for Eq. (5.12) is to start by a Langevin equation instead of the master equation (see Ref. [118]).

³The calculus involved is well described in Ref. [118].

The functions $\hat{S}(\mathbf{q})$ and $\hat{S}_n(\mathbf{q})$ are respectively the Fourier transform of the two-point (*cf.* Eq. 5.16) and the $(n - 1)^{\text{th}}$ order of the two-point equal time non-equilibrium correlation function (*cf.* Eq. 5.16). This procedure takes fully into account the composition distribution functional. Equation (5.19) is the first of an infinite hierarchy of coupled partial differential equations (pde), one for each moment. Indeed, each moment equation is such that it depends on the higher order moments. This equation is exact under the coarse-graining assumption for the free energy (5.3). Even by restricting $f(c)$ to the “ c^4 ” approximation (5.4), the hierarchy of pde will not be finite as \hat{S}_4 will be required to solve the equation of motion for \hat{S}_2 and \hat{S}_6 to solve for \hat{S}_4 and so on. A central problem to theories of SD is the closing of the infinite hierarchy of coupled pde required in the calculation of $\frac{\partial}{\partial t} \hat{S}_n(\mathbf{q}, t)$.

5.3 Estimates of the importance of nonlinear terms

Linearization schemes have been proposed to solve Equation (5.19). These include the linear theories due primarily to Hillert[55], Cahn[57] and Cook[30] which have been reviewed in the discussion of early theories of spinodal decomposition (Chapter III). Cahn’s linear equation (Eq. 1.21) is obtained if the thermal noise term, $2Mk_B T q^2$, is neglected as well as all correlation functions of order higher than two. If, instead, the thermal noise term is retained but highest order correlation functions, $\hat{S}(\mathbf{q}, t)$, are again neglected, then the CHC equation results (Eq. 3.6). Before introducing the approximation scheme of Langer, Bar-on and Miller which retains some nonlinearity of Eq. (5.19), this section introduces estimates of the importance of the nonlinear terms.

A criterion for the applicability of a mean field theory to a phase transition was introduced by Ginzburg who stated that below T_c the fluctuations in the order

parameter, which will be defined as

$$\phi \equiv c - c_c, \quad (5.20)$$

averaged over a region the size of the correlation length (a coarse-graining cell) must be small compared to the value of ϕ itself.[124] Binder generalized the Ginzburg criterion for SD in the way that follows.[125] By analogy to the formation of nuclei of second phase during nucleation from a metastable state, call $\phi(\infty)$ the value of the order parameter away from an "interface" and $\phi(0)$ the value at the center of a "second phase particle". Then, introducing $\delta\phi = \phi - \phi_0$ where $\phi_0 = (c_0 - c_c)$, the generalized Ginzburg criterion can be written as

$$\langle [\delta\phi(\mathbf{r})]^2 \rangle \ll [\phi(\infty) - \phi(0)]^2. \quad (5.21)$$

The Ornstein-Zernike form for the correlation function (the Fourier transform of Eq. (2.19)), is appropriate for a mean field theory. Thus, making the maximum possible choice of a coarse-graining cell, the lhs becomes[43]

$$\langle [\delta\phi(\mathbf{r})]^2 \rangle \propto \xi^{-1} (\sqrt{\kappa})^{-2} \quad (5.22)$$

where the proportionality constant includes a factor $k_B T$. Interpreting ξ in Eq. (5.22) as a characteristic wavelength of the phase separation process with maximum amplitude growth, *i.e.*

$$\xi^{-1} \propto (\sqrt{\kappa})^{-1} \left[\left| \frac{\partial^2 f(\phi)}{\partial \phi^2} \right| \right]^{\frac{1}{2}} \quad (5.23)$$

and, expanding $\partial^2 f(\phi)/\partial \phi^2$ about the value of the order parameter at the spinodal line, ϕ_{sp} , and using $\phi_{sp} \propto (1 - \frac{T}{T_c})^{1/2}$,

$$\xi^{-1} \propto (\sqrt{\kappa})^{-1} \left(1 - \frac{T}{T_c}\right)^{1/2} \left(1 - \frac{\phi}{\phi_{sp}}\right)^{\frac{1}{2}}. \quad (5.24)$$

Eq. (5.21) then becomes, with $\phi(0) = \phi_{sp}$ and $\phi(\infty) = \phi_0$,

$$k_B T (\sqrt{\kappa})^{-3} \left(1 - \frac{T}{T_c}\right)^{\frac{1}{2}} \left(1 - \frac{\phi}{\phi_{sp}}\right)^{\frac{1}{2}} \ll (\phi_0 - \phi_{sp})^2. \quad (5.25)$$

With $(\phi - \phi_{sp})^2 = \phi_{sp}^2 (1 - \frac{\phi}{\phi_{sp}})^2$,

$$k_B T (\sqrt{\kappa})^{-3} \left(1 - \frac{T}{T_c}\right)^{-\frac{1}{2}} \left(1 - \frac{\phi}{\phi_{sp}}\right)^{-\frac{3}{2}} \ll 1. \quad (5.26)$$

Using definition (5.20), the condition for validity of the linear theory can thus be expressed by the following inequality :

$$k_B T \ll (\sqrt{\kappa})^3 (1 - T/T_c)^{1/2} \left[\frac{c_0 - c_{sp}(T)}{c_c - c_{sp}(T)} \right]^{3/2}. \quad (5.27)$$

From the expression of the Landau-Ginzburg free energy functional, Eq. (5.3), $\sqrt{\kappa}$ is of order the range of the composition gradients and evidently $\sqrt{\kappa}$ represents the range of interaction. For alloy systems, Binder[125] argues that $\sqrt{\kappa}$ is sufficiently small such that the above inequality is never satisfied. Mean field theories should therefore be valid only in systems with long range interactions. Linear equations of motion such as the CHC equation are essentially a mean field formula and therefore only holds strictly for cases of infinite range interactions. They should then only be observed in systems such as polymer blends which fulfill condition (5.27). This prediction has recently been confirmed by computer simulations.[126]

Since linear theory or mean field approximation deals with the limit where the interaction force has a long range, Grant *et al.*[127] propose a perturbation expansion where the small parameter, ϵ , is proportional to the inverse of the range of the force. Following their work, it is convenient to convert Eq. (5.19) to a dimensionless form by making the following change of variables,

$$k = \left(\frac{\kappa}{\tau}\right)^{1/2} q, \quad (5.28)$$

$$\tau = \left(\frac{2M\tau^2}{\kappa}\right) t, \quad (5.29)$$

$$\psi = \left(\frac{u}{\tau}\right)^{1/2} (\delta c), \quad (5.30)$$

and to render the structure factor dimensionless,

$$\mathcal{S} \equiv \left(\frac{-\tau}{\kappa}\right)^{3/2} \hat{S}. \quad (5.31)$$

The resulting dimensionless equation of motion for the structure factor for a critical quench in the two-phase region is

$$\frac{\partial \mathcal{S}(k, \tau)}{\partial \tau} = -k^2 [(k^2 + 1)\mathcal{S}(k, \tau) + \mathcal{S}_4(k, \tau)] + \epsilon k^2 \quad (5.32)$$

where ϵ is the intensity of the thermal noise and is given by

$$\epsilon \equiv \frac{k_B T u}{r^2} \left(\frac{-\tau}{\kappa} \right)^{3/2}. \quad (5.33)$$

In Eq. (5.32), ϵ is the only quantity that was not scaled away. If one sets $\tilde{\psi} \equiv \psi \sqrt{\epsilon}$, then $\mathcal{S} \rightarrow \epsilon \mathcal{S}$, $\mathcal{S}_4 \rightarrow \epsilon^2 \mathcal{S}_4$ and the dimensionless equation of motion takes the form

$$\frac{\partial \mathcal{S}(k, \tau)}{\partial \tau} = -k^2 [(k^2 + 1)\mathcal{S}(k, \tau) + \epsilon \mathcal{S}_4(k, \tau)] + k^2. \quad (5.34)$$

The parameter ϵ determines the contribution of the fourth order term in energy and its strength with respect to the noise. From Eq. (5.33), $\epsilon \sim (\sqrt{\kappa})^{-3}$ and thus in the limit of infinite range interaction, when mean field theory is expected to be valid according to inequality (5.27), $\epsilon \rightarrow 0$ and the CHC equation of motion is recovered. The range of the free energies “interaction” is then proportional to $\sqrt{\kappa}$ since the parameter ϵ is small when the range of the interaction is large and CHC is expected to be valid. This is consistent with the heuristic picture that linear theory is expected to work when local composition fluctuations are small, corresponding to small but long wavelength fluctuations, with minimal composition gradients.

Eq. (5.34) provides a direct way to find the time regime of validity of CHC, t_{\max} if ϵ is nonzero (and small). An expansion on $\psi = \psi^{(0)} + \epsilon^{1/2} \psi^{(1)} + \dots$ breaks down for $\psi^{(0)} \approx \epsilon^{1/2} \psi^{(1)}$. The corresponding expansion for the dimensionless structure factor is $\mathcal{S}(k, \tau) = \epsilon \mathcal{S}^{(1)}(k, \tau) + \epsilon^{3/2} \mathcal{S}^{(2)}(k, \tau) + \dots$. Keeping only the leading term in the expansion for the structure factor, Equation (5.34) becomes

$$\frac{\partial}{\partial \tau} \mathcal{S}^{(1)}(k, \tau) = k^2(k^2 + 1)\mathcal{S}^{(1)}(k, \tau) + k^2. \quad (5.35)$$

To leading order in the expansion in the range of the force, the result of the CHC theory is reobtained. Expression (5.35) will break down when $\mathcal{S}^{(1)} \sim \epsilon \mathcal{S}^{(2)}$ i.e.

$e^{t_{\max}} \sim \epsilon$. Thus, $t_{\max} \sim -\ln \epsilon \sim \ln(\sqrt{\kappa})$.⁴ Grant *et al.*[127] provide calculations and considerations for the first order perturbation. The equation of motion obtained after considerable algebra for the structure factor to order ϵ^2 develops only a Gaussian one-point density distribution functional. To obtain a late time bimodal distribution would require higher order terms. To date, such a calculation has not been performed.

The small parameter ϵ can be expressed in terms of more familiar quantities. Introducing χ as the susceptibility and, as in the susceptibility sum rule of § 2.3 (*cf.* Eq. 2.23), with the lattice constant a_0 ,

$$\begin{aligned}\chi &\equiv \frac{1}{a_0^3} \frac{k_B T}{\partial^2 f / \partial (\delta c)^2} \\ &= \frac{1}{a_0^3} \frac{k_B T}{r}.\end{aligned}\quad (5.36)$$

With the thermal correlation length ξ defined as in Eq. (2.20) by

$$\begin{aligned}\frac{1}{\xi^2} &= \frac{1}{\kappa} \left(\frac{\partial^2 f}{\partial (\delta c)^2} \right)_{\text{coex}} \\ &= \begin{cases} 2r/\kappa & (T < T_c) \\ r/\kappa & (T > T_c) \end{cases}\end{aligned}\quad (5.37)$$

where, again, κ is the length scale for the interactions. Using the coexistence value for the “ c^4 ” model (Eq. 5.4), Equation (5.33) can now be written as

$$\epsilon = \frac{1}{\sqrt{2}} \frac{\chi}{(\delta c)_{\text{coex}}^2} \left(\frac{a_0}{\xi} \right)^3.\quad (5.38)$$

Near the critical point ξ , χ and $(\delta c)_{\text{coex}}$ are expected to follow power laws (*cf.* Table 1.1) with critical exponents ν , γ and β and critical amplitudes ξ_0 , C and B . Assuming hyperscaling, the critical exponents should obey

$$2\beta + \gamma' = 3\nu\quad (5.39)$$

⁴This result can also be obtained directly from the generalized Ginzburg criterion (Eq. 5.21) by recalling that fluctuations will grow exponentially if below q_c and asking how long the inequality will remain valid.[125] This result can also be interpreted in terms of a mean first passage-time for the decay of an unstable state.[128]

and Eq. (5.38) gives that

$$\epsilon \propto (a_0/\xi_0)^3 \quad (5.40)$$

which indicates that ϵ remains finite at the critical point. This result is consistent with the identification of ξ_0 with the range of the interaction in the mean field critical region.[125]

Most systems present short-range forces and $\epsilon \sim 1$. Then $t_{\max} \sim \ln 1$ is a very small quantity. For long-range force systems, such as polymer blends with a Flory-Huggins free energy[125,129], $a_0/\xi \ll 1$ and there is a range in which CHC should be valid.

5.4 The Langer-Bar-on-Miller Theory

5.4.1 Equation of motion

Langer, Bar-on and Miller[7] proposed a scheme to truncate Equation (5.19) and close the hierarchy of pde. The resulting equation of motion predicts how $\rho\{\delta c(\mathbf{r}), t\}$ will evolve in time. For high temperature or disordered systems $\rho\{\delta c(\mathbf{r}), t\}$ will be a very sharply peaked distribution centered at the average concentration c_0 . As the system is aged in the miscibility gap and two equilibrium phases are formed, $\rho\{\delta c(\mathbf{r}), t\}$ becomes a doubly peaked functional with the peaks located at the concentrations of the precipitate and matrix phases.

The LBM scheme rests on the following *Ansatz* for the two-point distribution function ρ_2 :

$$\rho_2[\delta c(\mathbf{r}), \delta c(\mathbf{r}_0)] \cong \rho_1[\delta c(\mathbf{r})] \rho_1[\delta c(\mathbf{r}_0)] \{1 + \gamma(|\mathbf{r} - \mathbf{r}_0|)\delta c(\mathbf{r})\delta c(\mathbf{r}_0)\}. \quad (5.41)$$

In this expression, $\rho_1[\delta c]$ is the one-point distribution function which must be normalized so that

$$\int_{-\infty}^{+\infty} \rho_1[\delta c] d(\delta c) = 1 \quad (5.42)$$

and

$$\int_{-\infty}^{+\infty} \rho_1[\delta c] \delta c d(\delta c) = 0. \quad (5.43)$$

The function $\rho_1[\delta c]$ is expected to become doubly peaked when phase separation occurs. The function $\gamma(\mathbf{r})$ appearing in Eq. (5.41) is proportional to the correlation function. By the definition of the two-point equal-time correlation function (Eq. 5.17) and using normalization conditions (5.42) and (5.43) :

$$S(|\mathbf{r} - \mathbf{r}_0|) = \langle (\delta c)^2 \rangle^2 \gamma(|\mathbf{r} - \mathbf{r}_0|). \quad (5.44)$$

The great simplification achieved by Eq. (5.41) is that all the $S_n(|\mathbf{r} - \mathbf{r}_0|)$ have the same \mathbf{r} -dependence as $S(|\mathbf{r} - \mathbf{r}_0|)$:

$$\begin{aligned} S_n(|\mathbf{r} - \mathbf{r}_0|) &= \int \mathcal{D}[\delta c] \rho_2[\delta c(\mathbf{r}), \delta c(\mathbf{r}_0)] \delta c(\mathbf{r})^{n-1} \delta c(\mathbf{r}_0) \\ &\cong \langle (\delta c)^n \rangle \gamma(|\mathbf{r} - \mathbf{r}_0|) \\ &\cong \frac{\langle (\delta c)^n \rangle}{\langle (\delta c)^2 \rangle} S(|\mathbf{r} - \mathbf{r}_0|). \end{aligned} \quad (5.45)$$

Equation (5.45) is useful in closing the hierarchy of coupled pde.

Eq. (5.19) then simplifies to the LBM equation of motion⁵:

$$\frac{\partial \hat{S}(q, t)}{\partial t} = -2Mq^2 (\kappa q^2 + A) \hat{S}(q, t) + 2Mk_B T q^2 \quad (5.46)$$

where $\hat{S}(q, t)$ is the structure function and

$$A = \sum_{n=2}^{\infty} \frac{1}{(n-1)!} \left. \frac{\partial^n f}{\partial c^n} \right|_{c_0} \frac{\langle (\delta c)^n \rangle}{\langle (\delta c)^2 \rangle}. \quad (5.47)$$

Equations (5.46) and (5.47) constitute a set of coupled differential equations. The LBM theory is derived by further imposing restrictions for the calculation of A .

It can be noted that if the source term in equation (5.46), the last term on the right hand side, is neglected, and the sum truncated at the first term in the expression for A in equation (5.47), then the Cahn-Hilliard equation (Eq. 1.21) is

⁵The hat notation to denote the Fourier transform of $S(\mathbf{r})$ for $S(q)$ will only be used when confusion is possible between the two in the text.

obtained. On the other hand, if the source term is kept but the sum still truncated at the first term for A , then the Cahn-Hilliard-Cook equation (Eq. 3.6) is obtained.

The explicit q -dependence of $\frac{\partial}{\partial t} \hat{S}_n(q, t)$ has been removed by using approximation (5.45) and its time dependence has been simplified to one time varying parameter, A . The infinite hierarchy of p.d.e. though simplified still remains to be closed. In the calculation of A , the sum (5.47) will have to be truncated.

Whereas in the Cook equation $\partial^2 f / \partial c_0^2$ was constant in time, $A = A(t)$ is not, a coupling between the modes is provided by A . There is no intrinsic q -dependence of A . The integral

$$\langle (\delta c)^2 \rangle = \frac{1}{(2\pi)^3} \int dq \hat{S}(q) \quad (5.48)$$

over the entire range of q -space up to the cut-off provides the "mean field" coupling (cf. Eq. 2.25). Equations (5.46) and (5.47) cannot be used in this form due to the hierarchy of coupled pde's: to solve $\partial S(q, t) / \partial t$ requires the solution of $\partial^3 S(q, t) / \partial t$ and so on *ad infinitum*.

Because $\langle \delta c^2 \rangle$ is a positive, increasing function of time, the characteristic wave number q_c must decrease. That is, the mean-square fluctuations, via the nonlinear part of $\frac{\partial f}{\partial c}$, cause a qualitatively correct coarsening of the precipitation pattern.

To solve the nonlinear equation (5.46), the density probability distribution functional (*i.e.* the one-point composition distribution functional) first proposed by Langer and Bar-on[122] is used by LBM. In this *Ansatz*, $\rho(\delta c)$ is parametrized by the sum of two Gaussians centered at $\delta c = b_1$ and b_2 and a width σ which evolve in time.

$$\rho(\delta c) = \frac{b_2}{(b_1 + b_2) \sigma \sqrt{2\pi}} \exp\left(-\frac{(\delta c - b_1)^2}{2\sigma^2}\right) + \frac{b_1}{(b_1 + b_2) \sigma \sqrt{2\pi}} \exp\left(-\frac{(\delta c + b_2)^2}{2\sigma^2}\right). \quad (5.49)$$

At $t = 0$, the system is in a single phase state, $b_1 = b_2 = 0$. At $t = 0$ when the solution is still in a disordered state, σ^2 is much greater than the product $b_1 b_2$ and $\rho(\delta c)$ will be a sharply peaked function centered at $\delta c = 0$ as described above. At

later aging times two distinct peaks in $\rho(\delta c)$ appear thus simulating the phase separation process. As time passes, these values get displaced towards the equilibrium two-phase concentrations. If the separation occurs at critical composition, then $b_1(t) = b_2(t) = b(t)$. Expressing $\rho(\delta c)$ as a doubly peaked function is an essential aspect of the nonlinear problem. As pointed out by LBM, the CHC linearization implies that $\rho(\delta c)$ remains peaked at $\delta c = 0$ and as a result is valid only at very early aging times. The moments of $\langle(\delta c)^2\rangle$ (cf. Eq. 5.14) just involves Gaussian integrals and

$$\langle(\delta c)^2\rangle = \sigma^2 + b_1 b_2. \quad (5.50)$$

In the mean field approximation, $\rho(\delta c)$ remains centered at zero at all times. So the LBM equation of motion differs from the mean field closing scheme[130] by the introduction of the two Gaussians for the density functional $\rho(\delta c)$. With b moving away from zero, the fourth cumulant,

$$\langle(\delta c)^4\rangle_c \equiv \langle(\delta c)^4\rangle - 3\langle(\delta c)^2\rangle^2. \quad (5.51)$$

is nonzero. In an earlier approximation, Langer[130] employed the time-dependent self-consistent Hartree approximation according to which $\rho(\{c\}, t)$ can be written, at all times, as the exponential of some negative quadratic form in the function $\delta c(\mathbf{r})$. Though this was an analytically legitimate approximation, $\delta c(\mathbf{r})$ had to remain single-peaked and centered at zero. The average of any product containing an odd number of factors $\delta c(\mathbf{r})$ will vanish and $\langle\delta c^4\rangle = 3\langle\delta c^2\rangle^2$ and the fourth cumulant is zero.

One consequence of using the “ c^4 ” approximation is that $\partial^3 f / \partial(\delta c)^3$ is zero. This poses a serious problem near the classical spinodal line when the coefficient r is very small. Other than for the very restrictive case when an alloy is at the critical composition and the coherent spinodal symmetric about this composition, the decomposition occurs via fluctuations which are not at all symmetric about $\delta c = 0$. [84] The approximation provided by Eq. (5.4) will give a poor picture near the boundaries of the spinodal region and a nonzero $\partial^3 f / \partial(\delta c)^3$ should be considered.

5.4.2 Scaled LBM equation of motion

In a practical system, the most direct route to use the LBM theory is to work in the dimensional form of the equation of motion, where the wavevectors, atomic mobility and free energy gradient coefficient assume their physical units, namely Eq. (5.46). However, it is instructive to examine the reduced form suggested by Langer *et al.*[7] for Eq. (5.46). The connection between the dimensional set of parameters and the reduced ones is straightforward and useful for comparison between discrete dynamics simulations and physical measurements.

In the reduced equation of motion for the structure factor derived in § 5.3 there was no explicit coarse-graining. However, in the LBM theory, the “mean field coupling”, implicit in the computation of $A(t)$ (Eq. 5.47), requires integrals with a high-wavevector cutoff, *i.e.* a coarse-graining length in real space.

Langer *et al.*[7] assumed that the free energy functional $f(\delta c)$ near the critical point was given by a scaled version of (5.4), for a coarse-graining size proportional to the correlation length ξ . Only one system-dependent dimensionless parameter, f_0 , entered their approximation for $f(\delta c)$. The value of this parameter was determined from known critical exponents and critical amplitudes of the three-dimensional Ising model.

Using ϕ as defined in Eq. (5.20), the free energy is expressed in a scaled form with ϕ_S (solvus), the value of ϕ at the miscibility gap boundaries. The intensive free energy $f(\phi)$ is expressed in terms of a scaled (dimensionless) intensive free energy, $\Phi(\phi/\phi_S)$ by the form

$$f(\phi) = \left(\frac{k_B T}{a^3} \right) f_0 \Phi(\phi/\phi_S) \quad (5.52)$$

where $k_B T/a^3$ has the units of J/m^3 and f_0 is unitless. The parameter f_0 turns out to be the only system-dependent quantity in the model. It is such that $\Phi(0) = 0$, $\Phi'(\pm 1) = 1$, $\Phi'(0) = 0$ and $\Phi''(0) = -1$.

For the particular case of the “ c^4 ” form of $f(\phi)$, Eq. (5.4), recalling that the

solvus line is $(-r/u)^{1/2}$, the following is obtained

$$f(\phi) = \frac{r^2}{u} \Phi(\phi/\phi_S) \quad (5.53)$$

with

$$\Phi(\phi/\phi_S) = -\frac{1}{2}(\phi/\phi_S)^3 + \frac{1}{4}(\phi/\phi_S)^4. \quad (5.54)$$

The normalization conditions for $\Phi(\phi/\phi_S)$ enumerated above are all satisfied by this form. Comparing (5.52) and (5.53), the “ c^4 ” free energy coefficients r and u can be expressed as

$$r = -\frac{k_B T f_0}{a^3 \phi_S^2} \quad (5.55)$$

and

$$u = \frac{k_B T f_0}{a^3 \phi_S^4}. \quad (5.56)$$

A relationship can be obtained between f_0 and the small parameter ϵ introduced in § 5.3. However, before substituting the expressions for r and u in Eq. (5.33), it is necessary to know the coarse-graining length dependence of κ . This is done by using the mean field result that the correlation length $\xi = q_c^{-1}$ obeys

$$\frac{1}{\xi^2} \cong \frac{1}{\kappa} \frac{\partial^2 f}{\partial \phi_S^2}, \quad (5.57)$$

thus

$$q_c^2 = \frac{k_B T f_0}{\kappa a^3 \phi_S^2} \Phi''(1) \quad (5.58)$$

and with $\Phi''(1) = 2$ (cf. Eq. 5.54),

$$\kappa = \frac{1}{q_c^2} \frac{k_B T f_0}{a^3 \phi_S^2}. \quad (5.59)$$

Now, substituting for r , u and κ in Eq. (5.33),

$$f_0 = \frac{q_c^3 a^3}{\epsilon} \quad (5.60)$$

i.e. $\epsilon \sim f_0^{-1}$. The parameter ϵ is the small parameter introduced in the discussion of the perturbation expansion in the long-range force limit by Grant *et al.*[127] (cf. § 5.3). Thus, f_0 is related to the range of the force as follows from arguments presented earlier.

Hence, besides the knowledge of the location of the solvus line and a free energy functional form there is only one system-dependent dimensionless constant needed. In a discrete dynamics simulation of the reduced equation of motion, these two quantities are chosen at the onset and the dynamic evolution of the structure factor is observed.

The reduced scattering vector is then $\bar{q} = q/q_c$ where q_c is identified with the critical value of q when $\phi = 0$ or

$$q_c^2 = \frac{k_B T f_0}{\kappa a^3 \phi_S^2}. \quad (5.61)$$

The reduced time, τ , and reduced structure function, \bar{S} , are given by

$$\tau = 2M\kappa q_c^4 \quad (5.62)$$

and

$$\bar{S}(\bar{q}, \tau) = \frac{f_0}{a^3 \phi_S^2} S(q, t). \quad (5.63)$$

Thus, equation (5.46) is rewritten in the very simple form

$$\frac{\partial \bar{S}(\bar{q}, \tau)}{\partial \tau} = -\bar{q}^2(\bar{q}^2 - \mu)\bar{S} + \bar{q}^2. \quad (5.64)$$

In Eq. (5.64), a^3 , the coarse graining volume has been scaled away and

$$\mu \equiv -\frac{1}{\langle y^2 \rangle} \left\langle y \frac{\partial \Phi(x_0 + y)}{\partial y} \right\rangle \quad (5.65)$$

with

$$y = \delta c / \phi_S, \quad x_0 = \phi_0 / \phi_S. \quad (5.66)$$

Figure (5.2) presents the scaled structure factor for a quench at critical composition and $f_0 = 5.8$. For decomposition occurring near the center of the spinodal region, the sequence of functions $\bar{S}(\bar{q})$ for increasing τ after quench exhibits a growing peak which moves toward lower \bar{q} and displays a crossover on the high- \bar{q} side.

Comparison of Monte Carlo simulation results with the LBM theory have shown reasonable agreement. However, the works of Billotet and Binder[131] and of Binder *et al.*[52] point out some of the difficulties associated with the use of

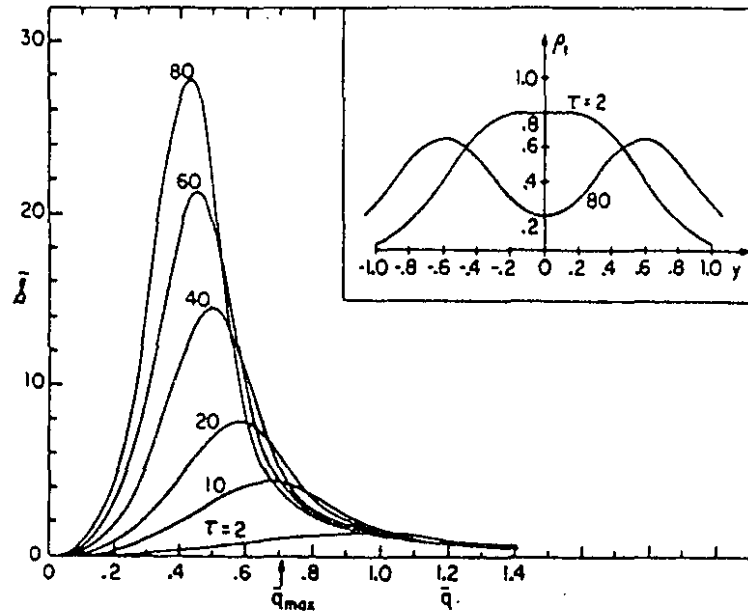


Figure 5.2: The scaled structure factor $\bar{S}(\bar{q}, \tau)$ for a quench at critical composition and $f_0 = 5.8$ at various scaled times τ . The inset depicts the distribution function $\rho(y)$ at two of these times. (From Langer *et al.*[7])

this theory. First, there is an unfortunate dependence of certain results on the (arbitrary) choice of the coarse graining cell size a . Namely, the results depend on the choice of the ratio a/ξ . Second, there is a spinodal curve implicit in the LBM theory, whose location is shifted from the classical curve and also depends on the choice of cell size. The third point, presented by Binder *et al.*[52] is that the LBM theory does not describe either the fluctuations due to nucleation and growth or the extended transition from spinodal decomposition to nucleation. This last point is based on the observation by these workers that the LBM theory exhibits metastable states with infinite lifetime in the region between the coexistence curve and the spinodal curve. Finally, Binder[51] has argued that the late time behavior of the LBM equation is inconsistent with the late stages $t^{1/3}$ growth law predicted by the Lifshitz-Slyozov-Wagner introduced in the next section.

5.5 Late stages

The equations of motion introduced for the early stages of SD break down when terms of higher order than those retained become important. This is the case during the late stages when domains of each phase coexist. In particular, Monte Carlo results[51] have shown that the LBM theory becomes inaccurate when domains reach sizes which are a few times the correlation length.

The studies reported in the experimental review (§ 3.3) established that the late stages present a scaling regime during which the microstructure remains self-similar for all times. A single time-dependent length scale then suffices to describe the time evolution of the structure factor. An appropriate choice for this length would be the average domain size, denoted⁶ as $R(t)$. The scaling assumption is that the wavevector q_m corresponding to the maximum of $S(q, t)$ is related to $R(t)$ by

$$q_m(t) = 2\pi R^{-1}(t) \quad (5.67)$$

and that the dimensionless $S(q/q_m(t), t)/R^3(t)$ should be time-invariant when plotted against $qR(t)$. Thus, a scaling function $F(q/q_m)$ can be introduced such that the scaling of the structure factors $S(q, t)$ can be written as

$$S(q, t) = \mathcal{C} q_m^{-3}(t) F\left(\frac{q}{q_m(t)}\right) \quad (5.68)$$

where \mathcal{C} is a dimensionless constant (independent of t) chosen such that $F(1) = 1$. For convenience, a dimensionless quantity $x(t)$ is introduced as

$$\begin{aligned} x(t) &\equiv \frac{q}{q_m(t)} \\ &= \frac{1}{2\pi} q R(t). \end{aligned} \quad (5.69)$$

If Equation (5.68) is valid the time dependent $R(t)$ and the scaling function $F(x)$ will suffice to describe $S(q, t)$ at any time during the late stages.

⁶ $R(t)$ should not be confused with the time-independent amplification factor in the CH equation of motion defined by Eq. (3.2).

Marro, Lebowitz and Kalos[132] and Furukawa[133] were the first to explicitly show that $S(q, t)$ in the late stages of SD in Monte Carlo studies obeys the scaling relationship given by Eq. (5.68).

The existence of a scaling function for the late stages implies that growth exponents can be obtained in that regime. Experimental determinations of the growth exponents were mentioned in § 3.3. Defining $S_m(t) \equiv S(q_m(t), t)$ as the maximum value of $S(q, t)$, the growth exponents will be denoted as n and n' and are defined by

$$R(t) \sim t^n \quad (5.70)$$

and

$$S_m(t) \sim t^{n'}. \quad (5.71)$$

When domains have reached the equilibrium composition, the question that can be asked is *what drives the system to further evolve and coarsen?* Indeed, late stages SD systems are still in a far-from-equilibrium state. However, in this regime, the only regions still out of equilibrium are the interfaces. Consequently, to predict the time evolution of $S(q, t)$ during the scaling regime, it is appropriate to focus on the motion of the interfaces which separate the domains, rather than on the domains themselves. The interface area density $\mathcal{A}(t)$ (Eq. 2.31) is high and therefore a large amount of surface free energy associated with these interfaces is present. As the domains of each phase grow, $\mathcal{A}(t)$ decreases and proportionally to it, the surface energy also decreases. As the coarsening proceeds (a process often called Ostwald ripening), small domains with large curvatures disappear, while large domains with small curvatures continue to grow. Thus, the essential physics must reside in the interfaces.

Studies of the late stages or scaling regime have primarily focused on the value of the growth exponent n , as well as on the scale invariant functions like $F(x)$. The value of n is of importance, because it is the signature of the thermodynamic forces which are responsible for the phase transition. For systems with a non-conserved order parameter (described by model A, *cf.* p. 10) the study of random interface

dynamics has provided strong predictions, notably a growth law (the Allen-Cahn law[134]) as well as a scaled form $F(x)$ [135]. However, for unmixing binary alloys (described by model B), to date, neither a growth law nor a scaling form has been derived directly from interface dynamics although n is believed to be $1/3$. The remainder of this section will address first the value of the growth exponent and then the scaling form $F(x)$.

5.5.1 Growth law

Attempts to obtain a theoretical value for the growth exponent n have been made through physical arguments and numerical simulations. The main physical arguments are examined and a survey of the principal numerical results then follows.

The basic assumptions commonly used are that in the late stages of phase separation (except in the critical region) domains are separated by well defined interfaces whose mean radius of curvature is sufficiently greater than the thickness of the interface ($\sim \xi$), but $\mathcal{A}(t)$ remains finite ($\neq 0$).[45] Further the interface is assumed to be smooth, *i.e.* finite curvatures are defined almost everywhere. Singularities such as corner, edge, contact and fractal surface, etc. are smoothed by the surface tension and are negligible.

The dynamics of the interfaces are sensitive to the presence or the absence of conservation laws. The order parameter which describes a spinodal system (model B) obeys a local conservation law.[136] This parameter is usually the local concentration of one of the components of the system, and therefore obeys a continuity equation. The decomposition will thus be limited by diffusion. As a result, changes in the system require diffusion of material across increasingly large distances and the late stages coarsening proceeds increasingly slowly (Eq. 5.70). This behavior contrasts with the rapid approach to completion which occurs in magnetic or structural phase transformations (model A). These systems possess no local conservation law and thus no long range material transport is required.

To develop an intuitive picture of the growth in a conserved order parameter system (model B) it is somewhat easier to start with a system with a nonconserved order parameter (model A). Since the reduction of surface energy drives the process, the interfacial motion acts to reduce the local surface area: curved interfaces move, and when part of an interface becomes flat, it stops moving. The interface velocity v , in the most simple case for model A, is a function of only the local curvature K .⁷ At late times the interfaces become gently curved, so K is small. A Taylor expansion then gives:

$$v(K) = DK + \dots, \quad (5.72)$$

with D a positive constant with units of $[m^2/s]$. Any time-dependent length made with D , the only parameter in the equation of motion, must obey, $R(t) = (Dt)^{1/2}$. Thus, $n = 1/2$ for the nonconserved system. Eq. (5.72) is the Allen-Cahn law[134] and has been verified through both experimental and theoretical studies.[137,138] The growth exponent n is independent of temperature. All of the temperature dependance is contained in the coefficient D . [139]

In the case of a system with a conserved order parameter, some of these considerations still apply. The velocity of the interfaces is such that, on average, the curvature is reduced, since the motion of the interfaces is driven by the minimization of surface free energy. However, when the order parameter is conserved, the interfacial motion is coupled to the motion of material "under" the interface. For an interface to flatten, material within curved regions must diffuse away. Thus, although $v = DK$ may still apply, the diffusion constant itself must now become, for example, a function of curvature. In their most general form, the interface equations of motion for a conserved order parameter system can involve the coupled nonlocal motion of many widely separated domains, and are quite intractable. There are two important situations, however, where simplifications occur: long-range and short-range diffusion.

The case of long-range diffusion during nucleation and growth is the subject of

⁷In fact, $K = K_1 + K_2$ where K_1 and K_2 are the principal curvatures of the interface.[134]

the theory of Lifshitz and Slyozov[140] and, independently, of Wagner[141] (LSW). The LSW theory assumes a system close to equilibrium, *i.e.* it deals with the case of small initial supersaturation in the asymptotic time regime ($t \rightarrow \infty$). The droplets are far apart as compared with their average size. The physical picture is one of widely spaced domains of one phase coarsening in the mean field limit near the coexistence curve. Each domain is solely characterized by its radius $R(t)$. Interactions between droplets can thus be ignored. A given droplet then grows by diffusion from the surrounding solution.

During the first stage of NG when nuclei of second phase form (*cf.* p. 39) there is a surface energy cost to the creation of bulk volumes of second phase. Thus there is a trade-off between the lowering of the free energy resulting from the creation of volumes of second phase and the rise in energy due to interfaces. At any time, second phase droplets smaller than a certain critical size, $\bar{R}_c(t)$ will “dissolve” as the energy balance between the surface and the bulk is unfavorable for their existence and droplets larger than $R_c(t)$ will grow. If Δ is the degree of supersaturation of the alloy and α is a parameter proportional to the surface tension between the two phases, then the LSW theory predicts that the time dependence of the mean droplet size is obtained by solving

$$\frac{dR}{dt} = \frac{D}{R} \left(\Delta(t) - \frac{\alpha}{R} \right). \quad (5.73)$$

Hence, $R_c(t) = \alpha/\Delta(t)$ and droplets with radius $R > R(t)$ grow while those for which $R < R_c$ disappear. Eq. (5.73) predicts for asymptotic times a power law growth with exponent $n = 1/3$ for large R .

The LSW theory also predicts the time-evolution of the composition distribution *i.e.* the time variation of $R_c(t)$ and the second phase particle size distribution by a system of two coupled nonlinear differential equations.[142] Thus a scaled form for the domain size distribution is also predicted. Essentially, these equations express that $R_c(t)$ increases with time and that large domains with a narrow distribution of sizes are obtained. Thus LSW provide a nonlinear equation of motion that can describe late stages behavior during a first order phase transition. The growth expo-

ment value and the domain size distribution function predicted by the LSW theory are universal and independent of the material parameters.

A number of numerical studies have confirmed the qualitative features of LSW theory.[143,144] Some of the experimental studies cited in § 3.3 have reported a growth exponent $n = 1/3$ in agreement with the LSW value. This was the case for instance in the study of the relaxation in the one phase region above a critical point in a binary fluid by Wong *et al.*[105]

When the simplifying assumptions that enter in the LSW theory are relaxed, for instance to describe systems conditioned into regions of the phase diagram away from the coexistence line, where volume fractions of each end-phase might be comparable, correlations between domains become important and significantly alter the shape of the composition distribution function.[145-148] However, early numerical tests of these correlations carried out by Beenakker[149] and Voorhees and Glicksman[150,151] all resulted in a growth law with $n = \frac{1}{3}$ in accord with the LSW value. These studies involve expansions with $(V_v^\alpha)^{1/2}$ as the small parameter and thus should work only for bulk compositions still not too distant from the coexistence line. The effects of correlations between domains were first noticed by Weins and Cahn.[152]

The situation in the case of the late stages of SD is very different from the idealized low supersaturation with isolated and widely spaced domains dealt with by the LSW theory. Figure (5.3) shows a typical microstructure for late stages SD with comparable volume fractions of the two phases obtained by Monte Carlo simulations.[153] The microstructure consists of a network of highly connected and interpenetrating domains.

Although long range diffusion is still expected to be the dominant mechanism of phase separation for late times, it is likely that other kinetic mechanisms are important during the intermediate stages of growth. In particular, transient behavior involving short range diffusion of material along interfaces is expected.

Before proposing a scenario for the effect of interconnected domains on inter-

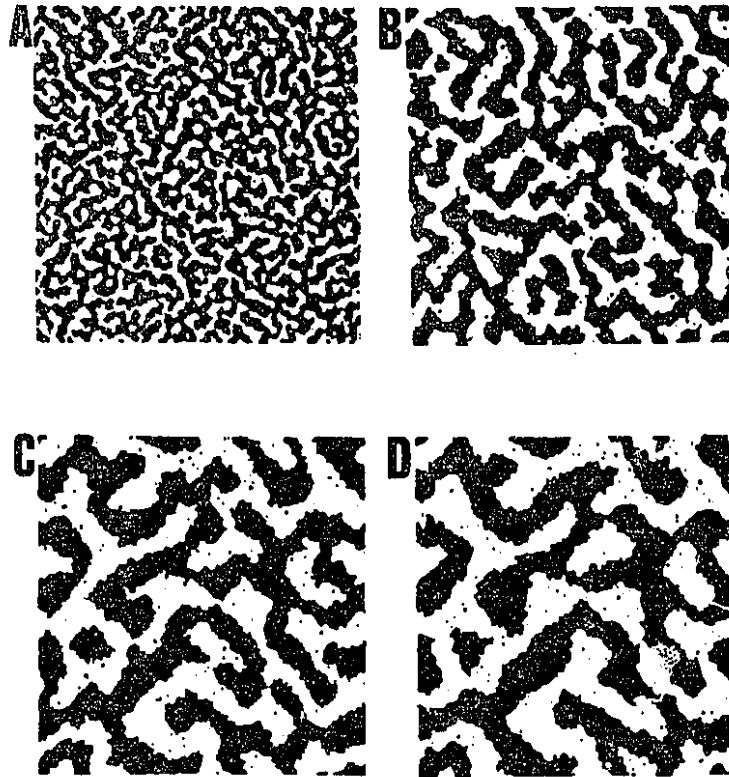


Figure 5.3: Late stage coarsening configurations from a MC study at times 1000, 20 000, 100 000 and 160 000 Monte Carlo time steps for spinodal decomposition. (From Roland and Grant[153].)

face velocity, short range interfacial diffusion is considered for systems with a conserved order parameter. Indeed, it is expected that surface reduction by smoothing of the interfaces should be important in a transient regime during which interfaces have high curvatures. It is assumed that the domain pattern can be characterized by a single length scale $R(t)$ as in the case of LSW long-range diffusion and that at asymptotic times, equilibrium is locally satisfied on length scales small compared to $R(t)$. This means that the interfaces between domains of the two phases have local radii of curvature of order $R(t)$ or greater.

For an element of curved interface to be in local equilibrium requires that the pressure due to surface tension, of order $\sigma/R(t)$, cancel that due to the local gradient in chemical potential, of order $c_0(\mu_\alpha - \mu_{\alpha'})$ with μ_α and $\mu_{\alpha'}$ the chemical potential in the two equilibrium compositions. Thus the chemical potential of the interface, μ_{int} is of order $\sigma/c_0R(t)$ and its variations from place to place are of the same order.

The gradients of the chemical potential of the interface are associated with gradients of curvature, K . The curvature is reduced by the flux of atoms on the interface, which will be of order

$$\mathcal{J} \sim -\nabla_s \mu_{\text{int}} \sim -\nabla_s K, \quad (5.74)$$

where the gradient is taken with respect to the arc length of the surface. The surface divergence of $-\mathcal{J}$ yields the increase in the number of particles per unit area per unit time. Therefore the velocity of a surface element along its normal due to surface diffusion is [153]

$$\frac{dR(t)}{dt} = D_s \nabla_s^2 K, \quad (5.75)$$

where D_s is a constant [m^3/s] independent of the local curvature but which depends on $f''(c)|_{c_0}$. Equation (5.75) predicts a growth exponent $n = 1/4$.

Long range inter-domain diffusion and short range diffusion along interfaces occur simultaneously during stages when interfaces have high curvatures. However, the smoothing of interfaces by interfacial diffusion does not contribute to domain growth. Rather, it is the long range thermally driven diffusion of atoms through the bulk (domains) that leads to the increase of $R(t)$. Interfacial diffusion contributes to the redistribution of long range inter-domain diffusing atoms that reach interfaces and thus limits the effectiveness of long range diffusion to increase $R(t)$. Indeed, these atoms ultimately have to be transported at the minimal curvature points on the interfaces (or leave the interface and diffuse to another point through the bulk solute). In general, the thermodynamic driving force for interfacial diffusion is much greater than thermal diffusion in the bulk. However, the interface area density $\mathcal{A} \sim 1/R(t)$, and thus in the time regime when local rearrangements are important, the growth rate may be limited by the relocation of solutes along the interfaces. The net result is a slower coarsening at the earlier stages of coarsening. At later times, when interfaces are gently curved, long range diffusing atoms achieve a better accretion success. They adhere to locations with less need for further transport along interfaces and the growth then no longer depends on interfacial diffusion. Thus, with this heuristic description, the growth exponent would be expected to progress from

1/4 (*cf.* Eq. 5.75) in a regime when interfacial diffusion is important to relocate new atoms on the interfaces to 1/3 in a regime when interfaces have smoothed out and inter-domain diffusion becomes the main contributor to interface motion.

To express the coarsening at times when the interfacial diffusion is important, Huse[154] introduces an effective growth exponent, n_{eff} ,

$$n_{eff}(t) = \frac{d \ln R(t)}{d \ln(t)}. \quad (5.76)$$

Thus, assuming a growth law with an exponent $n = 1/3$ in the limit of large R , as for the LSW theory, the effective exponent n_{eff} should obey

$$n_{eff}(t) = \frac{1}{3} - \frac{R_0}{R(t)} + \mathcal{O}(R^{-2}(t)), \quad (5.77)$$

with R_0 a length that reflects the importance of interfacial diffusion. If $R_0 > 0$, $n_{eff}(t)$ will asymptotically tend to 1/3 from below and coarsening will be slowed down by interfacial diffusion.

Physical arguments can also be given for inequalities which will bound the growth exponent n . One such argument has been given by Grant[155] in terms of the dynamical critical exponent z .

To understand his argument, the exponent z is first introduced, starting from the power law for the fall off to zero at T_c of the pair correlation function, $G(r)$, with distance r (*cf.* Table 1.1). Taking the Fourier transform of that relation gives

$$S(q) \sim q^{\eta-2}. \quad (5.78)$$

Thus in the limit of infinitesimal q and with the help of Eq. (2.22) which defines the differential susceptibility χ_s ,

$$\chi_s \propto \xi^{2-\eta} \quad (5.79)$$

with ξ diverging as given in Table (1.1). Comparison between the susceptibility sum rule (Eq. 2.23) and the thermodynamic driving force for diffusion (*cf.* p. 24) indicates that diffusion constants should vanish at the critical point proportionally to $\xi^{-2+\eta}$ (critical slowing down). However, the atomic mobilities remain finite at the

critical point. Therefore the dynamic scaling exponent z is introduced to express that the order parameter relaxation rate should go to zero as $\xi^{-z}(k\xi)^2$ with[13]

$$z = 4 - \eta. \quad (5.80)$$

This expression for the dynamical exponent z constitutes an exact result from critical dynamics for model B.

Grant's argument goes as follows. If one quenches close to T_c , time scales are affected by critical slowing down. Time scales must then be measured in units of the correlation time τ , and length scales in units of the correlation length ξ . Incorporating this into the growth law (Eq. 5.70) gives

$$R(t)/\xi \sim (t/\tau)^n. \quad (5.81)$$

The dynamical scaling assumption is[13] $\tau \sim \xi^z$ and thus[156]

$$R(t)/t^n \sim (T_c - T)^{\nu n(z - \frac{1}{n})}, \quad (5.82)$$

where ν is the correlation length exponent (*cf.* Table 1.1). Since the driving force for a first-order phase transition is due to thermodynamic forces, and not fluctuations, thermal fluctuations can only slow down domain growth, or leave it unaffected. Thus the inequality $z \geq 1/n$ must be satisfied. Using Eq. (5.80) this inequality becomes

$$n \geq 1/(4 - \eta). \quad (5.83)$$

Using $\eta \sim \frac{1}{18}$ for the Ising 3d model (*cf.* Table 1.1) condition (5.83) thus becomes that $n \gtrsim 0.25$.

An upper bound on the value of n has been given in a study by Yeung.[157] He considered the nonlinear Langevin equation for SD and found that a self-consistent requirement of being in the scaling regime for model B was that $n \leq 1/3$.

To complete this review of theoretical predictions for the growth exponent n , Monte Carlo (MC) studies on SD systems are examined. An interesting consequence of self-similarity (*i.e.* scaling) is that it is possible to address only length scales much

larger than that of the smallest topological details and thus small lengths can be ignored. Furthermore, rescaling of length and time lend themselves well to real space RG methods. In a recent MCRG study of late stages SD on the 2d Ising model, Roland and Grant[153] have obtained $n = 0.338 \pm 0.008$ and a strong transient time range involving an $n_{eff}(t) = \frac{1}{4}$. They observed that the transient was iterated away by the RG transformation, leaving $n = \frac{1}{3}$. This crossover from $t^{1/4}$ to $t^{1/3}$ scaling would be expected of short range diffusion effects as small topological details of the interfaces are iterated away.

Earlier MC studies have also confirmed a $n = 1/3$ growth law for late stages after some initial transients for systems quenched in a miscibility gap. This is the case, for instance, in the work of Lebowitz *et al.*[158] Huse also carried out a Monte Carlo simulations of SD and obtained values of $n_{eff}(t)$ between 0.12 and 0.25. From $n_{eff}(t)$ he extrapolates an asymptotic value (for $R^{-1}(t) \rightarrow 0$) of $n = 0.29 \pm 0.04$.

5.5.2 Scaling forms

To date there is no systematic derivation of an analytical form for the scaling function $F(x)$ for SD in conserved order parameter systems. Two semi-empirical forms are introduced in this section and compared to the data in § 6.3.

The only feature of $F(x)$ for which there is a heuristic theory in excellent agreement with experiment is the large x behavior. This is given by Porod's law, *cf.* Eq. (2.32) which predicts $F(x) \sim x^{-4}$ for large x , when interfaces exist.

The first scaling form is suggested by Fratzl and Lebowitz[159,160]. The starting point is the expression obtained by Debye *et al.*[161] for the correlation function for a random distribution of interfaces between two phases. Using the notation of Eq. (2.27) where V_v^α is the volume fraction of "minority" phase (the Al-rich phase in this work, for instance, though $V_v^\alpha \approx V_v^{\alpha'}$), then

$$S(r) = V_v^\alpha(1 - V_v^\alpha) \exp \left[-\frac{\mathcal{A}}{4V_v^\alpha(1 - V_v^\alpha)} \right] \quad (5.84)$$

where \mathcal{A} is the interface surface area per unit volume as defined in Eq. (2.31).

However, the long range diffusion fields required to satisfy composition conservation induce a modulation of $S(r)$ with a time-dependent wavelength related to the fastest growing mode[2], say λ_m ,

$$S(r) = V_v^\alpha(1 - V_v^\alpha) \exp \left[-\frac{\mathcal{A}}{4V_v^\alpha(1 - V_v^\alpha)} \right] \frac{\sin \frac{2\pi}{\lambda_m} r}{\frac{2\pi}{\lambda_m} r}. \quad (5.85)$$

This expression also ensures that the average composition within a volume of diameter λ_m will remain constant. The approximate scaling function $L_1(x)$ normalized so that $L_1(1) = 1$ is given by

$$L_1(x) = \frac{b_1}{b_1 + (x^2 - 1)^2}; \quad b_1 = \frac{4\gamma^2}{(1 - \gamma^2)^2}; \quad \gamma = \left[\frac{\mathcal{A}}{4V_v^\alpha(1 - V_v^\alpha)} \right] \left[\frac{\lambda_m}{2\pi} \right]. \quad (5.86)$$

Equation (5.86) is then tailored by an additional prefactor of $x^4/(x^4 + c)$ where c is a constant to suit the observed x^4 dependence of $S(x)$ ⁸ when $x \rightarrow 0$ obtained in MC simulations by Yeung[157] and others[162,163], yielding, after normalization,

$$F_{(\text{FL})}(x) = \frac{ax^4}{x^4 + c} \frac{b}{b + (x^2 - 1 + d)^2} \quad (5.87)$$

with

$$\begin{aligned} b &= \frac{4\gamma^2}{(1 - \gamma^2)^2} (1 - d)^2; \\ c &= \frac{d}{b - d(1 - d)}; \\ a &= (1 + c) \left(1 + \frac{d^2}{b}\right). \end{aligned} \quad (5.88)$$

Only two parameters need to be fit to with data, γ and d , both dimensionless. If the parameter d is set to zero in expressions (5.87) and (5.88), then expression (5.86) is recovered. According to Fratzl *et al.*[159] the parameter γ has a simple dependence on the relative fraction of the two phases in the system and seems to be independent of temperature. Figure (5.4) presents $F_{(\text{FL})}(x)$ calculated for $\gamma = 0.5$ and $d = 0.06$.

The second scaling form examined in this work is suggested by Ohta and Nozaki.[164] They apply a derivation that has proven successful for systems with

⁸See footnote on p. 117.

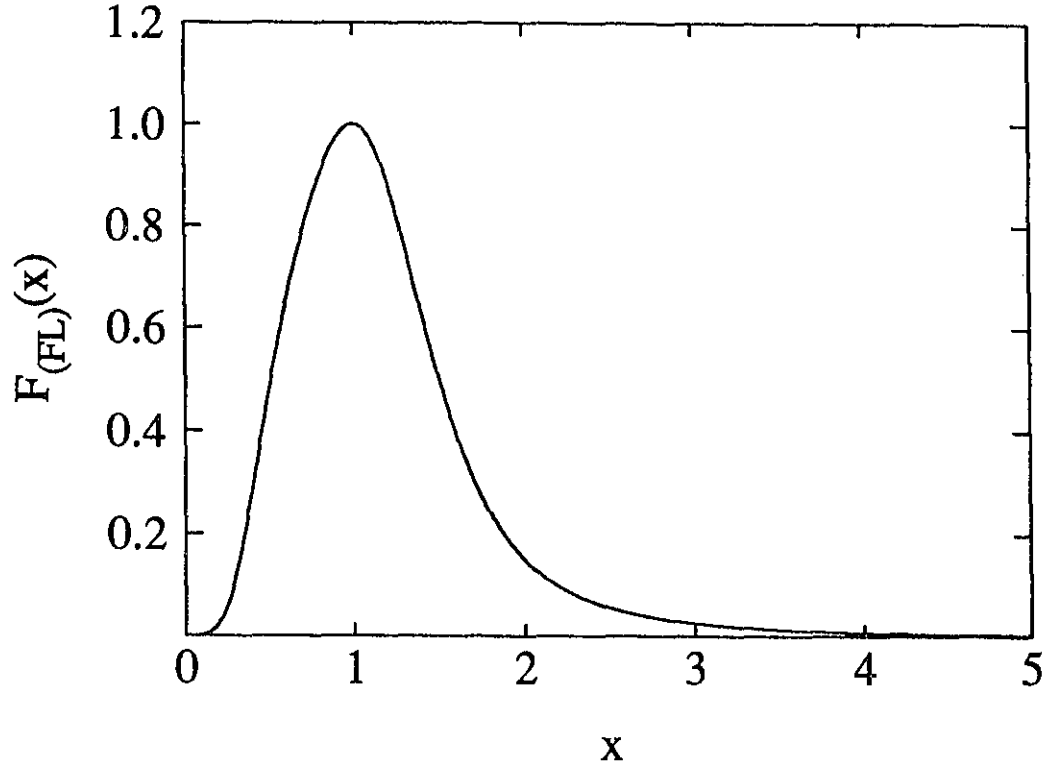


Figure 5.4: Scaling form $F_{(FL)}(z)$ calculated from Eqs. (5.87) and (5.88) based on the work of Fratzl and Lebowitz[159,160]. The parameter values were set to $\gamma = 0.5$ and $d = 0.06$.

a nonconserved order parameter (model A). However, that derivation has to be corrected to account for long-range diffusion fields in conserved order parameter systems. In terms of the Fourier component $\tilde{\delta c}(\mathbf{q}, t)$ of $\delta c(\mathbf{r}, t)$, following the notation of § 2.2, they propose the following equation of motion for the interfaces from arguments based on the motion of thin interfaces:

$$\frac{\partial}{\partial t} \tilde{\delta c}(\mathbf{q}, t) = q(-q^2 + \frac{1}{3}At^{-2/3})\tilde{\delta c}(\mathbf{q}, t). \quad (5.89)$$

The correlation function $\langle \delta c(\mathbf{r}, t)\delta c(\mathbf{o}, t) \rangle$ obtained from Eq. (5.89) is given by

$$\langle \delta c(\mathbf{r}, t)\delta c(\mathbf{o}, t) \rangle = \frac{1}{(2\pi)^3} \int d\mathbf{q} \exp(-q^2 t + Aqt^{1/3} + i\mathbf{q} \cdot \mathbf{r}) \quad (5.90)$$

where A is a constant. The position of the interfaces is given by $\delta c(\mathbf{r}, t) = 0$ as long as the length scale of the domains is sufficiently larger than the interface thickness and assuming saturated domains (*i.e.* at compositions given by either of the coexistence values).[135] Assuming Gaussianly correlated interface compositions $\{\delta c\}$ and using

a step function on the sign value of $\delta c(\mathbf{r}, t)$ in Eq. (5.90) the two-point real-space equal time correlation function, also denoted as $G(\mathbf{r}, t)$, can be rewritten as (cf. Eq. 5.16)[165]

$$S(\mathbf{r} - \mathbf{r}_0, t) = \left(\frac{2}{\pi}\right) \sin^{-1} \left[\frac{\langle \delta c(\mathbf{r}, t) \delta c(\mathbf{o}, t) \rangle}{\langle (\delta c)^2 \rangle} \right] \quad (5.91)$$

where $\langle (\delta c)^2 \rangle = \langle \delta c(\mathbf{o}) \delta c(\mathbf{o}) \rangle$. The structure factor is then obtained by the Fourier transform of Eq. (5.91). The structure factors are self-similar at all times and thus the scaling form is obtained from the computed $S(q, t)$ by inverting Eq. (5.68),

$$F_{(\text{ON})}(x) = C^{-1} R^{-3}(t) S(q, t) \quad (5.92)$$

where the length $R(t)$ is taken to be the first vanishing point of $G(\mathbf{r}, t)$. Alternately, $F_{(\text{ON})}(x)$ can also be computed from the ratio

$$F_{(\text{ON})}(x) = \frac{S(q, t)}{S_m(t)} \quad (5.93)$$

since $F(1) = 1$.

Figure (5.5a) shows the predicted scaling form using Eq. (5.92) within a multiplicative constant C^{-1} and with $A = 7.5$ (in Eq. 5.90), value suggested by Ohta and Nozaki[164] for a 3d system. A shoulder exists on the high- x tail of $F_{(\text{ON})}(x)$ as better evidenced in the logarithmic plot (Part b).

Part (c) of this figure shows the scaled correlation function $G(\mathbf{r}/R)$. In accord with the definition of $R(t)$, this plot shows that $G(1) = 0$. Finally, Part (d) introduces a plot of $x^4 F_{(\text{ON})}(x)$ versus x , known as a "Porod plot", where $F_{(\text{ON})}(x)$ was computed using Eq. (5.93). In accord with the normalization condition, $F(1) = 1$, this plots shows that $x^4 F(x)$ at $x = 1$ is unity. This representation is useful to verify the validity of sum rule (2.32) and will be used in the discussion of the late stages results (cf. § 6.3).

The shoulder displayed by $F_{(\text{ON})}(x)$ was not present in the Fratzl-Lebowitz scaling form (Fig. 5.4). However, in the derivation of $F_{(\text{ON})}(x)$, interface concentrations were assumed Gaussianly distributed. This assumption is only rigorously true in systems with a non-conserved order parameter (model A) and justification for this choice was not offered.

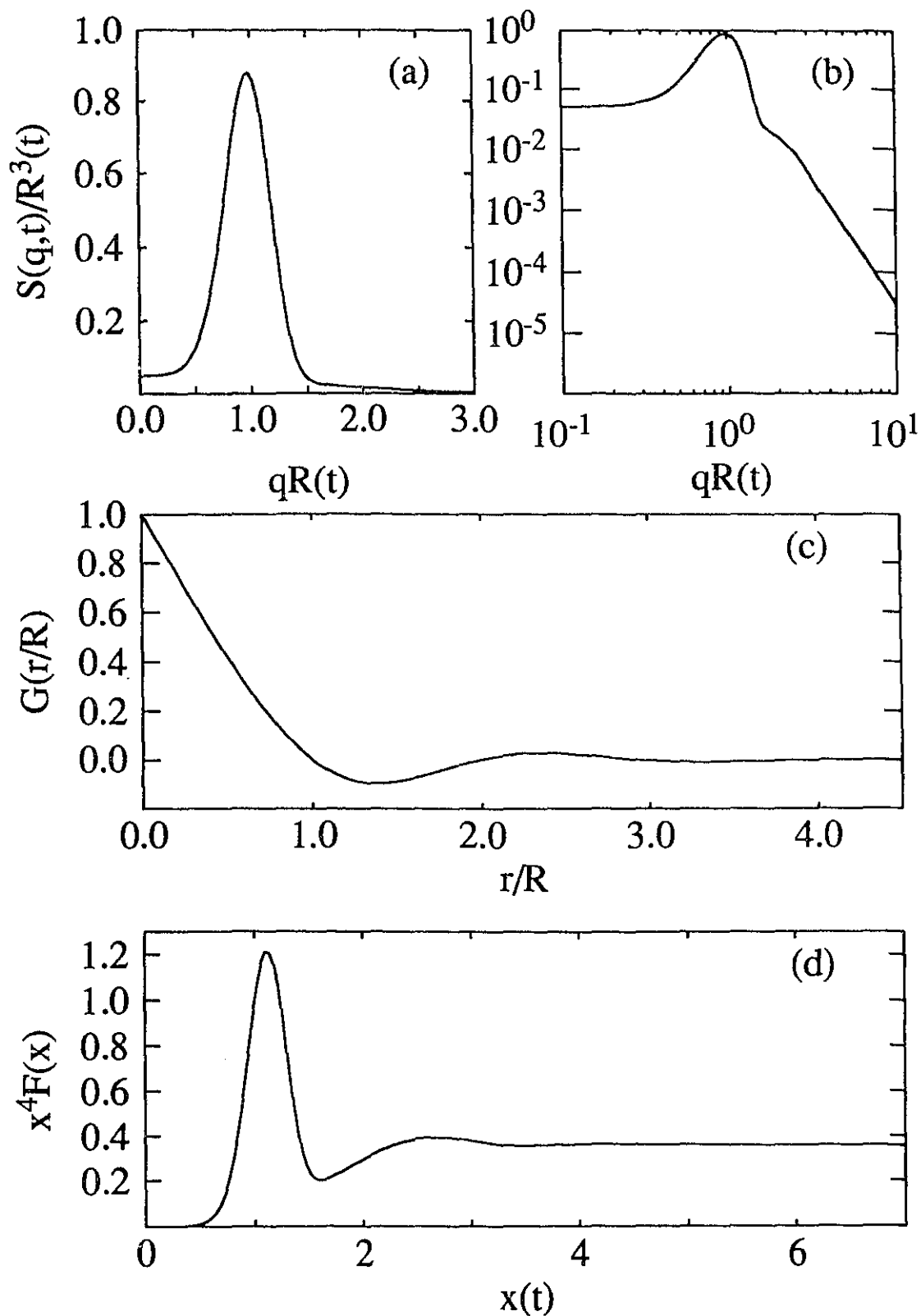


Figure 5.5: (a) Ohta-Nowaki scaling form obtained by taking the ratio of the Fourier transform of Eq. (5.91) and $R^3(t)$ (cf. Eq. 5.92). (b) Same plot on a logarithmic scale to emphasise the existence of a shoulder on the high $x = qR(t)$ tail. (c) Scaled correlation function $G(r/R)$. (d) Porod plot of $F_{(ON)}(x)$ computed using Eq. (5.93).

An artifact of $F_{(\text{ON})}(x)$ is that it does not vanish as $x \rightarrow 0$ but goes to about 7% of $F_{(\text{ON})}(1)$ instead. This suggests that $S(q=0, t)$ increases without bound in Eq. (5.68). This violates the susceptibility sum rule (Eq. 2.23) and would imply an increase in the number of atoms. Furthermore, as expected since $\lim_{x \rightarrow 0} F(x) \neq 0$, the logarithmic plot in Part (b) also indicates that the condition $\lim_{x \rightarrow 0} F_{(\text{ON})}(x) \sim x^4$ is not satisfied. However, the late stages structure factors measured in this dissertation are not sensitive to the very low x part of $F_{(\text{ON})}(x)$ and this feature should not affect fits to the Ohta-Nozaki scaling form.

Recent measurements on polymers by Bates *et al.*[90] have shown evidence of a shoulder at high- q . Thus, experimental evidence exists of the existence of an harmonic to the principal peak in a conserved order parameter system quenched in a miscibility gap as suggested by the $F_{(\text{ON})}(x)$ form.

Recently, Shinozaki and Oono[166] have studied the asymptotic $F(x)$ for SD in 3d at the critical composition by a (deterministic) cell-dynamical system. The form factor they obtain agrees well with with the Ohta-Nozaki form factor, away from small q . In particular, they obtain a significant second peak. Their results also satisfy Porod's law and the small- q exponent is consistent with $F(x) \sim x^\delta$ with $\delta \geq 4$. This result is in agreement with the MC results of Yeung.[157]

Chapter 6

Results and discussion

6.1 The data

Runs were performed both above and below T_c (597.15 K). Table (6.1) lists all the runs reported in this thesis. Runs labeled with a single letter (A through W) took 2 s (*cf.* § 4.4) and will serve for the early stage kinetics study (§ 6.2) while those labeled with two letters (AA through EE) took 60 s and will be used to study late-stage coarsening (§ 6.3).

For the data analysis, the last scattering pattern recorded before quenching the sample is subtracted from all structure factors measured during the isothermal aging. This subtraction removes any parasitic scattering and more importantly any constant grain boundary small angle scattering intrinsic to polycrystalline samples. The resulting structure factors are denoted as $\Delta S(q, t)$. The size of the background so removed is less than 25% of the scattering at a wavevector of $.01\text{\AA}^{-1}$ and falls off to 5% at $q = 0.03\text{\AA}^{-1}$. In addition to removing any constant temperature independent scattering, this subtraction also removes any equilibrium scattering contribution at T_a . In some cases, it will be necessary to correct for the absence of this temperature-dependent scattering in $\Delta S(q, t)$.

The time of recording of the first scan after temperature stabilization at the

Run	ET (s)	I	J	# bins	T (K)	Run	ET (s)	I	J	# bins	T (K)
Early stage study (2 s)						O	0.005	1	400	64	595.8
A	0.010	1	200	256	502.2	P	0.005	1	400	64	596.5
B	0.010	1	200	256	521.6	Q	0.010	1	200	256	596.8
C	0.010	1	200	256	541.4	R	0.005	2	200	64	596.9
D	0.010	1	200	256	551.1	S	0.005	2	200	64	599.1
E	0.010	1	200	256	558.7	T	0.005	2	200	64	599.5
F	0.010	1	200	256	572.8	U	0.005	2	200	64	605.0
G	0.010	1	200	256	587.1	V	0.005	2	200	64	606.5
H	0.005	1	400	64	589.1	W	0.010	1	200	256	611.8
I	0.005	1	400	64	592.3	Late stages study (60 s)					
J	0.005	1	400	64	592.5	AA	0.010	100	60	256	511.5
K	0.005	1	400	64	593.4	BB	0.010	100	60	256	536.9
L	0.005	1	400	64	593.4	CC	0.010	100	60	256	562.8
M	0.005	1	400	64	595.4	DD	0.010	100	60	256	577.9
N	0.005	1	400	64	595.7	EE	0.010	100	60	256	588.2

Table 6.1: List of runs reported in this work. All quenches are performed starting from the same annealing temperature, $T_a = 689.9$ K (*cf.* p. 92). T is the calibrated temperature (*cf.* § 4.4).

aging temperature, *i.e.* of the “quenched-in scattering pattern”, is chosen as ($t = 0$) for the early stage study runs. Thus, the $t=0$ scan shows the amount of structure that develops during the quench. Three such patterns are shown in Fig. (6.1).

The $\Delta S(q, t = 0)$ are modeled by a Lorentzian with maximum I_0 centered about $q_0 \neq 0$ and full width at half maximum (FWHM) Γ ,

$$\Delta S(q, t = 0) = \frac{I_0}{(q - q_0)^2 + (\Gamma/2)^2}. \quad (6.1)$$

The value of I_0 gives an indication of the amount of decomposition that has proceeded during the quench. The solid lines on Fig. (6.1) show the result for best fits to this model (the fits were performed over the range $[0.020, 0.086]$ \AA^{-1}). The best fit values of the parameters I_0 , Γ and q_0 for all 2 s runs are reported on Fig. (6.2). As

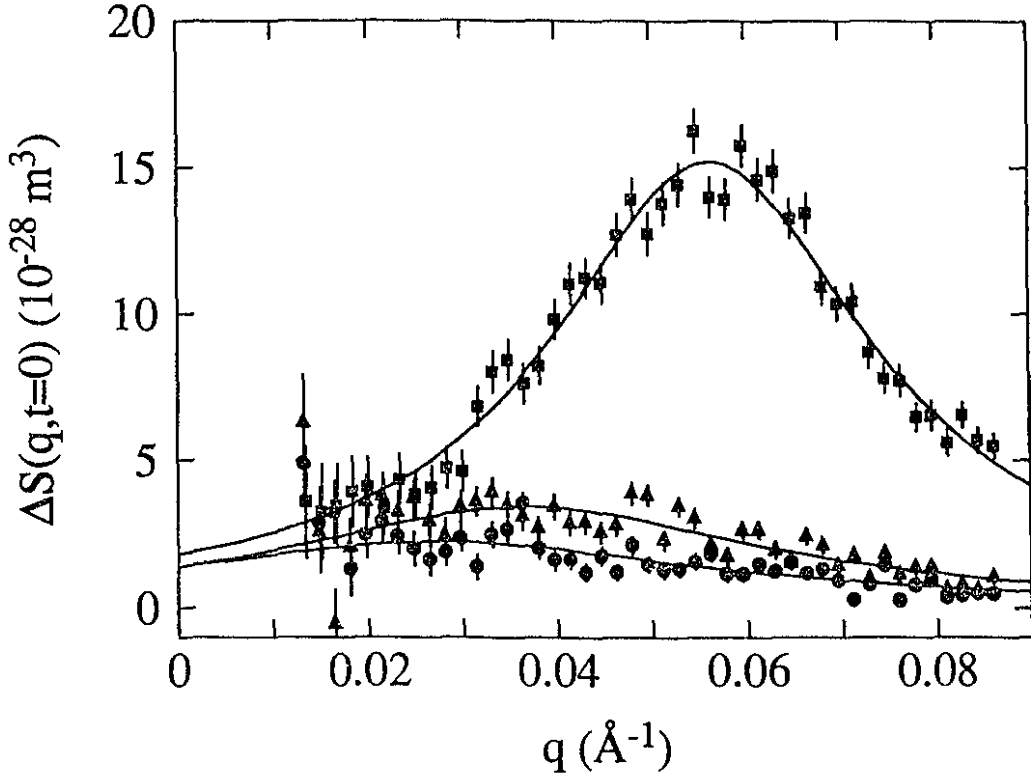


Figure 6.1: Quenched-in scattering $\Delta S(q, t = 0)$ for three runs : (●) above T_c at 605 K (run U), (▲) immediately below T_c at 597 K (run R) and (■) for a deeper quench, at 541 K (run C). The solid lines show in each case the model Lorentzian (Eq. 6.1).

the quench temperature is decreased, the scattering maximum, I_0 , is larger. Thus, for deeper quenches, the quenched-in $\Delta S(q, t = 0)$ increases. Also, with deeper quenches, q_0 is larger, reflecting the larger critical wavevectors associated with being farther from T_c . The FWHM, Γ , appears to be less sensitive to the quench temperature than the other two parameters.

Figure (6.3a) shows “time slices” of the evolution of $\Delta S(q, t)$ during run C, *i.e.* for a quench from 690 to 541 K. The points show the measured structure factors at various times after the sample began to phase separate. The solid lines are fits to the LBM theory discussed in § 6.2.3. Part (b) of Fig. (6.7) displays “ q -slices” rather than “time-slices” of $\Delta S(q, t)$. They are the time evolution of the structure factor at fixed values of the wavevector q . The bold line shows the recorded temperature.

For all runs, both above and below T_c it was found that the high q wavevectors relaxed faster than the low q wavevectors. As evidenced in Fig. (6.3b), the relaxation

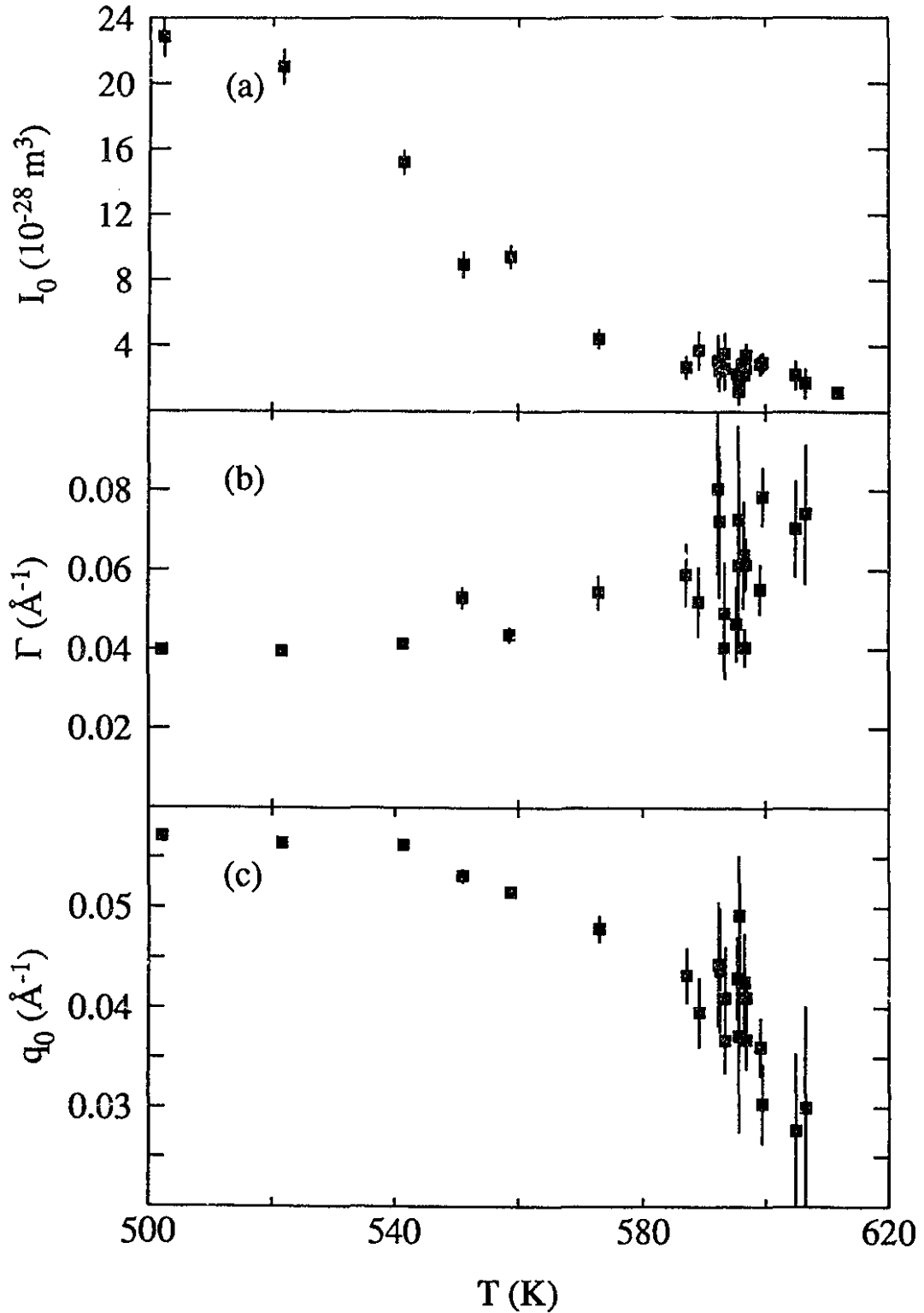


Figure 6.2: Parametrisation of quenched-in scattering $\Delta S(q, t = 0)$ for all runs using Eq. (6.1): (a) I_0 , (b) Γ , and (c) q_0 for all temperatures.

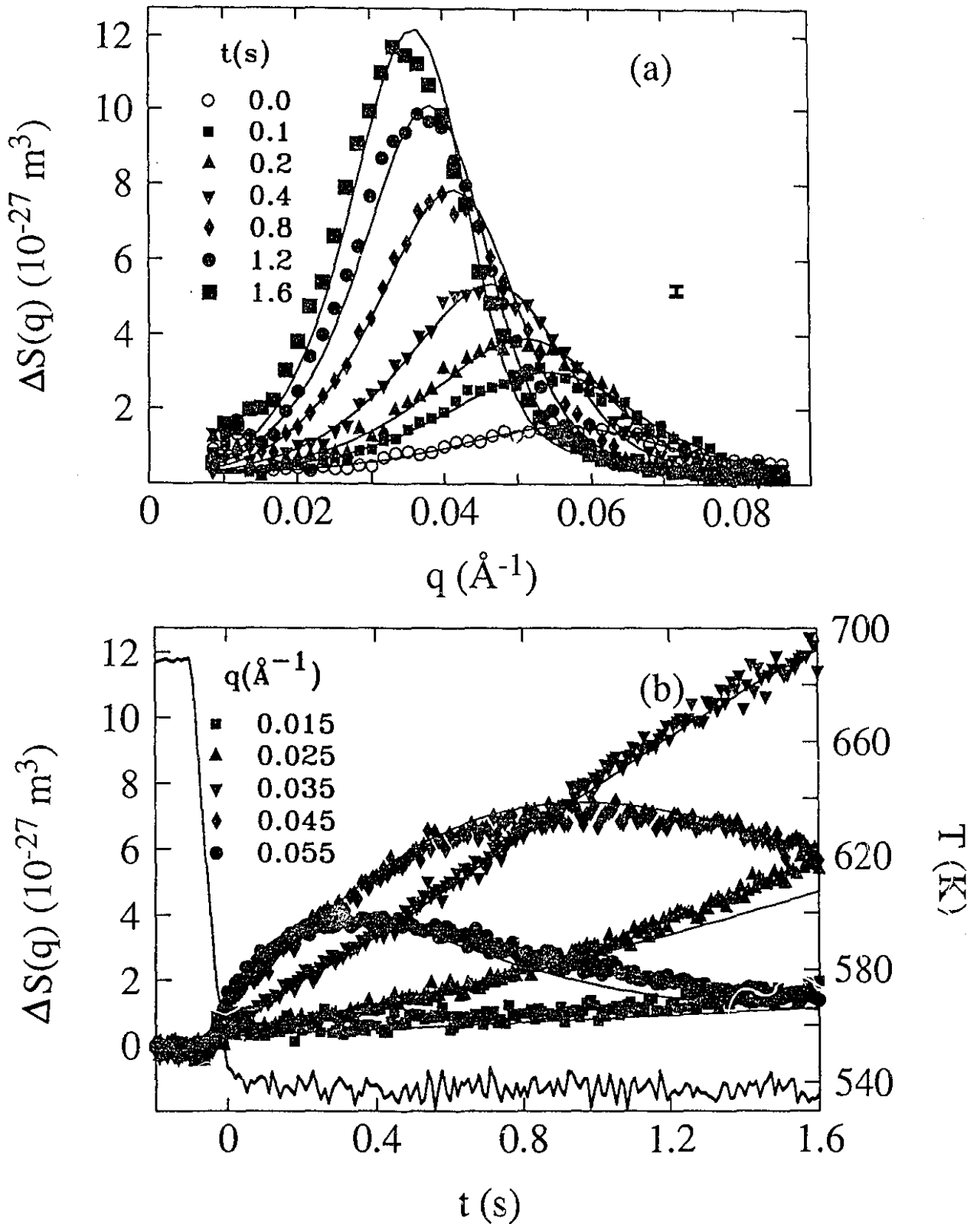


Figure 6.3: (a) Structure factors $\Delta S(q, t)$ during the early stage of spinodal decomposition at 541 K (run C) at selected times after a quench from 690 K. Solid lines show best fit to the LBM theory to the full 1.6 s (cf. § 6.2.3). A representative error bar is displayed to the right. (b) $\Delta S(q, t)$ for several fixed q . The bold solid line shows the temperature during the quench and during aging.

does not occur monotonically; the scattering intensities at the two higher values of q displayed (0.045 and 0.055 \AA^{-1}) first increase, reach a maximum, and then decrease. Thus, the evolution of $\Delta S(q, t)$ is nonlinear in time and hence does not display exponential growth. The time evolution of the $\Delta S(q, t)$ displays the well documented feature[2] of cross-over on the high q side. However, as a consequence of the non monotonic behavior, this crossover moves to lower q values as the decomposition proceeds. The $\Delta S(q, t)$ also sharpen as the maximum moves towards lower q .

The relaxation of composition fluctuations in the region above the top of the coherent miscibility gap after quenches from T_a to $T_q > T_c$ has also been measured. Fig. (6.4a) displays the structure factors $\Delta S(q, t)$ at selected times during the reequilibration of fluctuations at 599 K after a quench from 690 K (run S). Solid lines show the best fit to the LBM theory and will be discussed in § 6.2.3. Part (b) displays the same non-monotonic behaviour seen for quenches into the unstable region of the phase diagram, below T_c .

Figure (6.4) is representative of all the runs above T_c (S — W). As in Fig. (6.3) for run C in which $T < T_c$, in run S the wavevectors of higher q relax faster than those of lower q . Furthermore, a crossover of the tails is also observed. The non-monotonic increase of $\Delta S(q, t)$ for 0.025 and 0.035 \AA^{-1} also implies that the growth is nonlinear. These last two features are somewhat unexpected for a quench above T_c . *A priori* a linear, consequently monotonic, growth of $\Delta S(q, t)$ at all q would be expected since the amplitude of equilibrium fluctuations increases as the temperature is decreased in the one phase region, with the ensuing increase in scattering intensity over the wavevector range measured.

The measured nonlinear behavior in the runs above T_c can be attributed to two causes. So far it has been assumed that the calibrated temperatures were exact within the estimated standard deviation of 0.5 K during a run. However, some temperature smearing probably occurs in all runs due to an uneven temperature across the width of the sample with parts near the edges cooler than those near the center. The edges may even be at temperatures below T_c for the runs assumed to

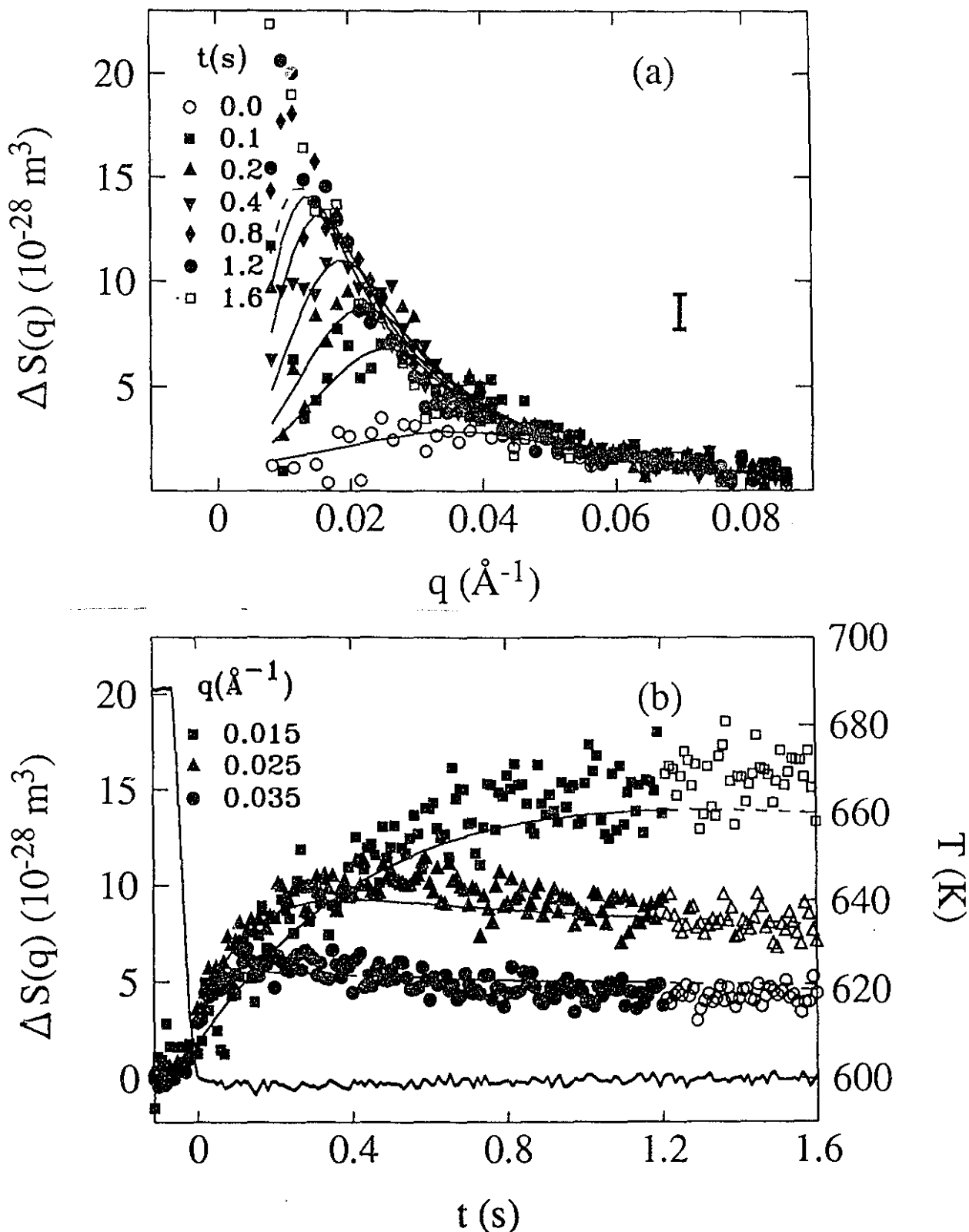


Figure 6.4: (a) Structure factors $\Delta S(q, t)$ during re-equilibration at 599 K (run S) at selected times after a quench from 690 K. Solid lines show best fit to the LBM theory to the full 1.6 s (cf. § 6.2.3). A representative error bar is displayed to the right. (b) $\Delta S(q, t)$ for several fixed q . The bold solid line shows the temperature during the quench and during aging.

lie immediately above T_c . This smearing is estimated to be of the order of a few degrees.¹

The nonlinear behavior is observed even during the run with the highest temperature, at 612 K (run W). Thus temperature smearing could not account for all of the nonlinearity. It is not unreasonable to expect nonlinear coupling between the modes even if the quench is not crossing a transition temperature. A simple heuristic argument can illustrate this point. During the course of the reequilibration of fluctuations, the short wavelength fluctuations (higher q modes) are in a local composition environment that depends on the longer wavelength fluctuations (lower q modes). The high q modes relax the fastest. However, as the slower long wavelength fluctuations reequilibrate the local composition distribution changes and the short wavelength fluctuations have to find a new equilibrium value. The observation of nonlinear growth in the one phase region means that it does not constitute a sufficient test to determine that a system is decomposing into two phases. It is therefore necessary to measure the time evolution of the reequilibration of fluctuations in the one phase region or of SD and to subsequently determine the sign of f'' by fitting an equation of motion for $\Delta S(q, t)$ in order to distinguish between the two.

Above T_c , the nonlinear "up-and-down" behavior is more important nearer to T_c but occurs at a faster rate the higher (above T_c) the temperature. It should be noted that the ordinate scale on Fig. (6.4) is an order of magnitude less than that of the $\Delta S(q, t)$ shown for a quench in the unstable region in Fig. (6.3).

¹This figure is based on an estimate by S. Brauer[167] of the parabolic temperature profile across the width of Fe_3B and Co_2B ribbons. For these samples with a width/thickness aspect ratio of $1.5\text{mm}/25\mu\text{m}$ held isothermally at about 673 K, he estimates the temperature difference between the center and the edges to be $\sim 35 \pm 10$ K. However, in the work of this thesis, the temperatures are between ~ 100 to 200 K lower and the $\text{Al}_{0.62}\text{Zn}_{0.38}$ sample, though of roughly the same width is only about $18 \mu\text{m}$ thick (cf. p. 86). Thus, the temperature difference between the center and the edges of the ribbon is not expected to be as large. As in this work, the Fe_3B and Co_2B ribbons were surrounded by ~ 1 atm. of He so that convection was responsible for heat dissipation and heating was provided by passing a current through the sample.

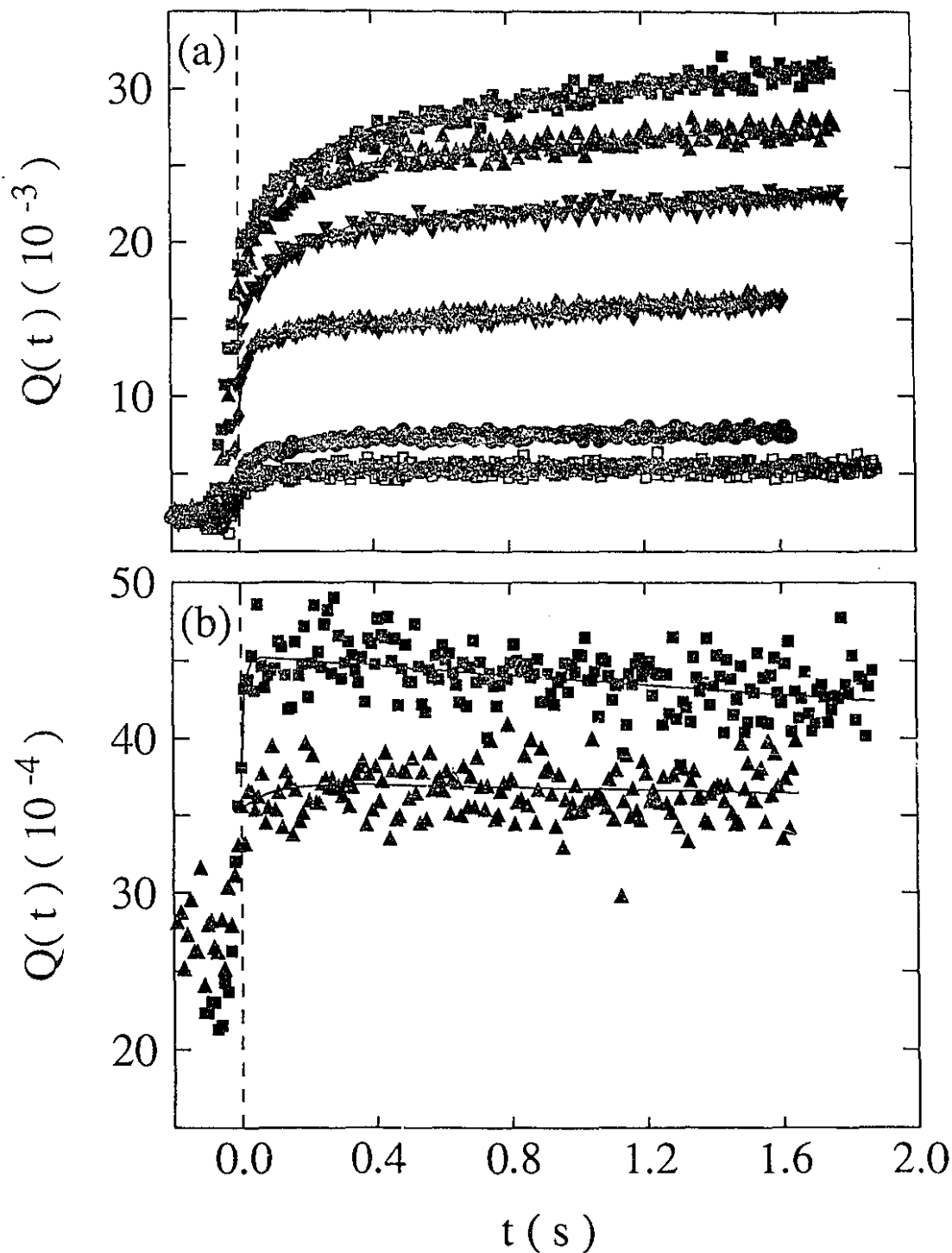


Figure 6.5: Integrated intensities $Q(t)$ for selected runs (a) below T_c : ■ : A (502.2 K); ▲ : B (521.6 K); ▼ : C (541.4 K); ◆ : E (558.7 K); ● : G (587.1 K); □ : J (592.5 K) and (b) above T_c : ■ : S (599.1 K); ▲ : W (611.8 K). The time $t = 0$ is the time of the first scan after the aging temperature has been reached (corresponding to the quenched-in $\Delta S(q, t = 0)$). The solid lines are obtained from fits to Eq. (6.2) (see text).

To close this survey of the data, the time evolution of the integrated intensities $Q(t)$ is described. From sum rule (2.25) $Q(t)$ is expected to go asymptotically to $\langle c - c_0 \rangle^2$. As in the expression for the sum rule, the integration over the measured q -range (0.01 to 0.085 \AA^{-1}) is performed on the structure factors $S(q, t)$ with no high temperature scattering subtraction. Above T_c , the time-dependent $Q(t)$ should reflect the reequilibration of the composition fluctuations. Below T_c , the main part of $Q(t)$ should result from the formation of regions of the phases α and α' . The contribution to $Q(t)$ by equilibrium fluctuations within each region and at interfaces should be small and should be decreasing as $Q(t)$ increases with time during the decomposition.

Figure (6.5) shows $Q(t)$ for selected runs both below and above T_c . Rather than the expected asymptotic increase to a fixed value for runs below T_c , $Q(t)$ is found to increase monotonically with time with no apparent saturation in all runs, as shown in Part (a) for selected runs. Indeed, after a rapid exponential increase, $Q(t)$ is seen to go asymptotically to a line of small positive slope. Similarly, for all runs above T_c , after a rapid exponential increase, $Q(t)$ follows a linear relationship with time, however, with a small negative slope as exemplified for selected runs in Part (b).

The fact that $Q(t)$ asymptotically approaches a linear time dependence rather than a fixed constant could be interpreted as a process with two time constants: a fast and a slow time constant. The integrated intensities $Q(t)$ were modelled by²

$$Q(t) = C + (A + Bt)(1 - \exp(-t/t_0)). \quad (6.2)$$

With this model, the fast time constant is t_0 and the slow one would be to first order A/B . The amount of quenched-in structure can be estimated from the value of C while the coherent solubility limit can be estimated by $C + A$. Figure (6.6) shows the obtained time constants and values of C for all runs A — Z. A plot of $C + A$ will be given in § 6.2.4 (Fig. 6.14). The unexpected decrease in $Q(t)$ after 0.2 s for

²The constant A in Eq. (6.2) should not be confused with the interface area density defined in Eq. (2.31).

$T > T_c$ may be due to scattering moving behind the beamstop.

The time constants t_0 and \mathcal{A}/\mathcal{B} are independent of the intensity normalization described in § 4.3. However, the value of $\mathcal{A} + \mathcal{C}$ depends directly on this normalization and the sum rule instructs that if the overall normalization procedure to obtain absolute structure factors is correct, then $(\mathcal{A} + \mathcal{C})^{\frac{1}{2}}$ should fall on the coherent solvus well below T_c . This is in fact the case, as will be shown in the plot (6.14) (*cf.* § 6.2.4).

6.2 Fit to early stage theories

6.2.1 An attempt at the CHC linear equation

As a first analysis of the time-evolution of the early stages data, the measured structure factors are compared to the evolution predicted by the CHC linear equation introduced in § 3.2 (Eq. 3.6). The CHC equation predicts the structure factor at any time from a boundary value, at $t = 0$, for example. For an infinitely fast quench (a “square quench”), the initial structure factor would be the quenched-in equilibrium scattering at the anneal temperature, $S_{OZ}(q)|_{T_a}$ (*cf.* Eq. 2.19). The CHC equation predicts that below T_c modes with $q < q'_c$ will grow and those with $q > q'_c$ will decay, where q'_c is the wavevector of crossover as shown on Fig (3.4). Furthermore, modes for which the amplification factor $R(q)$ (*cf.* Eq. 3.2) is positive will grow exponentially without bound. These are the modes with wavevectors $q < q_c$ ($< q'_c$) (the critical wavevector q_c corresponds to the reciprocal of the mean field correlation length, *cf.* Eq. 3.4). On the other hand, modes with $q > q_c$ asymptotically evolve to the equilibrium structure factor at the aging temperature, $S_{OZ}(q)|_{T_f}$.

Since no quench can be infinitely fast, starting with a quenched-in structure, and observing its isothermal evolution should be a sufficient test of CHC in the time regime available in the experiments performed. To obtain values for the parameters f'' , κ and M at the aging temperature T_f it would appear sufficient, since the CHC

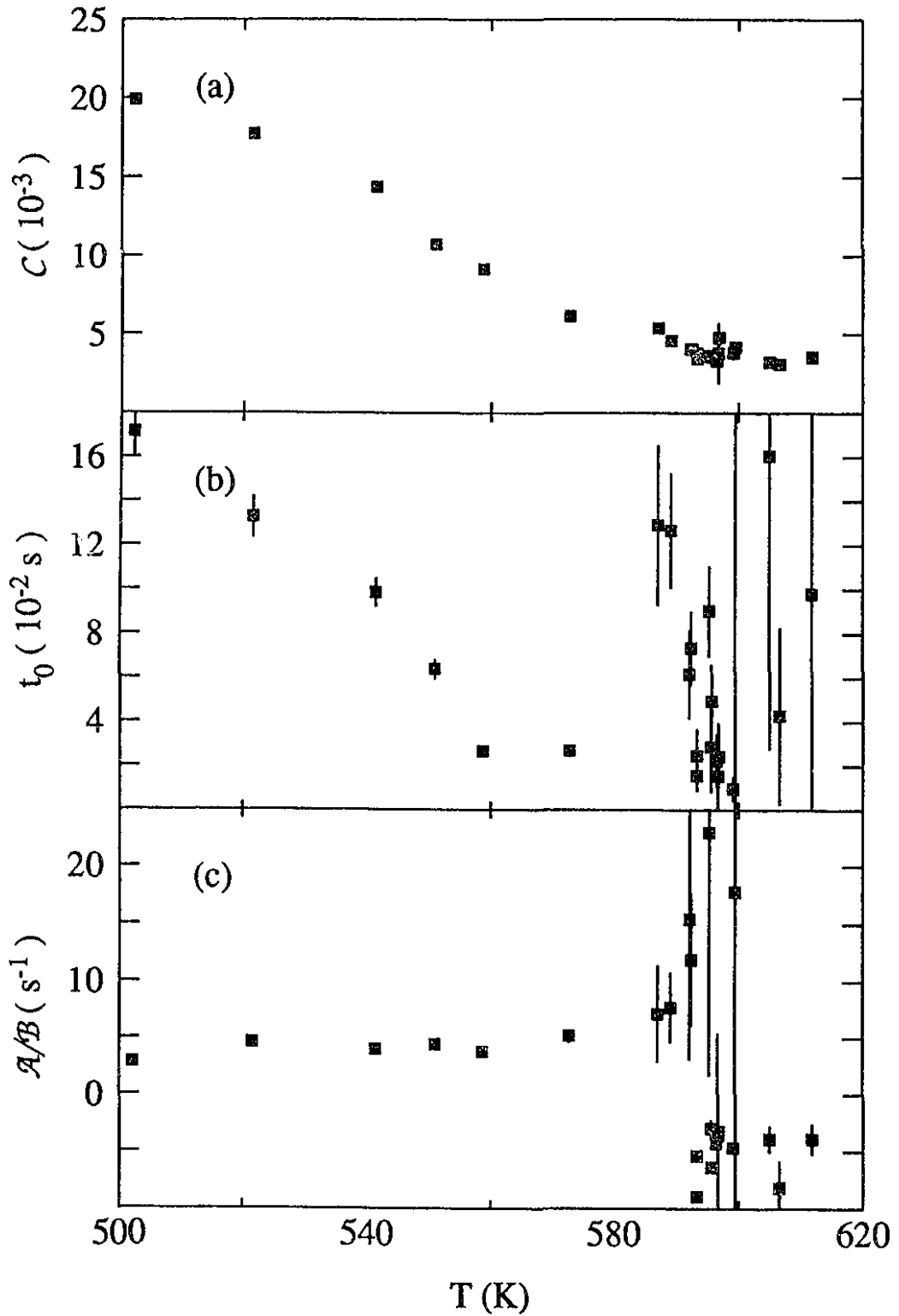


Figure 6.6: Results of fit of $Q(t)$ to Eq. (6.2) for all runs. (a) Estimate of quenched-in structure from C . Time constants for integrated intensities (b) t_0 and (c) A/B .

equation of motion is linear, to perform a fit to the measured structure factors in the range $q > q_c$ using

$$S(q, t') = S(q, t) + [S_{Oz}(q)|_{T_q} - S(q, t)] \times \{1 - \exp(2R(q)(t' - t))\} \quad (6.3)$$

with $t' > t$. This model equation has the advantage that no knowledge of the high temperature equilibrium structure factor $S_{Oz}(q)|_{T_*}$ is required.

In practice low q small angle scattering due to grain boundaries, has not been taken into account in Eq. (6.3). If this scattering is independent of time and temperature, then taking differences between the measured $S(q, t)$ at two times, cancels it out. This works for the $S(q, t')$ and $S(q, t)$ outside the brackets in Eq. (6.3) but it is not possible to cancel the constant low q small angle scattering which is part of $S(q, t)$ inside the brackets. Thus, instead of using the measured $S(q, t)$, the $\Delta S(q, t)$ introduced in § 6.1 which have the last scan before the quench subtracted should be used. However, as pointed on p. 140 all $\Delta S(q, t)$ then have the high temperature equilibrium scattering resulting from thermal fluctuations $S_{Oz}(q)|_{T_*}$ (Eq. 2.19) subtracted. This quantity should be added back since these fluctuations represent the initial state that subsequently evolves in time. Hence, to test the CHC equation, it is necessary to use an expression where knowledge of $S_{Oz}(q)|_{T_*}$ is required. For convenience, $S_{Oz}(q)|_{T_*}$ and $S_{Oz}(q)|_{T_q}$ are rewritten, using q_c^2 (cf. Eq. 3.3) as

$$S_{Oz}(q) = \frac{k_B T}{\kappa(q_c^2 + q^2)}. \quad (6.4)$$

The fits should therefore be to

$$\begin{aligned} \Delta S(q, t) = & \Delta S(q, 0) \\ & + \left[\frac{k_B T}{\kappa(q_c^2 + q^2)} \Big|_{T_q} - \left(\Delta S(q, 0) + \frac{k_B T}{\kappa(q_c^2 + q^2)} \Big|_{T_*} \right) \right] \\ & \times \left[1 - \exp(-2Mq^2\kappa_q(q_c^2 + 2q^2)t) \right]_{T_q}. \end{aligned} \quad (6.5)$$

This expression yields the correct asymptotic result for $q > q_c$: $\lim_{t \rightarrow \infty} \Delta S(t) = S_{Oz}(q)|_{T_q} - S_{Oz}(q)|_{T_*}$.

Fig. (6.7) shows the measured $\Delta S(q, t)$ for seven times during the aging for a relatively deep quench, run C (541 K), and the solid and dashed lines correspond

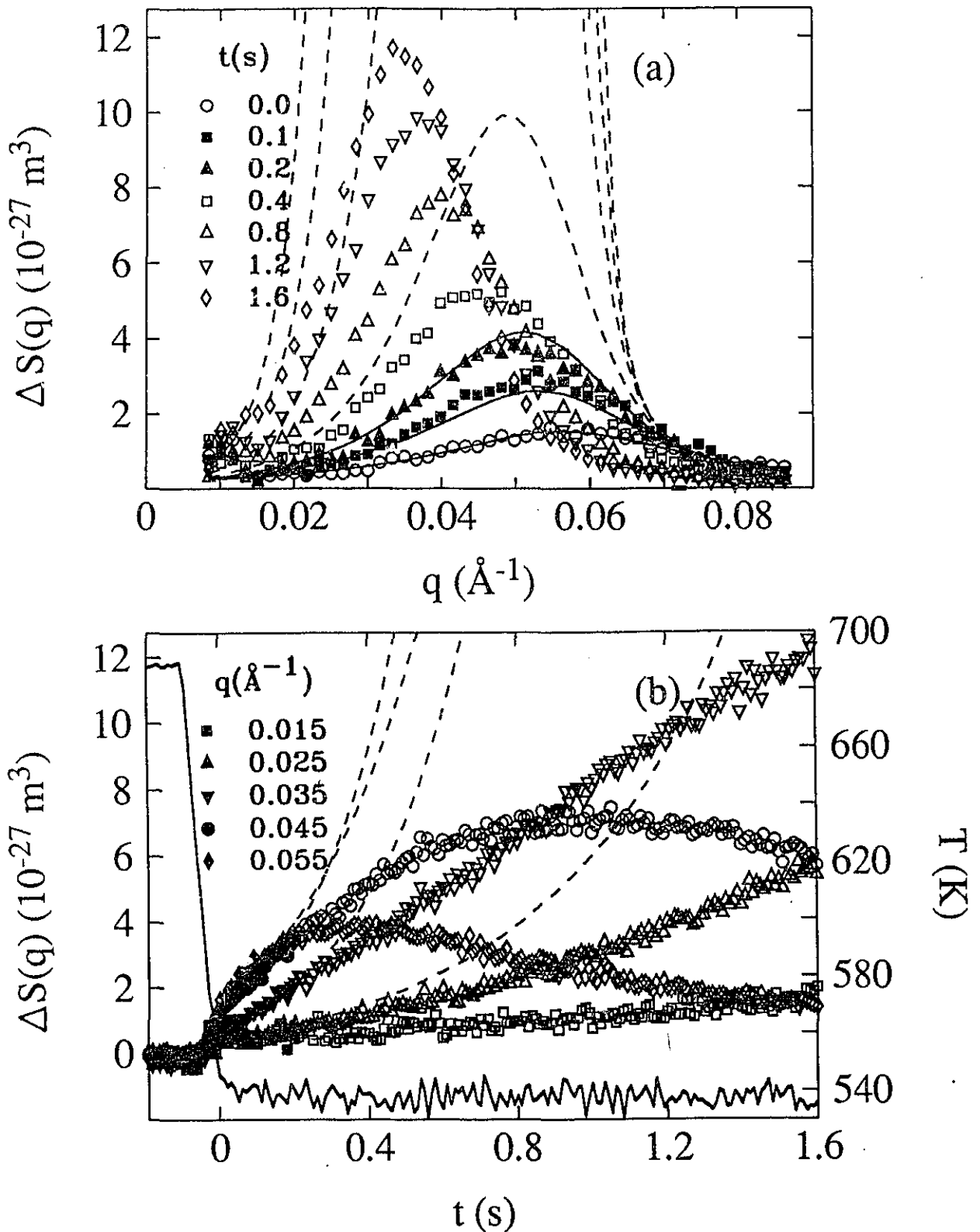


Figure 6.7: (a) Evolution of the structure factor $\Delta S(q, t)$ during the isothermal aging at 541 K (run C). The initial $\Delta S(q, t = 0)$ corresponds to the normalized quenched-in pattern with the last high temperature scan before the quench subtracted off. (b) “ q -slices” (see text). The dashed lines show the best fit predictions from the CHC theory (cf. Eq. 6.5) after a fit to the first 0.2 s (solid lines).

to the model equation (Eq. 6.5). The annealing temperature parameters used were taken from § 4.4. The best fit values obtained for the parameters at the aging temperature from fitting to the first 0.2 s (20 scans) were $\kappa = (4.8 \pm 0.1) \times 10^{-11}$ J/m, $f'' = (-1.85 \pm 0.07) \times 10^7$ J/m³ and $M = (1.13 \pm 0.04) \times 10^{-24}$ m⁵/Js. The equation of motion is then solved with these parameters for the times 0.4, 0.8, 1.2 and 1.6 s to show how the predicted structure factors deviate from the measured $\Delta S(q, t)$ and present an increase which is slower than exponential growth. The apparent success of CHC at the earliest times is intrinsic to fitting an exponential relationship that propagates the initial structure factor, in a time regime where the profile does not change appreciably. The real test came from systematic fits to increasingly longer time domains (*i.e.* up to 0.05, 0.1, 0.15, 0.2, etc. seconds). In all cases, a breakdown of CHC with respect to the measured $\Delta S(q, t)$ is obtained in the scans following those included in the fitting range. For instance, when best fit structure factors are computed up to 0.1 s, the structure factors predicted for $t = 0.2$ s depart appreciably from measured $\Delta S(q, t)$. As the quench temperature is set nearer to T_c ($T < T_c$), the best fit to the model progressively reproduce with less success the structure factors over the time range of the fits, and this at increasingly earlier times.

The fact that nonlinear effects are observed even at temperatures in the neighborhood and above T_c as displayed in Fig. (6.4) means that the CHC linear equation cannot describe the measured time evolution of $\Delta S(q, t)$ at these temperatures (the nonlinearity is observed at temperatures beyond the estimated temperature smearing from $T < T_c$). Since f'' increases with temperature above T_c , in binary alloys in which $\kappa > 0$, $S_{OZ}(q)$ monotonically increases with temperature for all q . Thus the monotonic behavior built-into the CHC equation means that it is not even possible to find scattering wavevectors where the intensity would decrease at any time as observed in the data.

6.2.2 The LBM scheme

In this first nonlinear analysis of the data, the sample is assumed to be at critical composition and the coherent miscibility gap is assumed to be symmetric about that composition.³ In the LBM theory, the density probability distribution functional is taken to be the sum of two Gaussians with peak positions b_1 and b_2 and width σ (cf. Eq. 5.49). Assuming critical composition of the sample brings the simplification that $b_1(t) = b_2(t) \equiv b(t)$. Furthermore, combined with the choice of the “c⁴” model it also means that $\frac{\partial^3 f}{\partial c^3}|_{c_0} = 0$ in the expression for A (Eq. 5.47).

To the fitting parameters κ , r , u and M , two final parameters are required, the wavevector cutoff q_{max} and b_0 . Integrals in reciprocal space have to be evaluated up to a cutoff (cf. p. 105). This cutoff should be of the order of the inverse mean field correlation length ξ^{-1} and for the corresponding real space coarse-graining length a ,

$$q_{max} = [6\lambda^2]^{\frac{1}{3}}/a. \quad (6.6)$$

In the limit where q_{max} goes to infinity, the existence of q^{-2} tails in the structure factor makes the integrals over $S(q)$ diverge. For instance, the integral over $S_{OZ}(q)|_{T_c}$ (Eq. 2.19) is not bounded for large q since the integrand is constant at large q , i.e.

$$\lim_{q \rightarrow \infty} \frac{4\pi k_B T q^2}{\kappa(q^2 + \xi^{-2})} = \frac{4\pi k_B T}{\kappa}. \quad (6.7)$$

Instead of starting the LBM calculations with a system in a single phase state at $t = 0$, as described in § 5.4.1, it is assumed that a certain amount of phase separation has occurred during the quench. The LBM equation of motion is nonlinear and history dependent. Given an initial scattering pattern the amount of phase separation determined by the parameter $b(t)$ is needed for the LBM equations to generate $S_{LBM}(q, t')$ at all later times. Explicitly, for $t = 0$, to account for the quenched-in $\Delta S(q, t = 0)$, the parameter $b_0 \equiv b(0)$ is set to a nonzero value. Thus the composition distribution is already assumed double-peaked at the earliest scans.

³The second of these conditions is known from § 1.3 not to be satisfied and a re-analysis with $\frac{\partial^3 f}{\partial c^3} \neq 0$ and results for off-critical quenches are forthcoming.[168]

When the Landau-Ginzburg coarse-grained free energy (Eq. 5.3) is used with the “ c^4 ” approximation (Eq. 5.4), then the calculation of A (Eq. 5.47) simplifies to:

$$\begin{aligned} A &= r + \frac{u \langle (\delta c)^4 \rangle}{6 \langle (\delta c)^2 \rangle} \\ &= r + \frac{u}{6} \left[3 \langle (\delta c)^2 \rangle + \frac{\langle (\delta c)^4 \rangle_c}{\langle (\delta c)^2 \rangle} \right] \end{aligned} \quad (6.8)$$

where the cumulant $\langle (\delta c)^4 \rangle_c$ was defined in Eq. (5.51).

The initial structure factor given to the LBM algorithm, $S_{\text{LBM}}(q, t = 0)$, consists of two parts. One is the quenched-in structure factor $\Delta S(q, t = 0)$ parametrized by a Lorentzian centered at zero, Eq. (6.1). However, as in the case of the CHC equation, as well as the constant term due to grain boundary scattering, the subtraction has removed the high temperature equilibrium scattering needed by LBM. Thus, the second part is the estimate of the temperature-dependent scattering for the equilibrium fluctuations at T_c , $S_{OZ}(q)|_{T_c}$ (Eq. 2.19). This contribution was estimated from the temperature dependence of the scattering above T_c in § 4.4. Although the values estimated are small ($0.034 \times 10^{-27} \text{ m}^3$ at 0.01 \AA^{-1}) it is important to include them. Afterwards, the theoretical structure factors $S_{\text{LBM}}(q, t)$ have $S_{OZ}(q)|_{T_c}$ subtracted to compare with data, thus compensating for the missing $S_{OZ}(q)|_{T_c}$ in $\Delta S(q, t)$.

The assumptions of a critical quench and a symmetric gap imply that $b_1(t) = b_2(t)$ and

$$\langle (\delta c)^3 \rangle = \langle (\delta c)^5 \rangle = 0 \quad (6.9)$$

at all times. Integration of the parametrized form of $\rho(\delta c)$ (Eq. 5.49) gives relations to compute the averages $\langle (\delta c)^2 \rangle$, $\langle (\delta c)^4 \rangle_c$ and $\langle (\delta c)^6 \rangle$ at any given time in terms of the parameters b and σ :

$$\langle (\delta c)^2 \rangle = \sigma^2 + b^2, \quad (6.10)$$

$$\langle (\delta c)^4 \rangle_c = -2b^4, \quad (6.11)$$

$$\langle (\delta c)^6 \rangle = 15\sigma^6 + 45\sigma^4 b^2 + 15\sigma^2 b^4 + b^6. \quad (6.12)$$

The differential equations for the time dependent behavior of $\langle (\delta c)^2 \rangle$ and $\langle (\delta c)^4 \rangle_c$ are derived using the Fokker-Planck equation (Eq. (5.12)). These differ-

ential equations depend on the higher moment $\langle(\delta c)^6\rangle$. New averages are computed after each time increment step and are then used to uniquely determine b and σ . Thus a new form of $\rho(\delta c)$ is established which, in turn, allows the computation of the average $\langle(\delta c)^6\rangle$. This sequence of computations complete one iteration cycle.

The computation procedure is thus as follows.⁴ At any time t , $S_{\text{LBM}}(q, t)$, $b(t)$ and $\sigma(t)$ are known. The algorithm loops through the following for each time step Δt :

- Compute $\langle(\delta c)^2\rangle$ and $\langle(\delta c)^4\rangle_c$ at time $t + \Delta t$. From the equation of motion for the single-point distribution function, using Eq. (5.14):

$$\frac{d}{dt}\langle(\delta c)^2\rangle = 2M \left[W + k_B T \left(\frac{1}{10\pi^2} q_{\text{max}}^5 \right) \right] \quad (6.13)$$

$$\frac{d}{dt}\langle(\delta c)^4\rangle_c = 4M \left[W \frac{\langle(\delta c)^4\rangle_c}{\langle(\delta c)^2\rangle} + \frac{3}{5} q_{\text{max}}^2 u \left(\langle(\delta c)^6\rangle - \frac{\langle(\delta c)^4\rangle_c^2}{\langle(\delta c)^2\rangle} \right) \right] \quad (6.14)$$

with

$$W = -\frac{1}{2\pi^2} \int_0^{q_{\text{max}}} q^4 (\kappa q^2 + A) S_{\text{LBM}}(q, t) dq, \quad (6.15)$$

where A , $\langle(\delta c)^2\rangle$, $\langle(\delta c)^4\rangle$ and $\langle(\delta c)^6\rangle$ are calculated using Eqs. (6.8), (6.10), (6.11) and (6.12) respectively and definition (5.51) for $\langle(\delta c)^4\rangle_c$.

- Compute $S_{\text{LBM}}(q, t + \Delta t)$ from Eq. (5.46).
- Using Eq. (6.11), $b(t + \Delta t)$ is obtained and then using Eq. (6.10), $\sigma(t + \Delta t)$ is obtained.

The effect of the short-wavelength cutoff inherent to the LBM scheme was investigated in two different ways. In the first, q_{max} was fixed independently of T and r . This would be equivalent to a fixed temperature independent coarse-graining length in real space (*cf.* Eq. 6.6). In the second procedure the cutoff was constrained to be proportional to the inverse of the correlation length (Eq. 5.37)

$$\begin{aligned} q_{\text{max}} &= \alpha/\xi \\ &= \alpha\sqrt{-2r/\kappa} \end{aligned} \quad (6.16)$$

⁴The code to compute $S_{\text{LBM}}(q, t)$ was provided by K.R. Elder.

for $T < T_c$.⁵ The motivation for this choice is determined by the fact that the length scale in the description of SD dynamics has to satisfy the conditions for a mesoscopic scale as discussed on page 103. The proportionality constant α should be of order unity. With Eq. (6.6), the coarse-graining length is then

$$a = \frac{(6\pi^2)^{\frac{1}{3}}}{\alpha} \xi. \quad (6.17)$$

6.2.3 Fit results

Fits have been made to the measured scattering patterns for all temperatures investigated. With fits performed at a fixed q_{max} independent of T and r , the temperature dependence obtained for the parameters is unphysical. Specifically, best fit $|r|$ were found to increase as T_c is approached although one expects $r \rightarrow 0$ as $T \rightarrow T_c$. With fits performed such that the cutoff q_{max} satisfies Eq. (6.16) with α fixed and nominally chosen of order unity, the fitting results in the expected decrease of $|r|$ as T_c is approached. However, if a different value of α is picked, an equivalent fit is obtained and the best fit values of r and u differ but κ , q_{max} and M are unaffected. If α is allowed to vary during the fit with the other parameters κ , r , u , M and b_0 , then the fitting procedure does not converge indicating that the fit is overdetermined. With a fixed α , the second procedure corresponds to the use of a temperature dependent coarse-graining length since ξ is temperature dependent (*cf.* § 5.1). In the remainder of this dissertation, the results are thus analysed with the cutoff constrained proportional to ξ^{-1} . The value $\alpha = 2.59$ has been chosen for reasons to be given in § 6.2.5.

For all runs, fits were performed to all scans up to 1.6 s, *i.e.* to 160 or 320 $\Delta S(q, t)$ for scans every 0.01 or 0.005 s respectively. The agreement between best fit $S_{LBM}(q, t)$ and $\Delta S(q, t)$ is very good for quenches below T_c .⁶ This was exemplified

⁵For $T > T_c$, $q_{max} = \alpha\sqrt{r/\kappa}$.

⁶As mentioned on p. 156, to compensate for the missing $S_{OZ}(q)|_{T_c}$ in the $\Delta S(q, t)$, the theory $S_{LBM}(q, t)$ have this quantity subtracted off on all plots. However, for the discussion of the fits, these curves will be referred to as $S_{LBM}(q, t)$, and the removal of the $S_{OZ}(q)|_{T_c}$ will not be

in Fig. (6.3a) for run C (541 K), where best fit theory $S_{\text{LBM}}(q, t)$ are shown as solid lines. In this run, a scattering pattern was measured every 0.01 s ($ET = 0.01$, *cf.* Table 6.1), and thus 160 complete $\Delta S(q, t)$ were fit. The corresponding best fit parameters for this run are $\kappa = 4.54 \pm 0.01 \times 10^{-11}$ J/m, $r = -4.77 \pm 0.01 \times 10^7$ J/m³, $u = 1.368 \pm 0.001 \times 10^9$ J/m³ and $M = 1.145 \pm 0.009 \times 10^{-24}$ m⁵/Js. The value of the parameter κ is close to that obtained when fitting the first 0.2 s with the CHC equation of motion and the values of M are identical (*cf.* p. 154). However, the parameter r is larger by more than a factor of two from the best fit f'' in the CHC equation of motion. This difference is somewhat expected since there is an additional free energy parameter, u , in the LBM equation of motion. An estimate of f'' using Eq. (5.4) gives

$$f''(\delta c) = r + 3u(\delta c)^4, \quad (6.18)$$

and a value of $|r|$ larger than $|f''|$ since $r < 0$ and $3u(\delta c)^4 > 0$ after phase separation starts.

All fits have comparable quality as that shown in Fig. (6.3) and show that this model effectively parametrizes the data. Systematic fits were also performed for all runs for times up to 0.2, 0.4, 0.8 and 1.2 s and in all cases it was verified both that the best fit values for all parameters did not vary beyond one standard deviation and that the extrapolated $S_{\text{LBM}}(q, t = 1.6 \text{ s})$ was still of comparable quality of fit to the $\Delta S(q, t = 1.6 \text{ s})$ as that which resulted from fitting the full 1.6 s.⁷ In the last section that deals with the comparison of $\Delta S(q, t)$ with the LBM equation of motion, § 6.2.7, a breakdown between $S_{\text{LBM}}(q, t)$ and experimental $\Delta S(q, t)$ does occur but at times beyond those investigated in the early stage runs.

The relaxation of composition fluctuations after a quench to a temperature above T_c ($r > 0$) is not described with equal success as the phase separation below T_c . Nevertheless, the results are still quite satisfactory. In Fig. (6.4a), for run S

mentioned explicitly.

⁷This is in sharp contrast with the observation on p. 154 that the structure factors computed using CHC systematically departed from $\Delta S(q, t)$ after the time interval of the fit.

(599.1 K), the solid lines display the best fit $S_{\text{LBM}}(q, t)$ to the full 1.6 s. At high wavevectors, best fit $S_{\text{LBM}}(q, t)$ track relatively well the experimental $\Delta S(q, t)$. The generated $S_{\text{LBM}}(q, t)$ present a non-monotonic growth as do $\Delta S(q, t)$ even though the value of the free energy parameter r is slightly positive. At low q , the measured $\Delta S(q, t)$ grows faster than the model $S_{\text{LBM}}(q, t)$. The best fit values of the parameters for this run are $\kappa = 1.03 \pm 0.01 \times 10^{-10}$ J/m, $r = 8.7 \pm 1.9 \times 10^4$ J/m³, $u = 3.3 \pm 1.3 \times 10^{10}$ J/m³ and $M = (7.6 \pm 0.3) \times 10^{-24}$ m⁵/Js. As can be noticed from comparing these values with the best fit values for run C quoted above, error bars for the free energy parameters (r and u) for runs above T_c are much larger than for deep quench runs.

Best fit values of κ , r , u , M and b_0 have been obtained, for all early stage runs, both above and below T_c . Best fit results for the first four parameters are summarized in Fig. (6.8) for fits to 1.6 s. The parameter b_0 , which characterizes the amount of quenched-in structure is shown in Fig. (6.9). It increases with the depth of the quench and scales with the integrated intensity of this scattering (about 60% of the final scattering for $\alpha = 2.59$). The values of b_0 are consistent with a smooth extrapolation of $b(t)$ back to $b(0)$ for each run. The values of the free energy gradient parameter, κ , are positive, as expected for a phase separating system and are of the same order of magnitude as the estimates shown in Fig. (1.5). They depend little on temperature and peak slightly below T_c . The parameter r is monotonic and goes through zero at T_c in agreement with the temperature calibration from the single phase equilibrium structure factors (*cf.* § 4.4). The parameter u varies slightly with temperature showing a slight anomaly at T_c . The mobility M is an increasing function of temperature, also showing an anomaly near T_c . The curves in Part (d) of Fig. (6.8) are based on tracer diffusivities measurements and will be described in § 6.2.6.

During the fitting, the two free energy parameters r and u were highly anti-correlated. In practice, as $r < 0$ and $u > 0$, this means that these two parameters were varying the same way in absolute value during the search for best fit. Fur-

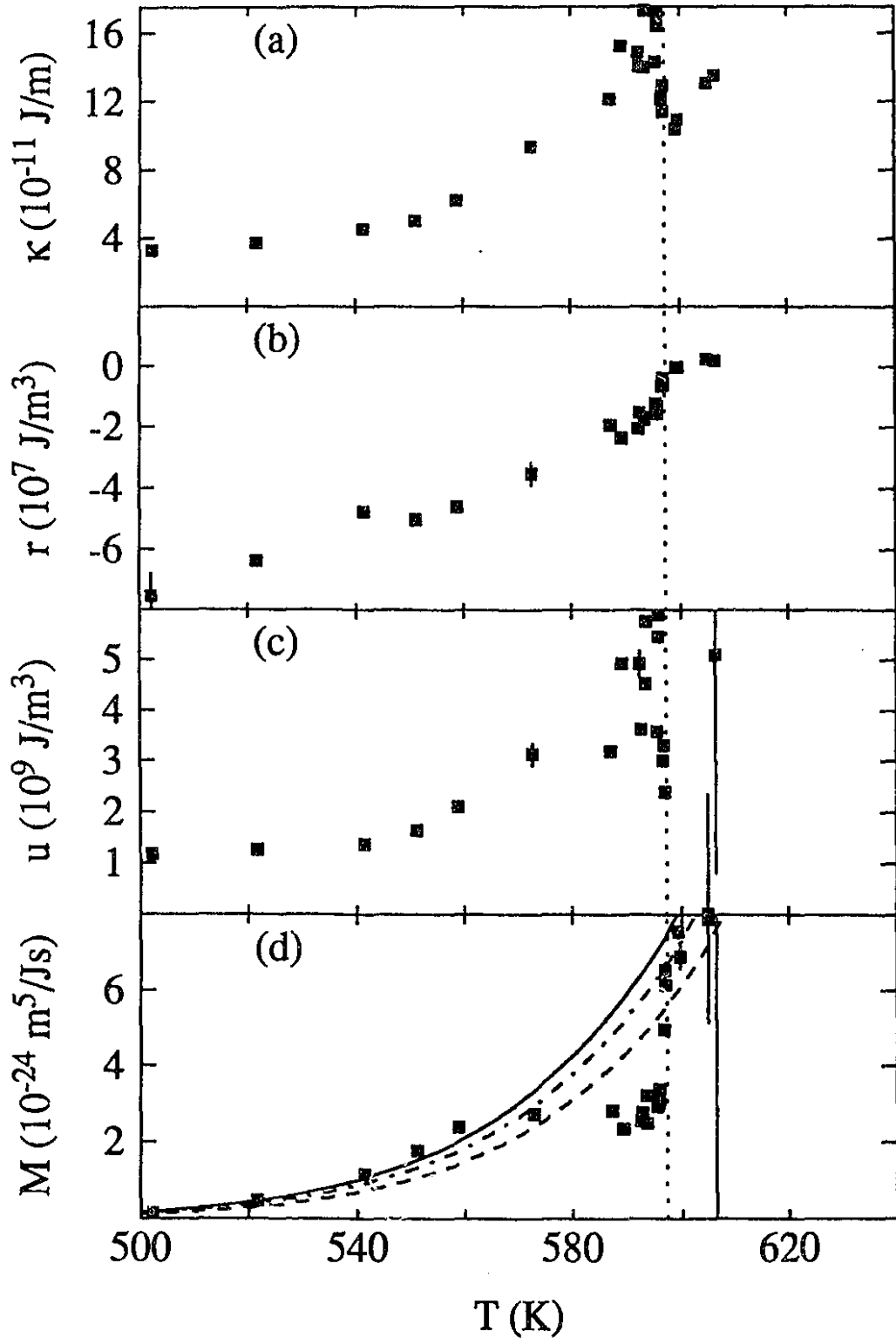


Figure 6.8: Best fit parameters from LBM for all temperatures investigated (with α set to 2.59). (a) κ . (b) r . (c) u . (d) M . The solid line is obtained from Eqs. (6.42) and (1.11) with activation energy and frequency factor interpolated from Hilliard *et al.*[169]. Similarly, the dashed and the dot-dashed lines are obtained from values of E_{0Zn} and D_{0Zn}^* interpolated from Čermák *et al.*[170] and Gódehy *et al.*[171,172] respectively (cf. §6.2.6).

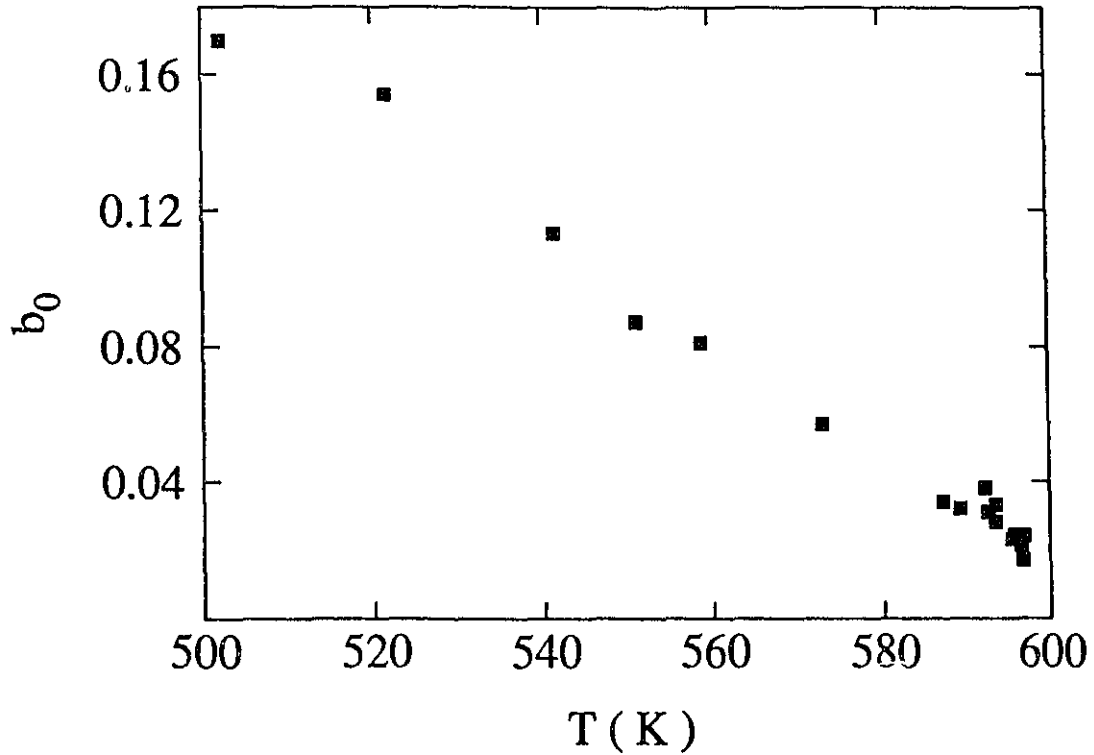


Figure 6.9: Best fit values of b_0 for all runs with $T < T_c$ for $\alpha = 2.59$.

thermore, when r and u were both adjusted, *i.e.* free to vary, the goodness of fit estimator, χ^2 , was relatively insensitive to large anticorrelated variations in the values of these parameters. These observations turn out to contribute to an interesting, fortuitous but systematic feature of the theory and will be further elaborated upon in § 6.2.4.

In the study of relaxation, the fits are not very sensitive to the value of the free energy parameter r . This suggests that it is only possible to obtain an upper bound for this parameter since it affects $S_{LBM}(q, t)$ in the low q range only ($< 0.02 \text{ \AA}^{-1}$). This is easily seen from the expression of the equilibrium structure factor (Eq. 2.19). When r is increased by an order of magnitude the $S_{OZ}(q)$ starts to differ appreciably only at values of $q < 0.02 \text{ \AA}^{-1}$. The same remarks apply in the calculation of W (Eq. 6.15) where again any wavevector q such that $r \ll \kappa q^2$, will not be affected by a change in r . This point will also be reexamined in § 6.2.4.

To complete this survey of best fit results, the effect of a change in the calibra-

tion factor in Eq. (4.14) on the model parameters is examined. Finally, the values of the thermal noise term which was introduced in the scaled equation of motion (Eq. 5.32) and the reduced time also used in that equation are computed for all runs, using the best fit parameter values.

The effect of the overall intensity calibration of $\Delta S(q, t)$ on the best fit parameters can be summarized simply. If the calibrated structure factors, $\Delta S(q, t)$, are scaled up by a factor \mathcal{J} , *i.e.* $\Delta S \rightarrow \mathcal{J}\Delta S$, then $\kappa \rightarrow \kappa/\mathcal{J}$, $\tau \rightarrow \tau/\mathcal{J}$, $u \rightarrow u/\mathcal{J}^2$ and $M \rightarrow \mathcal{J}M$, and the quenched-in $\Delta S(q, t = 0)$ and the equilibrium $S_{OZ}(q)|_{T_c}$ are increased by the same factor \mathcal{J} .

Table (6.2) lists the calculated values of ϵ using Eq. (5.33) and of τ using Eq. (5.29) for $\alpha = 2.59$ for all the runs to 1.6 s. The values of ϵ are relatively independent of the temperature but are relatively high, indicating a highly nonlinear situation. The values of τ peak near the maximum decomposition rate temperature (between 551 and 559 K). Closer to T_c , the values of τ/t decrease, being of order unity for the runs closest to T_c . The dimensionless τ and ϵ are unaffected by the overall intensity calibration of $\Delta S(q, t)$.

6.2.4 Coarse-graining length dependence of r , u , κ and M

The dependence of r , u , κ and M on α was investigated by fixing α in the range $1/\sqrt{2}$ to $2\sqrt{2}$ and computing best fit values. The goodness of fit estimator, χ^2 , did not change, indicating that the fits obtained were equivalent. As pointed by Eq. (6.16), this allowed the investigation of the effect of the cutoff in terms of a fixed number of inverse correlation lengths at all temperatures on the values of the parameters and consequently, of the obtained phase diagram. It was found that $r \sim \alpha^{-2}$ and $u \sim \alpha^{-3}$ and that κ and M were unaffected by the choice of α . In other terms, the constant of proportionality between q_{max} and $\sqrt{-2r/\kappa}$ could be varied without affecting the quality of the fits provided r is divided by α^2 and u is divided by α^3 . From the α -dependence of r and u and Eqs. (5.29) and (5.33) $\tau \sim \alpha^{-4}$ and $\epsilon \sim \alpha^{-2}$.

T	ϵ	τ/t
(K)		$(0.01 \text{ s})^{-1}$
502.2	5.01 \pm 0.69	0.505 \pm 0.117
521.6	5.03 \pm 0.09	1.049 \pm 0.022
541.4	4.84 \pm 0.01	1.149 \pm 0.007
551.1	4.92 \pm 0.09	1.769 \pm 0.036
558.7	4.87 \pm 0.01	1.620 \pm 0.008
572.8	4.60 \pm 0.63	0.725 \pm 0.162
587.1	4.40 \pm 0.07	0.176 \pm 0.003
589.1	4.42 \pm 0.09	0.171 \pm 0.005
592.3	4.94 \pm 0.50	0.144 \pm 0.024
592.5	4.62 \pm 0.03	0.090 \pm 0.001
593.4 ¹	4.96 \pm 0.11	0.088 \pm 0.002
593.4 ²	5.53 \pm 0.09	0.128 \pm 0.003
595.4	4.97 \pm 0.10	0.061 \pm 0.002
595.7	5.92 \pm 0.13	0.071 \pm 0.003
595.8	5.47 \pm 0.11	0.085 \pm 0.002
596.5	7.40 \pm 0.18	0.033 \pm 0.002
596.8	9.50 \pm 0.53	0.015 \pm 0.002
596.9	6.68 \pm 0.11	0.038 \pm 0.001

Table 6.2: Values of ϵ and τ for $\alpha = 2.59$ as calculated from Eq. (5.29) and Eq. (5.33). The errors are calculated from the standard deviations of best fit κ , τ , u and M .

¹Run K.

²Run L.

The $\tau \sim \alpha^{-2}$ scaling implies a unique wavevector cutoff q_{max} for each temperature. Figure (6.10) shows the value of q_{max} selected by the fitting procedure for all runs A — Z. It increases with the depth of the quench ($q_{max} = 0.375 \text{ \AA}^{-1}$ at 541 K), and is minimum non-zero near T_c ($q_{max} = 0.004 \text{ \AA}^{-1}$ at 597 K). Near T_c , q_{max} even moves below the detector window *i.e.* below the maximum q measured. In these instances, the modes with wavenumbers above q_{max} appear to have already reequilibrated at the time of the first isothermal scan at T_q . This will be further elaborated below.

The separation of $\langle(\delta c)^2(t)\rangle$ into $b^2(t)$ and $\sigma^2(t)$ (*cf.* Eq. 6.10), including the

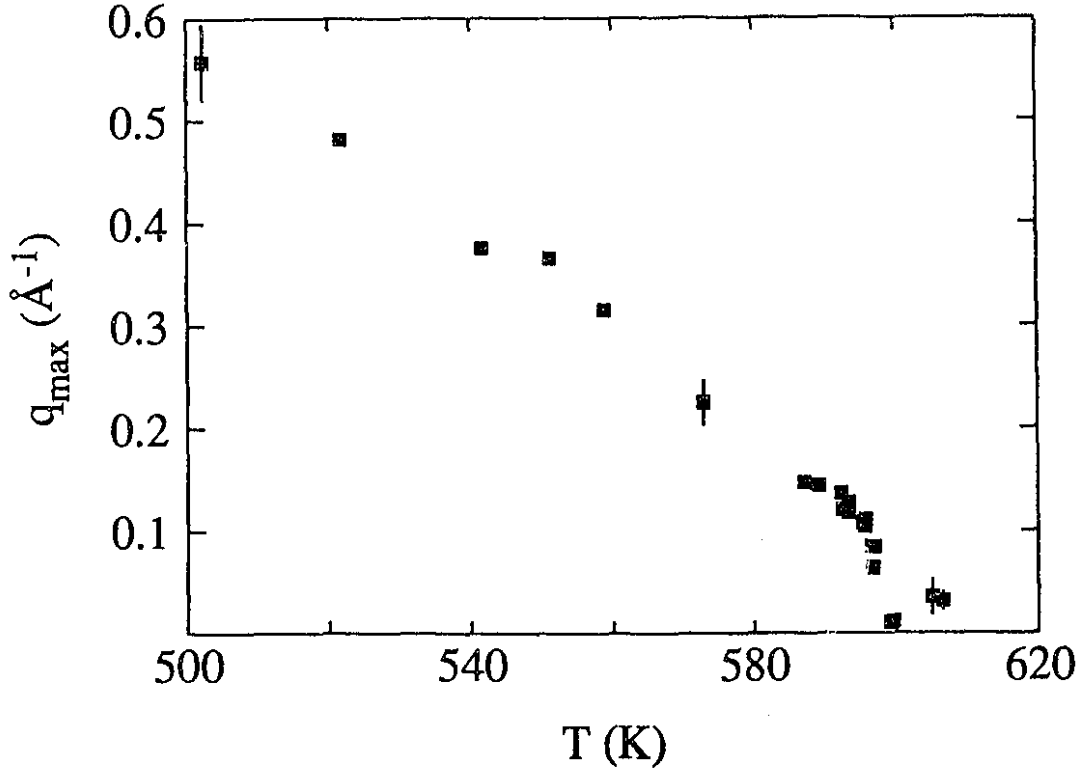


Figure 6.10: Wavevector cutoff q_{\max} selected by the fitting procedure for all early stage runs when q_{\max} is constrained proportional to ξ^{-1} following Eq. (6.16).

$t = 0$ values, depends on α . However, $\langle \delta c^2(t) \rangle$ is independent of the choice of α since it is calculated directly from the data. As α is increased, $b(t)$ (and b_0) decreases while $\sigma(t)$ increases. This implies that the choice of α affects the extent to which the LBM algorithm assumes the decomposition has proceeded before the isothermal aging began (*i.e.* before the first scan after the quench was recorded). Figure (6.11a) shows $b(t)$ for both $\alpha = 1$ and $\alpha = 2.59$. Part (b) of this figure presents $-A(t)$ in each case. There is no obvious quantitative scaling relationship between either $A(t)$ or $b(t)$ and α . For all runs below T_c the model equation used for the time dependence of the integrated intensity, Eq. (6.2) was also applied to the time-dependence of $b(t)$ (above T_c , $b(t) = 0$ for all times). In all cases, Eq. (6.2) tracked very well $b(t)$ as shown by the solid lines on Fig. (6.11a) for run C. The obtained best fit values of $A + C$ were found to be relatively independent of α . These are reported later in Fig. (6.14). Also, going from $\alpha = 1$ to $\alpha = 2.59$, by analogy to the linear CH

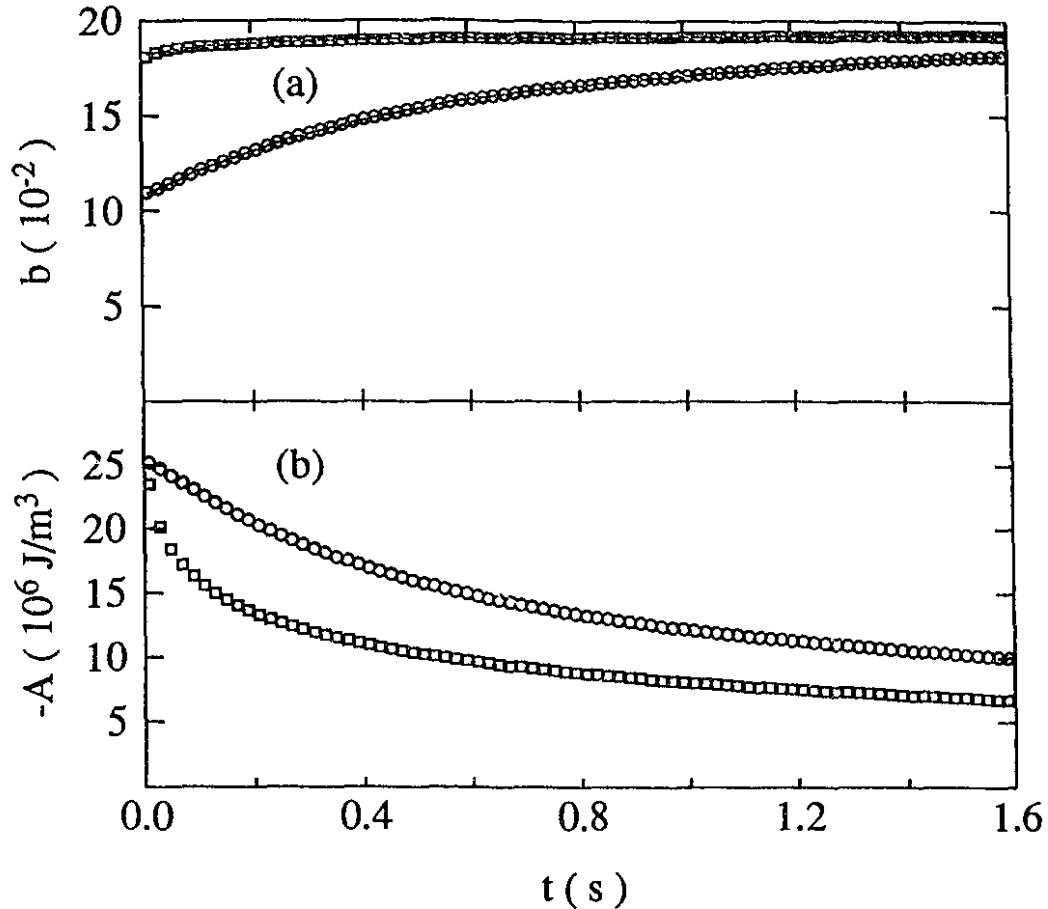


Figure 6.11: Time-evolution of $b(t)$ (cf. Eq. 6.10) and of the coupling term $A(t)$ (cf. Eq. 5.47) for run C (541 K) with $\alpha = 1$ (\square) and $\alpha = 2.59$ (\circ). Every second point has been plotted only. The solid lines in (a) are best fit curves to Eq. (6.2) (see text).

equation, the “critical” wavenumber q_c , calculated using Eq. (3.3) decreases from 0.376 to 0.145 \AA^{-1} . In the CH theory, q_c corresponds to the location of the crossover point, and thus, extending the analogy, the latter value is more commensurate to the observed location of the crossover point in the early scans.

Since $\langle(\delta c)^2(t)\rangle$ consists of two terms (cf. Eq. 6.10), Figure (6.11a) gives an incomplete picture of the SD process. Figure (6.12) presents the calculated one-point composition density functional $\rho(\delta c)$ for discrete values of δc at selected times between 0.01 and 1.6 s for $\alpha = 1$ (a) and $\alpha = 2.59$ (b). This figure clearly illustrates the influence of α on the range of the decomposition process assumed in the best fit LBM result. For instance, at $\alpha = 2.59$, Fig. (6.11a) shows that the value of $b(t)$ starts off at about 60% of the asymptotic value reached. The corresponding time evolution of $\rho(\delta c)$ (part b) displays a major change in profile, progressing from a single broad peak distribution to one in which the differentiation of two symmetric

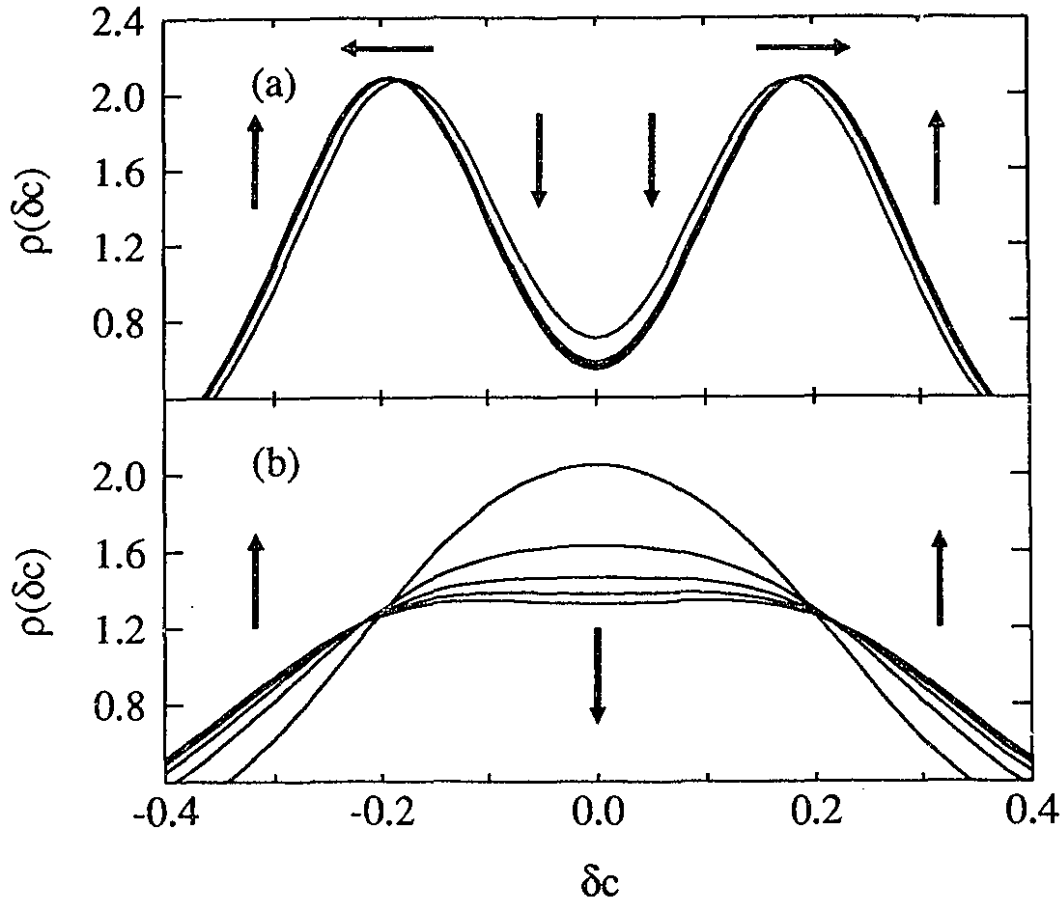


Figure 6.12: Calculated time-evolution of the one-point composition density functional, $\rho(t)$, for run C (541 K) with (a) $\alpha = 1$ and (b) $\alpha = 2.59$ at $t = 0.01, 0.40, 0.80, 1.20$ and 1.60 s. The arrows indicate the direction of the change in the profile of $\rho(\delta c)$ as SD proceeds.

peaks about $\pm b(t)$ becomes more obvious. For $\alpha = 1$, Fig. (6.11a) showed that the separation into domains of distinct phases was near completion in the decomposition stages captured. For this α , the evolution of $\rho(\delta c)$ (part a) indicates that most of the composition fluctuations are occurring about compositions which are well defined and near the final $b(t)$.

Fig. (6.13) shows the breakdown between the two terms contributing to $\partial S_{\text{LBM}}(q, t)/\partial t$ in Eq. (5.46) (solid curve). The dashed curve gives $-2Mq^2(\kappa q^2 + A)S_{\text{LBM}}(q, t)$ and the dotted curve gives $2Mk_B T q^2$. The salient features displayed by the solid curve are that for any given time (i) a wavevector will grow at a maximum rate, (ii) another will be stationary (a time-dependent cross-over point) and (iii) high q modes, such that

$$2Mq^2(\kappa q^2 + A)S_{\text{LBM}}(q, t) \simeq 2Mk_B T q^2 \quad (6.19)$$

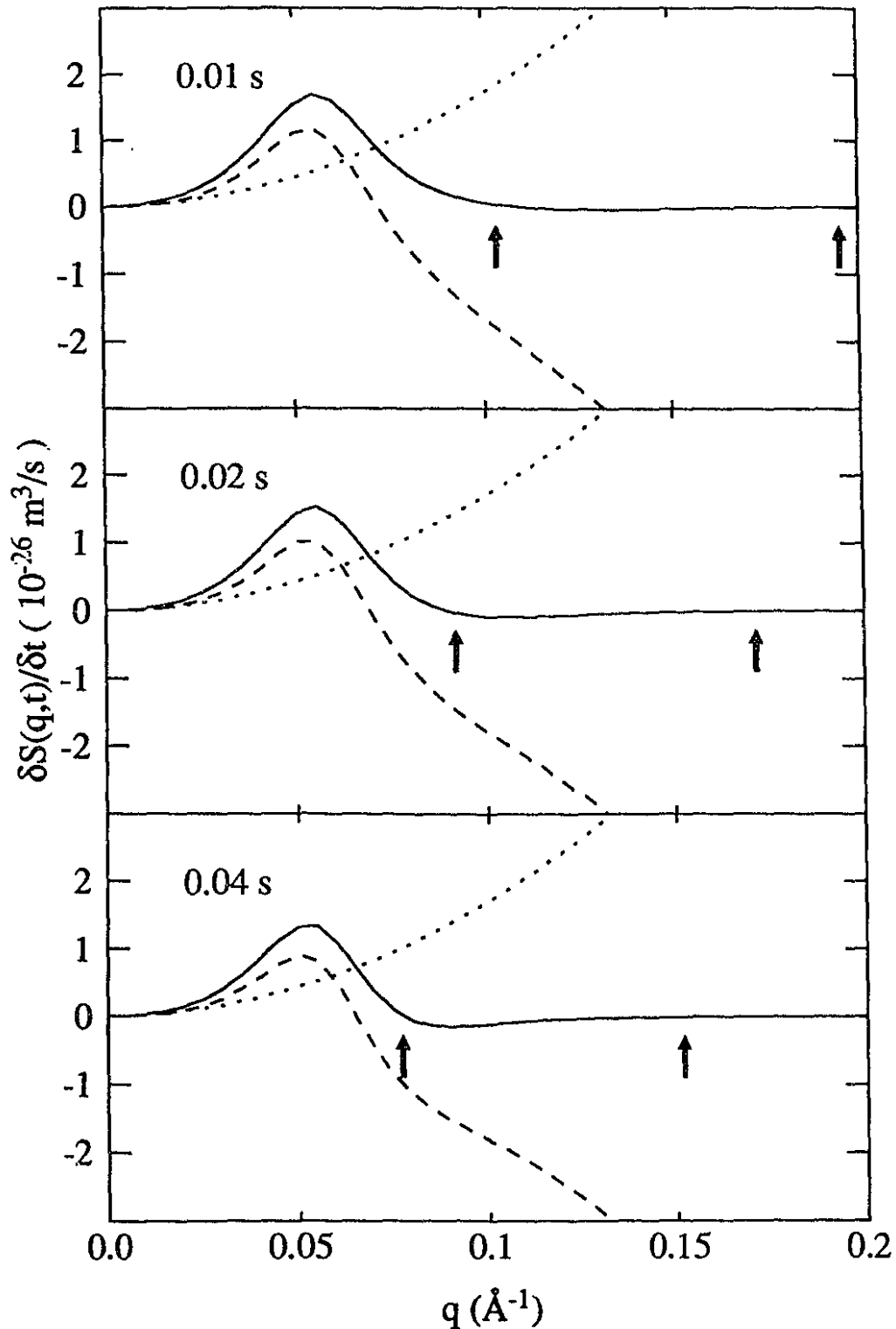


Figure 6.13: Contributions from the amplification term $-2Mq^2(\kappa q^2 + A)S_{LBM}(q,t)$ (dashed line) and the thermal term $2Mk_B T q^2$ (dotted line) to the time evolution of $S_{LBM}(q,t)$ by the LBM equation. The values used for the parameters correspond to best fit results for run C (541 K) with $\alpha = 2.59$. For each time, the left arrow points to the value of $q \neq 0$ for which $\partial S_{LBM}(q,t)/\partial t = 0$ and the right arrow is a guide to the eye to indicate the lower limit of the q -range for which $\partial S_{LBM}(q,t)/\partial t$ essentially vanishes.

have reequilibrated to thermal equilibrium at the aging temperature *i.e.* they are described by $S_{OZ}(q)|_{T_t}$.

Similarly to the CHC equation (Eq. 3.6), condition (6.19) indicates that the asymptotic $S_{LBM}(q, t)$ is reached at a given q when

$$S_{LBM}(q, t) = \frac{k_B T}{\kappa q^2 + A(t)}. \quad (6.20)$$

However, in Eq. (3.6), only modes of wavevectors for which the time-independent $R(q) < 0$ will reach equilibrium. In the LBM scheme, A reflects the mean field coupling between all the modes and is thus time-dependent. In Eq. (6.8), with $r < 0$, $u > 0$ and $\langle (\delta c)^4 \rangle_c < 0$ (*cf.* Eq. 6.11) the net effect of an increase in $\langle (\delta c)^2 \rangle$ is that $|A|$ decreases with time. Thus, the threshold value for modes to grow or decay is time-dependent and moves towards smaller q in time. As the cross-over sweeps by a given wavevector, the intensity at this q which has been increasing until then, starts to decrease towards the equilibrium intensity. The decrease of A with time is also responsible for the slower growth of modes for $S_{LBM}(q, t)$ than with linear theory exponential growth. Linear theory would be obtained by keeping only the first term (r) in Eq. (6.8).

Point (iii) can equivalently be arrived at from the LBM algorithm (*cf.* p. 157). The quantity W defined in Eq. (6.15) provides the mean field coupling between the modes. In Eq. (6.13), the time derivative $\frac{d}{dt} \langle (\delta c)^2 \rangle$ will vanish when $W = -\frac{k_B T}{10\pi^2} q_{max}^5$, *i.e.*

$$\frac{1}{(2\pi)^3} \int_0^{q_{max}} q^2 (\kappa q^2 + A) S_{LBM}(q, t) dq = \frac{k_B T}{10\pi^2} q_{max}^5. \quad (6.21)$$

Any increase of q_{max} beyond a sufficiently large value will contribute to an equal increment on both sides of this equation. Thus modes beyond this q_{max} do not contribute to $\frac{d}{dt} \langle (\delta c)^2 \rangle$. For large q and t the $S_{LBM}(q, t)$ that would satisfy this equality is again given by Eq. (6.20). Thus, although Eq. (6.21) is never satisfied when the integral is performed over the entire q -range at any time during SD, the contributions from high q modes to both sides of Eq. (6.21) are equal when condition (6.19) is valid. Thus reequilibrated modes do not contribute more than equilibrium

thermal noise to integral (6.15), that is they decouple from lower wavenumber modes. As the decomposition progresses, modes of successively lower q stop contributing to the mean field coupling.

As it turns out, the value of q_{max} selected by the fitting procedure is in the q -range where Eq. (6.19) is satisfied immediately after the quench. For instance, in Fig. (6.13), the value of q_{max} picked by the fit to LBM is 0.375 \AA^{-1} (run C). This is beyond the right arrow in Part (a) which indicates (as a subjective guide to the eye) a lower limit for the q -range such that $\partial S_{LBM}(q, t)/\partial t \rightarrow 0$. Since modes at progressively lower q values have reequilibrated as the aging proceeds, q_{max} could reflect the highest q modes that have not yet reequilibrated by the time the first scan after the quench is recorded, *i.e.* in $\Delta S(q, t = 0)$. Under this assumption, as faster quench rates are achieved to a given aging temperature, an increase of q_{max} is expected. It is not clear that an experiment independent significance can be assigned to q_{max} for cases where the quench is not ideally instantaneous.

Since the free energy parameter r always appears summed with κq^2 (*cf.* Eqs. 6.8 and 6.1b), it mostly contributes to the computations at low q . Thus if r is in the range where it is small with respect to κq^2 , changing its value will have little influence on $S_{LBM}(q, t)$. Furthermore, since the detector imposes a low q limit on $\Delta S(q, t)$, there is no direct comparison with $S_{LBM}(q, t)$ in the very low q range. Thus in that q range, the value of r affects $S_{LBM}(q, t)$ only through the integral in expression (6.15), *i.e.* the mean field coupling. But as $q \rightarrow 0$ the integrand also goes to zero and thus contributions to the integral become smaller. Thus, the fits are not sensitive to changes in r when the value of this parameter is small. This lack of sensitivity for r can be used to explain the observed scaling of r and u with powers of α . Since q_{max} is uniquely picked by the fitting algorithm for each run, the value of the parameter r is completely determined by the choice of α in Eq. (6.16) and has to obey $r \sim \alpha^{-2}$. That is to say, the value of r does not affect $S_{LBM}(q, t)$ in as much as u is then chosen so that the numerical value $A(t)$ accounts for the coupling between modes (Eq. 5.47) in a rescaled phase diagram (*cf.* Eq. 5.5) and produces

very similar $S_{\text{LBM}}(q, t)$. This ties in well with the anticorrelation between r and u during the fits reported in § 6.2.3.

The scaling of r and u with α was verified to be *accidental* by observing that extrapolation of $S_{\text{LBM}}(q, t)$ for much longer times (up to 10 s) did not produce rigorously identical results for $\alpha = 1/\sqrt{2}$ and $\alpha = 1$.

The α -dependence of r , u , and κ can also be examined by rewriting the expressions for r , u and κ given in Chapter V (Eqs. 5.55, 5.56 and 5.59) using the defining equation for α (Eq. 6.17) and the relation between α and the coarse-graining length a (Eq. 6.17) as

$$r = -\frac{1}{6\pi^2} \left(\frac{k_B T f_0}{\phi_S^2} \right) q_{\text{max}}^3 \quad (6.22)$$

$$u = \frac{1}{6\pi^2} \left(\frac{k_B T f_0}{\phi_S^4} \right) q_{\text{max}}^3 \quad (6.23)$$

$$\kappa = \frac{\alpha^2}{12\pi^2} \left(\frac{k_B T f_0}{\phi_S^2} \right) q_{\text{max}}. \quad (6.24)$$

It is possible to obtain the conditions that $r \sim \alpha^{-2}$, $u \sim \alpha^{-3}$ and that κ does not depend on α from the three equations above by setting $f_0 \sim \alpha^{-1}$ since $\phi_S = \sqrt{-r/u} \sim \alpha^{1/2}$.

However, this raises a contradiction when considering f_0 as introduced in Eq. (5.52). According to the LBM paper[7], the dependence on α of the intensive free energy $f(\phi)$ should be comprised in f_0 , *the only adjustable system dependent parameter, i.e. $f_0 \sim \alpha^{-3}$* is expected. This α scaling of f_0 is obtained by rewriting the susceptibility sum rule, Eq. (2.23), in terms of Eq. (5.52),

$$S(0) = \frac{a^3 \phi_S^2}{f_0 \Phi''(1)} \quad (6.25)$$

and also using Eq. (2.22) for the differential susceptibility the following expression for f_0 is obtained :

$$f_0 = \left(\frac{a}{a_0} \right)^3 \frac{\phi_S^2}{\chi_s \Phi''(1)}. \quad (6.26)$$

Next, using Eq. (6.17) and the power law relations listed in Table (1.1) this equation becomes

$$f_0 = \frac{6\pi^2}{\alpha^3} \left(\frac{\xi_0}{a_0} \right)^3 \frac{B^2}{C \Phi''(1)} \varepsilon^{-3\nu' + 2\beta + \gamma'} \quad (6.27)$$

where ϵ is the reduced temperature as defined by Eq. (1.2). In this equation, ξ_0 is the critical amplitude of the correlation length, C that of the differential susceptibility and B that of the coexistence curve. Assuming hyperscaling to hold (*i.e.* Eq. 5.39), f_0 can thus be written as :

$$f_0 \approx \frac{6\pi^2}{\alpha^3} \left(\frac{\xi_0}{a_0} \right)^3 \frac{B^2}{C\Phi''(1)}. \quad (6.28)$$

This derivation produces the $f_0 \sim \alpha^{-3}$ scaling. However, the observed accidental scaling of r and u with α and hence of the phase diagram (which is the topic of the next section) implies that the critical amplitudes would also scale with α . The natural scaling relations to assume for a “ c^4 ” free energy, based on the α scaling of r and u , are $B \sim \alpha$, $C \sim \alpha^2$ and $\xi_0 \sim \alpha$. Thus, Eq. (6.28) then produces $f_0 \sim \alpha^{-1}$.⁸

According to Equation (6.28), f_0 is expected to be temperature independent. Rewriting Equation (5.60) to relate f_0 to α and ϵ ,

$$f_0 = \frac{6\pi^2}{\alpha^3} \frac{1}{\epsilon} \quad (6.31)$$

and using the values of ϵ tabulated for $\alpha = 2.59$ in Table (6.2) gives $f_0 \approx 0.25$ with a scatter between temperatures comparable to that of ϵ . Langer *et al.*[7] have proposed an estimate of f_0 using Eq. (6.28) with numerical estimates for the simple-cubic Ising model[11,173] of $B = 1.57$, $C = 0.193$ and $\xi_0/a_0 = 0.248$. The value they

⁸It is easy to propose a simple situation where the observed *accidental* scaling would result. If $\phi/\phi_S \ll 1$ then $\left(\frac{\phi}{\phi_S}\right)^2 \gg \left(\frac{\phi}{\phi_S}\right)^4$ and Eq. (5.54) becomes

$$\Phi(\phi/\phi_S) \approx -\frac{1}{2}(\phi/\phi_S)^2. \quad (6.29)$$

From the dependence $\phi_S \sim \alpha^{1/2}$, this gives $\Phi\left(\frac{\phi}{\phi_S}\right) \sim \alpha^{-1}$. This makes the intensive free energy $f(\phi) \sim \alpha^{-2}$ according to Eq. (5.53). Finally, rewriting Eq. (5.52) as :

$$f(\phi) = \left(\frac{k_B T}{6\pi^2} \right) f_0 \Phi(\phi/\phi_S) q_{max}^3 \quad (6.30)$$

it can be seen that to self-consistently satisfy $f(\phi) \sim \alpha^{-2}$, Eq. (6.29) and Eq. (6.30), it is necessary that $f_0 \sim \alpha^{-1}$, which is precisely the relationship that was suggested by Eqs. (6.22, 6.23 and 6.24). However, the limit $\phi/\phi_S \ll 1$ is not expected to apply in this work and the source of the α -scaling appears to be less tractable than this simple scenario.

obtain for $\alpha = 1$, $f_0 = 5.777$ is of the same order as the value obtained in this work, $f_0 = (2.59)^3(0.25) = 4.34$ when scaled to the same α (*cf.* Eq. 6.31).

To close this section, Binder's formulation of the Ginzburg criterion for the case of SD (Eq. 5.27) is examined in terms of ϵ or f_0 . At compositions close to the critical composition Equation (5.27) simplifies to

$$k_B T \ll (\sqrt{\kappa})^3 (1 - T/T_c)^{1/2}. \quad (6.32)$$

Using Eq. (6.27) with mean field exponents given in Table (1.1),

$$f_0 \propto \alpha^{-3} \left(1 - \frac{T}{T_c}\right)^{1/2} \xi_0^3 B^2 / C \quad (6.33)$$

and, noting that $\xi_0 \propto \sqrt{\kappa}$ in this regime,

$$f_0 \propto (\sqrt{\kappa})^3 \left(1 - \frac{T}{T_c}\right)^{1/2} \quad (6.34)$$

which is precisely the rhs of Eq. (6.32). Thus the Binder condition for linear CHC theory to be valid in the early time regime of SD simplifies to

$$f_0 \gg 1. \quad (6.35)$$

Thus, the parameter f_0 , which is related to the range of interaction in the system, $\sqrt{\kappa}$, must be very large in order to observe CHC type decomposition.

Condition (6.35) is not satisfied in this work. This agrees with the fact that nonlinear effects are important even at the earliest aging times with the immediate shift of the peak in $\Delta S(q, t)$ to smaller q . The values of ϵ listed in Table (6.2) reflect the immediate importance of the nonlinear terms at the earliest scans measured. Even for these times it was shown in § 6.2.1 that the CHC equation of motion does not track the measured $\Delta S(q, t)$. An estimate of the time range of validity of the CHC theory (*cf.* p. 115) $t_{\max} \sim -\ln \epsilon$ is negative for the ϵ obtained in Table (6.2). Assuming that the LBM theory is an accurate description of the early stages of phase separation and invoking the Binder criterion implies the CHC equation should never be valid for the Al-Zn system.

6.2.5 The coherent solubility curve

With the free energy parameters r and u in the LBM equation of motion, it is possible to obtain the mean field coherent coexistence line. For a LG free energy functional, δc_{coex} is located at $\sqrt{\frac{-r}{u}}$ (cf. Eq. 5.5). However, the dependence of r and u on the choice of α has demonstrated that a unique free energy cannot be determined from measured $\Delta S(q, t)$ using the LBM theory alone.

The sum rule (2.25) which relates the integrated intensity $Q(t)$ to composition fluctuations also says that well below T_c , $Q^{1/2}(t)$ should fall on the coexistence line provided the normalization to absolute intensities is correctly performed.⁹ This provides a means to choose the value of α uniquely since the location of δc_{coex} scales as $\alpha^{1/2}$ (cf. Eq. 5.5). The value $\alpha = 2.59$ used in the discussion of § 6.2.3 was chosen so that $\sqrt{-r/u}$ matched well the square root of the integrated intensity for the six runs well below T_c , as shown on Fig. (6.14). The circles in this figure show the values of $\sqrt{-r/u}$ with $\alpha = 2.59$. The integrated intensities correspond to the values at $t = 1.6$ s and the square root of these values are shown as squares.

The calculated δc_{coex} can also be compared to the square root of the integrated intensity predicted from the coherent solvus calculated for the two regular solution parametrizations of the miscibility gap boundary in § 1.3. The first parametrization was that of Lašek[21] (cf. Fig. 1.3) shown as a solid curve in Figure (6.14) and the second was suggested by Löffler *et al.*[26] (see footnote p. 18) and is shown as a dashed line. Due to the asymmetry of the coherent solvus in the AlZn alloy, even when the bulk sample composition is close to the critical composition as in this work, both the Al-rich (c_α) and Zn-rich ($c_{\alpha'}$) phase compositions have to be included in the calculation of $Q(t)$. Unfortunately, this also means that the complete solvus line cannot be derived from measurements at a single alloy composition.¹⁰

⁹This is valid at temperatures where contributions from thermal fluctuations to the scattering intensity are negligible compared to the scattering due to thermodynamically driven fluctuations (including domains). This condition is not satisfied near T_c and above.

¹⁰Two off-critical alloy compositions have also been investigated and the results will be reported separately.

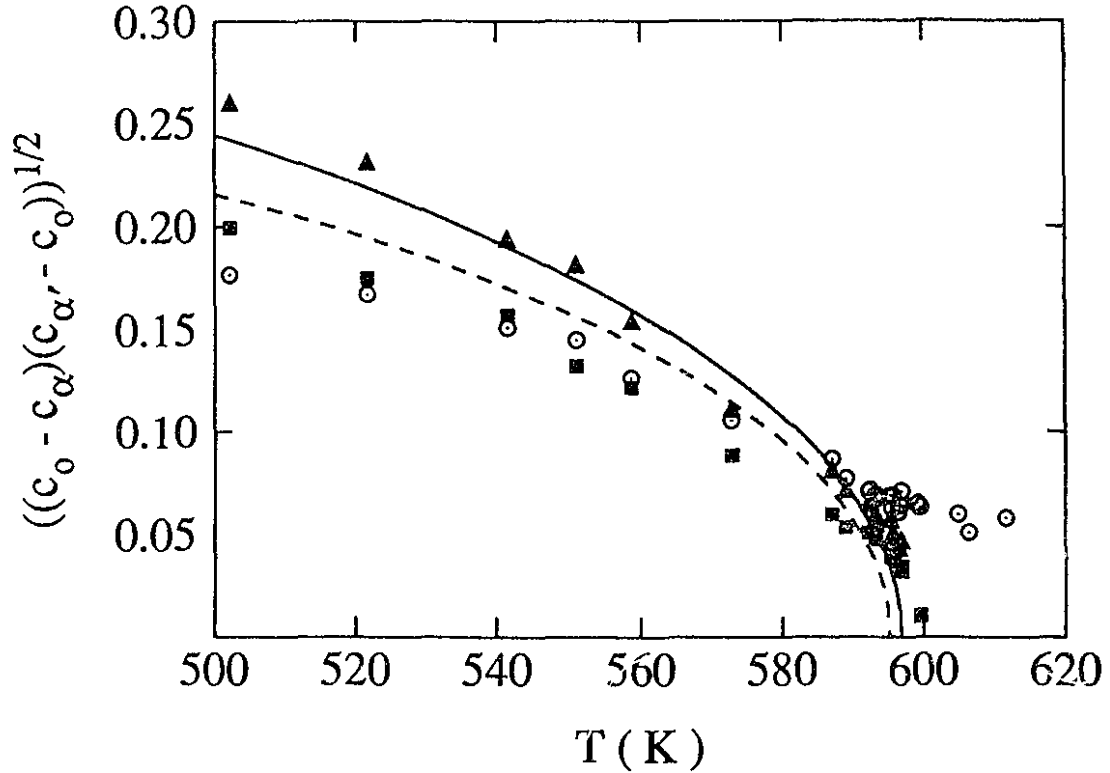


Figure 6.14: Square root of the measured intensity, $Q^{1/2}(t)$, at $t = 1.6$ s for all runs (■). Coherent solubility line δc_{coex} predicted from best fit free energy parameters r and u (○) with $\alpha = 2.59$ chosen to match $Q^{1/2}(t = 1.6s)$ for the six runs well below T_c . The best fit value of $\mathcal{A} + \mathcal{C}$ for $b(t)$ as described by the text (▲) and the integrated intensity predicted from the coherent solvus calculated using two different regular solution parametrizations introduced in § 1.3 (i) from Lašek[21] *cf.* Fig. 1.3 (solid curve) and (ii) from Löffler *et al.*[26], see footnote p. 18) are also shown. The compositions c_α and $c_{\alpha'}$ are respectively the coexistence compositions to the left and the right of the coherent miscibility gap.

The agreement between the solid curve and the square root of the measured integrated intensities (■) favorably supports the conversion factors employed to convert scattering intensity to structure factors.

Finally, the extrapolated values for $b(t)$ are plotted (▲) from the best fit values of $\mathcal{A} + \mathcal{C}$ obtained for $b(t)$ (*cf.* p. 165). As expected, since $\langle(\delta c)^2\rangle$ is the sum of two terms, σ^2 and b^2 , $b(t \rightarrow \infty)$ is lower than $Q^{1/2}(t)$. This parameter was included on Fig. (6.14) as it provides a good indication of the degree of phase separation. Furthermore, if the LBM theory could describe the SD until late stages, the one-point distribution functional should become a very sharp distribution about $\pm b(t \rightarrow \infty)$. However, the $S_{LBM}(q, t)$ will be shown to depart appreciably from

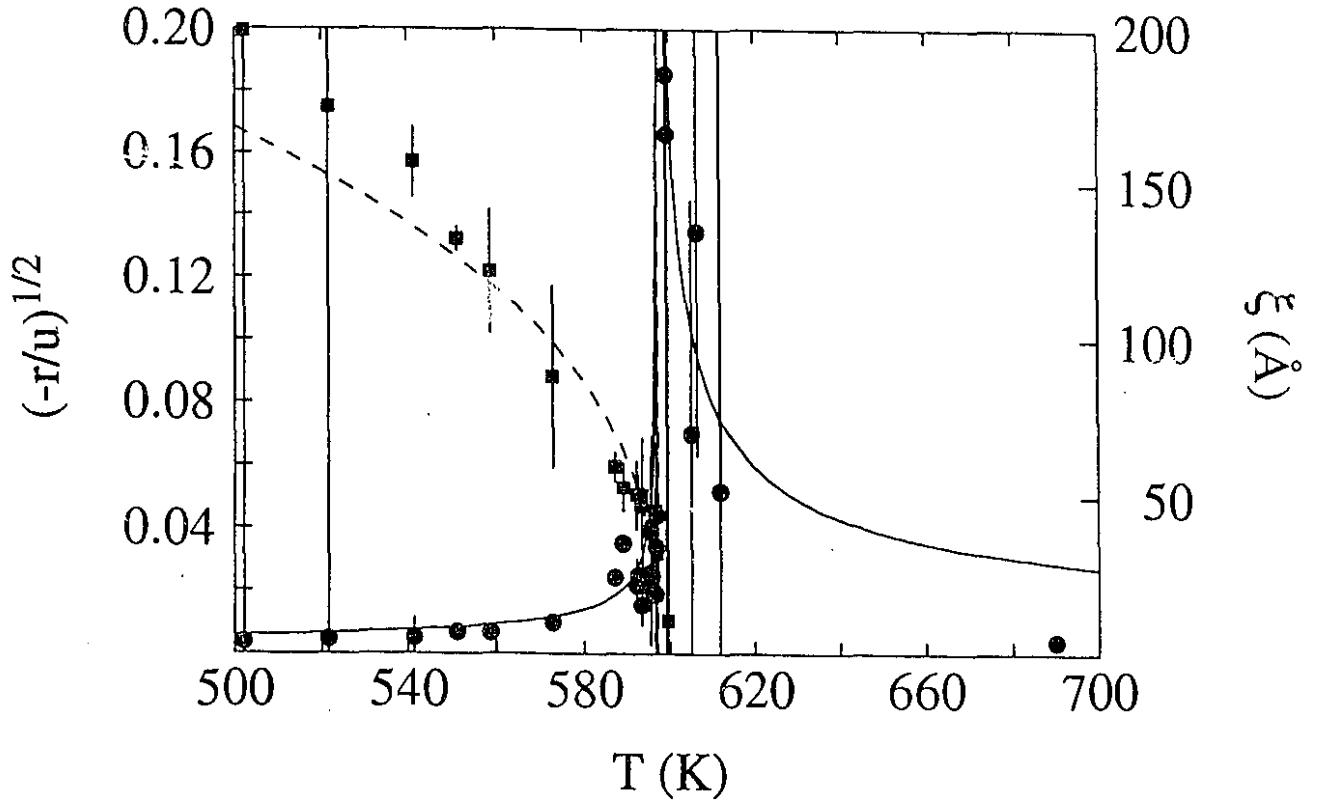


Figure 6.15: Best fit power law relation for the order parameter and the correlation length : Mean field correlation length ξ (●) and mean field coexistence line $\delta c_{coex} = \pm \sqrt{-r/u}$ (■). The dashed line shows the mean field coexistence line obtained by fixing the critical exponent $\beta = 0.5$, the mean field value. The solid line shows the mean field correlation length with the mean field critical exponent $\nu = 0.5$ (cf. Table 1.1).

$\Delta S(q, t)$ for times later than 1.6 s (§ 6.2.7).

With α set to 2.59, $\mathcal{A} + \mathcal{C}$ can be seen on Fig. (6.14) to go above the value of $\sqrt{\frac{-r}{u}}$. However, the curves in part (a) of Fig. (6.11) suggest that the initial increase is followed by an asymptotic behavior somewhat superimposed on a linear sloping background. Hence the asymptote appears not to saturate at a constant value. This is verified by extending the model times to 60 s.

Although the data near T_c is too limited for measurement of critical exponents, it is still interesting to compare the predicted mean field coexistence line and the correlation line with the power laws introduced in § 1.2 for the critical region. Figure (6.15) shows the power law behavior of the mean field coexistence line δc_{coex} (●) and of the correlation length ξ (■). The dashed line represents the mean field

coexistence line obtained by fixing the critical exponent in $\delta c_{coex} \sim B|\varepsilon|^\beta$ to the mean field value, $\beta = 0.5$. If, instead, a fit restricted to the data within 5% of T_c is performed, the critical exponent β obtained is 0.38 ± 0.04 , which compares well with the value 0.339 given in Table (1.1) for the 3-d Ising model. On the other hand, if the power law fit is performed over the whole range of data shown, the result is $\beta = 0.46 \pm 0.02$ which is closer to the mean field value.

The solid lines display the best fit result to the power law relationship for the mean field correlation length ξ (Eq. 5.37) which diverges at T_c as $\xi \sim \xi_\pm |\varepsilon|^{-\nu}$ ($T \gtrless T_c$) (cf. Table 1.1). The best fit value $\nu = 0.52 \pm 0.04$ obtained corresponds well to the mean field value $\nu = 0.5$ which has been given in Table (1.1).¹¹

Fitting the $\Delta S(q, t)$ with the LBM theory was found not to determine uniquely values of r and u . The numerical value of r and u for $\alpha = 2.59$ can be further investigated using the contact with the true thermodynamic free energy in the stable one-phase region as predicted by the regular solution model (RSM) which was used to model the miscibility gap in § 1.3. This is accomplished by matching the location of the solvus c_{solvus}

$$c_{solvus}^{(RSM)} = c_{solvus}^{(LBM)} \quad (6.36)$$

and the values of f'' along this line

$$\left. \frac{\partial^2 f^{(RSM)}}{\partial c^2} \right|_{c_{solvus}} = \left. \frac{\partial^2 f^{(LBM)}}{\partial c^2} \right|_{c_{solvus}} \quad (6.37)$$

However, in the RSM, f'' has a different value on the Al-rich (α) and the Zn-rich (α') branches of the solvus line. Thus, as pointed above, it is not possible to determine the position of the two branches with measurements performed at a single composition.

First, with the LG free energy employed in the LBM equation of motion,

$$\left. \frac{\partial^2 f^{(LBM)}}{\partial c^2} \right|_{c_{solvus}} = 4r \quad (6.38)$$

¹¹The values of the critical amplitudes used to produce the solid line were $\xi_- = 2.3 \pm 0.2 \text{ \AA}$ and $\xi_+ = 11 \pm 6 \text{ \AA}$.

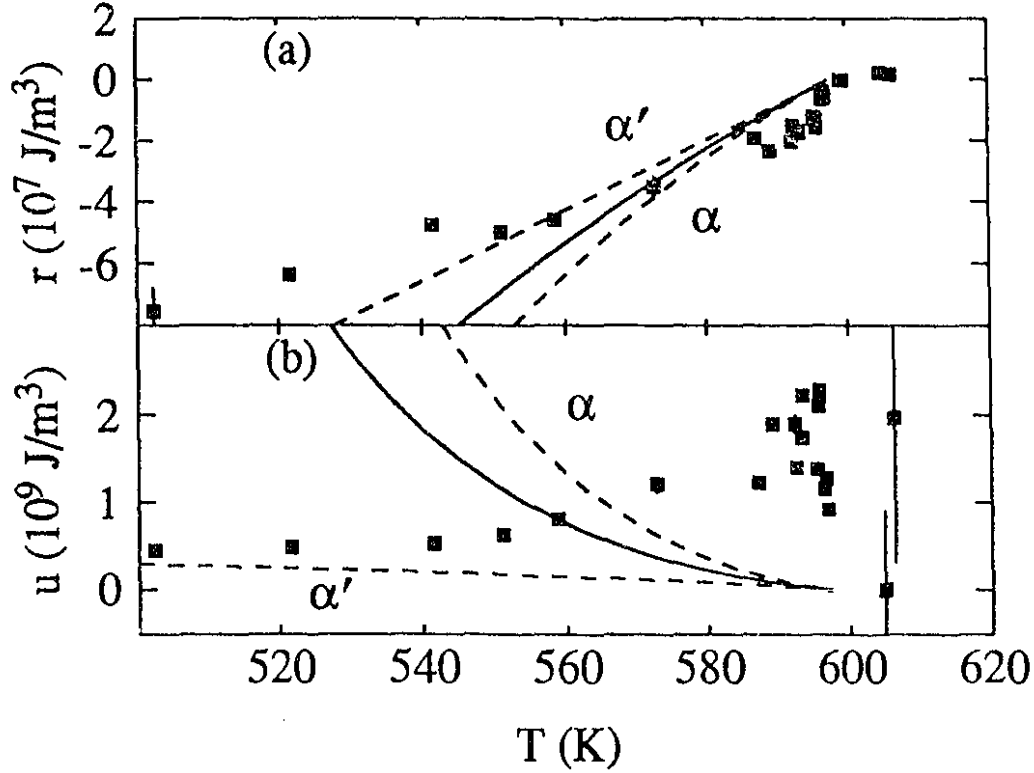


Figure 6.16: Contact between the regular solution free energy and the Landau-Ginzburg free energy functional. (a) The dashed lines labeled (α) and (α') display the value of r computed using Eq. (6.38) along the solvus line on the Al-rich (α) and the Zn-rich (α') sides respectively. The points show the values of r obtained from best fit LBM equation of motion for runs A through W for 1.6 s with $\alpha = 2.59$ (cf. Fig. 6.8). The solid line shows a weighted average of the two dashed curves (cf. Eq. 6.40). (b) Same as in (a) for the parameter u using Eq. (6.39) for the computation of the values and Eq. (6.41) for the average.

Since $(c_{\text{solvus}} - c_c)^{\text{(LBM)}} = \pm \sqrt{-r/u}$ then

$$\frac{1}{c_{\text{solvus}}^2} \frac{\partial^2 f^{\text{(LBM)}}}{\partial c^2} \Big|_{c_{\text{solvus}}} = 4u. \quad (6.39)$$

Second, for the RSM, using matching conditions (6.36) and (6.37) and Eqs. (6.38) and (6.39) the corresponding RSM values of r and u are obtained by the weighted averages

$$\bar{r}^{\text{(RSM)}} = \frac{1}{c_{\alpha'} - c_{\alpha}} \left[\frac{\partial^2 f^{\text{(RSM)}}}{\partial c^2} \Big|_{c_{\alpha}} (c_0 - c_{\alpha}) + \frac{\partial^2 f^{\text{(RSM)}}}{\partial c^2} \Big|_{c_{\alpha'}} (c_{\alpha'} - c_0) \right] \quad (6.40)$$

and

$$\bar{u}^{\text{(RSM)}} = \frac{1}{c_{\alpha'} - c_{\alpha}} \left[\frac{\partial^2 f^{\text{(RSM)}}}{\partial c^2} \Big|_{c_{\alpha}} (c_0 - c_{\alpha}) + \frac{\partial^2 f^{\text{(RSM)}}}{\partial c^2} \Big|_{c_{\alpha'}} (c_{\alpha'} - c_0) \right] \quad (6.41)$$

where c_α and $c_{\alpha'}$ are the RSM coexistence values on the Al and Zn-rich sides of the miscibility gap respectively.

Figure (6.16) shows r and u values along both branches of the solvus and a weighted average in each case, namely Part (a) shows that the order of magnitude and temperature dependence of r agrees with the prediction of the RSM along the solvus. However, in Part (b), u and $\bar{u}^{(RSM)}$ disagree on the temperature dependence. The RSM predicts a decrease as T_c is approached from below while the values obtained from fitting to the LBM theory show the opposite trend. This difference may be attributed to the anomaly mentioned earlier. Namely, it was found that r appeared to be governed entirely by the choice of α to give the required q_{max} resulting in a constraint on the value of u to generate the appropriate $A(t)$. It thus appears that even if the choice of an appropriate value of α allows one to produce the coherent coexistence line, the resulting values of r and, particularly u , are probably not "good" free energy parameters to extrapolate into the thermodynamic region of the phase diagram.

6.2.6 Interdiffusion

Obtained best fit mobilities M can be checked against tracer diffusion data in AlZn alloys using Eq. (1.12). Based on the results of other workers that the interdiffusion coefficient in AlZn solid solutions at $c_0 < 0.4$ is governed by the zinc tracer diffusivity[169] D_{Zn}^* , it is a good approximation to write

$$M = \frac{c_0(1 - c_0)}{N_V k_B T} (1 - c_0) D_{Zn}^* . \quad (6.42)$$

In the derivation of the LBM equation of motion it was assumed that M is independent of the local composition $c(\mathbf{r})$. Equation (6.42) satisfies this condition since M is considered sufficiently approximated by a composition independent value corresponding to the value for the bulk composition c_0 .

Fig. (6.8d) shows the mobility obtained from this relation with $D_{Zn}^*(T)$ computed from an Arrhenius equation (Eq. 1.11) with activation energy E_{0Zn} and fre-

Author	E_{0Zn} ($\times 10^{-19}$ J)	D_{0Zn}^* ($\times 10^{-6}$ m ² /s)
Hilliard[169]	1.66 ± 0.06	1.4 ± 0.8
Čermák[170]	1.7315 ± 0.0675	2.48 ± 1.72
Gödény[171,172]	1.69 ± 0.03	1.8 ± 0.3

Table 6.3: Interpolated activation energy, E_{0Zn} , and pre-exponential factor, D_{0Zn}^* , (cf. Eq. 1.11) for Zn self-diffusion in $Al_{0.67}Zn_{0.38}$ measured by tracer diffusion.

quency factor D_{0Zn}^* interpolated for $c_0 = 0.38$ for the three measurements of tracer diffusion in concentrated AlZn alloys reported in literature. In each case, the interpolated values of E_{0Zn} and D_{0Zn}^* from the two compositions that bracket c_0 are given in Table (6.3).¹² The activation energies E_{0Zn} were interpolated linearly and the pre-exponential factors D_{0Zn}^* were interpolated logarithmically. The values of E_{0Zn} are of order 1 eV (for instance, $E_0 = 1.04$ eV for the result of Hilliard *et al.*[169]). The errors are interpolated from their values at the bracketing compositions and are thus estimates. The value of the atomic density N_V is taken from Table (1.2). The agreement between the calculated and the best fit M is particularly striking in view of the fact that the lowest temperatures for which self-diffusion coefficients of Zn were measured by these workers were in the one-phase region. For instance, the measurements of Hilliard *et al.*[169] at the lowest temperatures were 633 K for $c = 0.369$ and 598 K for $c = 0.494$. The error bars on the calculated M are more than 50% of the values due to large error bars in D_{0Zn}^* .

Equation (6.42) is the most direct comparison between M and diffusion data. However, in the past (cf. § 1.4), the interdiffusion constant \bar{D} would be obtained from fits to the CHC equation of motion. In the formulation of the LBM equation of motion, atomic mobilities M are obtained separately from the thermodynamic driving force. Hence, to compare best fit M to interdiffusion constants, it would be necessary to know the second derivative of the free energy with respect to com-

¹²These compositions are respectively 0.369 and 0.494 for Ref. [169], 0.3127 and 0.4151 for Ref. [170], and 0.289 and 0.400 for Ref. [171,172].

position that is, to “recouple” the thermodynamic driving force with the mobilities using Eq. (1.25).

Two situations allow the approximation of f'' by r in Eq. (1.25). Firstly, at early stages of SD when $\delta c \approx 0$ the “ c^4 ” free energy model (Eq. 5.4) gives $f'' = r$ and

$$\tilde{D} = Mr. \quad (6.43)$$

The second case is at the other extreme, when the local compositions are near equilibrium values. The contact between the coarse-grained free energy and the free energy obtained by the regular solution model performed in the preceding section and shown in Fig. (6.16) indicated that in this case $f'' \approx r$. This allows the evaluation of \tilde{D} along the solvus also using Eq. (6.43). Using either the RSM value model of f'' or LBM best fit r with $\alpha = 2.59$ will provide the same thermodynamic driving force. Since $r \sim \alpha^{-2}$ and M is independent of α , $\tilde{D} \sim \alpha^{-2}$. As an example of a typical value in this work, at 541 K, $\tilde{D} = -5.0 \times 10^{-17} \text{ m}^2/\text{s}$ for $\alpha = 2.59$. With expression (6.43), \tilde{D} turns out to be independent of the overall intensity calibration for $\Delta S(q, t)$ (cf. p. 163).

In homogenizing systems, the temperature dependence of the thermodynamic driving force is weak.[174] However, since f'' vanishes at T_c and has a different sign on either side of T_c in systems which undergo SD, the thermodynamic driving force is strongly temperature dependent. In this case, Hilliard[32] suggests to expand $f''(T)$ about T_c ,

$$f''(T) = (T - T_c) \frac{\partial f''}{\partial T} = -(T - T_c) s'', \quad (6.44)$$

where $s'' = \partial^2 s / \partial c^2$ (s is the entropy per unit volume) has negligible temperature dependence. Equations (1.12 and (1.25) can be combined to write

$$\tilde{D} = \frac{c_0(1 - c_0)f''(T)}{N_V k_B T} [c_0 D_A^* + (1 - c_0) D_B^*] \quad (6.45)$$

which can then be rewritten as

$$\frac{\tilde{D} T}{T - T_c} = -\frac{c_0(1 - c_0)s''}{N_V k_B} [c_0 D_A^* + (1 - c_0) D_B^*]. \quad (6.46)$$

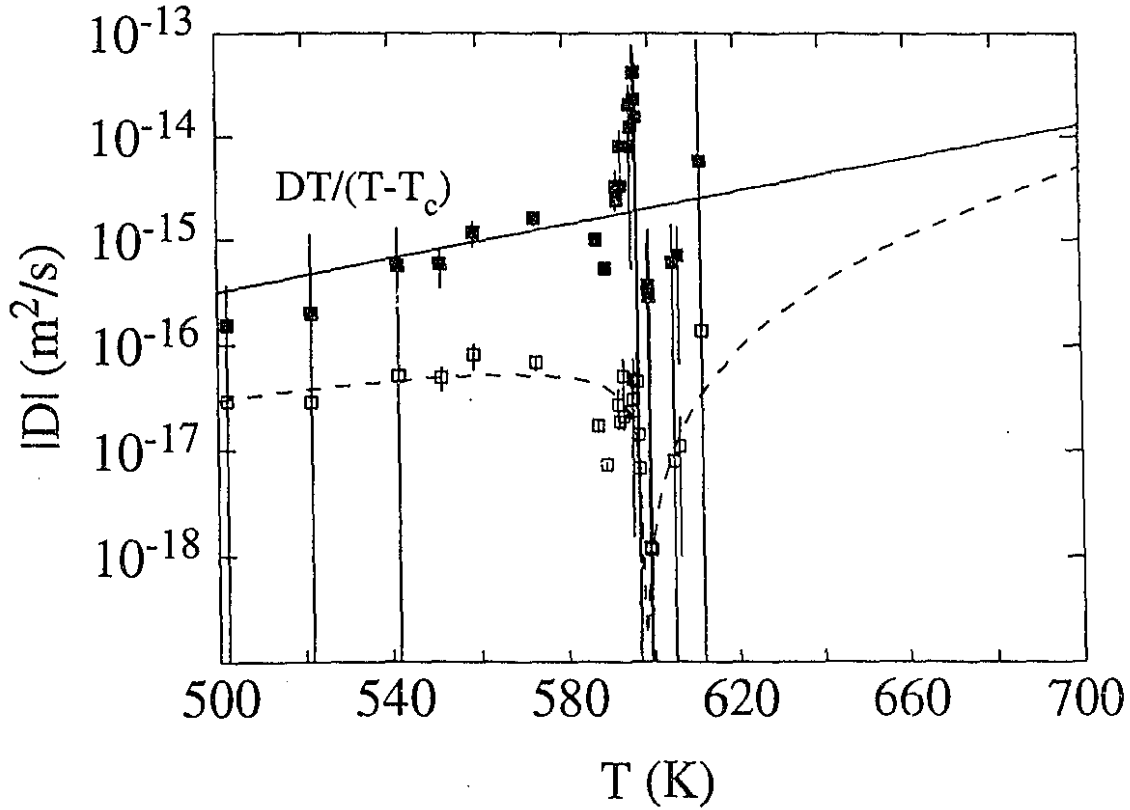


Figure 6.17: Interdiffusivity \bar{D} obtained from Eq. (6.43) (\square). Below T_c , $-\bar{D}$ is plotted. The dashed line is intended as a guide to the eye. The solid symbols (top curve) correspond to the product $\bar{D}T/(T - T_c)$ following a representation suggested by Hilliard.[32] The solid line shows that the Arrhenius curve for $\bar{D}T/(T - T_c)$ both above and below T_c (see footnote p. 183).

Based on relation (6.46), Hilliard then suggests to present interdiffusion data near the spinodal line as an Arrhenius plot of $\bar{D}T/(T - T_c)$. A straight line would be expected if the activation energies of the tracer diffusivities of the two constituents are not too different or if the one tracer diffusivity dominates over the other. Such a plot is shown in Fig. (6.17) with the results of Eq. (6.43) with $\alpha = 2.59$. The solid symbols (top curve) correspond to $\bar{D}T/(T - T_c)$. The solid curve $\bar{D}T/(T - T_c)$ versus T with a logarithmic ordinate axis shows that the Arrhenius plot extrapolates well into the spinodal. The two parameters required in the Arrhenius relation to produce the solid line, E_0 and A , are highly correlated when performing a fit with the data and the range of data is limited to two decades. Thus, best fit E_0 and A could not be

determined accurately.¹³ The bottom set of points in this figure show \bar{D} calculated from Eq. (6.43) (\square). This quantity is discontinuous at T_c ($\bar{D} \rightarrow 0$) since $r \rightarrow 0$ as $T \rightarrow T_c$. Below T_c , the points show $-\bar{D}$.

In substitutional solid solutions such as AlZn alloys, the interchange of atoms (Al \leftrightarrow Al, Al \leftrightarrow Zn and Zn \leftrightarrow Zn) occurs through vacancies.[28] More generally, the tracer self-diffusion of Zn (and though much smaller, Al) by means of a vacancy mechanism is closely related to the motion of the vacancies, which may be used to define a vacancy diffusion coefficient. Thus, it is important to have an equilibrium concentration of vacancies in the alloy at the aging temperature to measure appropriate diffusion properties. If the concentration of vacancies is higher than the equilibrium value, then the diffusion constants observed will be higher than should otherwise be observed. In a quench-and-age experiment, the possibility exists for the presence of "quench vacancies" retained from the initial one-phase high temperature state. These quench vacancies are gradually eliminated from the system by being trapped at zone interfaces or removed at sinks. Thus, these should decrease with time until the density of vacancies reaches the value corresponding to the expected "thermal vacancy" concentration. These are then in equilibrium at the aging temperature and their number should remain constant. In a scenario in which the vacancy concentration would not have reached an equilibrium value after a quench and thus would still evolve over the course of the time resolved measurement¹⁴ the diffusion constant would decrease during the experiment, *i.e.* the time separating two successive interchanges of atoms (or atom-vacancy interchanges) would not be constant.

¹³The values obtained in producing the best fit solid line to

$$\bar{D}T(T - T_c) = A \exp(-E_0/k_B T)$$

on Fig. (6.17) were $E_0 = 9 \pm 5 \times 10^{-20} \text{J}$ ($0.6 \pm 0.3 \text{ eV}$) and $A = 1 \pm 6 \times 10^{-9} \text{ m}^2/\text{s}$.

¹⁴Such a scenario is proposed by Hennion *et al.*[60] in their measurement of nucleation and growth in single crystal AlZn. They suggest that quench vacancies are responsible for a high diffusion constant during the initial stages of phase separation in their experiments.

No attempt is performed to estimate the vacancy concentration relaxation time. Facts in this study suggest that they have probably reached equilibrium concentrations by the time the isothermal annealing begins. Firstly, the aging temperatures are higher than any previous work on SD in AlZn alloys and a polycrystalline sample was used. Therefore there should be more sites for the quenched-in vacancies to become inactive and their diffusion to these sites should be faster than at lower temperatures. Also, the existence of a maximum decomposition rate above which the process is limited by the driving force and below which it is diffusion limited supports the view that the vacancies intervening in the diffusion at the aging temperature are not quenched-in but thermally activated. Finally, the best evidence is that the measured tracer diffusivity of Zn (*i.e.* self-diffusion of Zn at thermal equilibrium) extrapolates well into the spinodal region for the deeper quenches as presented in Fig. (6.8d).

Finally, it should be noted that vacancy mediated diffusion has recently been used in a MC simulation study by Yaldram *et al.* on a two-dimensional lattice.[175] They found that diffusion depends on the atoms with the higher jump rate (*cf.* p. 108) or, equivalently, the higher self-diffusion coefficient, in agreement with the working hypothesis used to produce Eq. (6.42). Their results essentially do not differ from the usual Kawasaki spin-exchange dynamics employed in MC studies of diffusive problems (*i.e.* atom-atom swaps).

6.2.7 Breakdown of LBM

The comparison of the predicted evolution of $S_{\text{LBM}}(q, t)$ for later times and the $\Delta S(q, t)$ collected in the long runs (AA — EE) was performed. Though there is always a temperature difference between the two runs in any pair of a fast run and a long run, it is possible to get an estimate of the performance of LBM at later times to describe the measured $\Delta S(q, t)$. Fig. (6.18) shows the $S_{\text{LBM}}(q, t)$ calculated up to 52.6 s from best fit parameters to short run C (541 K) reported in § 6.2.3 (solid lines). The experimental $\Delta S(q, t)$ (points) correspond to deconvolved structure factors for

run BB (537 K). This late stages run has the temperature nearest to that of run C. This Figure shows that at 2.6 s, the $S_{\text{LBM}}(q, t)$ still tracks well the data whereas the $S_{\text{LBM}}(q, t)$ growth is slower than the measured $\Delta S(q, t)$ for later times. Also, the maximum in the extrapolated $S_{\text{LBM}}(q, t)$ does not move to lower q as rapidly as that in the measured $\Delta S(q, t)$. At higher temperatures, as the maximum of $\Delta S(q, t)$ moves earlier to lower q , the breakdown between $S_{\text{LBM}}(q, t)$ and measured $\Delta S(q, t)$ occurs faster.

For the long scans, $t = 0$ is defined as the time at which the measured sample temperature crosses T_c . For instance, in the case of run BB, the first scan read after reaching the aging temperature was recorded 0.6 s after T_c was crossed. Since one scan is recorded every second ($\text{ET} = 0.01, I = 100$, cf. Table 6.1), then the third scan at the aging temperature is stored at $t = 2.6$. This first $\Delta S(q, t)$ shown corresponds to that scan. However, each recorded scan in the long runs integrates over a longer time and a readout at 1.6 s would compare best to an earlier scan during a fast run ($\text{ET} = 0.01, I = 1$). Nevertheless, this discrepancy is negligible in the check of the late time extrapolation of the $S_{\text{LBM}}(q, t)$, as evidenced by Fig. (6.18).

Fig. (6.19) compares the time dependence of the wavevector q_m corresponding to the maximum of $\Delta S(q, t)$ for runs C and BB (points) and of $S_{\text{LBM}}(q, t)$ (line). As observed in Fig. (6.18), the coarsening displayed by $S_{\text{LBM}}(q, t)$ is slower than that of $\Delta S(q, t)$. It is found that extrapolation of $S_{\text{LBM}}(q, t)$ with the parameters from the best fit to run C (up to 1.6 s) results in a time dependence of q_m which goes asymptotically to $t^{1/6}$ as shown by the slope of the solid line in the figure. A regime with slow $t^{1/6}$ coarsening was reported in the original LBM work[7]. However, after $\approx 50\tau$, they also report a transition to a $t^{0.212}$ coarsening. Figure (6.19) presents no evidence of such a transition for $q_m(t)$ for $S_{\text{LBM}}(q, t)$ even though for run C, Table (6.2) gives $\tau/t = 114.9 \pm 0.7 \text{ s}^{-1}$ and thus the $S_{\text{LBM}}(q, t)$ were computed up to 6894τ . The absence of transition regime in the generated $S_{\text{LBM}}(q, t)$ is not explained even though, as was mentioned in § 6.2.4, the calculated value of the system dependent parameter f_0 from best fit results to early stages $\Delta S(q, t)$ is of

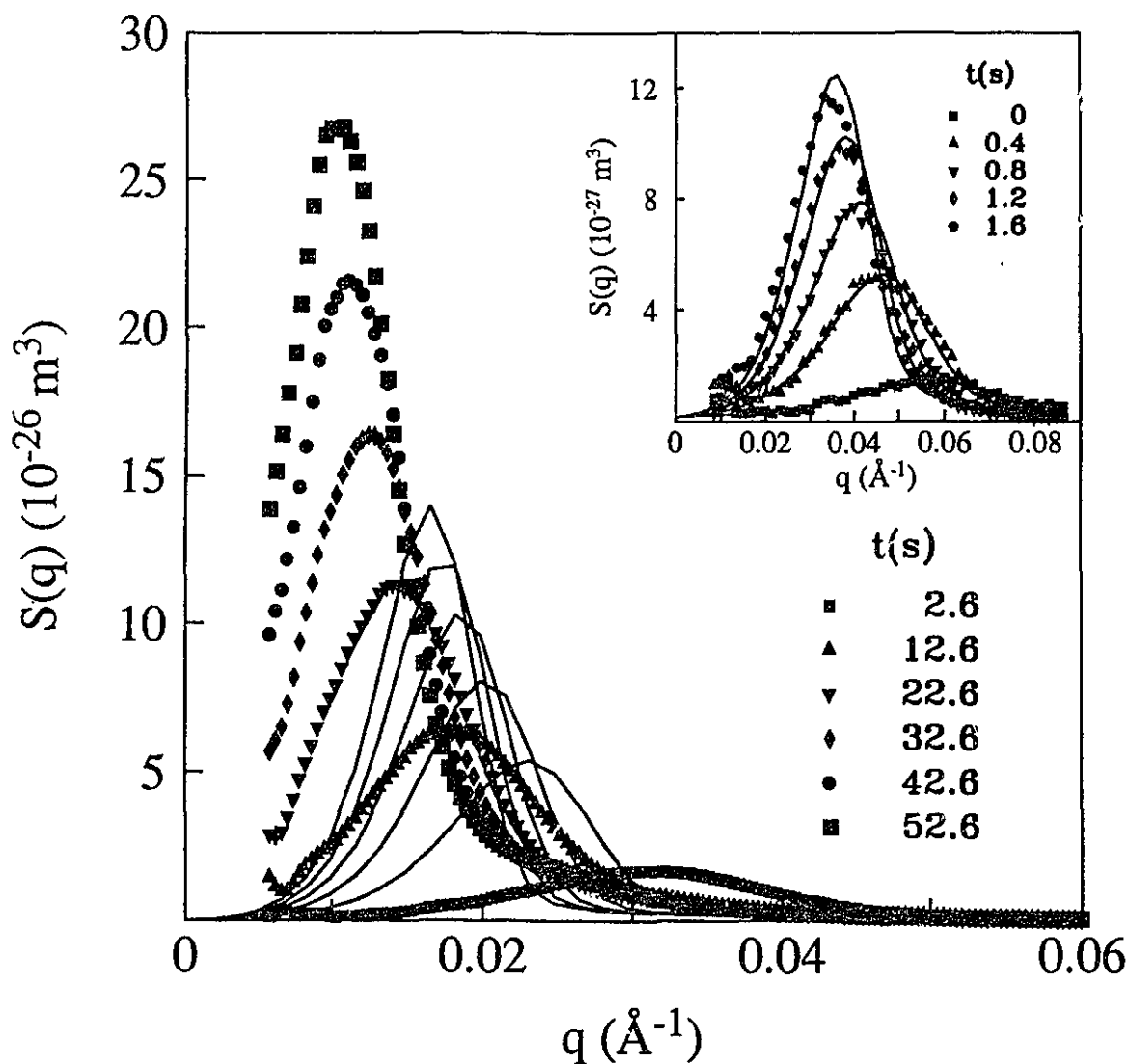


Figure 6.18: Breakdown of LBM after early stages. The points correspond to the deconvolved $\Delta S(q, t)$ for run BB, at $T = 537$ K. The solid curves show the $\Delta S_{\text{LBM}}(q, t)$ calculated from the parameters obtained from the fit to 1.6 s for run C (541 K). The first $\Delta S_{\text{LBM}}(q, t)$ calculated for $t = 2.6$ s is completely covered by the experimental $\Delta S(q, t)$ for that time. The bumpiness in $\Delta S_{\text{LBM}}(q, t)$ at the later times is due to the discretization in q . The inset shows $\Delta S(q, t)$ for run C with the best fit ΔS_{LBM} to 1.6 s. The $t = 0$ data is the quenched-in structure factor.

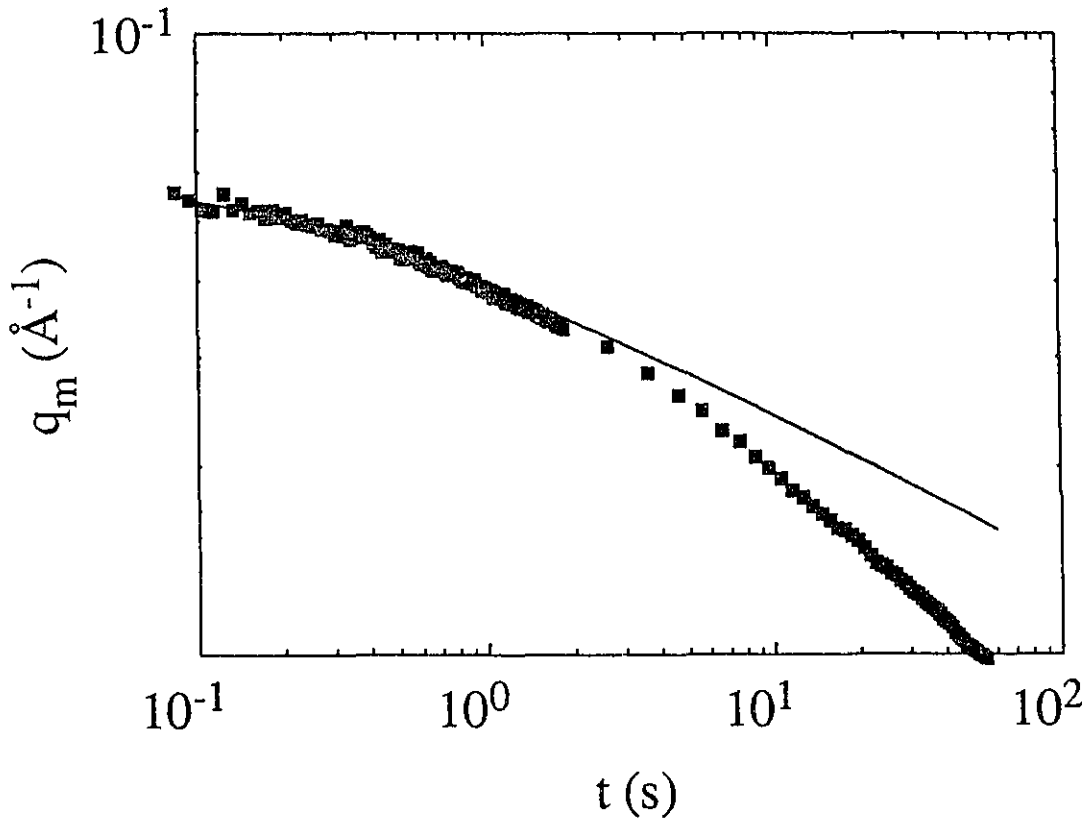


Figure 6.19: Late time coarsening with LBM. The points show the position of the maxima of $\Delta S(q, t)$ for runs C and BB, q_m for all scans. The solid line shows q_m obtained from $S_{\text{LBM}}(q, t)$ up to $t = 60$ s.

the same order as the estimated value used by Langer *et al.*[7] to generate their $S_{\text{LBM}}(q, t)$.

Finally, this investigation of the time at which the $S_{\text{LBM}}(q, t)$ departs significantly from the measured $\Delta S(q, t)$ confirms that fits to times up to 1.6 s are expected to be equivalent. Since the values of τ are temperature-dependent, with maximum values for quenches to temperatures near that of maximum phase separation rate (*cf.* Table 6.2), a logical choice would have been to fit up to equal values of τ for all temperatures in order to obtain the temperature dependence of the model parameters. However, since the breakdown between the LBM and measured structure factors occurs for times longer than the duration of the fast run, the fits can equivalently be performed up to 1.6 s for all runs. As noted in § 6.2.3, this was also verified by performing fits for up to 0.1, 0.2, 0.4, 0.8, 1.2 s in all cases and obtaining parameter values within the error bars of those obtained for the fits to 1.6 s.

6.3 Late stages

6.3.1 Growth law and scaling

The data collected for late-stage studies (*i.e.* up to 60 s) will now be discussed. Three aspects will be addressed: the scaling exponents n and n' , the scaling form $F(x)$, and the high wavenumber tail of $\Delta S(q, t)$ (*cf.* § 5.5).

For this part of the analysis it is necessary to use deconvolved scans. The deconvolution procedure has been the topic of § 4.5.2 and the resulting unsmearred structure factors for runs AA (511 K) and EE (588 K) were presented in Fig. (4.15). It was seen that the effect of the deconvolution is more important near the beamstop. The maximum of $\Delta S(q, t)$ is found closer to the beamstop at an earlier time, the higher the run temperature, due to a combination of both higher decomposition rates for the runs of high τ (*cf.* Table 6.2) and the decrease of q_c (*i.e.* larger ξ) as T increases. Furthermore, for the runs corresponding to the higher temperatures, CC, DD and EE, there is a time at which the peak maximum is blocked by the beamstop (35.4, 27.5 and 19.6 s respectively after the sample temperature has crossed T_c in the quench process).

A usual graphical check for scaling is to plot the scaled quantities $S(q, t)/S_m(t)$ versus $x \equiv q/q_m(t)$ with $S_m(t)$ the maximum of $S(q, t)$ and $q_m(t)$ the corresponding wavevector, as defined in § 5.5, and to verify that the obtained profiles overlap for all times in the scaling regime. Figure (6.20) shows such a plot for run BB (536.9 K) at selected times. However, this plot makes use of the $\Delta S(q, t)$, which have the high temperature scattering subtracted, instead of using $S(q, t)$. Since the equilibrium scattering at T_c is small compared to the late-stage $S(q, t)$ for runs AA — EE ($< 10^{-29} \text{ m}^3$, *cf.* Fig. 4.11), using $\Delta S(q, t)$ instead of $S(q, t)$ should not affect appreciably the results.

Except for the first scan (at $t = 2.6$ s), all scans displayed on this plot *should* have been recorded at intermediate or late stages. However, the structure factors do not quite scale, *i.e.* the displayed $\Delta S(q, t)/\Delta S_m(t)$ do not identically overlap.

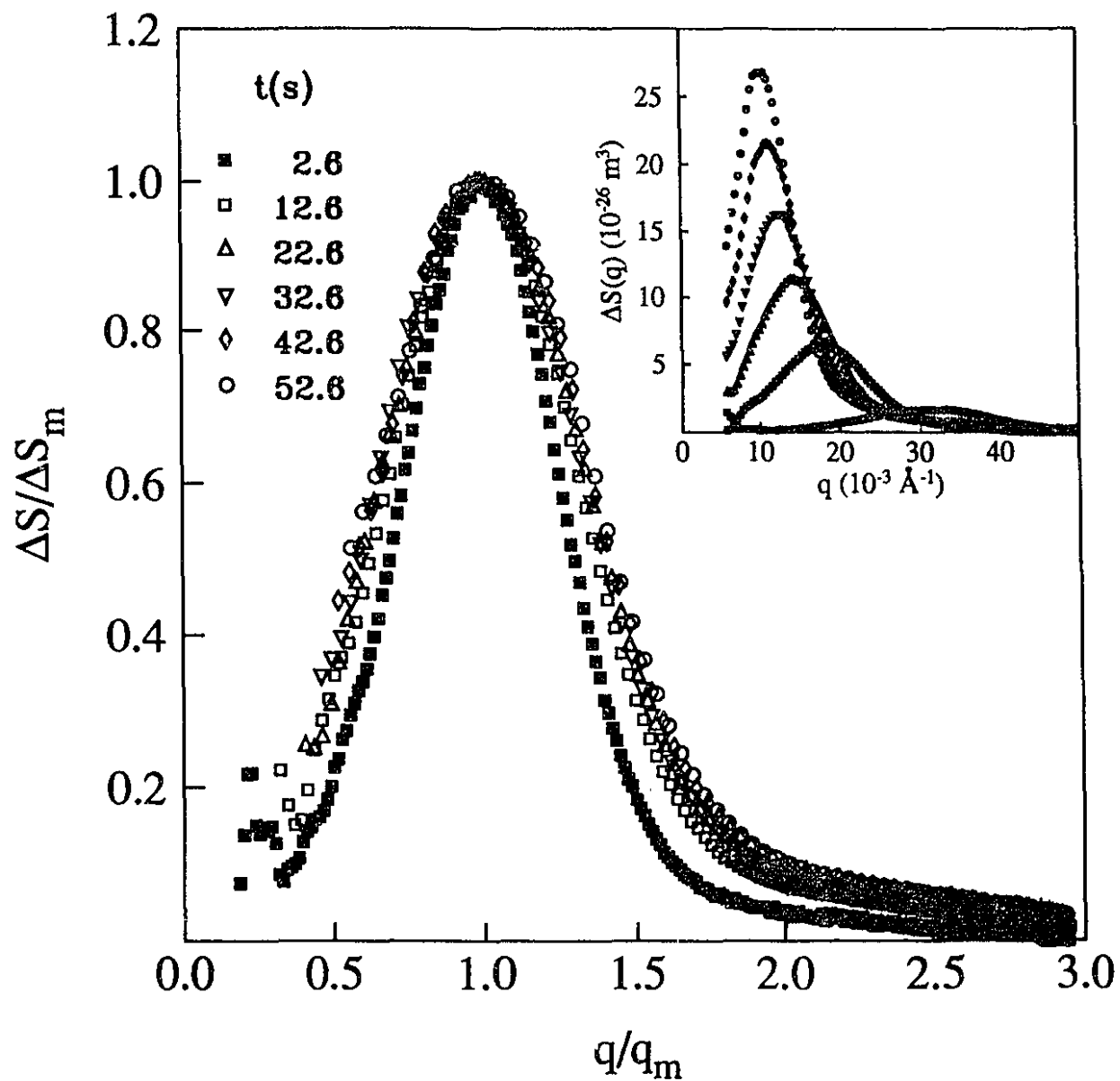


Figure 6.20: "Classical" scaling plot: late-stage scaled structure factors for run BB (537 K). The scaled scattering function does not quite scale. A scan was recorded every 1.0 s, hence the displayed $\Delta S(q, t)/\Delta S_m(t)$ are ten scans apart. The inset shows the $\Delta S(q, t)$ before scaling.

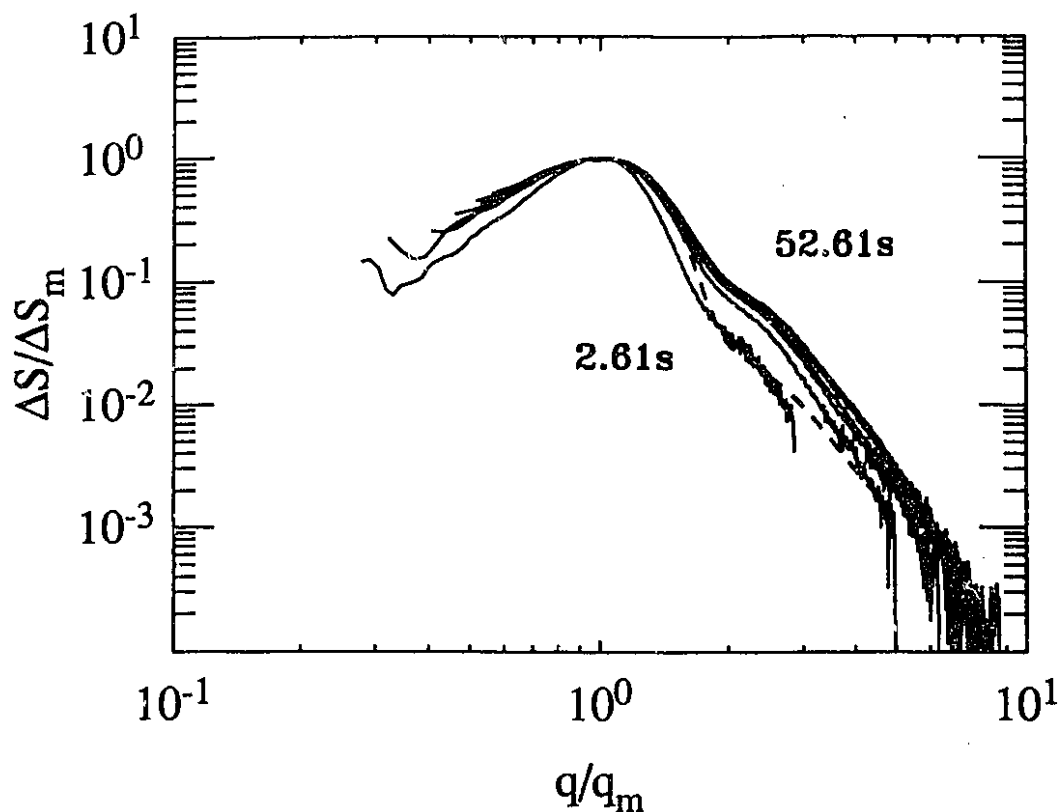


Figure 6.21: Logarithmic plot displaying the scaled structure factors $\Delta S(q, t)/\Delta S_m(t)$ at $T = 537$ K for the same times as Fig. (6.20). A shoulder is observed on the high q tail. The dashed line shows the best fit result to the Ohta-Nozaki scaling form, $F_{(ON)}(z)$ (*cf.* text).

When all scans of run BB are examined, it is found that from $t \sim 11$ s, the scaled scattering profiles broaden more slowly than at earlier times. This deviation from scaling is well outside the experimental error. Examination of the inset to Fig. (6.20) indicates that $\Delta S_m(t)$ undergoes an almost fivefold increase in this “quasi scaling” regime. All runs performed for the late-stage studies (AA through EE) have been found to display a similar quasi scaling feature.

A logarithmic plot displaying the same scaled structure factors for run BB is given in Fig. (6.21). This representation shows the extent to which the $\Delta S(q, t)/\Delta S_m(t)$ are broadening with time. On the high q side $\Delta S(q, t)/\Delta S_m(t)$ does not drop as q^{-4} (the dashed line, which will be described below, has a q^{-4} tail). Hence, Porod’s law (Eq. 2.32) is not satisfied.

Fig. (6.21) also shows that the scaled structure factors present a shoulder at

approximately $3q_m$. This shoulder is one of the most interesting results of the late stages study. Experimentally, a shoulder at high q has been reported for light scattering measurements on deuterated polymers[90] and in neutron scattering measurements of the static structure of porous glasses.[176] A computer simulation study on a cell-dynamical-system by Shinozaki[166] also produced a structure factor with a shoulder (*cf.* § 5.5.2). However, its existence had never been reported clearly for a binary alloy.

In Fig. (5.5), it was shown that the analytical expression for the Ohta-Nozaki scaling form $F_{(ON)}(x)$ (Eq. 5.91) also possesses a shoulder. The dashed line in Fig. (6.21) shows a best fit to $F_{(ON)}(x)$ for the $t = 12.62$ s “scaling profile” (the second solid curve from the bottom) with $A = 4.02$. Comparison between the dashed line and the corresponding $\Delta S/\Delta S_m$ shows that the best fit $F_{(ON)}(x)$ drops too steeply above q_m . In fact, the measured scattering at the shoulder is at least three times larger than would be predicted by $F_{(ON)}(x)$.

Figure (6.22) shows the best fit Fratzl-Lebowitz scaling form, $F_{(FL)}(x)$ (Eq. 5.87) obtained for $\Delta S(q,t)/\Delta S_m(t)$ also for run BB at $t = 12.61$ s. This logarithmic plot shows again the departure from a q^{-4} tail at high q observed in the data since $F_{(FL)}(x)$ (solid curve) has this q^{-4} dependence. Evidently, the $F_{(FL)}(x)$ scaling form needs to be modified for these data since it does not possess a shoulder at high q .

Figure (6.23) presents a Porod plot, ($q^4\Delta S$ versus q), for run CC at four different times. (At $t = 2.46$ s, the SD has not yet entered the late stages.) Such a plot is useful to check sum rule (2.32) since for this rule to be valid $q^4\Delta S(q,t)$ should tend to a constant. This is not the case here since $q^4\Delta S(q,t)$ still varies for large q as expected from the absence of a q^{-4} tail in Fig. (6.21). This Porod plot also hints at the existence of a second shoulder at the latest times (at $\sim 0.075 \text{ \AA}^{-1}$ for $t = 52.46$ s).

Shoulders at high q are not unexpected in late stages of SD and have been observed for instance during the SD of polymer mixtures as mentioned above. The

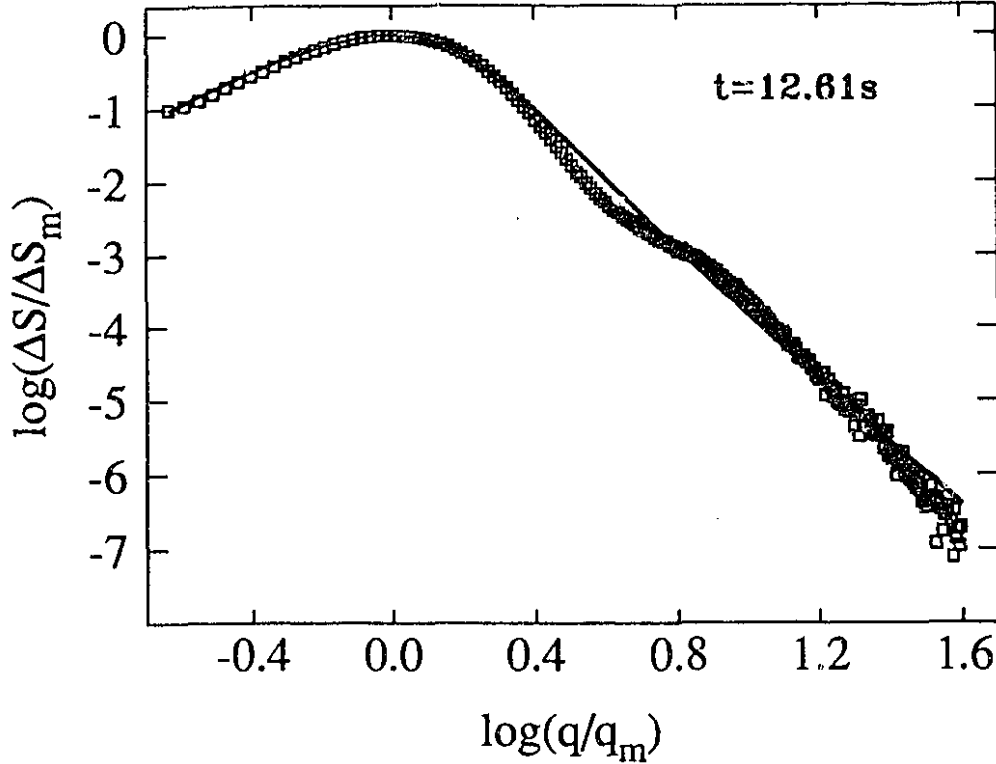


Figure 6.22: Scaled structure factor for run BB ($T = 537$) K at $t = 12.61$ s (\square) with best fit Fratzl-Lebowitz scaling form, $F_{(FL)}(x)$ (Eq. 5.87) with $d = 0.06$ and $\gamma = 0.407$ (solid curve).

scattering from randomly distributed sharp interfaces with, however, a characteristic length scale, $\xi \sim q_c^{-1}$ should give rise to higher order harmonics. Furthermore, the observed late stages $q^4 \Delta S(q, t)$ are reminiscent of those observed by workers in studies of atomic dynamics in liquids[177] where many oscillations exist about a constant value. In the case of liquids, however, instead of $q^4 S(q)$ going to a constant for large q , the invariant is $q^2 S(q)$. Spooner *et al.*[178] have reported that a Porod asymptote is reached in a Porod plot of neutron scattering data obtained during SD in a FeCr alloy. However, they do not report a shoulder at high q .

Fig. (6.24) shows the time dependence of $\Delta S_m(t)$, the maximum of $\Delta S(q, t)$, and the corresponding q_m^{-1} for the run BB (537 K). The solid lines are best fit to power laws with

$$\Delta S_m(q_m, t) = \Delta S_0(t + t_0)^{3n'} \quad (6.47)$$

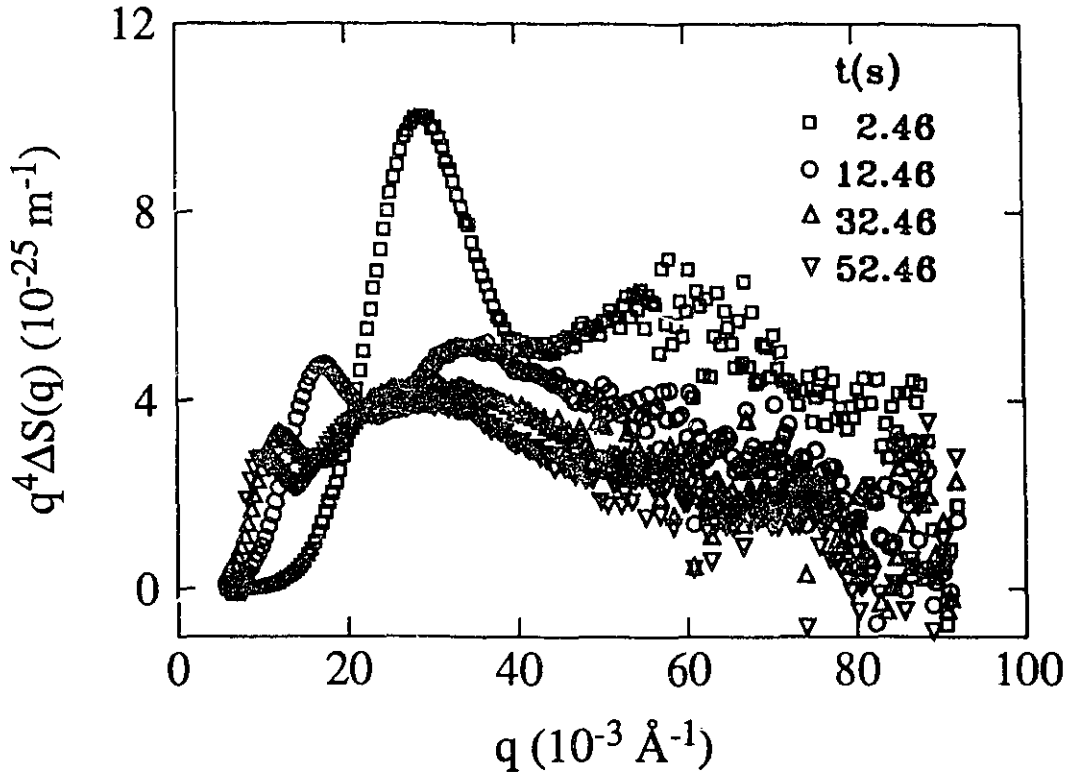


Figure 6.23: Porod plot for run CC ($T = 563$ K) at selected times.

and

$$q_m(t) = q_0(t + t_0)^{-n}. \quad (6.48)$$

The best fit values for the parameters ΔS_0 , t_0 and n' in Eq. (6.47) and for q_0 , t_0 and n in Eq. (6.48) are listed in Table (6.4) along with values for the other runs. All runs (AA — EE) displayed similar quality power law fits. The uncertainties reported for the numerical values of the parameters correspond to the calculated standard deviations with the goodness of fit estimator $\chi^2 = 1$ when all points are assumed to have an equal weight in the least squares fit.

The growth exponent $n = 0.42$ for $q_m^{-1}(t)$ in run BB as well as values obtained for all runs are higher than the value $n = 1/3$ predicted by the LSW law (*cf.* p. 128). These values indicate that coarsening occurs at a faster rate than predicted from long range diffusion fields.

The result that growth exponents are greater than $1/3$ for all late-stage runs is

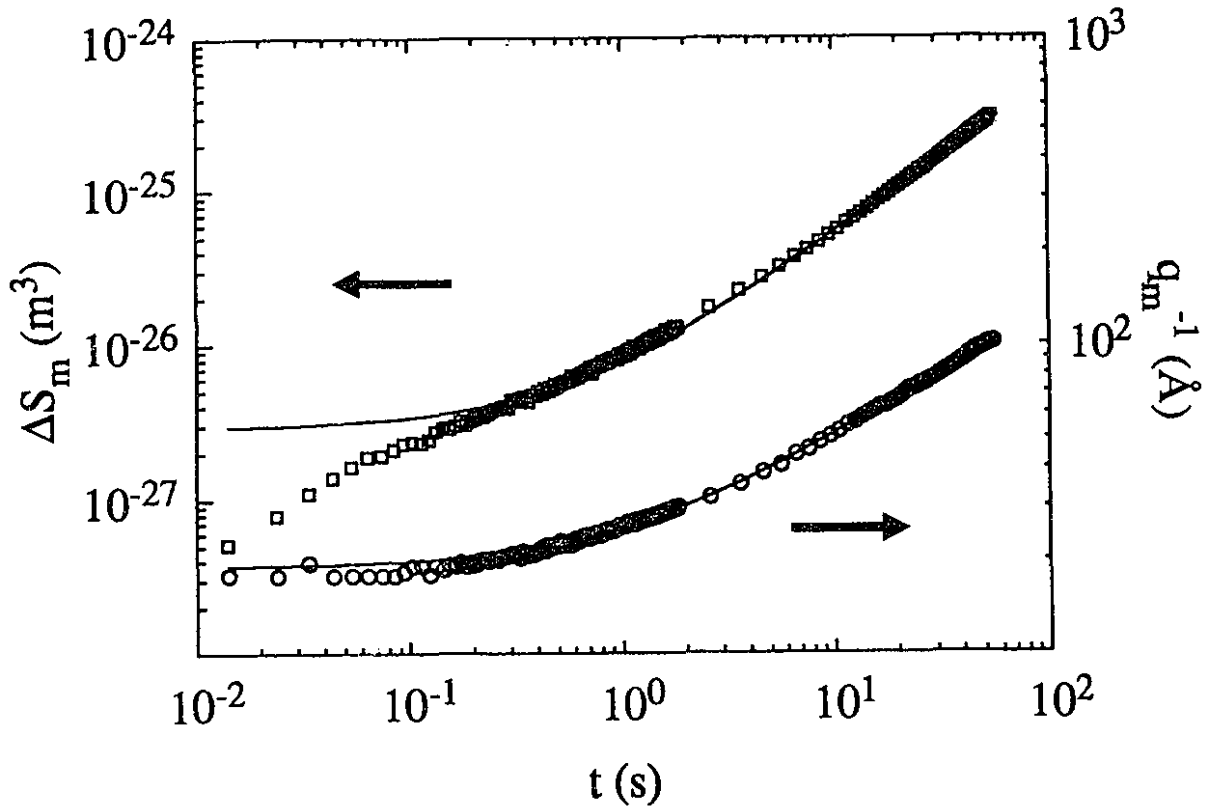


Figure 6.24: Time dependence of the maximum of the structure factor, S_m (\square), and the corresponding q_m^{-1} (\circ) for run BB ($T = 537$ K). The solid lines are power law fits to Eqs. (6.47) and (6.48).

somewhat unexpected. According to Equation (5.77), $n_{eff}(t)$ should asymptotically tend to $1/3$ from *below* (linearly in $1/R(t)$ with ($R_0 > 0$)). Furthermore, experimental work on other systems with a conserved order parameter (*cf.* p. 62) had yielded values $n \leq 1/3$.

Effective growth exponents $n_{eff}(t)$ (Eq. 5.76) were computed for all late-stage runs (AA — EE) using

$$n_{eff} = -\frac{d \ln q_m}{d \ln t} \quad (6.49)$$

and Fig. (6.25) gives the results. Thus, $n_{eff}(t)$ goes asymptotically to a value *above* $1/3$ from below, *i.e.* $n_{eff}(t)$ crosses $1/3$. This suggests that the phenomenological description of the motion of structureless interfaces put forth in § 5.5.1 would have to be modified.

The lack of power law behavior may be due to coupling to other dynamic

T (K)	$\Delta S_m(q_m, t) = \Delta S_0(t + t_0)^{3n'}$			$q_m(t) = q_0(t + t_0)^{-n}$		
	ΔS_0 (10^{-27}m^3)	t_0 (s)	n'	q_0 (10^{-2}\AA^{-1})	t_0 (s)	n
511	2.26	1.44 ± 1.68	0.33 ± 0.05	8.9 ± 1.0	2.98 ± 0.67	0.45 ± 0.03
537	4.76	0.57 ± 0.45	0.34 ± 0.02	5.3 ± 1.7	1.03 ± 0.13	0.42 ± 0.01
563	6.72	0.44 ± 0.17	0.35 ± 0.01	3.29 ± 0.12	0.26 ± 0.06	0.39 ± 0.01
578	6.04	0.34 ± 0.26	0.37 ± 0.03	3.00 ± 0.10	0.33 ± 0.05	0.43 ± 0.01
588	3.95	0.40 ± 0.24	0.40 ± 0.03	3.07 ± 0.24	0.62 ± 0.19	0.47 ± 0.02

Table 6.4: Best-fit parameter values to growth laws (6.47) and (6.48) for all late stages runs (AA — EE). The temperatures are listed to the nearest degree (*cf.* Table 6.1).

processes. Recently, Enomoto and Kawasaki[179,180] have examined the effect of elastic interactions among droplets on the growth exponent during droplet growth. The predicted effect depends on the sign of the difference in the shear modulus between the interior and exterior of second phase particles. This was checked in a quantitative evaluation of the effect of the elastic energy on the coarsening process of spherical droplets by numerical calculations and computer simulations. An enhancement of precipitate growth as $R(t) \sim t^{1/2}$ after the $R(t) \sim t^{1/3}$ stage is predicted when the shear modulus is larger inside the inclusion than outside. This case could be likened to that observed in Fig. (6.25).

Most of the cases examined by computer simulations by Enomoto and Kawasaki[179,180] were for relatively low second phase volume fractions, $V_v^\alpha \sim 0.01$. However, some simulations with $V_v^\alpha \sim 0.1$ have also presented an effect of the elastic field at the interface though somewhat delayed in time. They relate this delay to the correlation effects between domains. Though V_v^α and $V_v^{\alpha'}$ in this study depend on the aging temperature (c_0 is not exactly at the critical composition and the gap is asymmetric), they are close to 0.5 in all late-stage runs. Thus, it may be appropriate to attribute values of n larger than $1/3$ obtained in this work to elastic interactions between domains, however the available computer simulations for comparison were performed for much smaller volume fractions.

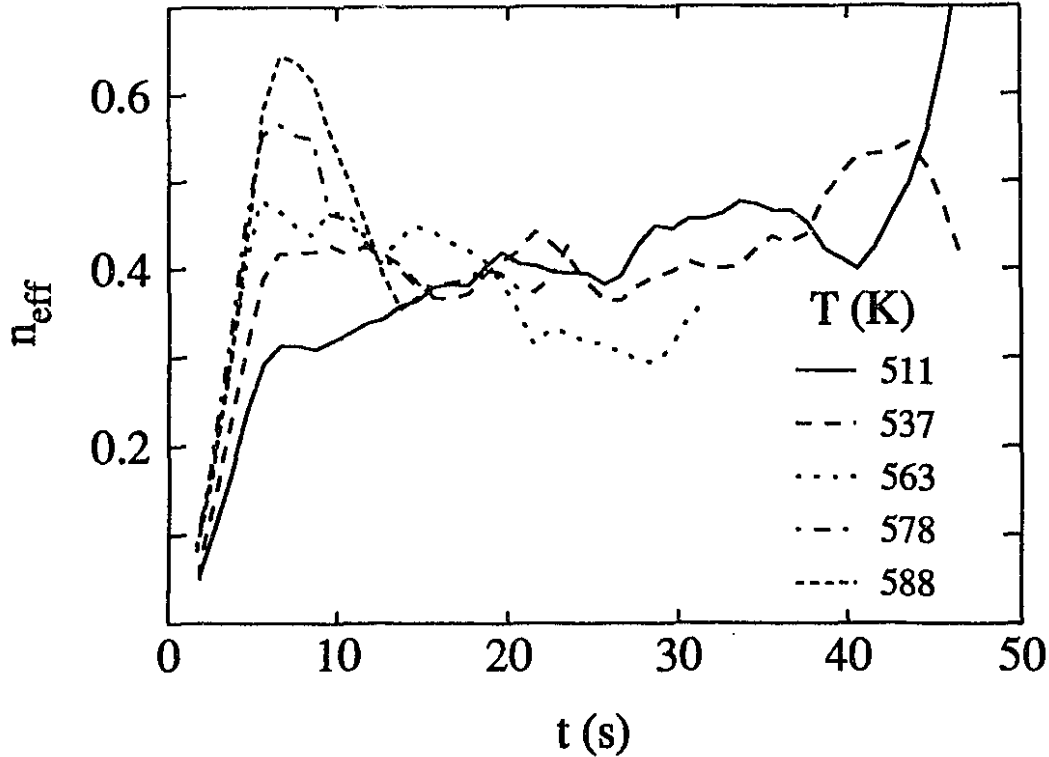


Figure 6.25: Calculated effective exponent for all late stages runs, $n_{eff}(t)$, as defined by Eq. (5.76).

There has not yet been an experimental account of a system crossing over from a growth exponent of $1/3$ to a $1/2$ exponent due to elastic effects. However, the case of a system with a shear modulus larger in the matrix phase than in the second phase particles has been examined in a measurement of the growth of second phase inclusions in $Ti_{0.80}Mo_{0.20}$ by Fratzl *et al.*[181] In this system a stage with $R(t) \sim t^{1/3}$ was observed, followed by a decrease in the growth exponent. The growth eventually stops completely.

A measurement of phase separation in the binary alloy MnCu by Gaulin *et al.*[83] reports scaling and a growth exponent of $n = 1/3$. However, in this alloy, the variation of solid solution lattice parameters[182] in the range of phase separation composition is small, which leads to a minimal strain energy effect.

Finally, it is interesting to note that if no instrumental unsmearing had been performed to the measured scattering intensity patterns, the effective exponent obtained would have been nearer to $1/3$.

6.3.2 Interface width correction

The late stages of SD involve at least two length scales: the average domain size $R(t)$ and the width w of the interfaces. The nonzero width w has not been considered yet in the discussion of late-stage SD. This width is essentially due to thermal fluctuations which roughen the interface and thus $w \sim \xi$. Since short length scale features show up at high wavevectors in the structure factor, interfaces between domains will affect $S(q, t)$ at the high q tail. This section introduces a correction to the high q tail of the scaling function to account for w .

In the previous section, it was shown that the late stages $\Delta S(q, t)$ did not present the expected q^{-4} tail predicted by Porod's law (Fig. 6.23). Instead, the $\Delta S(q, t)$ were found to drop faster than q^{-4} for all runs (AA — EE). This faster decrease corresponds to the expected effect of nonzero interfacial widths. Indeed, the derivation of Porod's law is based on a model in which there are sharp interfaces between the domains *i.e.* $w = 0$. In practice, this means that Porod's law is not expected to work unless the domain size is much greater than the interfacial width.

A correction for the finite width w of the interfaces can be attempted by introducing a dimensionless shaping (or enveloping) time independent function $\mathcal{S}(q, w)$ to the scaling function $F(x)$. [183] Equation (5.68) can thus be rewritten as

$$S(q, t) = C\mathcal{S}(q, w)q_m^{-3}(t)F(x) \quad (6.50)$$

subject to $\lim_{q \rightarrow 0} \mathcal{S}(q, w) = 1$.

The form used for $\mathcal{S}(q, w)$ will be an hyperbolic tangent:

$$\mathcal{S}(q, w) = \left[\frac{q\pi w}{2} \operatorname{csch} \left(\frac{q\pi w}{2} \right) \right]^2. \quad (6.51)$$

The only adjustable parameter in the Eq. (6.51) is the time-independent width w . Its value was obtained by fitting

$$S_w(q, t) = 2\pi\mathcal{A}(t)q^{-4}\mathcal{S}(q, w) \quad (6.52)$$

to the measured $\Delta S(q, t)$ over a q -range beyond the shoulder. In Eq. (6.52), which is a modified form of Porod's law to take account of w , the constant \mathcal{A} is the same

as defined in Eq. (2.31) and is a measure of the interfacial area per unit volume. The values of w are expected to be temperature-dependent, and to increase as the aging temperature approaches T_c .

For the q -range restricted to $[0.048, 0.089] \text{ \AA}^{-1}$, the best fit results to Eq. (6.52) are reported in Table (6.5).¹⁵ The noise in $q^4 \Delta S(q, t)$ (*cf.* Fig. 6.23) is reflected by the large uncertainties in the best fit values reported for $\mathcal{A}(t)$ in Table (6.5). The temperature dependence of w is not obvious from the values listed in Table (6.5) due to the large errors for the three runs corresponding to the higher aging temperatures. The interpretation of the best fit values for w is limited by the noise at high q and by the possibility of yet an additional shoulder at the latest times measured.

Furthermore, at a given temperature, the position of the first shoulder is a function of time; as time increases, the shoulders moving to lower wavevectors. Hence, when fitting Eq. (6.52) over a fixed range of q , the relative location with respect to the shoulder maximum changes in time as the shoulder moves. The fitting range of q was chosen such that in all cases the shoulder maximum was below the lower limit. However, any additional prospective shoulder would be likely to influence the fit result as it sweeps by the q -window during the evolution of $\Delta S(q, t)$. An estimation of the effect of the relative location of the shoulder maximum with respect to the fitting range on best fit values of w yielded at most 10% variation in w for $12 \lesssim t \lesssim 52$ s. This effect is in general monotonic over the times investigated, resulting in an increase of best fit w with time. However all such estimates of w lie within the error bars of the values listed in Table (6.5).

Figure (6.26a) shows $S(q, w)$ calculated from Eq. (6.51) with $w = 15.1 \text{ \AA}$. Part (b) shows the q^{-4} Porod tail and a corrected $S(q, w)q^{-4}$ for $t = 12.61$ s, which overlaps with the measured data (run BB). The form $S(q, w)$ used corresponds to the one shown in (a). Although the best fit w for this earlier time differs from the value

¹⁵As was the case for Table (6.4) the uncertainties on the parameter values correspond to the calculated standard deviations with $\chi^2 = 1$. However, in the present case, the standard deviations calculated for each $q^4 \Delta S(q, t)$ were used to weight the data points in the least squares fit to Eq. (6.52).

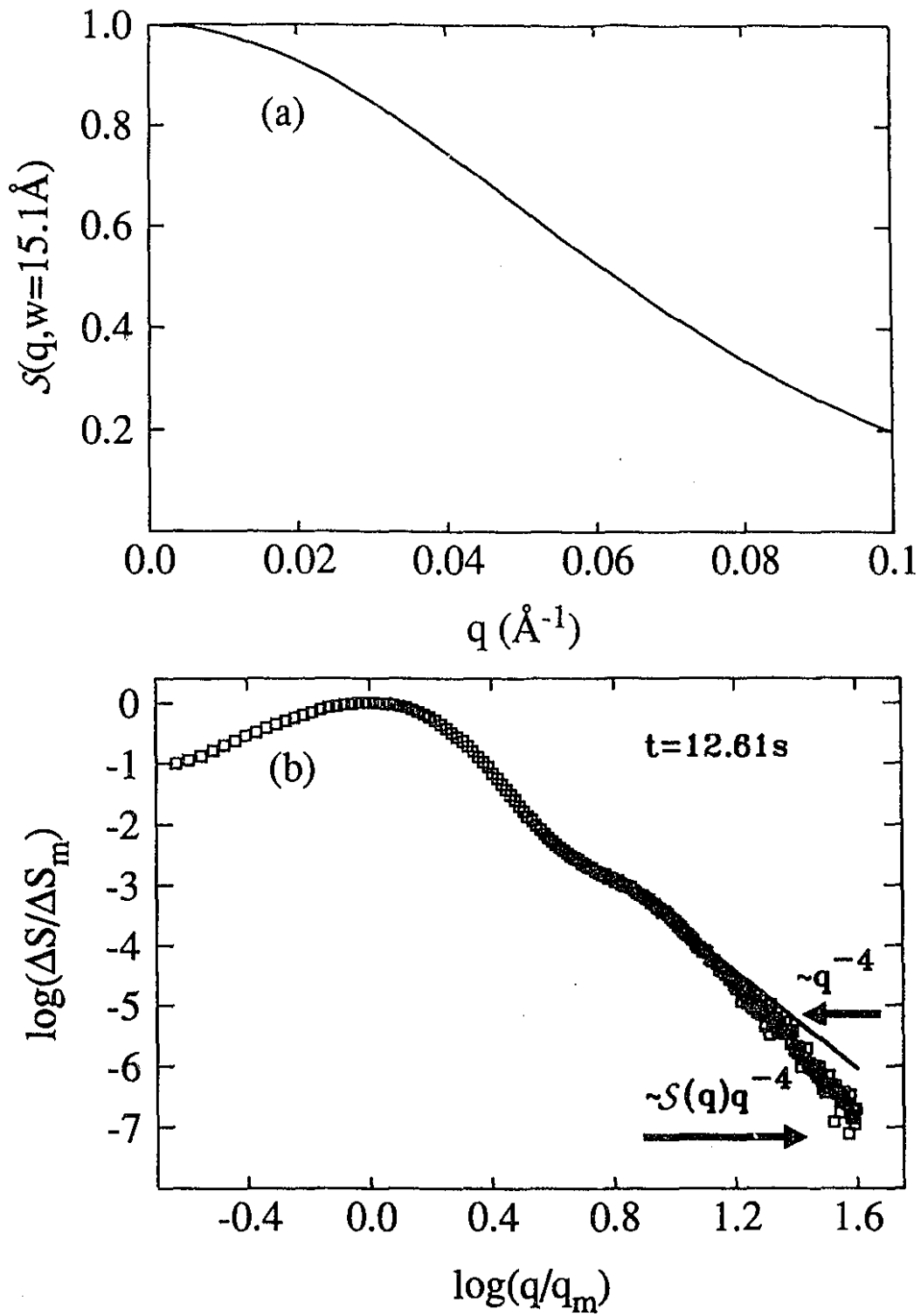


Figure 6.26: (a) Interfacial width correction term $S(q, w)$ calculated from Eq. (6.51) with $w = 15.1 \text{\AA}$. (b) Porod tail (q^{-4}) and corrected to account for finite interfacial width ($S(q, w)q^{-4}$) with S shown in (a). The data correspond to run BB.

T	t	$A(t)$	w
(K)	(s)	(10^7m^{-1})	(\AA)
511	52.64	2.38 ± 0.69	15.2 ± 3.8
537	52.61	1.69 ± 0.48	17.2 ± 3.5
563	52.46	0.83 ± 0.87	20.1 ± 12.2
578	52.51	0.58 ± 1.26	24.0 ± 23.5
588	52.64	0.17 ± 0.17	11.8 ± 16.1

Table 6.5: Best fit width correction parameter values to account for deviations from $\Delta S(q, t) \sim q^{-4}$ at large q (6.52) for all late-stage runs (AA — EE). The temperatures are listed to the nearest degree (cf. Table 6.1).

reported in Table (6.5) for $t = 52.61$ s, it is still within the error bars of that value.

Figure (6.27) compares the Ohta-Nozaki scaling form $F_{(\text{ON})}(x)$ given by Eq. (5.90) corrected for the interfacial width using Eq. (6.52) to the scaled $\Delta S(q, t = 12.61$ s) for run BB. The solid line represents the uncorrected best fit $F_{(\text{ON})}(x)$ with $A = 4.0$ and the dashed line is the corrected $F_{(\text{ON})}(x)$ using Eq. (6.51) with $w = 16.0$ \AA . Although the high q tail of the corrected $F_{(\text{ON})}(x)$ displays a decay with the same power as the scaled data, the value of $F_{(\text{ON})}(x)$ at the shoulder is too small to model the data, as remarked in the previous section.

A best fit value w can be determined by the procedure above to obtain a “corrected” Porod tail that tracks the high q dependence of measured $\Delta S(q, t)$. However, an additional check on the applicability of Porod’s law can be performed by rewriting Eq. (2.32) as[45]

$$\int_0^\infty [q^4 S(q) - 2\pi A] dq = 0 \quad (6.53)$$

This equation is not satisfied by Fig. (6.23) since $q^4 \Delta S(q, t)$ is not constant with q for large q .

Figure (6.28) displays the $\Delta S(q, t)$ modified by the inverse of the width correction prefactor. This figure is representative of the result obtained for all runs AA — EE and shows that Eq.(6.53) cannot be satisfied. Even with the interfacial width correction term to make $\lim_{q \rightarrow \infty} S^{-1}(q, w) q^4 \Delta S(q)$ a nonzero constant, the

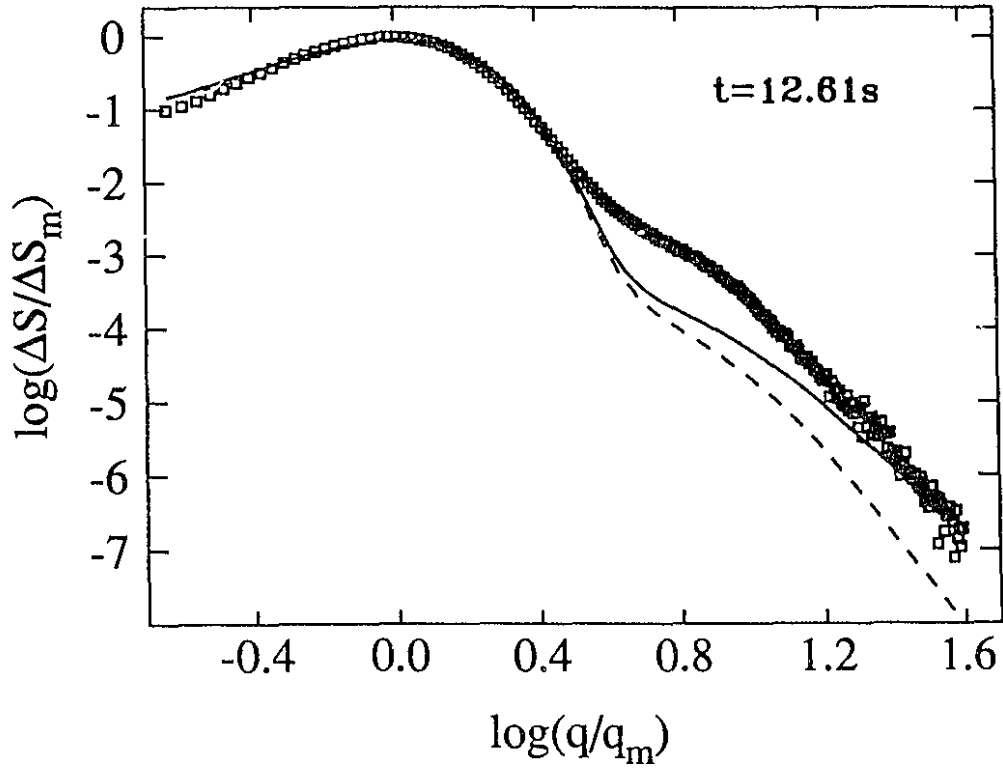


Figure 6.27: Scaling profile for run BB ($T = 537$ K). The solid line shows a best fit to the Ohta-Nozaki form, $F_{(ON)}(z)$ (Eq. 5.93). The dashed line shows $S(q, w = 16 \text{ \AA})F_{(ON)}(z)$ to account for finite interfacial width as discussed in text.

main peak in $q^4 S^{-1}(q, w)(q, t)\Delta S(q)$ is always too small and the integral (6.53) is negative. At the later times the peak in $\Delta S(q, t)$ is higher, but since it is located at a lower q , its contribution to the $q^4 \Delta S(q)$ part of the integrand decreases (as shown by Fig. 6.28), and the integral is increasingly negative. Consequently, although the high q tails that do not obey Porod's law can be rationalised in terms of interfacial width effects, the simple use of a shaping function employed in this section appears to be insufficient to reconcile measured $\Delta S(q, t)$ with the sum law (2.32).

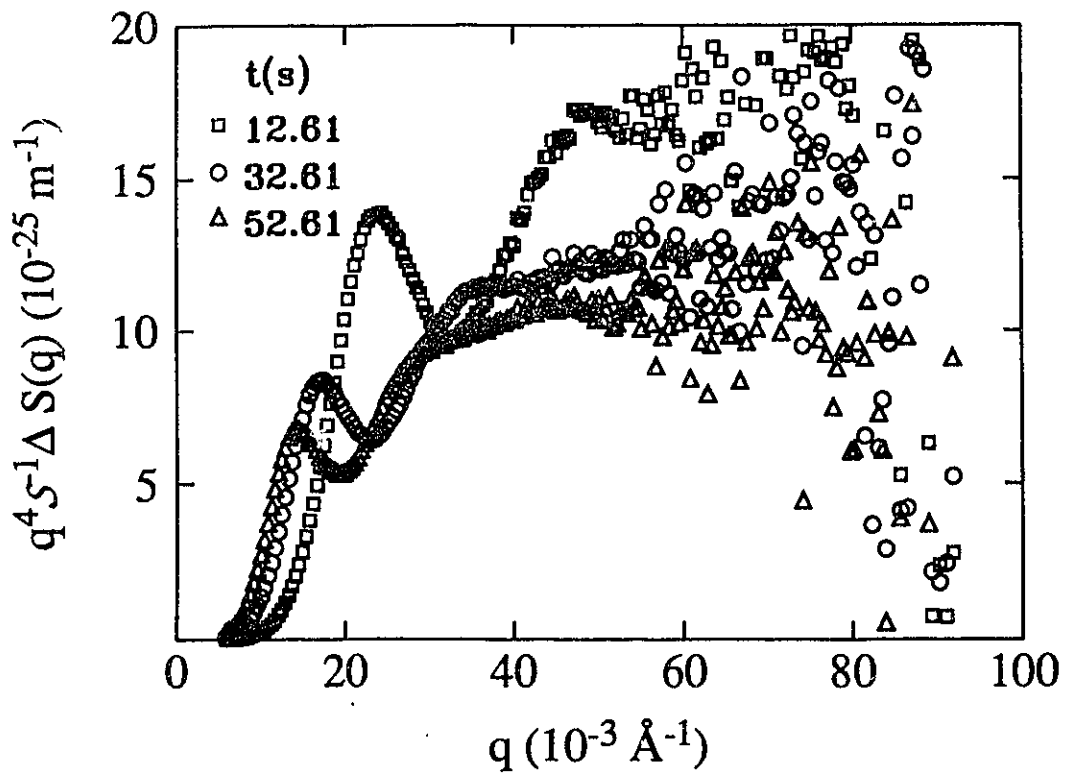


Figure 6.28: Porod plot with $S^{-1}(q, w = 17.2 \text{ \AA})$ used as *prefactor to the data* for $T = 537 \text{ K}$ (run BB) at selected times. (The value $w = 17.2 \text{ \AA}$ corresponds to the value given in Table (6.5) for $t = 52.61 \text{ s}$.)

Chapter 7

Conclusions

This thesis has presented *in situ* measurements of time resolved structure factors for (a) early stage and (b) late-stage phase separation kinetics following the quench of the binary alloy $\text{Al}_{0.62}\text{Zn}_{0.38}$ in the unstable region of its phase diagram. The experimental time resolution (up to 5 ms) was made possible by the use of a bright synchrotron x-ray source, a position sensitive detector, fast counting electronics and a rapid temperature change by resistive heating. The measurements allowed the first experimental check of three important aspects of critical phenomena in alloys:

- The first extensive experimental verification of the validity of the nonlinear equation of motion for the evolution of the structure factor in an alloy during early stages of SD introduced by Langer, Bar-on and Miller (LBM).[7] The early stage regime of the measurements was confirmed by the determination of the integrated intensity. The Cahn-Hilliard-Cook linear equation of motion was found insufficient to describe the evolution of $S(q, t)$ over the early time regime measured. However, fits with the LBM theory tracked successfully the measured structure factors and best fit parameters have been obtained. These include the free energy parameters r and u , the gradient energy coefficient κ and the atomic mobility M .

- The nonlinear relaxation of fluctuations after a quench in the one-phase region above T_c . The time-evolution of $S(q, t)$ for $T > T_c$ presents features similar to those for the phase decomposition at $T < T_c$. In particular, there are high q modes which grow initially and subsequently decay.
- The first measurement of non scaling features in the structure factors during the late stages of SD in a binary alloy, including the existence of a shoulder on the high wavevector side of the main peak. These effects may be attributed to elastic effects between domains of the two product phases.

The early time regime investigated is of considerable scientific interest because it is only in the early stage of the phase separation that SD can be unambiguously identified. The main conclusions from the fit of the LBM theory to the structure factors measured during the early stages of SD may be summarized as follows:

- The high wavenumber cutoff q_{max} had to be constrained proportional to the inverse of the mean field correlation length with a proportionality constant α . The choice of α influences the range of the decomposition process assumed in the best fit LBM result, as verified by the composition distribution functional during the isothermal aging.
- The decomposition which occurs during the quench can be accounted for by considering an initial composition distribution functional doubly peaked about nonzero $\pm b_0$. As expected, b_0 increases with the depth of the quench inside the spinodal region. Its value decreases with an increase of the cutoff factor α .
- The gradient free energy coefficient κ increases with temperature and peaks near T_c . It is independent of α .
- The “ c^4 ” free energy parameters r and u obtained were highly anticorrelated during the fit. The best fit r depends linearly on $|T - T_c|$ and scales as α^{-2} . The value of u increases slightly with temperature showing a slight anomaly at

T_c and scales as α^{-3} . The calculated $\sqrt{-r/u}$ allowed the determination of the mean field phase diagram (coexistence line) which scales as $\alpha^{1/2}$. From this scaling relationship the numerical value of α was chosen such that the predicted integrated intensity at the resulting mean field coexistence line agreed with the measured integrated intensity for the quenches away from T_c . Agreement was then found between the calculated coexistence line and a prediction by a regular solution model.

- The atomic mobility M was determined separately from the thermodynamic driving force. It increases exponentially with temperature and is independent of α . A comparison of M with the temperature-dependent values calculated from three tracer diffusivity measurements in the literature showed remarkable agreement.
- A thermal noise strength term ϵ was computed for all runs and relatively high values are obtained as expected from the highly nonlinear characteristics observed for the decomposition.
- At times of order 2.6 s, the LBM equation of motion becomes inadequate to predict the evolution of the measured structure factors.

To perform the instrumental deconvolution for the PSD a new computational technique was developed and used for the late-stage data. The results of the measurements of late-stage SD are:

- A shoulder is observed at high q . This is the first time this feature is reported for a binary alloy.
- The measured scattering profiles do not quite scale during the time of the measurement. Comparison of the measured structure factors with two scaling forms was unsuccessful although the form suggested by Ohta and Nozaki presents a profile similar to the data. In particular, this form has a shoulder at high q as observed experimentally.

- Growth exponents were calculated to be $0.40 \lesssim n \lesssim 0.45$. These values are larger than reported earlier for a conserved order parameter system. They are however not inconsistent with recent predictions for alloys in which the shear modulus is larger inside precipitates than in the matrix phase.
- High q tails do not go as q^{-4} as expected from Porod's law for systems with sharp interfaces. A correction was suggested to account for interfaces with a width of order of the correlation length and explain the departure from ideal q^{-4} tails.

While this research has satisfied the goals stated in the introduction and in doing so has yielded a new and valuable verification of early stage theory as well as some unexpected late-stage results, it also raised several new questions which require new analyses of the present data and further experiments for their answer.

- Re-analyse the measurements presented in this dissertation and analyse additional measurements at compositions away from the critical composition using a non-symmetric form of the free energy functional instead of the " c^4 " form. This work is necessary to resolve both branches of the asymmetric solvus and thus further verify the LBM equation of motion.
- Reduce the thickness of the ribbons. Thinner ribbons would give faster quench rates, resulting in a decrease of the quenched-in structure.
- Perform new measurements optimized with a better temperature control to study the critical region (critical exponents). Although the temperature control for the measurements presented in this dissertation was more than adequate for the investigation of the kinetics of SD, it could be improved further to minimize the temperature smearing across the width of the sample for instance. The present results should be compared with results obtained with narrower ribbons or with a beam more collimated in the horizontal direction (the direction of the ribbon width).

- Investigate of the influence of elastic constraints on the growth exponent. Structure factors should be measured beyond the times studied in this dissertation to investigate the possibility of a scaling form at later times with a growth exponent of $1/2$ as predicted by Enomoto and Kawasaki.[179,180] A systematic study at various alloy compositions should also be performed to complement late-stage results.
- Apply coherent small angle x-ray scattering[184] to the study of SD in single crystals of AlZn to obtain higher order correlation functions. This is possible since the speckle patterns obtained by coherent scattering correspond to a complete Fourier transform of the real-space structure.

The first item is presently under investigation by the author.

References

- [1] K.R. Elder, Ph.D. thesis, University of Toronto, 1989.
- [2] J.D. Gunton, M. San Miguel and P.S. Sahni, "The Dynamics of First-Order Phase Transitions" in *Phase Transitions and Critical Phenomena*, Vol. 8, edited by C. Domb and J.L. Lebowitz (Academic Press, New York, 1983), p. 267.
- [3] V.P. Skripov and A.V. Skripov, *Sov. Phys. Usp.* **22**, 389 (1979).
- [4] J.W. Cahn, *Acta metall.* **9**, 795 (1961).
- [5] M. Sutton and G.B. Stephenson, *Physics in Canada* **44**, 131 (1988).
- [6] M. Sutton, Y.S. Yang, J. Mainville, J.O. Ström-Olsen, Z. Altounian, G.B. Stephenson, K.F. Ludwig, Jr., in *Proceedings of the Sixth International Conference on Rapidly Quenched Metals (RQ6)*, edited by R.W. Cochrane and J.O. Ström-Olsen [*Material Science and Engineering* **97**, 307-311 (1988)].
- [7] J.S. Langer, M. Bar-on and H.D. Miller, *Phys. Rev. A* **11**, 1417 (1975).
- [8] H. Chen, *Journal of Metals* **38** (10), 36 (1986).
- [9] H.-E. Stanley, *Introduction to Phase Transitions and Critical Phenomena* (Oxford University Press, New York, 1971).
- [10] L.E. Reichl, *A Modern Course in Statistical Physics* (University of Texas Press, Austin, Texas, 1980).
- [11] M.E. Fisher, *Rep. Prog. Phys.* **30**, 615 (1967).
- [12] M.E. Fisher, *Rev. Mod. Phys.* **46**, 597 (1974).
- [13] P.C. Hohenberg and B.I. Halperin, *Rev. Mod. Phys.* **49**, 435 (1977).
- [14] *Binary Alloy Phase Diagrams*, Vol. 1, edited by T.B. Massalski (American Society for Metals, Metals Park, OH, 1986,), p. 184.
- [15] M. Hansen, *Constitution of binary alloys, 2nd ed.* (McGraw-Hill, New York, 1958), p. 148.
- [16] R. Kikuchi and D. de Fontaine, *Scr. Metall.* **10**, 995 (1976).
- [17] J.W. Cahn and J.E. Hilliard, *J. Chem. Phys.* **28**, 258 (1958).
- [18] T.R. Anantharaman and K.G. Satyanarayana, *Scr. Metall.* **7**, 189 (1973).
- [19] G. Laslaz, Ph.D. thesis, Grenoble, 1978.
- [20] D. de Fontaine, "Clustering Effects in Solid Solutions" in *Treatise on Solid State Chemistry*, Vol. 5, edited by N.B. Hanay (Plenum Press, Oxford, 1970), p. 129.
- [21] J. Lašek, *Czech. J. Phys. B* **15**, 848 (1965).
- [22] A. Münster and K. Sagel, *Z. Phys. Chem.* **7**, 296 (1956).
- [23] B.K. Kardasev, S.P. Nikanorov and J. Lašek, *Czech. J. Phys. B* **18**, 275 (1968).

- [24] E.C. Ellwood, *J. Inst. Metal.* **80**, 217 (1952).
- [25] D. Schwahn and W. Schmatz, *Acta metall.* **26**, 1571 (1978).
- [26] H. Löffler and O. Simmich, *phys. stat. sol. (a)* **30**, 495 (1975).
- [27] R. Kikuchi, *J. Chem. Phys.* **47**, 1664 (1967).
- [28] N.L. Peterson, *Solid State Phys.* **22**, 409 (1968).
- [29] J.W. Christian, *The Theory of Transformations in Metals and Alloys Part I: Equilibrium and General Kinetic Theory*, 2nd ed. (Pergamon Press, 1975).
- [30] H.E. Cook, *Acta metall.* **18**, 297 (1970).
- [31] E.L. Huston, J.W. Cahn and J.E. Hilliard, *Acta metall.* **14**, 1053 (1966).
- [32] J.E. Hilliard, "Spinodal decomposition" in *Phase Transformations*, edited by H.I. Aaronson (Amer. Soc. Metals, Metals Park, OH, 1970), p. 497.
- [33] D. de Fontaine, "Development of Fine Coherent Precipitate Morphologies by the Spinodal Mechanism" in *Ultrafine Grain Metals*, edited by Burke and V. Weiss (Syracuse University Press, NY, 1970), p. 93.
- [34] J.W. Cahn and J.E. Hilliard, *J. Chem. Phys.* **31**, 688 (1959).
- [35] A.L. Greer and F. Spaepen, *Synthetic Modulated Structures* (Academic Press, New York, 1985), p. 419.
- [36] L.S. Darken, *Trans. Amer. Inst. Min. (Metall.) Engrs.* **175**, 184 (1948).
- [37] W.M. Paulson and J.E. Hilliard, *J. Appl. Phys.* **48**, 2117 (1977).
- [38] H.E. Cook and J.E. Hilliard, *J. Appl. Phys.* **40**, 2191 (1969).
- [39] E.M. Pfaffsky and J.E. Hilliard, *J. Appl. Phys.* **40**, 2198 (1969).
- [40] B.E. Warren, *X-Ray Diffraction* (Addison-Wesley, Reading, MA., 1969).
- [41] V.F. Sears, *Theory of thermal neutron scattering* (Atomic Energy of Canada Ltd. report 6326, 1978).
- [42] V. Gerold and G. Kostorz, *J. Appl. Cryst.* **11**, 376 (1978).
- [43] K. Huang, *Statistical Mechanics*, 2nd ed. (Wiley, NY, 1987).
- [44] G. Porod, "General Theory" in *Small Angle X-ray Scattering*, edited by O. Glatter and O. Kratsky (Academic Press, N.Y., 1982), p. 17.
- [45] H. Tomita, *Prog. Theor. Phys.* **72**, 656 (1984).
- [46] A. Guinier and G. Fournet, *Small-Angle Scattering of X-rays* (Wiley, NY, 1955).
- [47] G. Porod, *Kolloidzshr.* **124**, 83 (1951).
- [48] G.B. Stephenson, Ph.D. thesis, Stanford University, 1982.
- [49] D.J. Bergman and B.I. Halperin, *Phys. Rev. B* **13**, 2145 (1976).
- [50] K. Binder and D. Stauffer, *Adv. Phys.* **25**, 343 (1976).

- [51] K. Binder, *Phys. Rev. B* **15**, 4425 (1977).
- [52] K. Binder, C. Billotet and P. Miold, *Z. Phys. B* **30**, 183 (1978).
- [53] M. Rao, M.H. Kalos, J.L. Lebowitz and J. Marro, *Phys. Rev. B* **13**, 4328 (1976).
- [54] A. Sur, J.L. Lebowitz, J. Marro and M.H. Kalos, *Phys. Rev. B* **15**, 3014 (1977).
- [55] M. Hillert, *Acta metall.* **9**, 525 (1961).
- [56] J.W. Cahn, *Acta metall.* **10**, 179 (1962).
- [57] J.W. Cahn, *Trans. Am. Inst. Min. Engrs.* **242**, 166 (1968).
- [58] K.B. Rundman and J.E. Hilliard, *Acta metall.* **15**, 1025 (1967).
- [59] J.S. Langer and A.J. Schwartz, *Phys. Rev. A* **21**, 948 (1980).
- [60] M. Hennon, D. Ronzaud and P. Guyot, *Acta metall.* **30**, 599 (1982).
- [61] G. Laslaz, P. Guyot and G. Kostorz, *J. Phys. Paris* **38**, (C7) 406 (1977).
- [62] G. Laslaz, G. Kostorz, M. Roth, P. Guyot and R.J. Stewart, *phys. stat. sol. (a)* **41**, 577 (1977).
- [63] N. Luiggi, J.P. Simon and P. Guyot, *Acta metall.* **28**, 1115 (1980).
- [64] M. Murakami, O. Kawano, Y. Murakami and M. Morinaga, *Acta metall.* **17**, 1517 (1969).
- [65] U.K. Malhotra and K.B. Rundman, *Metallurg. Trans.* **3**, 1521 (1972).
- [66] R. Ciach, H. Löffler, J. Salawa and G. Wendrock, *phys. stat. sol. (a)* **53**, 441 (1979).
- [67] J.J. Hoyt, B. Clark, D. de Fontaine, J.P. Simon and O. Lyon, *Acta metall.* **37**, 1597 (1989).
- [68] A.F. Bonfiglioli and A. Guinier, *Acta metall.* **14**, 1213 (1966).
- [69] S. Agarwal, M.J. Koczak and H. Herman, *Scr. Metall.* **7**, 401 (1973).
- [70] S. Agarwal and H. Herman, *Scr. Metall.* **7**, 503 (1973).
- [71] A. Junqua, J. Mimault, J. Delafond and J. Grilhe, *Scr. Metall.* **8**, 317 (1974).
- [72] A. Naudon, J. Allain, J. Delafond, A. Junqua and J. Mimault, *Scr. Metall.* **8**, 1105 (1974).
- [73] R. Acuña and A. Bonfiglioli, *Acta metall.* **22**, 399 (1974).
- [74] J. Delafond, A. Junqua, J. Mimault and J.P. Rivière, *Acta metall.* **23**, 405 (1975).
- [75] T.L. Bartel and K.B. Rundman, *Metall. Trans.* **6A**, 1887 (1975).
- [76] G. Laslaz and P. Guyot, *Acta metall.* **25**, 277 (1977).
- [77] T. Ungár, J. Lendvai and I. Kovács, *Philosophical Magazine A* **43**, 927 (1981).
- [78] M. Furusaka, Y. Ishikawa and M. Mera, *Phys. Rev. Letters* **54**, 2611 (1985).

- [79] J.J. Hoyt and D. de Fontaine, *Acta metall.* **37**, 1611 (1989).
- [80] V. Gerold and W. Merz, *Scr. Metall.* **1**, 33 (1967).
- [81] J.E. Hilliard and K.B. Rundman, *Scr. Metall.* **1**, 37 (1967).
- [82] J.W. Cahn, *J. Chem. Phys.* **42**, 93 (1965).
- [83] B.D. Gaulin, S. Spooner and Y. Morii, *Phys. Rev. Lett.* **59**, 668 (1987).
- [84] J.W. Cahn, *Acta metall.* **14**, 1685 (1966).
- [85] H.O. Carmesin, D.W. Heerman and K. Binder, *Z. Phys. B* **65**, 89 (1986).
- [86] J.C. LaSalle and L.H. Schwartz, *Acta metall.* **34**, 989 (1986).
- [87] M. Furusaka, Y. Ishikawa, S. Yamaguchi and Y. Fujino, *J. Phys. Soc. Jpn.* **55**, 2253 (1986).
- [88] M. Furusaka, Y. Ishikawa, S. Yamaguchi and Y. Fujino, *Physica* **120B + C**, 383 (1983).
- [89] M. Okada and C.C. Han, *J. Chem. Phys.* **85**, 5317 (1986).
- [90] F.S. Bates and P. Wiltzius, *J. Chem. Phys.* **91**, 3258 (1989).
- [91] Y.C. Chou and W.I. Goldberg, *Phys. Rev. A* **20**, 2105 (1979).
- [92] J.S. Huang, W.I. Goldberg and A.W. Bjerkaas, *Phys. Rev. Lett.* **32**, 921 (1974).
- [93] G.B. Stephenson, *Journal of Non-Crystalline Solids* **66**, 393 (1984).
- [94] G.B. Stephenson, W.K. Warburton and A. Bienenstock, *Phys. Rev. B* **43**, 13417 (1991).
- [95] Y.C. Chou and W.I. Goldberg, *Phys. Rev. A* **23**, 858 (1981).
- [96] A. Craievich and J.M. Sanchez, *Phys. Rev. Lett.* **47**, 1308 (1981).
- [97] S. Komura, K. Osamura, H. Fujii and T. Takeda, *Phys. Rev. B* **30**, 2944 (1984).
- [98] S. Komura, K. Osamura, H. Fujii and T. Takeda, *Phys. Rev. B* **31**, 1278 (1985).
- [99] A.R. Forouhi and D. de Fontaine, *Acta metall.* **35**, 1863 (1987).
- [100] S. Katano and M. Iizumi, *Physica* **120B + C**, 392 (1983).
- [101] S. Katano and M. Iizumi, *Phys. Rev. Lett.* **52**, 835 (1984).
- [102] N.-C. Wong and C.M. Knobler, *J. Chem. Phys.* **69**, 725 (1978).
- [103] N.-C. Wong and C.M. Knobler, *Phys. Rev. A* **24**, 3205 (1981).
- [104] E.D. Siggia, *Phys. Rev. A* **20**, 595 (1979).
- [105] N.-C. Wong and C.M. Knobler, *Phys. Rev. Lett.* **43**, 1733 (1979).
- [106] S. Nojima, K. Tsutsumi and T. Nose, *Polymer Journal* **14**, 225 (1982).
- [107] G.B. Stephenson, *Nucl. Instrum. Methods Phys. Res. Sect. A* **266**, 447 (1988).

- [108] National Synchrotron Light Source Annual Report, eds. W. Thomlinson and S. White-DePace, Report BNL-51947 (1985).
- [109] E.D. Specht, Ph.D. thesis, Massachusetts Institute of Technology, 1987.
- [110] Y.S. Yang, Ph.D. thesis, McGill University, Montreal, 1990.
- [111] J.D. Brock, Ph.D. thesis, Massachusetts Institute of Technology, 1987.
- [112] G.B. Stephenson, K.F. Ludwig, Jr., J.L. Jordan-Sweet, J. Mainville, Y.S. Yang, M. Sutton, in *Proceedings of the 3rd International Conference on Synchrotron Radiation Instrumentation*, edited by M. Ando and T. Miyahara [Rev. Sci. Instrum. **60**, 1537 (1989)].
- [113] B.D. Cullity, *X-ray Diffraction* (Addison-Wesley, 1967).
- [114] F.J. Zutavern, S.E. Schnatterly, E. Kallne, C.P. Franck, T. Aton and J. Rife, Nucl. Instrum. Methods **172**, 351 (1980).
- [115] *International Tables for X-ray Crystallography*, Vol. 3 (Kynoch Press, Birmingham, England, 1962).
- [116] R.C. Weast, *CRC Handbook of Chemistry and Physics*, 56th ed. (CRC Press, Cleveland, 1975).
- [117] D.I. Svergun, *Structure analysis by small-angle x-ray and neutron scattering* (Plenum Press, NY, 1987).
- [118] J.D. Gunton and M. Droz, *Introduction to the Theory of Metastable and Unstable States* (Springer-Verlag Lecture Notes in Physics, Berlin, 1983).
- [119] J.S. Langer, Ann. of Phys. **65**, 53 (1971).
- [120] K. Kaski, K. Binder and J.D. Gunton, Phys. Rev. B **29**, 3996 (1984).
- [121] J.S. Langer, Physica **73**, 61 (1974).
- [122] J.S. Langer and M. Bar-on, Ann. of Phys. **78**, 421 (1973).
- [123] J.S. Langer, Ann. of Phys. **54**, 258 (1969).
- [124] J. Als-Nielsen and R.J. Birgeneau, Am. J. Phys. **45**, 554 (1977).
- [125] K. Binder, Phys. Rev. A **29**, 341 (1984).
- [126] D.W. Heermann, Phys. Rev. Lett. **52**, 1126 (1984).
- [127] M. Grant, M. San Miguel, J. Viñals and J.D. Gunton, Phys. Rev. B **31**, 3027 (1985).
- [128] F. Haake, J.W. Haus and R. Glauber, Phys. Rev. A **23**, 3255 (1981).
- [129] K. Binder, J. Chem. Phys. **79**, 6387 (1983).
- [130] J.S. Langer, Acta metall. **21**, 1649 (1973).
- [131] C. Billotet and K. Binder, Z. Phys. B **32**, 195 (1979).
- [132] J. Marro, J.L. Lebowitz and M.H. Kalos, Phys. Rev. Lett. **43**, 282 (1979).
- [133] H. Furukawa, Phys. Rev. Lett. **43**, 136 (1979).

- [134] S.M. Allen and J.W. Cahn, *Acta metall.* **27**, 1085 (1979).
- [135] T. Ohta, D. Jasnow and K. Kawasaki, *Phys. Rev. Lett.* **49**, 1223 (1982).
- [136] J.S. Langer, "Spinodal decomposition" in *Fluctuations, Instabilities and Phase Transitions*, edited by T. Riste (Plenum Press, NY, 1975), p. 19.
- [137] E.T. Gawlinski, M. Grant, J.D. Gunton and K. Kaski, *Phys. Rev. B* **31**, 281 (1985).
- [138] K. Kawasaki, M.C. Yalabik and J.D. Gunton, *Phys. Rev. A* **17**, 455 (1978).
- [139] M. Grant and J.D. Gunton, *Phys. Rev. B* **29**, 6266 (1984).
- [140] I.M. Lifshitz and V.V. Slyozov, *J. Phys. Chem. Solids* **19**, 35 (1961).
- [141] C. Wagner, *Z. fuer Electrochem.* **65**, 581 (1961).
- [142] I.M. Lifshitz and L.P. Pitaevskii, *Physical Kinetics, Landau and Lifshitz Course of Theoretical Physics*, Vol. 10 (Pergamon Press (London, 1981).
- [143] M. Kalos, J.L. Lebowitz, O. Penrose and A. Sur, *J. Stat. Phys.* **18**, 39 (1978).
- [144] O. Penrose, J.L. Lebowitz, J. Marro, M.H. Kalos and A. Sur, *J. Stat. Phys.* **19**, 243 (1978).
- [145] J.A. Marqusee and J. Ross, *J. Chem. Phys.* **80**, 536 (1984).
- [146] K. Kawasaki, Y. Enomoto and M. Tokuyama, *Physica* **135A**, 426 (1986).
- [147] Y. Enomoto, M. Tokuyama and K. Kawasaki, *Acta metall.* **34**, 2119 (1986).
- [148] M. Marder, *Phys. Rev. A* **36**, 858 (1987).
- [149] C.W. Beenakker, *Phys. Rev. A* **33**, 4482 (1986).
- [150] P.W. Voorhees and M.E. Glicksman, *Acta metall.* **32**, 2001 (1984).
- [151] P.W. Voorhees and M.E. Glicksman, *Acta metall.* **32**, 2013 (1984).
- [152] J.J. Wiens and J.W. Cahn, "The effect of size and distribution of second phase particles and voids on sintering" in *Sintering and Related Phenomena*, edited by G. Kuczynski (Plenum, London, 1973), p. 151.
- [153] C. Roland and M. Grant, *Phys. Rev. B* **39**, 11971 (1989).
- [154] D.A. Huse, *Phys. Rev. B* **34**, 7845 (1986).
- [155] M. Grant, *Phys. Rev. Lett.* **62**, 1065 (1989).
- [156] A. Milchev, K. Binder and D.W. Heermann, *Z. Phys. B* **63**, 521 (1986).
- [157] C. Yeung, *Phys. Rev. Lett.* **61**, 1135 (1988).
- [158] J.L. Lebowitz, J. Marro and M.H. Kalos, *Acta metall.* **30**, 297 (1982).
- [159] P. Fratzl and J.L. Lebowitz, *Acta metall.* **37**, 3245 (1989).
- [160] P. Fratzl, J.L. Lebowitz, O. Penrose and J. Amar, *Phys. Rev. B* **44**, 4794 (1991).

- [161] P. Debye, H.R. Anderson, Jr. and H. Brumberger, *J. Appl. Phys.* **28**, 679 (1957).
- [162] H. Furukawa, *Physica* **123A**, 497 (1984).
- [163] H. Furukawa, *J. Phys. Soc. Japan* **58**, 216 (1989).
- [164] T. Ohta and H. Nozaki, "Space-Time Organization in Macromolecular Fluids" in *Springer Series in Chemical Physics*, Vol. 51, edited by F. Tanaka, M. Doi, T. Ohta (Springer-Verlag, Berlin, 1989), p. 51.
- [165] T. Ohta, *Ann. of Phys.* **158**, 31 (1984).
- [166] A. Shinozaki and Y. Oono, *Phys. Rev. Lett.* **66**, 173 (1991).
- [167] S. Brauer, Private communication.
- [168] J. Mainville, M. Sutton, G.B. Stephenson, K.R. Elder, to be published.
- [169] J.E. Hilliard, B.L. Averbach and M. Cohen, *Acta metall.* **7**, 86 (1959).
- [170] J. Čermák, K. Číha and J. Kučera, *phys. stat. sol. (a)* **62**, 467 (1980).
- [171] I. Gödény, D. Beke and G. Groma, *phys. stat. sol. (a)* **32**, 195 (1975).
- [172] I. Gödény, D.L. Beke, F.J. Kedves and G. Groma, *Z. fur Metallkde* **72**, 97 (1981).
- [173] H.B. Tarko and M.E. Fisher, *Phys. Rev. Lett.* **31**, 926 (1973).
- [174] J.E. Reynolds, B.L. Averbach, M. Cohen and J.E. Hilliard, *Acta metall.* **5**, 29 (1957).
- [175] K. Yaldram and K. Binder, *Acta metall. mater.* **39**, 707 (1991).
- [176] P. Wiltzius, F.S. Bates and S.B. Dierker, *Phys. Rev. A* **36**, 2991 (1987).
- [177] N.H. March and M.P. Tosi, *Atomic Dynamics in Liquids* (MacMillan, London, 1976).
- [178] S. Spooner, "A Small-Angle Neutron Scattering Study of the Decomposition of Fe-28Cr-10.5Co" in *Kinetics of Aggregation and Gelation*, edited by F. Family, D.P. Landau (Elsevier Science Publishers, B.V., 1984), p. 67.
- [179] K. Kawasaki and Y. Enomoto, *Physica A* **510**, 463 (1988).
- [180] Y. Enomoto and K. Kawasaki, *Acta metall.* **37**, 1399 (1989).
- [181] P. Fratzl, F. Langmayr, G. Vogl and W. Miekeley, *Acta metall. mater.* **39**, 753 (1991).
- [182] N. Cowlam, *Met. Sci.* **12**, 483 (1978).
- [183] K.R. Elder, B. Morin, M. Grant and R.C. Desai, *Phys. Rev. B* **44**, 6673 (1991).
- [184] M. Sutton, S.G.J. Mochrie, T. Greytak, S.E. Nagler, L.E. Berman, G.A. Held and G.B. Stephenson, *Nature* **352**, 608 (1991).